

TECHNISCHE UNIVERSITÄT MÜNCHEN

Walter Schottky Institut und Physik-Department

**Ultrafast Photocurrents and Terahertz Radiation in
Gallium Arsenide and Carbon based Nanostructures**

Hans Leonhard Prechtel

Vollständiger Abdruck der von der Fakultät für Physik der Technischen Universität München zur Erlangung des akademischen Grades eines

Doktors der Naturwissenschaften

genehmigten Dissertation.

Vorsitzender: Univ.-Prof. Dr. M. Zacharias

Prüfer der Dissertation:

1. Univ.-Prof. Dr. A. Holleitner
2. Univ.-Prof. Dr. D. Grundler

Die Dissertation wurde am 05.07.2011 bei der Technischen Universität München eingereicht und durch die Fakultät für Physik am 20.07.2011 angenommen.

1. Auflage August 2011

Copyright 2011 by

Verein zur Förderung des Walter Schottky Instituts der Technischen Universität München e.V., Am Coulombwall 4, 85748 Garching.

Alle Rechte vorbehalten. Dieses Werk ist urheberrechtlich geschützt. Die Vervielfältigung des Buches oder von Teilen daraus ist nur in den Grenzen der geltenden gesetzlichen Bestimmungen zulässig und grundsätzlich vergütungspflichtig.

Titelbild: **Center:** Artistic view of the laser-based measurement scheme developed in this thesis. With kind support of Christoph Hohmann, *Nanosystems Initiative Munich* (NIM).

Upper inset: Scanning electron micrograph of a suspended gallium arsenide nanowire contacted in a metal stripline circuit by focused-ion-beam deposition of platinum/carbon. Scalebar, 3 µm.

Lower inset: Scanning electron micrograph of a suspended carbon nanotube network grown by chemical vapor deposition and contacted in a metal stripline circuit. Scalebar, 3 µm.

Druck: Printy Digitaldruck, München (<http://www.printy.de>)

ISBN: 978-3-941650-31-2

Summary

In this thesis we developed a measurement technique based on a common pump-probe scheme and coplanar stripline circuits that enables time-resolved photocurrent measurements of contacted nanosystems with a micrometer spatial and a picosecond time resolution. The measurement technique was applied to low-temperature grown gallium arsenide (LT-GaAs), carbon nanotubes (CNTs), graphene, and *p*-doped gallium arsenide (GaAs) nanowires.

The various mechanisms responsible for the generation of current pulses by pulsed laser excitation were reviewed. Furthermore the propagation of the resulting electromagnetic radiation along a coplanar stripline circuit was theoretically and numerically treated.

The ultrafast photocurrent response of low-temperature grown GaAs was investigated. We found two photocurrent pulses in the time-resolved response. We showed that the first pulse is consistent with a displacement current pulse. We interpreted the second pulse to result from a transport current process. We further determined the velocity of the photo-generated charge carriers to exceed the drift, thermal and quantum velocities of single charge carriers. Hereby, we interpreted the transport current pulse to stem from an electron-hole plasma excitation.

We demonstrated that the photocurrent response of CNTs comprises an ultrafast displacement current and a transport current. Therefore, CNT networks can be exploited as ultrafast photodetectors with a switching time in the picosecond timescale. The data further suggested that the photocurrent is finally terminated by the recombination lifetime of the charge carriers. To the best of our knowledge, we presented in this thesis the first recombination lifetime measurements of contacted, suspended, CVD grown CNT networks.

In addition, we studied the ultrafast photocurrent dynamics of freely suspended graphene contacted by metal electrodes. At the graphene-metal interface, we demonstrated that built-in electric fields give rise to a photocurrent with a full-

Summary

width-half-maximum of a few picoseconds and that a photo-thermoelectric effect generates a current with a decay time of about hundred picoseconds. Furthermore, we showed that in optically pumped graphene electromagnetic radiation up to 1 THz is generated.

We also investigated the time-integrated photocurrent and photoconductance processes of suspended *p*-doped gallium arsenide nanowires contacted by a focused ion beam deposition technique. The observed photocurrent is generated at the Schottky contacts between the nanowire and metal source-drain electrodes, while the observed photoconductance signal can be explained by a photogating effect induced by optically generated charge carriers located at the surface of the nanowire. Both optoelectronic effects are sensitive to the polarization of the exciting laser field, enabling polarization dependent photodetectors.

We furthermore studied the time-resolved photocurrent dynamics of *p*-doped gallium arsenide nanowires lying on a sapphire substrate and contacted by optical lithography. In the experiments we were able to resolve displacement currents, transport currents of holes, as well as carrier lifetime limited currents. Our results are very well reproduced by numerical simulations of bulk GaAs photoswitches performed by Dunn et al. We were able to spatially relate the time-integrated measurements to the time-resolved measurements. We discovered that the time-integrated measurements are dominated by a transport current, which is limited by the recombination lifetime of photo electrons and holes in the GaAs nanowire. The data further suggested that a photo-thermoelectric current is generated in the nanowires for excitation close to the contacts. There, we found a photocurrent with an exponential decay of only a few picoseconds.

Zusammenfassung

In der vorliegenden Arbeit wurde eine optoelektronische Messtechnik entwickelt, die auf einem bekannten Pump-Probe-Schema in Verbindung mit Wellenleiterschaltkreisen aufbaut. Die Messtechnik ermöglicht die optoelektronische Charakterisierung von Nanostrukturen mit einer Mikrometer-Ortsauflösung und Pikosekunden-Zeitauflösung. Mit dieser Messtechnik wurden bei niedriger Temperatur gezüchtetes Galliumarsenid (LT-GaAs), Kohlenstoff-Nanoröhren (KNR), Graphen und Galliumarsenid (GaAs) Nanodrähte untersucht.

Zunächst wurde ein Überblick über verschiedene, kurze Strompulse erzeugende Mechanismen gegeben, welche bei gepulster Laseranregung auftreten können. Die Propagation der dabei entstehenden elektromagnetischen Strahlung entlang eines Wellenleiterschaltkreises wurde theoretisch und mit numerischen Simulationen behandelt.

Die ultraschnelle Photostromantwort von LT-GaAs wurde mittels der entwickelten Messtechnik untersucht. Dabei wurden zwei Photostrompulse in den zeitauflösten Messungen entdeckt. Es wurde gezeigt, dass der erste Puls einem Verschiebungsstrompuls entspricht. Der zweite Puls wurde als ein Transportstrom interpretiert. Des Weiteren wurde die Geschwindigkeit der optisch erzeugten Ladungsträger bestimmt. Die dabei ermittelte Geschwindigkeit übersteigt typische Driftgeschwindigkeiten, thermische Geschwindigkeiten und Quantengeschwindigkeiten von einzelnen Ladungsträgern. Daher wurde gefolgert, dass der Transportstrompuls durch eine Elektron-Loch-Plasma-Anregung erzeugt wird.

Es wurde gezeigt, dass die ultraschnelle Photostromantwort eines freitragenden Netzwerkes aus Kohlenstoff-Nanoröhren einen Verschiebungsstrom und einen Transportstrom umfasst. Daher können derartige Kohlenstoff-Nanoröhren-Netzwerke in ultraschnellen Photodetektoren mit Schaltzeiten im Pikosekunden-Bereich Einsatz finden. Die Messdaten legen des Weiteren nahe, dass der Photostrom durch die Rekombination der optisch erzeugten Ladungsträger zeitlich limitiert ist. Nach

Zusammenfassung

unserem bestem Wissen wurde in dieser Arbeit zum ersten Mal die Rekombinationslebensdauer in einem kontaktierten, freitragenden, CVD-gezüchteten Kohlenstoff-Nanoröhren-Netzwerk bestimmt.

Des Weiteren wurde die ultraschnelle Photostromantwort von kontaktiertem und freitragendem Graphen untersucht. Es wurde gezeigt, dass intrinsische elektrische Felder am Graphen-Metall-Übergang einen Verschiebungsstrom mit einer Halbwertsbreite von wenigen Pikosekunden erzeugen, sowie dass dort ein photothermoelektrischer Strom mit einer Abklingzeit im Bereich von 130 Pikosekunden entsteht. Das optische Pumpen des freitragenden Graphen hingegen erzeugt elektromagnetische Strahlung im Frequenzbereich bis 1 THz.

Es wurden auch die zeitintegrierten Photostrom- und Photoleitwertsprozesse in freitragenden, *p*-dotierten GaAs-Nanodrähten untersucht, welche mittels eines Fokussierten-Ionen-Strahl-Verfahrens kontaktiert wurden. Dabei wurde ein Photostromprozess an den Schottky-Kontakten zwischen dem Nanodraht und den Metallkontakten beobachtet. Der beobachtete Photoleitwertsprozess konnte durch einen Photogatingprozess erklärt werden, der durch die optisch erzeugten Ladungsträger an der Oberfläche des Nanodrahtes hervorgerufen wird. Beide optoelektronischen Effekte reagieren empfindlich auf die Polarisation des anregenden Laserlichtes, wodurch ein polarisationsempfindlicher Photodetektor ermöglicht wird.

Schließlich wurden die zeitaufgelösten Photostromdynamiken in einem *p*-dotierten GaAs Nanodraht untersucht, welcher auf einem Saphir-Substrat aufliegt und mittels optischer Lithographie kontaktiert wurde. In diesen Experimenten konnten Verschiebungsströme, Loch-Transportströme und Ladungsträgerlebenszeit-limitierte Ströme identifiziert und zeitlich aufgelöst werden. Die Messungen wurden sehr gut durch numerische Simulationen eines Volumen-GaAs Photoschalters von Dunn et al. reproduziert. Die zeitintegrierten Messungen konnten den zeitaufgelösten Messungen zugeordnet werden. Dabei stellte sich heraus, dass die zeitintegrierten Messungen durch einen Transportstrom dominiert werden, welcher durch die Rekombinationslebensdauer der optisch erzeugten Elektronen und Löcher im GaAs-Nanodraht begrenzt ist. Die Messungen legten die Vermutung nahe, dass ein photothermoelektrischer Strom in den Nanodrähten bei Anregung in der Nähe der Kontakte erzeugt wird. Dieser Strom klingt auf einer Zeitskala von wenigen Pikosekunden exponentiell ab.

Contents

Summary	I
Zusammenfassung	III
Introduction	1
1 Generation of current pulses and electromagnetic radiation	5
1.1 Charge carrier lifetime limited current	7
1.2 Displacement currents by nonuniform illumination	9
1.3 Transport current	11
1.4 Photo-thermoelectric current	13
1.5 Generation and propagation of electromagnetic radiation	16
1.6 Propagation of voltage pulses on striplines	18
1.6.1 Dispersion	19
1.6.2 Attenuation	21
1.6.3 Propagation of a Gaussian-shaped pulse	23
1.7 Localized electric field redistribution at zero propagation distance .	24
1.8 Spurious current pulses in stripline circuits	26
2 Principles of time-resolved photoresponse sampling in stripline circuits	27
2.1 Optical and electronic measurement setup	27
2.2 Experimental details	29
2.2.1 Optical setup	30
2.2.2 Electronic setup	32
2.3 Sample preparation	33
2.3.1 Wafer materials for the sampling circuit	33
2.3.2 Optical lithography	34
2.3.3 Mask design	35
2.3.4 Definition of a trench in the stripline	36
2.3.5 Growth of carbon nanotubes	38
2.3.6 Growth and transfer of graphene	39

Contents

2.3.7	Growth of GaAs nanowires	40
2.3.8	Transfer and contacting of nanowires utilizing FIB	41
2.3.9	Transfer and contacting of nanowires by optical lithography .	42
3	Spatially resolved ultrafast transport current in GaAs photoswitches	43
3.1	Sample preparation and experimental procedure	44
3.2	Time-resolved displacement currents	44
3.3	Time-resolved transport currents	47
3.4	Measurements at zero-propagation length	48
3.5	Carrier velocities and plasma oscillations	48
3.6	Conclusions	53
4	Time-resolved picosecond photocurrents in contacted carbon nanotubes	55
4.1	Optoelectronic properties of carbon nanotubes	56
4.2	Carbon nanotubes in a stripline circuit	56
4.3	Electric fields in a carbon nanotube network	60
4.4	Time-resolved displacement and transport currents	61
4.5	Carrier recombination lifetime	65
4.6	Temperature dependence of I_{Sampling}	65
4.7	Conclusions	68
5	Ultrafast photocurrents and terahertz generation in graphene	71
5.1	Optoelectronic properties of graphene	72
5.2	Experimental procedure	73
5.3	Photocurrent generation at a graphene-metal interface	73
5.3.1	Displacement current	76
5.3.2	Photo-thermoelectric current	79
5.4	Terahertz generation in freely suspended graphene	82
5.5	Conclusions	87
6	Photocurrent dynamics in GaAs nanowires	89
6.1	Introduction to GaAs nanowires	90
6.2	Optoelectronic properties of nanowires contacted by focused ion beam	90
6.2.1	Photocurrent and photoconductance	91
6.2.2	Dielectric confinement	94
6.2.3	Defect enhanced charge carrier recombination	95
6.3	Photocurrent dynamics in nanowires contacted by optical lithography	96
6.3.1	Time-integrated photocurrent measurements	97
6.3.2	Spatially resolved measurements of I_{Sampling}	98
6.3.3	Fitting the data	99
6.3.4	Current amplitude considerations	103
6.3.5	Displacement and thermoelectric current	104

6.3.6 Recombination lifetime τ_{rec}	106
6.3.7 Transport current of holes	107
6.3.8 I_{Sampling} for $V_{\text{SD}} = 0\text{V}$	109
6.4 Conclusions	111
7 Conclusions and outlook	113
A Properties of stripline circuits	117
B Additional data	119
B.1 Time-resolved photocurrent measurements on LT-GaAs without Al-GaAs	119
B.2 Time-resolved photocurrent measurements on LT-GaAs at room temperature and at 77K	121
B.3 Measurements of a bare trench	122
B.4 Spatially resolved photocurrent scans of graphene at 77K	124
B.5 Raman measurements of carbon nanotubes	125
B.6 Raman measurements of graphene	128
C Numerical Simulations	131
C.1 Finite-element-simulation parameters	131
C.1.1 Transient thermal transport of gold on sapphire	131
C.1.2 Effective index of diffraction simulation parameters	131
C.2 Finite-Differences-Time-Domain simulation parameters	132
Publications	135
Bibliography	137
Acknowledgements	157

Contents

Introduction

The conversion of light to other forms of energy, for example to heat or electrical energy, is of great importance for solving the energy demand of modern society. The underlying physical processes of the conversion are in principle known, but the dynamics (i.e. the speed) of the reactions are still subject to fundamental research. Nevertheless, for a complete physical understanding and a consequent further development also the knowledge of the underlying dynamics is needed.

Experimentally, the investigation of the conversion of light to current (e.g. the photovoltaic process) has long been limited to slow dynamics. Yet, from time-resolved purely optical measurements it is known that the coupling of electrical charges to light can happen on the timescale of femtoseconds. The availability of sufficiently fast electronic equipment has been a major barrier for the electronic investigation for a long time. With the emergence of oscilloscopes reaching the 100 GHz regime, intrinsic properties of the devices (RC-time, impedance mismatch, small signal-to-noise ratio) are now limiting the investigations.

In the experiments presented in this thesis we utilize the high bandwidth of pulsed laser sources to investigate the electronic response of contacted, nanostructured devices to the excitation with light. We develop a measurement technique based on a common pump-probe scheme and coplanar stripline circuits, that enables a time-resolved photocurrent measurement with a micrometer spatial and a picosecond time resolution. In this technique, we avoid the limitations and problems posed by standard electrical measurements:

- In the presented measurement technique, the time-resolution is governed by the optical measurement setup. Thereby we are not limited to the bandwidth of electrical equipment.
- We perform an electrical on-chip, low-frequency current measurement and consequently avoid a wave-impedance mismatch of the device under test with

Introduction

the electrical circuitry.

- We excite the device under test with light. Thereby we can probe states far away from the Fermi level. This is in contrast to purely electrical measurements, where only states close to the Fermi-level can be investigated.
- The device under test is optically excited at the repetition rate of the laser. Several million single excitations contribute to the measurement signal at typical integration or averaging times. The signal-to-noise ratio is thereby greatly improved.

We utilize this measurement technique to investigate fundamental optoelectronic processes in carbon based and gallium arsenide based nanostructures. Carbon based nanomaterials have attracted great attention in the scientific community in the last decade. The base material carbon is inherently non-toxic, sustainable, and abundant. For example, carbon nanotubes are rolled-up sheets of graphitic atomic monolayers with nanometer diameter and micrometer length. Potential applications exploit for example their one-dimensional electronic structure or their extraordinary mechanical stiffness. Andre Geim and Konstantin Novoselov were awarded the Nobel Price in Physics 2010 '*for groundbreaking experiments regarding the two-dimensional material graphene*' [Nob11]. Graphene, the graphitic monolayer with C-atoms arranged in a hexagonal lattice, is praised to substitute silicon as the building material for future computer chip generations. Even though this scenario is fairly unlikely, graphene exhibits unique physical properties which spur fundamental research and could eventually lead to specific applications in other fields. For example, the industrial production of 30-inch transparent graphene electrodes for touch-screen applications has been demonstrated [Bae10]. In this manner, the use of the expensive and scarce material indium in the transparent conductor indium-tin-oxide (ITO) can be avoided.

In nanostructures a wealth of optoelectronic processes occur depending on the material, the excitation position and further experimental parameters. We are able to identify and resolve the time evolution of displacement currents, the transport and the recombination lifetime of photogenerated electrons and holes, plasmons, as well as photo-thermoelectric effects in our measurements.

On the one hand, our experiments clarify and characterize the current generation mechanisms in the nanostructures (e.g. the controversy about intrinsic fields and photo-thermoelectric effects at a graphene-metal interface). On the other hand,

they open the possibility of building future optoelectronic devices, for example ultrafast photodetectors made out of carbon nanotubes or terahertz lasers based on optically pumped graphene.

This thesis is structured into 7 chapters:

- In chapter 1 we give a brief review of various mechanisms responsible for the generation of current pulses by pulsed laser excitation. The propagation of the resulting electromagnetic radiation along a coplanar stripline circuit is also discussed.
- In chapter 2 we introduce the measurement principles for spatially and time-resolved photocurrent measurements. The optical and electronic measurement setup as well as the sample processing is described in detail.
- In chapter 3 we investigate the ultrafast photocurrent response of low-temperature grown gallium arsenide.
- In chapter 4 we study the ultrafast photocurrent dynamics in freely suspended carbon nanotubes in the time-domain.
- In chapter 5 we examine the ultrafast photocurrent dynamics of freely suspended graphene contacted by metal electrodes.
- In chapter 6 we investigate the time-integrated photocurrent and photoconductance processes of suspended *p*-doped gallium arsenide nanowires contacted by a focused ion beam deposition technique. We furthermore study the time-resolved photocurrent dynamics of *p*-doped gallium arsenide nanowires lying on a sapphire substrate and contacted by optical lithography.
- In chapter 7 we give a summary of the obtained results and conclude with an outlook for future experiments.

Introduction

Chapter 1

Generation of current pulses and electromagnetic radiation in stripline circuits

The irradiation of short light pulses onto a coplanar stripline circuit (CPS) or coplanar waveguide circuit (CPW) can lead to the propagation of electromagnetic radiation along the metal structure. Both circuits consist of thin metal strips arranged on a semiconducting substrate, and are schematically depicted in Figure 1.1. The illuminated semiconductor surface and the adjacent metal contacts are generally referred to as a photoswitch (PS). In this chapter, I will give a brief review of various mechanisms responsible for the generation of propagating electromagnetic radiation. This chapter does not intend to be complete. For example, rather slow processes like the dynamics of a surface voltage [Ros08] and bolometric photoconductance effects [Itk06] acting within a photoswitch, are intentionally omitted.

In section 1.1 a basic model of charge carrier lifetime limited current bursts is introduced. This model assumes among other things ohmic contacts and uniform illumination of photoswitches. The non-uniform illumination of photoswitches generates a displacement current, which is described in section 1.2. The optical excitation of a semiconducting substrate can generate electrons and holes, which propagate due to drift and diffusion onto the metal contacts. The contribution of these photocarriers to the time-resolved current is described in terms of a transport current in section 1.3. The absorption of intense laser light can create a local temperature increase, which can lead to a photo-thermoelectric current. Section 1.4

introduces this concept and comprises basic numerical simulations of the temperature decay of a heated metal contact. The irradiation of short light pulses can result in the generation of an oscillating electromagnetic field in the photoswitch. The generation of such electromagnetic radiation and its propagation along the stripline circuit is described in section 1.5. The electromagnetic pulses experience dispersion and attenuation during propagation along the stripline, independent of the generation mechanism. Section 1.6 briefly describes the influence of the stripline geometry and the substrate material on the propagating electromagnetic radiation. The field redistribution after optical excitation at zero propagation distance is described in section 1.7. The effects described there apply also to time-resolved measurements of photoswitches not embedded in stripline circuits. The chapter ends in section 1.8 with some general remarks on the analysis of time-resolved measurements in stripline circuits.

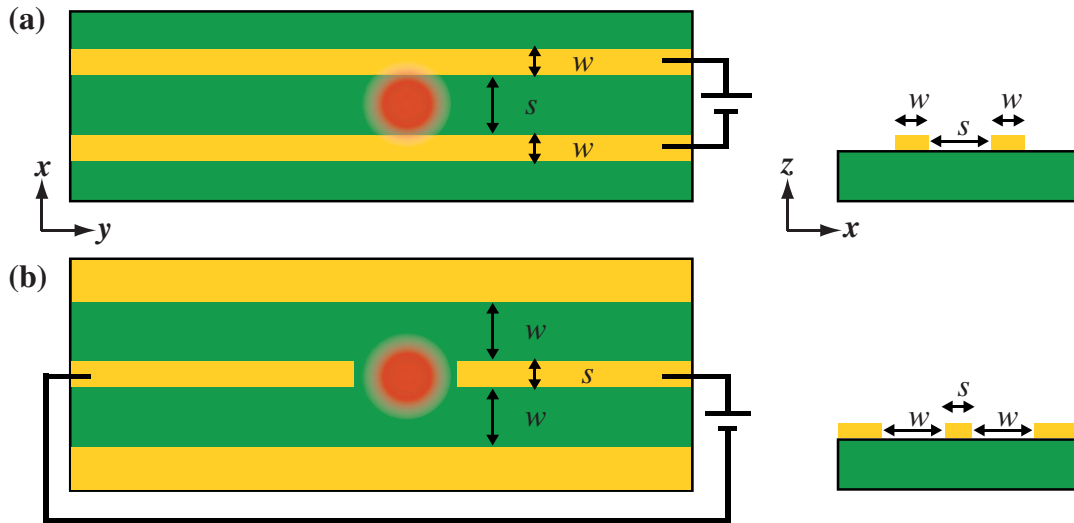


Figure 1.1 — (a) Schematic top view (left) and side view (right) of a coplanar stripline circuit (CPS) and a focused excitation laser beam. The width w and separation s of the metal strips (indicated in yellow) is used to describe the dimension of the circuit, often abbreviated with $w/s/w[\mu\text{m}]$ [Has90]. **(b)** Same view of a coplanar waveguide circuit (CPW). Here, the width w and separation s refer to the non-metal regions.

1.1 Charge carrier lifetime limited current

In 1983 D.H. Auston investigated the '*Impulse response of photoconductors in transmission lines*' [Aus83]. The following section is based on his findings. The presented model is valid in case that:

1. retardation effects can be neglected, i.e. the dimensions of the photoconductor and the transmission-line cross section are small relative to the distance that a signal travels in the shortest time of interest;
2. the capacitance of the transmission-line is time-invariant;
3. the current density is linearly proportional to the local electric field;
4. the contacts between the metal stripline and the photoconductor are ohmic;
5. the photoconductor is uniformly illuminated.

The first three conditions are usually fulfilled in typical transmission-line geometries. Furthermore, ohmic contacts can be obtained for common semiconductors, for example by annealing of gold based contacts on GaN [Koi99]. Low-temperature-grown gallium arsenide (LT-GaAs), a widely used photoconductor with short carrier lifetime, exhibits ohmic contacts with gold without the need of annealing [Yam90]. Finally, uniform illumination of the photoconductor between the metal contacts can be achieved by focusing the incident light to a focus spot of appropriate size (see [Aus83] for optimum focusing conditions).

Assuming furthermore a photoconductor with a carrier relaxation time τ_r and a photoconductance $G(t)$ of

$$G(t) = G_0 + g(t) = \begin{cases} 0; & t < 0 \\ g_0 e^{-t/\tau_r}; & t \geq 0 \end{cases}. \quad (1.1)$$

Then the following expression for the time-dependent voltage wave $v(t)$ along a CPS/CPW due to the light pulse can be derived in this model [Aus83]:

$$v(t) = \frac{g_0 V_b}{2C_g} \left| \frac{e^{-t/\tau_r} - e^{-t/\tau_C}}{\frac{1}{\tau_C} - \frac{1}{\tau_r}} \right| \quad (1.2)$$

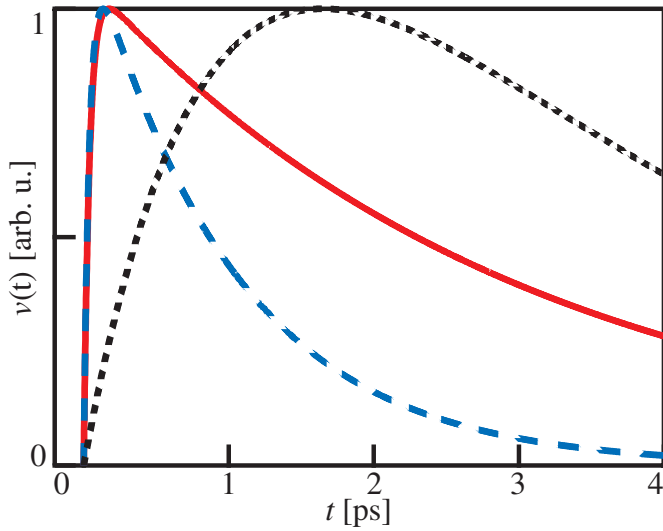


Figure 1.2 — Time-dependent normalized voltage $v(t)$ at a photoswitch due to an incident light pulse for different time-constants τ_C and τ_r . The dynamics are governed by equation 1.2. Blue dashed line: $\tau_C = 0.04\text{ ps}$ and $\tau_r = 1\text{ ps}$. Red solid line: $\tau_C = 0.04\text{ ps}$ and $\tau_r = 3\text{ ps}$. Black dotted line: $\tau_C = 1\text{ ps}$ and $\tau_r = 3\text{ ps}$.

with the capacitive time-constant $\tau_C = 2Z_0C_g$, V_b a DC-bias at the transmission line gap, C_g the capacity of the gap and Z_0 the characteristic impedance of the transmission line. According to eq. 1.2, τ_C and τ_r determine the dynamics of the illuminated photoswitch. C_g and Z_0 , and therefore τ_C , can be evaluated using for example a finite element method [COM07]. Typical values of the impedance Z_0 and the capacity per unit length C_g for micrometer sized striplines are on the order of 40 to 200 Ω and ten to hundred pF/m, respectively. Assuming an illuminated gap length of 10 μm , an upper limit of τ_C can be estimated to be 0.4 ps for typical transmission lines [Gup96]. For the coplanar stripline geometry employed in the experiments in chapter 4 and 5, the impedance was calculated to be $Z_0 = 178.9\Omega$ with a capacitance of $40 \pm 11\text{ pF m}^{-1}$ (see section A). This results in $\tau_C \approx 50\text{ fs}$. Typical recombination lifetimes τ_r of fast photoconductors are in the order of hundreds of femtoseconds, and therefore much larger than τ_C . Since $\tau_C < \tau_r$, in equation 1.2 the risetime of $v(t)$ is determined by τ_C and the decay by τ_r . Figure 1.2 illustrates the dependence of $v(t)$ on τ_C and τ_r . For the same capacitive time-constant $\tau_C = 40\text{ fs}$ and varying τ_r from 1 ps to 3 ps, only the decay of $v(t)$ changes (dashed blue and red line). An increase of τ_C to 1 ps and keeping $\tau_r = 3\text{ ps}$ results in a slower rise of $v(t)$ along with a time-delayed maximum.

We can therefore conclude, that the decay of the voltage-wave $v(t)$ at a photoswitch is governed by the recombination lifetime of the optically excited charge carriers, provided that τ_C is sufficiently small and that the conditions mentioned above (especially ohmic contacts and uniform illumination) are satisfied. An example of a charge carrier lifetime limited current can be found in chapter 4 and in [Ket86, Pre11b]. We finally note, that photoswitches with short carrier lifetime τ_r are often called *Auston switches*.

1.2 Displacement currents by nonuniform illumination

Subpicosecond electrical pulse generation using nonuniform illumination has been experimentally [Kro89, Ale94] and theoretically [Pet87, San89, Zho95b, Zho96] investigated. A comprehensive review of experimental and theoretical findings is given in [Zho95a]. The decay of the voltage-wave $v(t)$ after nonuniform optical pulse-excitation is, in contrast to the case of uniform illumination, not governed by the charge carrier lifetime τ_r . The physical mechanism is schematically illustrated in Figure 1.3. Here, we consider a $15\mu\text{m}$ wide semiconducting photoswitch with a DC-Bias V_{SD} applied to two ohmic metal contacts. The resulting band diagram $E(x)$ is illustrated in Figure 1.3a. The electric field $\mathbf{F}(x)$ is constant between the metal contacts (see Figure 1.3b, solid black line). Optical excitation with a laser pulse (with energy E_{Laser}) is only locally applied, e.g. in the middle of the photoswitch. The local optical excitation of charge carriers from the valence band (VB) to the conduction band (CB) results in a local increase of photoconductance. These charge carriers redistribute in the electric field \mathbf{F} generating a depolarization field antiparallel to \mathbf{F} . The electric field \mathbf{F} in the illuminated area is therefore effectively screened, while the field in the unilluminated area is increased to maintain the applied bias V_{SD} (see Figure 1.3b, dashed red line). According to Maxwell's equation a temporal field change generates a transient displacement current density \mathbf{j}_d [Zho95b]:

$$\mathbf{j}_d = \epsilon_r \epsilon_0 \frac{\partial \mathbf{F}}{\partial t} \quad (1.3)$$

with ϵ_r the relative dielectric constant, ϵ_0 the vacuum permittivity. This displacement current does not depend on the charge carrier lifetime τ_r but is an instantaneous electromagnetic field response to an abrupt local conductance change. Only an externally applied or intrinsic electric field \mathbf{F} and an abrupt conductance change

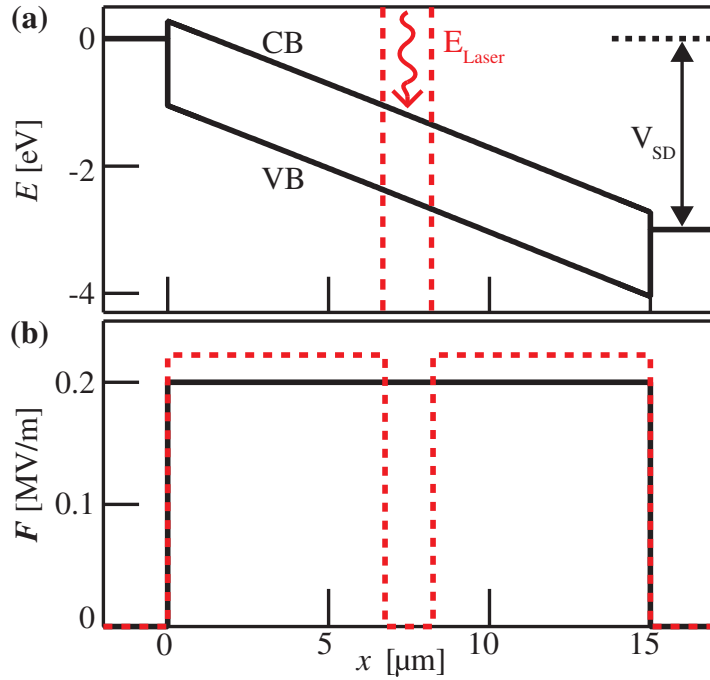


Figure 1.3 — (a) Band diagram $E(x)$ of a $15\text{ }\mu\text{m}$ wide semiconducting photoswitch with a DC-Bias V_{SD} applied to two ohmic metal contacts. A laser pulse (with energy E_{Laser}) focused to a small region in between the contacts excites charge carriers from the valence band (VB) to the conduction band (CB). **(b)** Electric field $F(x)$ before (black line) and directly after (dashed red line) illumination [Pre10].

is required for the generation of short displacement current pulses. Examples for picosecond electrical pulse generation in a photoconductive switch with long charge carrier lifetime τ_r can be found in [Kro89, Pre11b]. It should be noted here, that experimentally a displacement current can also be observed for uniform illumination, since the photoconductor underneath the metal contacts will naturally not be illuminated. Yet, the absorption profile of the incident light in the semiconductor will lead to the excitation of charge carriers at a certain depth, causing effectively a non-illuminated region between the metal contacts and the photo-charge carriers [Dun96, Wil97].

1.3 Transport current

Section 1.1 describes the dynamics of an optically generated voltage pulse $v(t)$ by the interplay of a capacitive response time τ_C and a photoconductance decay with characteristic timescale τ_r (usually associated with the charge carrier lifetime). This simple model omits drift and diffusion of the photo-charge carriers. While the displacement current response is an instantaneous response (neglecting retardation effects), a current associated with the transport of charge carriers is delayed by the propagation of the charge carriers onto the metal contacts. Experimental observation of transport currents can be found in [Mey88], [Boe93], [Son93], [Ale94] and [Pre10]. A numerical treatment of displacement and electron and hole transport current has been conducted in [Pet87], and 2-D Monte-Carlo and 1-D drift-diffusion simulations are carried out in [Dun94] and [Dun96], respectively. A comparison of a 1-D and 2-D drift-diffusion model including diffraction is carried out in [Wil97]. This section reviews the drift-diffusion model and results of [Dun96].

Generally, the transport current density \mathbf{j}_c is composed of the electron current density \mathbf{j}_n and the hole current density \mathbf{j}_p :

$$\mathbf{j}_c = \mathbf{j}_n + \mathbf{j}_p \quad (1.4)$$

In a simple drift-diffusion model the following set of equations needs to be solved.

$$\frac{\partial n}{\partial t} = -R(t) + \frac{1}{q} \frac{\partial \mathbf{j}_n}{\partial x} + G(t) \quad (1.5)$$

and

$$\frac{\partial p}{\partial t} = -R(t) - \frac{1}{q} \frac{\partial \mathbf{j}_p}{\partial x} + G(t). \quad (1.6)$$

Here, q is the elementary charge, n and p are the electron and hole densities, and $G(t)$ and $R(t)$ are the electron-hole-pair generation and recombination rates. The electric field \mathbf{F} is determined by

$$\frac{\partial \mathbf{F}}{\partial x} = \frac{q}{\epsilon_r \epsilon_0} (p - n + N), \quad (1.7)$$

where ϵ_r is the relative dielectric constant, ϵ_0 is the vacuum permittivity, and N is the net donor density. Furthermore, drift and diffusion of the charge carriers is

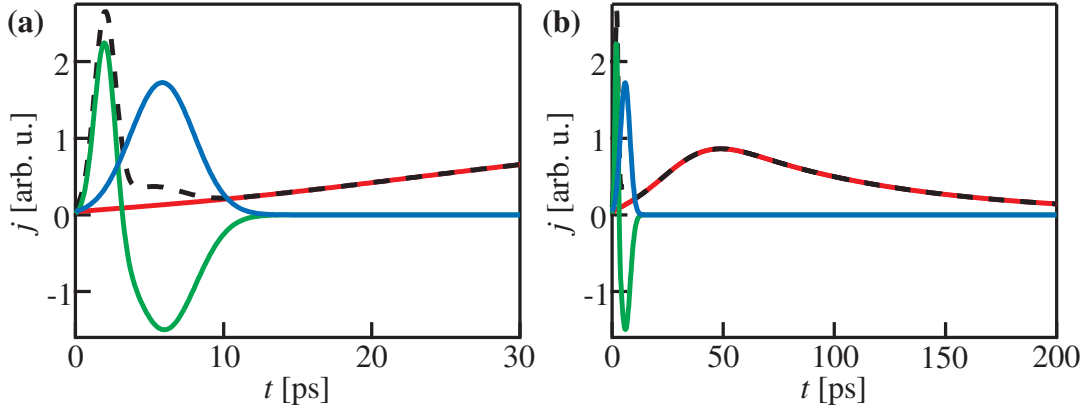


Figure 1.4 — Typical currents in a GaAs photoswitch. The displacement current density \mathbf{j}_d is depicted in green, the electron current density \mathbf{j}_n in blue, the hole current density \mathbf{j}_p in red, and the resulting total current density \mathbf{j}_0 in dashed black. The currents are depicted between zero and 30 ps in (a) and up to 200 ps in (b). Adapted from [Dun96].

described by:

$$\mathbf{j}_n(x, t) = qv_n(\mathbf{F})n(x, t) + qD_n \frac{\partial n(x, t)}{\partial x} \quad (1.8)$$

and

$$\mathbf{j}_p(x, t) = qv_p(\mathbf{F})p(x, t) - qD_p \frac{\partial p(x, t)}{\partial x}. \quad (1.9)$$

The first and the second term in this equation describe the drift and the diffusion of the charge carriers, respectively. Here, D_n and D_p are the electron and hole diffusion constants, and $v_n(\mathbf{F})$ and $v_p(\mathbf{F})$ are the electric field dependent electron and hole velocities. The resulting electron and hole transport current densities \mathbf{j}_n and \mathbf{j}_p exhibit different temporal dynamics due to the usually differing electron and hole mobilities. Figure 1.4 depicts the dynamics of the different current densities in a typical GaAs photoswitch. For a 3 μm-wide GaAs photoswitch, the faster electrons reach the anode 5 ps after the displacement current peak, while the holes take ~ 50 ps to reach the cathode [Dun96]. The width of the electron transport peak is only ~ 4 ps. In this scenario, the electron transport current \mathbf{j}_n furthermore influences the electric field distribution at the anode, effectively reducing the local electric field. This in turn generates a displacement current \mathbf{j}_d in the opposite direction and with similar magnitude to the electron transport current. Therefore, a second peak appears in the total current after the displacement current peak (see Figure 1.4), which mainly consists of the electron transport current \mathbf{j}_n which is reduced by a secondary dis-

placement current. A later current increase on a rather slow timescale can then be associated with the transport current density \mathbf{j}_p of holes. The decay of the hole transport current is governed by the charge carrier recombination dynamics on a typical timescale of $\tau_r \approx$ hundreds of ps and by the arrival of the holes at the metal contact.

1.4 Photo-thermoelectric current

For a bulk semiconductor, the densities of charge carriers n and p can be described by a Fermi-Dirac distribution:

$$n \propto \int_{E_c}^{\infty} \frac{\sqrt{E}}{1 + e^{\frac{E-E_F}{k_b T}}} dE \quad (1.10)$$

$$p \propto \int_{-\infty}^{E_v} \frac{-\sqrt{E}}{1 + e^{\frac{E-E_F}{k_b T}}} dE, \quad (1.11)$$

with k_b Boltzmann's constant, E_v the valence band energy, E_c the conduction band energy, E_F the Fermi energy and T the temperature. The densities n and p increase with temperature T . Therefore, spatial gradients $\partial n / \partial x$ and $\partial p / \partial x$ between hot and cold regions are created. Charge carriers will then diffuse from areas of high temperature and respective high densities towards areas of lower temperature and respective lower charge carrier densities. If the densities and/or diffusivities for electrons and holes are unequal, a potential difference U_{thermo} is generated between the hot and cold regions. Generally, the associated thermovoltage V_{thermo} depends linearly on the temperature difference ΔT between the hot and the cold region [Row05, Sny08]:

$$V_{\text{thermo}} = S \cdot \Delta T. \quad (1.12)$$

The temperature dependent material parameter S is the thermopower, also known as Seebeck coefficient. The thermovoltage at a junction of two materials with different thermopowers S_1 and S_2 can then be expressed as [Row05]:

$$V_{\text{thermo}} = (S_1 - S_2) \cdot \Delta T. \quad (1.13)$$

If a load R is attached, this thermovoltage V_{thermo} can drive a thermocurrent I_{thermo} :

$$I_{\text{thermo}} = \frac{(S_1 - S_2) \cdot \Delta T}{R}. \quad (1.14)$$

So far, we have only considered a static temperature difference. The situation becomes more complex for excitation of a photoswitch with short light pulses. There, the change in the charge carrier densities is dominated by the interband excitation with the characteristic photon energy E_{laser} . The diffusion current will then be dominated by optically excited charge carriers with equal density $n_{\text{optical}} = p_{\text{optical}}$. An intraband relaxation of these potentially hot charge carriers by the excitation of phonons will subsequently create a temperature increase of the charge carriers and phonon baths [Sha99]. Generally, the temperature is not well defined for the case of short optical excitation, since the energy distributions of the electrons, holes and phonons are not in equilibrium on short time-scales. An analytical description of these dynamics is beyond the scope of this brief introduction.

Nevertheless one can consider the simpler case of local heating of one metal contact by a short laser pulse. Within the adiabatic approximation¹ (i.e. the charge carriers in the photoswitch follow the Fermi-Dirac distribution at every position), one can extend equation 1.14 to describe the resulting thermocurrent density in a quasi-static model:

$$\mathbf{j}_{\text{thermo}}(\vec{x}, t) = \frac{S(\vec{x}) \cdot \nabla T(\vec{x}, t)}{R}. \quad (1.15)$$

Then the resulting thermocurrent $\mathbf{I}_{\text{thermo}}$ is defined by the dynamics of the temperature profile $\nabla T(\vec{x}, t)$. Yet, the electrons in gold follow a non-Fermi energy distribution directly after femtosecond-excitation [Fan92]. Their thermalization time after a 180 fs laser-pulse excitation can be as long as $\sim 1 \text{ ps}$ [Fan92, Sun93]. For a non-transparent gold film, the electron cooling follows an exponential decay again on a 1 ps timescale [Sun93]. The cooling of the electron temperature is therefore too fast to be treated in the quasi-static approach of equation 1.15. However, the phonon temperature of the metal strip decays on a timescale of hundreds of picoseconds through transverse heat diffusion and coupling with the substrate [van88, Pad86]. The heat transport into the photoswitch is elementary for the photo-thermoelectric current, since it defines the temperature gradient along the photoswitch. However, the amount of heat transported into the photoswitch will be small compared to the

¹The change of the metal lattice temperature is slow compared to the time the charge carriers need to adopt to the temperature profile by diffusion and relaxation.

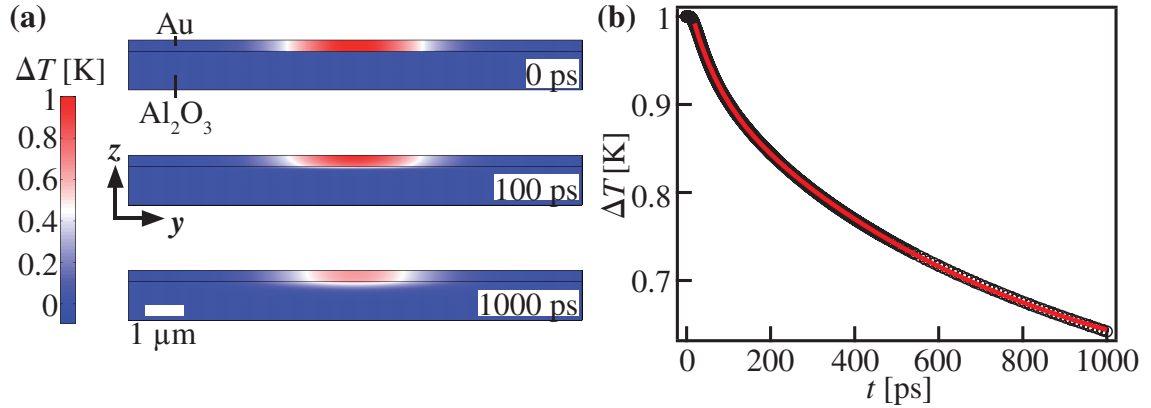


Figure 1.5 — Finite element simulation of the time evolution of the temperature profile $\Delta T(y, z, t)$ in a metal film on an insulating substrate. A Gaussian temperature profile is generated at $t = 0\text{ ps}$ in 300 nm of gold (Au), which is on top of a $1\text{ }\mu\text{m}$ thick sapphire (Al_2O_3) substrate. (a) Temperature profile $T(y, z)$ for $t = 0\text{ ps}$, $t = 100\text{ ps}$ and $t = 1000\text{ ps}$ from top to bottom plotted in color code. (b) Time evolution of the temperature ΔT at the point of the heat injection in the middle of the metal strip. For simulation parameters see Appendix C.1.1.

amount transported along the metal, especially for nanostructured photoswitches. Neglecting furthermore hot electron effects and the (phononic) heat transport into the semiconductor material, one can simplify equation 1.15:

$$\mathbf{j}_{thermo}(\vec{x}, t) = \frac{S(\vec{x})}{R} \cdot (T_{\text{metal}}(t) - T_{\text{bath}}) = \frac{S(\vec{x})}{R} \cdot \Delta T_{\text{metal}}(t) \quad (1.16)$$

with $T_{\text{metal}}(t)$ the temperature at the metal contact and T_{bath} the bath temperature. In this model the photo-thermoelectric current \mathbf{j}_{thermo} is governed only by the local temperature difference ΔT_{metal} of the metal contact.

In the remaining part of this section, we present numerical simulations to investigate the temperature decay of a thin metal film on a dielectric substrate. The time evolution of the temperature profile $\Delta T(y, z, t)$ in a gold film on a sapphire (Al_2O_3) substrate governed by heat conduction can be investigated with a finite element simulation [COM07]. Figure 1.5a shows the time-evolution of a Gaussian temperature profile² with an amplitude of $\Delta T = 1\text{ K}$ generated at $t = 0\text{ ps}$. The temperature profiles $\Delta T(y, z, t)$ for $t = 100\text{ ps}$ and $t = 1000\text{ ps}$ clearly show a decrease of temperature in the metal. Furthermore, only a small temperature increase

²The spatial profile of a focused laser beam is usually Gaussian shaped. We therefore consider an initial temperature profile $T(y, t = 0) \propto e^{-(y-y_0)^2}$.

can be found in the sapphire substrate. Figure 1.5b shows the temperature decay in the center of the Gaussian temperature profile (in the middle of the metal strip). A least-squares fit with a double-exponential decay yields decay-constants of $(63 \pm 1)\text{ps}$ and $(739 \pm 4)\text{ps}$. Even though this simulation only takes conductive heat transport into account (neglecting for example radiative heat loss and high energy electronic heat transport [Bro87, Mar93]), it already shows that a temperature decay on the timescale of hundreds of picoseconds can be expected. Therefore, a thermoelectric current can contribute to the photocurrent dynamics on a picosecond timescale.

1.5 Generation and propagation of electromagnetic radiation

The previous sections of this chapter covered mechanisms generating short current pulses in stripline circuits. In the cases described above, there is a net current flow for each excitation laser pulse. Obviously, these currents also contribute in a time-integrated photocurrent measurement. Pulsed photo-excitation of a bulk semiconductor surface can also lead to the generation of electromagnetic radiation in the THz-regime without a net-current flow between metal contacts [Zha92, Hu94, Ker97, Gli08]. Generally, the generation mechanisms for displacement currents and transport currents (see sections 1.2 and 1.3) also apply for intrinsic fields. For example surface depletion fields, p - n junction fields or strain induced piezoelectric fields are perpendicular to the surface [Zha92]. There, the resulting displacement and transport currents will also be directed perpendicular to the surface. Therefore, they will not contribute to a net-current parallel to the surface. Furthermore, the direction of these current pulses will set the polarization of the radiated electromagnetic fields according to Maxwell's equations [Hu94]. In the case of current pulses perpendicular to the surface, the radiated electric field will be polarized perpendicular to the surface. Such polarized electric fields can not be detected in a lateral stripline geometry, because there the detection is only sensitive to electric fields polarized parallel to the surface and perpendicular to the direction of propagation.

A Hertzian dipole in between two metal strips however, oscillating parallel to the surface and perpendicular to the metal strips will generate electromagnetic radiation with appropriate polarization for stripline-detection. The radiation will

couple into the stripline circuit, although no time-*integrated* current will be generated, since the time-average of the oscillation equals zero. A Finite-Differences-Time-Domain (FDTD) simulation using a freely available software package [Osk10] can be employed to investigate such a electromagnetic field generation and propagation in the time-domain. Figure 1.6a shows a sketch of a metal stripline on a gallium arsenide substrate. A source (indicated by a red arrow) located in between the metal strips generates a x -polarized, Gaussian shaped electric field with center frequency f and width Δf . Figures 1.6b and 1.6c show the spatial distribution of the x -component E_x of the electric field at the surface of the sample in a color scale. A center frequency of $f = 24\text{ THz}$ and width $\Delta f = 15\text{ THz}$ is chosen for demonstration purposes only. At $t = 0\text{ ps}$ (Figure 1.6b) the source located at $x = 35\mu\text{m}$ from the left simulation border in between the striplines is generating the electromagnetic fields. At $t = 0.3\text{ ps}$, the thereby generated electromagnetic pulse has propagated along the stripline into the center of the simulation area (Figure 1.6c). This simulation shows that electromagnetic radiation generated in between two metal strips and polarized in the x -direction couples into the stripline circuit. In a FDTD simulation the magnitude of the field-flux coupled into the stripline-circuit F_{WG} can be compared to the magnitude radiated in the direction normal to the surface F_{air} . Figure 1.6a shows sketches of $20\mu\text{m} \times 20\mu\text{m}$ sized windows used for computing the field fluxes F_{air} and F_{WG} . Both windows are set $130\mu\text{m}$ apart from the source. Figure 1.7 shows both field fluxes as a function of frequency f . In this simulation, the electric field source has a center frequency $f = 0.3\text{ THz}$ and a frequency width $\Delta f = 0.2\text{ THz}$. The field flux F_{WG} (solid black line in Figure 1.7) at the center-frequency is enhanced by a factor of about 4.6×10^4 when compared to the field flux F_{air} above the surface (dashed black line in Figure 1.7)). A further increase of the propagation distance both along the stripline and perpendicular to the surface further increases the enhancement factor. While the electric field \vec{F} of a spherical wave decreases with the distance r with $|\vec{F}| \sim r^{-1}$, it has been shown that the electromagnetic field of picosecond pulses can propagate along striplines for several millimeters with experiencing a small loss of only $\sim 35\%$ [Gri87]. Measuring the THz-wave generation on-chip in a stripline circuit is therefore several orders of magnitude more sensitive than measuring in a free-space setup, if the sensitivities of the employed THz-detectors are equal. However, omitting the trench and the metal stripline greatly reduces the field flux F_{WG} (solid red line in Figure 1.7), and in turn, the enhancement factor is reduced to 150 when compared to the field flux F_{air} above the surface (dashed red line in Figure 1.7).

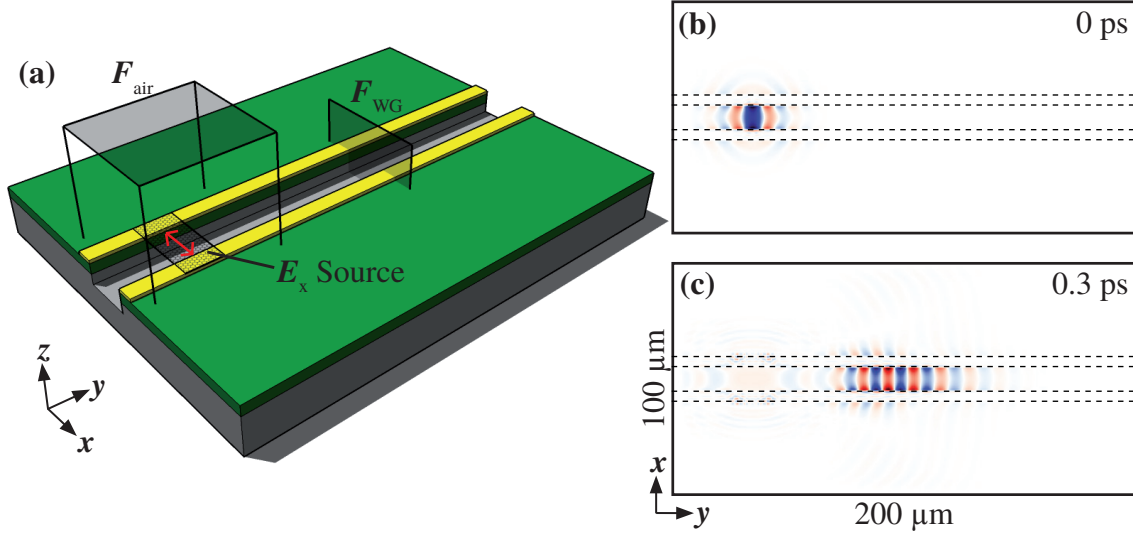


Figure 1.6 — Finite-Differences-Time-Domain (FDTD) simulation [Osk10] of electromagnetic field generation and propagation in a stripline circuit in the time-domain. A source E_x generates an x -polarized, Gaussian shaped electric field. (a) Sketch of the simulation geometry. Metal strips are indicated in yellow, gallium arsenide substrate in green and grey. F_{air} and F_{WG} indicate areas for calculating the passing field flux above and in the stripline circuit, respectively. (b) Spatial distribution of the x -component of the electric field E_x at the sample surface at $t = 0 \text{ ps}$. Striplines are indicated by dashed lines, the center frequency is $f = 24 \text{ THz}$ with a width of $\Delta f = 15 \text{ THz}$. (c) Spatial distribution of E_x for $t = 0.3 \text{ ps}$. The color scales are not normalized. For simulation parameters see Appendix C.2.

1.6 Propagation of voltage pulses on striplines

A propagating voltage-wave $v(\vec{r}, t)$ experiences dispersion and losses. Dispersion means, that wave components with different frequencies propagate at different velocities. Loss means, that the amplitude decreases with propagation distance. This section will shortly review the dispersion and losses of voltage-waves in coplanar stripline circuits. Finally, the propagation of a Gaussian-shaped voltage pulse will be computed using analytical formulas for dispersion and losses.

The propagation of waves on stripline-circuits can be described in the frequency domain. The Fourier-Transform of the voltage pulse $v(y, t)$ is [Veg86, Has86]:

$$V(y, \omega) = V(0, \omega) \cdot e^{-\left(\alpha(\omega) + i\beta(\omega)\right) \cdot y}. \quad (1.17)$$

$\alpha(\omega)$ is the attenuation constant and $\beta(\omega)$ the propagation constant, which is defined

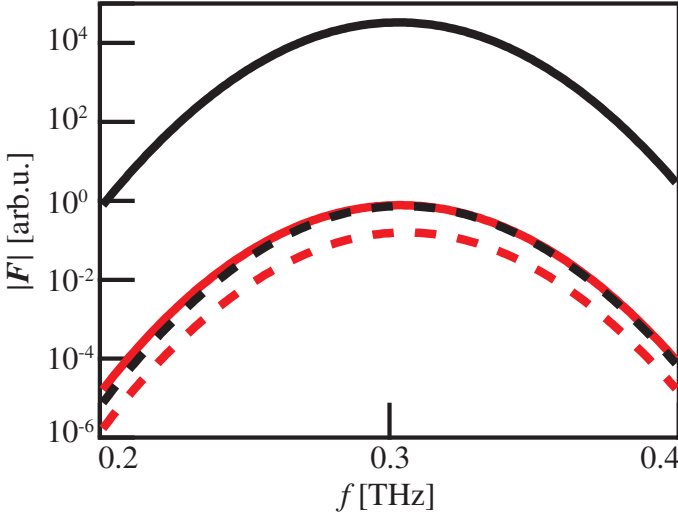


Figure 1.7 — Field flux \mathbf{F}_{WG} coupled into the stripline circuit (solid black line) and field flux \mathbf{F}_{air} radiated normal to the surface (dashed black line) as a function of frequency f in a FDTD simulation [Osk10] (center frequency $f = 0.3 \text{ THz}$, frequency width $\Delta f = 0.2 \text{ THz}$). Field fluxes for a simulation geometry without metal strips and trench are strongly reduced (\mathbf{F}_{WG} red line, \mathbf{F}_{air} dashed red line). For simulation parameters see Appendix C.2.

as:

$$\beta(\omega) = 2\pi \cdot (\omega/c) \cdot n_{\text{eff}}(\omega), \quad (1.18)$$

with $n_{\text{eff}}(\omega)$ the effective index of diffraction, ω the frequency of the electromagnetic wave, and c the speed of light in vacuum. The knowledge of $n_{\text{eff}}(\omega)$ and $\alpha(\omega)$ enables therefore the calculation of the propagated voltage-pulse $v(L, t)$ by an inverse Fourier-transform of 1.17 [Veg86]:

$$v(L, t) = \frac{1}{2\pi} \int_{-\infty}^{\infty} V(y=0, \omega) e^{i\omega t - [\alpha(\omega) + i\beta(\omega)] \cdot L} d\omega \quad (1.19)$$

1.6.1 Dispersion

Generally, the frequency dependent dielectric functions of the metal and the substrate, as well as the geometrical shape of the stripline determine the effective index of diffraction n_{eff} . A finite element simulation [COM07] can be used for these purposes. Figure 1.8 shows the simulated index of diffraction n_{eff} for a coplanar stripline ($w = 5 \mu\text{m}$, $s = 15 \mu\text{m}$) on a gallium arsenide and on a sapphire substrate. A frequency dependent, complex dielectric function $\tilde{\epsilon}(\omega)$ is used for the substrate

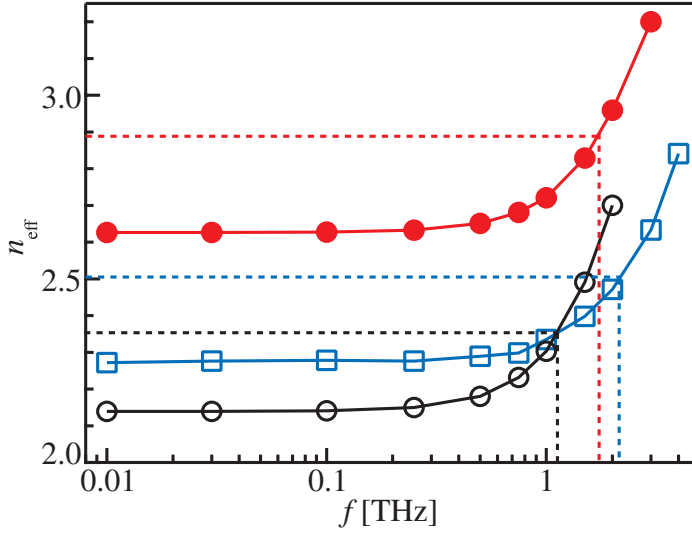


Figure 1.8 — Finite-element-simulation [COM07] of the effective index of diffraction n_{eff} as a function of frequency f for a coplanar stripline ($w = 5 \mu\text{m}$, $s = 15 \mu\text{m}$) on a gallium-arsenide substrate (red circles), on a sapphire substrate (blue squares), and on a gallium arsenide substrate with a $12 \mu\text{m}$ deep trench in between the stripline (open black circles). Dashed lines indicate the frequency corresponding to a 10 % increase of n_{eff} . Solid lines are guides to the eye. For simulation parameters see Appendix C.1.2.

material [Bla82, Ada89, Gri90]. The metal stripes are modeled as ideal conductors. For the GaAs substrate (red circles in Figure 1.8) at low frequencies the quasi-static effective index of diffraction is $n_{\text{eff}} \approx 2.63$. The dispersion frequency f_{disp} is usually defined by the point of inflection of $n_{\text{eff}}(f)$ [Has86]. In our numerical simulations however we do not obtain n_{eff} for such large values of f . We alternatively quantify the dispersion by the frequency $n_{10\%}$, at which n_{eff} increases by 10 %. For the gallium arsenide substrate $n_{10\%}$ is about 1.75 THz. If a $12 \mu\text{m}$ deep trench in the GaAs substrate in between the stripline is considered (open black circles in Figure 1.8) the quasi-static index of diffraction is reduced to ~ 2.14 . Furthermore, a steeper increase of n_{eff} with frequency f results, reducing the dispersion frequency to $n_{10\%} \approx 1.1 \text{ THz}$. Sapphire is known to be transparent to electromagnetic waves in the THz-regime [Gri90], while GaAs absorbs due to coupling to transversal-optical phonons. Therefore the stripline on a sapphire substrate has a higher dispersion frequency of $n_{10\%} \approx 2.16 \text{ THz}$ (see blue squares in Figure 1.8). Sapphire is therefore superior to gallium arsenide as a low-dispersion substrate material. For simulation details see Appendix C.1.2.

An analytical approximation can also be fitted to the results of a full-wave, spectral-domain analysis for coplanar waveguides and striplines [Has90]:

$$n_{\text{eff}}(f) = \sqrt{\epsilon_q} + \frac{\sqrt{\epsilon_r} - \sqrt{\epsilon_q}}{1 + a(f_{\text{disp}}/f)^{1.8}}, \quad (1.20)$$

with the quasi-static permittivity

$$\epsilon_q = \frac{\epsilon_r + 1}{2}, \quad (1.21)$$

and the surface-wave TE₁ mode cutoff frequency

$$f_{TE} = c/4d\sqrt{\epsilon_r - 1}. \quad (1.22)$$

ϵ_r is the relative substrate permittivity, c is the speed of light in vacuum, and a is a parameter related to the stripline geometry [Has90]:

$$\begin{aligned} \log(a) &\approx u \log(s/w) + v \\ u &\approx 0.54 - 0.64q + 0.015q^2 \\ v &\approx 0.43 - 0.86q + 0.54q^2 \\ q &= \log(s/d) \end{aligned} \quad (1.23)$$

s and w are the separation and the width of the coplanar metalstrips as defined in Figure 1.1 and d is the substrate thickness. The expression 1.23 agrees quite well with the finite-element-simulation presented in Figure 1.8 and is useful for an analytical pulse-propagation using equation 1.19.

1.6.2 Attenuation

Voltage pulses propagating on striplines experience losses. These can be categorized in frequency independent metal losses, dielectric losses ($\propto f$), surface wave losses ($\propto f^2$) and radiation losses ($\propto f^3$). The radiation losses dominate at high frequencies [Pha90]. Electromagnetic pulses on a stripline propagate with a group velocity that can exceed the speed of light in the underlying substrate. Consequently shock-waves similar to Cherenkov radiation are generated [Gri87]. The attenuation $\alpha_{\text{rad}}(\omega)$ associated with the radiative losses follows a cubic frequency dependence under quasi-static approximations (i.e. constant permittivity) [Rut83]. Near THz

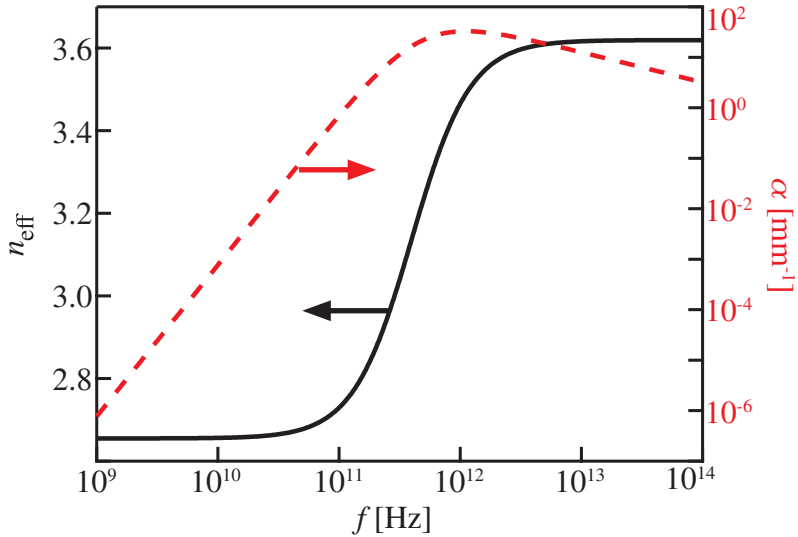


Figure 1.9 — Effective index of diffraction $n_{\text{eff}}(f)$ and radiative attenuation $\alpha_{\text{rad}}(\omega)$ of a coplanar stripline ($5\mu\text{m}$ width and $5\mu\text{m}$ separation) on a gallium arsenide substrate. Values have been obtained using equations 1.20 and 1.24 [Has90, Fra91].

frequencies the quasi-static approximations are not valid and the frequency dependence of $\epsilon(f)$ has to be accounted for [Fra91]:

$$\alpha_{\text{rad}}(f) = \pi^5 \frac{3 - \sqrt{8}}{2} \sqrt{\frac{\epsilon_{\text{eff}}(f)}{\epsilon_r}} \left(1 - \frac{\epsilon_{\text{eff}}(f)}{\epsilon_r}\right)^2 \frac{(s + 2w)^2 \epsilon_r^{3/2}}{c^3 K'(k) K(k)} f^3 \quad (1.24)$$

where $\epsilon_{\text{eff}}(f)$ and ϵ_r are the effective and substrate permittivities, and $k = s/(s + 2w)$. $K'(k)$ and $K(k)$ are complete elliptical integrals of the first kind. It should be noted here, that ϵ_{eff} approaches the substrate permittivity ϵ_r for high frequencies. Then the electromagnetic pulses travel effectively with the speed of light in the substrate material and losses due to shock-wave generation occur. Figure 1.9 shows the attenuation $\alpha_{\text{rad}}(\omega)$ and the effective index of diffraction n_{eff} of a $5/5/5\mu\text{m}$ coplanar stripline on a gallium arsenide substrate calculated with equations 1.24 and 1.20, respectively. Experimentally, the attenuation has been determined to be $\alpha(\omega) \approx 0.2\text{ mm}^{-1} \cdot f^{1/2} + 0.65\text{ mm}^{-1} \cdot f^3$ for a $5/15/5\mu\text{m}$ ($w/s/w$) coplanar stripline on a sapphire substrate, which is in good agreement with equation 1.24. A comparison of the attenuation of low permittivity substrates (sapphire, quartz and plastic) can be found in [Yan08].

1.6.3 Propagation of a Gaussian-shaped pulse

The propagation of a voltage pulse $v(L, t)$ can be calculated using the inverse Fourier-transform in equation 1.19, given that the effective index of diffraction $n_{\text{eff}}(\omega)$ and the attenuation $\alpha(\omega)$ are known. We consider here a Gaussian shaped voltage pulse with 1 ps width, that is propagating on a 5/5/5 μm ($w/s/w$) coplanar stripline on a GaAs substrate. The analytical approximation in equation 1.20 is used for $n_{\text{eff}}(\omega)$. Furthermore, only the radiative losses given in equation 1.24 are considered. Both $n_{\text{eff}}(\omega)$ and $\alpha(\omega)$ are displayed in Figure 1.9 for the stripline geometry under investigation. Figure 1.10 shows the initial Gaussian shaped voltage pulse (solid black line), along with pulses propagated about $L = 100 \mu\text{m}$ (red lines), $300 \mu\text{m}$ (blue lines) and 1 mm (green lines). Solid lines correspond to propagation considering both dispersion and attenuation, while dashed lines show propagated pulses without attenuation. It should be noted here, that the inverse Fourier-transform performed in equation 1.19 yields complex values for $v(L, t)$. Figure 1.10 shows only the real part of $v(L, t)$.

Several conclusion can be drawn from Figure 1.10. The propagated pulses

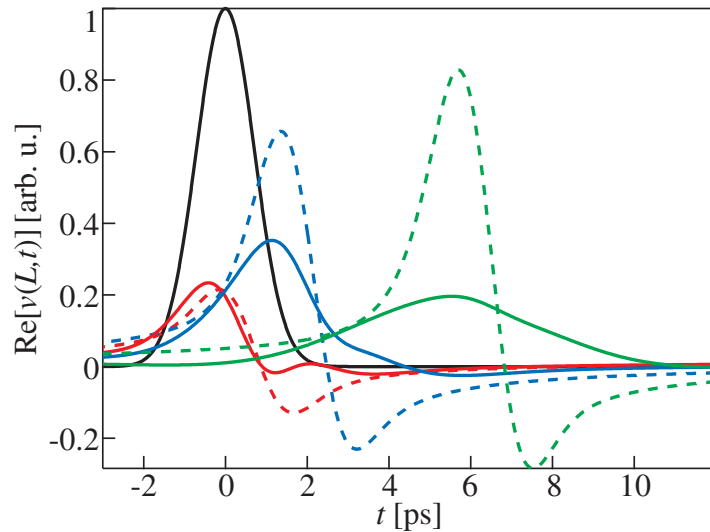


Figure 1.10 — Real-part of a propagating Gaussian shaped pulse $\text{Re}[v(L, t)]$ on a coplanar stripline ($s = 5 \mu\text{m}$, $w = 5 \mu\text{m}$) on a gallium arsenide substrate. The initial Gaussian shaped pulse (width 1 ps, black line) is propagated about $L = 100 \mu\text{m}$ (red lines), $300 \mu\text{m}$ (blue lines) and 1 mm (green lines). Solid lines correspond to propagation including dispersion and attenuation. Dashed lines correspond to propagation including only dispersion.

appear at later times t , as is expected from the propagation about a distance L . Furthermore, the dispersion leads to *ringing* of the propagated pulses. That means, the propagated pulses have a leading, negative edge. For stronger dispersion and longer propagation distances oscillations can occur [Veg86]. The attenuation reduces the negative, leading edge. For propagation distance of $L = 100\mu\text{m}$ and $L = 300\mu\text{m}$ this can lead to the generation of a second pulse (solid red and solid blue lines). Experimentally, such *ringing* should not be mistaken with a transport current as described in section 1.3. At longer propagation distances ($L = 1\text{ mm}$), a considerable broadening of the peak can be observed (solid green line). The apparent increase of the amplitude for $L = 300\mu\text{m}$ compared to $L = 100\mu\text{m}$ is an artefact arising from the inverse Fourier-transformation, in which $v(L, t)$ is complex and has both real and imaginary contributions. Here, the increase of the real part $\Re v(L, t)$ goes along with a decrease of the imaginary part $\Im v(L, t)$, leading to the apparent increase.

1.7 Localized electric field redistribution at zero propagation distance

Non-uniform illumination of a photoswitch can generate a displacement current, as described in section 1.2. The initial, fast change of the local electric field due to the polarization of charge carriers generates a short pulse, which can couple into and propagate along a stripline circuit. The thereby generated displacement current pulse is given by equation 1.3:

$$\mathbf{j}_d = \epsilon \epsilon_0 \frac{\partial \mathbf{F}}{\partial t} \quad (1.25)$$

In this excitation scheme, the length of the generated electrical pulses do not depend on the recombination lifetime of the substrate material [Kro89, Kei92]. Following the initial fast field screening, the electric field relaxes back to the initial field distribution [San89, Zho95a, Zho96, Zho95b]. This relaxation happens on a much longer timescale, comparable to the charge carrier lifetime [Zho95a]. Consequently, the associated *relaxation* displacement current is very slow with a comparatively small amplitude. It should be pointed out here, that only the time-derivative of the electric field \mathbf{F} couples into the stripline via a displacement current.

Experimentally one can get access to the electric field distribution and its relaxation by illuminating the photoswitch with a second, time-delayed light pulse

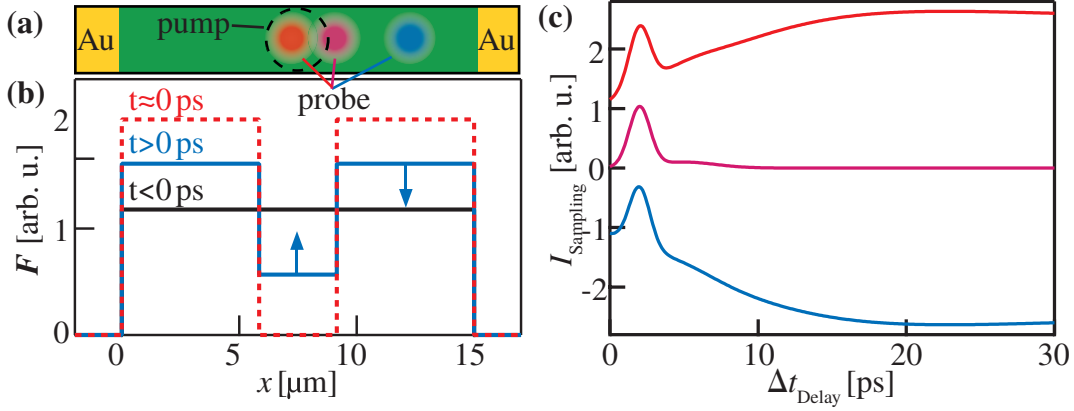


Figure 1.11 — Sketch of a time-resolved measurement at zero propagation distance, where the electric field redistribution can be probed. (a) Focussed pump laser spot (dashed black circle) and different probe laser spots (colored circles) in between a photoswitch with two gold contacts. The time-resolved current I_{Sampling} is measured at one contact. (b) Electric field $F(x)$ in between the photoswitch before illumination ($t < 0 \text{ ps}$, black line), directly after illumination ($t \approx 0 \text{ ps}$, red dashed line), and after the electric field has relaxed halfway to the initial distribution ($t > 0 \text{ ps}$, blue line). The blue arrows indicate the field relaxation direction. (c) Time-resolved current I_{Sampling} at the photoswitch. Following the displacement current pulse a positive (red line) or negative (blue line) shoulder can be observed, which are associated with the field redistribution in the probe region [Ale94]. Line colors correspond to the probe positions indicated in (a). Lines are offset for clarity.

(probe) after the first light pulse (pump). In Figure 1.11a both the pump and the probe beam are depicted as being positioned in between the stripline, i.e. at zero propagation distance, and an *auto-correlation* is performed. In this measurement scheme the time-integrated current I_{Sampling} between the metal contacts is recorded as a function of the time-delay Δt_{delay} between the pump and the probe beam. For details on this scheme³ see chapter 2. In a simple picture the pump beam generates a drop of the electric field $F(x, t \approx 0 \text{ ps})$ in the excitation region ($6 \mu\text{m} < x < 9 \mu\text{m}$) and an increase in the non-excited region, as depicted in Figure 1.11b (dashed red line). The electric field $F(x, t > 0 \text{ ps})$ relaxes back to the initial distribution for $t > 0 \text{ ps}$ (solid blue line in Figure 1.11b). The probe beam generates a displacement current proportional to the electric field $F(x_{\text{Probe}}, t = \Delta t_{\text{delay}})$ in the probe-region x_{Probe} at the time Δt_{Delay} of the probe incidence. In this scheme, the time-evolution of the electric field $F(x, t)$ can be investigated by measuring I_{Sampling} as a function of Δt_{Delay}

³Here, the field probe used for the time-resolved measurements in chapter 2 is omitted.

and the probe position x_{Probe} .

Experimentally, the slow field relaxation in I_{Sampling} has the shape of a positive or negative *shoulder* [Ale94], depending on the pump and the probe position in between the stripline. Numerical investigations of the time-dependent electric fields at zero propagation distance have been carried out [Zho96, Zho95a, Zho95b], clarifying the observed shoulders to be due to the electric field relaxation. As shown in Figure 1.11c, the current I_{Sampling} at the photoswitch can exhibit an increase or a decrease (the so-called *shoulder*), depending on the probe position [Ale94]. The line colors in Figure 1.11c correspond to the excitation positions shown in Figure 1.11a. Positioning the probe beam at the edge of the pump beam (purple probe spot in Figure 1.11a) induces a *balanced* excitation/probing and no field redistribution (i.e. *shoulder*) will be observed (purple line in Figure 1.11c).

1.8 Spurious current pulses in stripline circuits

The analysis of experimental time-resolved current data aims at identifying the current generation mechanisms and consequently deducing physical properties, e.g. the recombination lifetime τ or the charge carrier transport velocity in the semiconductor building the photoswitch. This task is complicated by the overlap of the different currents (e.g. transport and displacement current, see section 1.3). Furthermore, the dispersion of propagating pulses can lead to *ringing*, which can be mistaken for a current signal generated in the photoswitch (see section 1.6). Additionally, spurious current signals can be generated by the reflection of propagating pulses at stripline discontinuities, e.g. the termination of the stripline. This effect can be minimized by increasing the length of the stripline circuit, for example by curling the stripline on the substrate (see section 2.3.3 for details). Also, radiated terahertz signals can be reflected at sample edges if a substrate transparent in the THz regime is used (e.g. sapphire) [McG99]. From geometrical considerations the arrival time of these signals can be evaluated by considering the propagation length and the substrate material index of diffraction at THz frequencies. Furthermore, reflections of the optical pump/probe laser pulses (e.g. at the backcontact for transparent substrates, or at a trench surface) can also lead to the generation of spurious current signals. All these effects can not be generally ruled out, but must be checked for each individual sample.

Chapter 2

Principles of time-resolved photoresponse sampling in stripline circuits

This chapter will introduce the measurement principles for spatially and time-resolved photocurrent measurements. The optical and electronic measurement setup as well as the sample design (including substrate materials, lithography and optical masks) will be described.

2.1 Optical and electronic measurement setup

The measurement principle is based on an optical pump-probe scheme introduced by D.H. Auston as early as 1975 [Aus75]. In the following years, the measurement scheme was scrutinized and extended to the correlation of two different photoconductors [Aus80b, Aus82]. A first theoretical description as given in section 1.1 of the *impulse response of photoconductors in transmission lines* was achieved in 1983 [Aus83]. Figure 2.1 shows a sketch of a typical sample geometry. Basic elements are a metal stripline (i.e. two parallel metal strips) and a perpendicular metal strip (i.e. the *field probe*) on a *fast* photoconductor (e.g. low temperature grown gallium-arsenide, LT-GaAs). The *stripline circuit* comprises a voltage source applying a bias voltage V_{SD} to the outer metal strip, while the metal strip between the outer strip and the field probe is kept at ground bias. A current I_{Photo} is measured between the two metal strips. The *sampling circuit* comprises a current-voltage converter con-

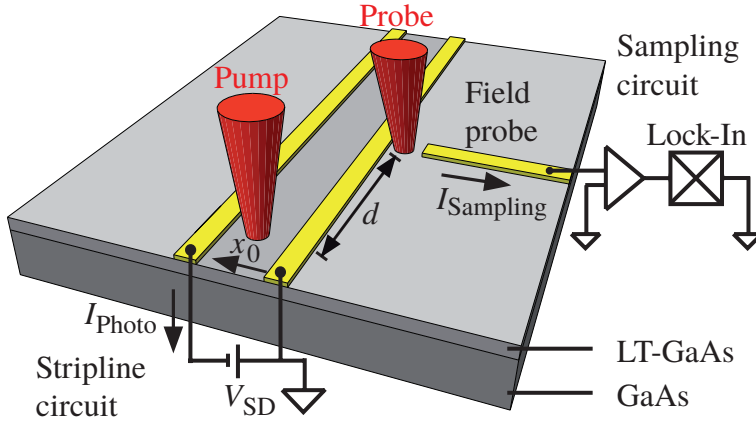


Figure 2.1 — Sketch of a typical time-resolved pump-probe photocurrent measurement setup. Metal strips are depicted in yellow.

nected to the field probe, which keeps the potential at *virtual ground* level. The voltage output of the $I - V$ converter is fed into a *lock-in* amplifier, which detects the time-resolved current I_{Sampling} . First, the light of a titanium:sapphire laser is split into a pump- and a probe-beam by an optical beam splitter, as depicted in Figure 2.2. Both beams are focused through an objective of a microscope onto the sample. The probe-beam is focused at a position x_0 in between the stripline. Hereby, the two metal strips form a photoswitch for the stripline circuit (Fig. 2.1). The pump-laser spot has a size of $\approx 3 \mu\text{m}$, and the laser pulse duration is $\approx 160 \text{ fs}$. After optical pump-excitation, an electro-magnetic pulse starts to propagate along the coplanar stripline [Aus83]. At a distance d , the field-probe of the sampling circuit is short-circuited by the probe-pulse for the duration of the lifetime of the photo-generated charge-carriers in the LT-GaAs at this position. Only the transient electric field of the coplanar stripline located at the field-probe during this time-period drives the current I_{Sampling} in the sampling circuit (Fig. 2.1), since both the central metalstrip and the field probe are kept at ground potential. Varying the time-delay Δt_{delay} between the optical pump-pulse and the probe-pulse gives access to the time evolution of $I_{\text{Sampling}} = I_{\text{Sampling}}(\Delta t_{\text{delay}})$. The time-delay Δt_{delay} is set by a delay stage (see Figure 2.2) or alternatively by an oscillating retroreflector in the optical circuit (see section 2.2.1). The position of the pump-spot x_0 in between the stripline is set by a scanning-mirror with a resulting spatial resolution of $\approx 100 \text{ nm}$, while the position of the probe-spot is kept constant throughout the experiments.

The laser power of the pump (probe) pulse is usually chosen to be in the

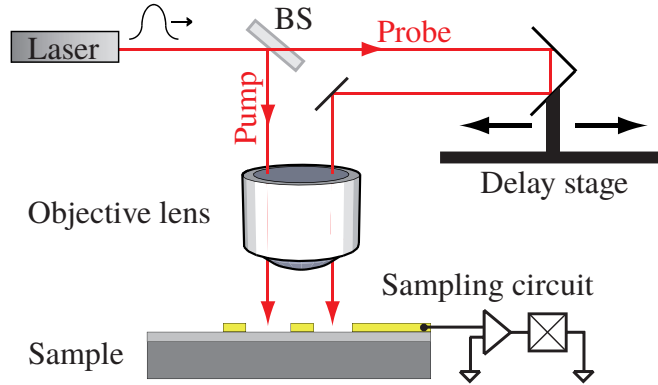


Figure 2.2 — Simplified sketch of the optical measurement setup.

range of $100\mu\text{W}$ - $1000\mu\text{W}$ (50mW - 120mW). The presented results in chapters 3, 4, 5 and 6 depend linearly on the laser power of the probe-pulse. All data are taken at room temperature, unless stated otherwise. They are taken in vacuum ($\approx 1 \times 10^{-5}$ mbar) to prevent the effect of photo-desorption of oxygen on the surface of the sample under investigation.

A photocurrent cross-correlation [Aus80b] of two different materials can be achieved by removing the wafer material between the two metal strips forming the stripline, and replacing it with a different material or nanostructure [Pre11b, Pre11c]. Then the pump beam excites the new material/nanostructure, while the probe beam still excites the wafer material. If the response function of the Auston switch at the field probe is known, then the response of the device under investigation can be deduced by deconvolution of the measured I_{sampling} with the response function of the field probe. A fast response function of the field probe is desirable for achieving a high temporal resolution of the deduced device response.

2.2 Experimental details

Experimental details on the optical setup (e.g. layout of optical elements on an optical table) and electronic setup (e.g. connection diagram of voltage sources and current amplifier) are given in this section.

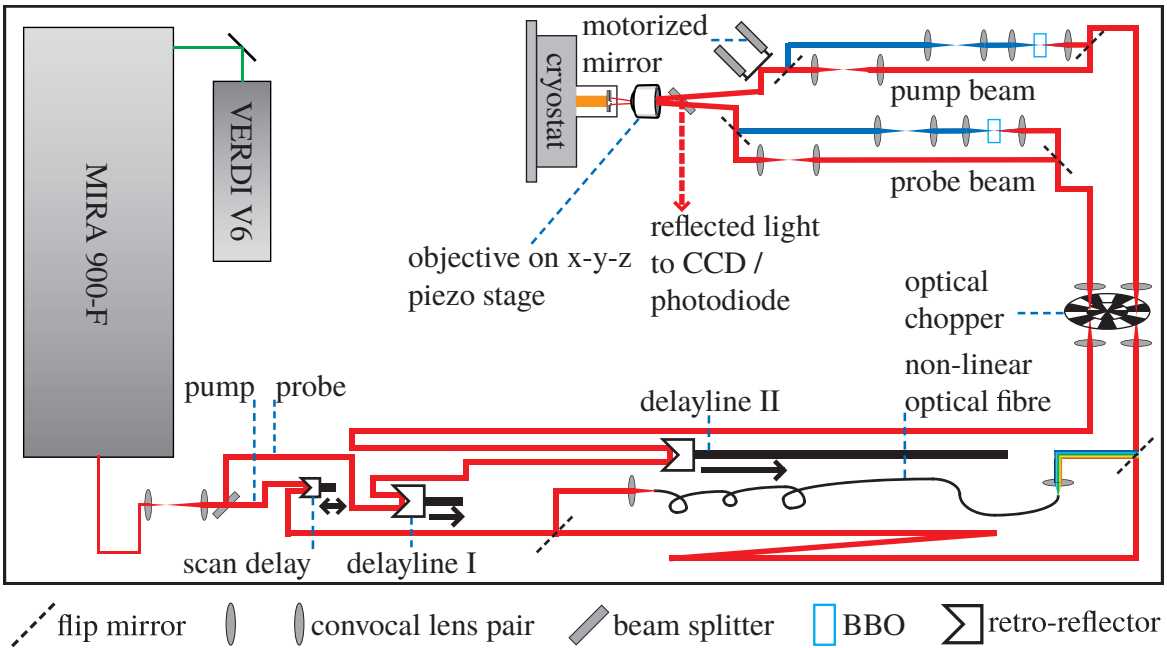


Figure 2.3 — Detailed sketch of a two-color pump-probe measurement setup arranged on an optical table (3 m x 1.5 m). Mirrors have been omitted for simplicity.

2.2.1 Optical setup

A detailed sketch of a two-color pump-probe measurement setup arranged on an optical table (Newport, ST-UT2, 3m x 1.5 m, with vibration isolation) is given in Figure 2.3. A titanium:sapphire (Ti:Sa) laser (Coherent MIRA 900-F) is pumped by a CW semiconductor laser at 532 nm (Coherent VERDI V6 or V5). The Ti:Sa laser generates optical pulses (160 fs length, 76 MHz repetition rate) at a tunable wavelength of 700 nm - 1000 nm. First of all, the beam is expanded in a confocal lens pair and then split into a pump and a beam in a pulse-length conserving 50 : 50 beam-splitter (Newport 10RQ00UB.4). The pump beam is first guided into a scan delay (APE-BerlinScan-Delay 50), which is a retroreflector that can oscillate at low frequencies ≤ 20 Hz generating a sinusoidal time-delay with an amplitude of ≤ 50 ps. This device is only used in the time-resolved detection scheme without a lock-in amplifier (see section 2.2.2). Then the pump beam can be guided by a flip mirror into a highly nonlinear optical fibre (Thorlabs NL-PM-750) for supercontinuum generation, or alternatively it can be guided along a standard, wavelength-conserving

path of equal optical path length¹. Dielectric filters are then used to select a small wavelength range of the generated continuum, and subsequently the two alternative pump beam paths are rejoined with a flip mirror. The probe beam after the beam splitter is first guided into a first delayline, which consists of a retroreflector fixed on an one-axis stage motorized by a stepper motor (Thorlabs ZST-13B) with 13 mm travel and a calculated microstepping resolution of 26 nm (≈ 0.2 fs). A second delay line has a travel range of 70 cm with minimal step-size of 30 μ m (≈ 0.2 ps). Finally both the pump and the probe beam are guided through two confocal lens pairs, at which focus a optical chopper blade is rotating. A two-frequency chopper blade modulates the pump beam at a frequency f_{pump} and the probe beam at $f_{\text{probe}} = \frac{7}{5} \cdot f_{\text{pump}}$. The optical frequency of the pump and probe beam can independently be doubled from 700 nm - 1000 nm to 350 nm - 500 nm using a Beta-Barium Borate (BBO) crystal in between a confocal lens pair with short focal length. Finally, confocal lens pairs are used for adjusting the divergence of the optical beams. A motorized mirror is used in the pump beam path to position the pump beam on the sample independently of the probe beam. Again, high resolution stepper motors are used for this purpose (Thorlabs ZST-13B). Both beams are guided through an objective lens (Mitutoyo 10x *Plan Apo Infinity-Corrected Long working distance objective*; NA=0.28; working distance 33.5 mm; or Newport 15x reflective microscope objective 50105-02; NA = 0.52; working distance 24 mm). The objective is mounted on an analog 3-axes Piezo-stage (Physik Instrumente, P-611.3 *NanoCube* with Controller E-664). The piezo controller input voltages are provided by a computer data acquisition card (National Instruments, PCI-6289 and BNC-2120). The pump (probe) beam enters the objective under an angle α_{pump} (α_{probe}) with respect to the optical axes. They are therefore focused on the sample on two different positions corresponding to an angle $-\alpha_{\text{pump}}/\text{mag}$ ($-\alpha_{\text{probe}}/\text{mag}$) with respect to the optical axes, where *mag* is the magnification of the microscope objective. The angle α_{pump} can be changed vertically and horizontally by the two stepper motors of the motorized mirror. A second beam splitter (92:8) is used for beam sampling. Light reflected from the sample is guided either to a CCD or to a photodiode. In that way, the sample can be imaged. The optical path lengths of the pump and the probe beam should be equal for all colors. For that purpose path extensions have been incorpo-

¹The nonlinear optical fibre has an index of diffraction of ≈ 1.5 and a length of 1 m. Therefore the standard path between the separating and the rejoining flip mirror needs to be ≈ 0.5 m longer than the fibre beam path. For that purpose a standard beam path extension has been incorporated, as is shown in Figure 2.3 at the bottom right (below the fibre).

rated into the probe beam and the *red* pump beam, since the index of diffraction of the nonlinear fibre is ≈ 1.5 . The two alternative paths for frequency doubling of the pump or the probe beam using a *BBO* are arranged in a way to keep the path length with respect to the *red* paths equal.

The sample is kept in vacuum ($\approx 10^{-5}$ mbar) in an optical flow cryostat (Janis *ST-500H*, 4K - 300K). Electrical connections to the sample are achieved with vacuum SMA feedthroughs and low-capacitance coaxial cables (e.g. Axon, *Picocoax PCX 40 C 05*).

2.2.2 Electronic setup

A simplified sketch of the electronic measurement setup is given in Figure 2.4. A bias voltage V_{SD} (Yokogawa, 7651 programmable DC source) is applied to the outer metal strip using conventional coaxial cables, while the metal strip adjacent to the field probe is kept at ground potential. A current-voltage ($I - V$) converter (DL Instruments, *Ithaco 1211* current preamplifier) is attached to the field probe. For time-resolved measurements of $I_{Sampling}$ (see Figure 2.1) the output of the $I - V$ converter is fed into a *lock-in* amplifier (EG&G, 7265) or an oscilloscope (Tektronix, *TDS1012*). For lock-in detection of the time-resolved $I_{sampling}$ the sum frequency $f_{pump} + f_{probe}$ is used as the reference frequency. The time-evolution of $I_{sampling}(\Delta t_{delay})$ is investigated by changing the probe optical path length using delayline *I* or *II*, which creates a time delay Δt_{delay} between the pump and probe pulses. At the same time the scan delay is kept still. Alternatively, $I_{sampling}$ can be measured using the oscilloscope connected to the output of the $I - V$ converter, while the scan delay oscillates at 20Hz. Obviously the chopper system is then turned off. For time-integrated measurements of I_{Photo} (see Figure 2.1) the $I - V$ converter is connected to the *middle* (otherwise grounded) metal strip. The output of the $I - V$ converter is fed into the *lock-in* amplifier (using f_{pump} as reference signal), or alternatively into a multimeter (HP, 34401A). In this arrangement the piezo stage is usually horizontally and vertically scanned to investigate the spatial photocurrent response of the device under test. All electrical connections between the devices and the cryostat feedthroughs are made using conventional or double-shielded, low-noise coaxial cables (Arnotec, *Multiflex 86*).

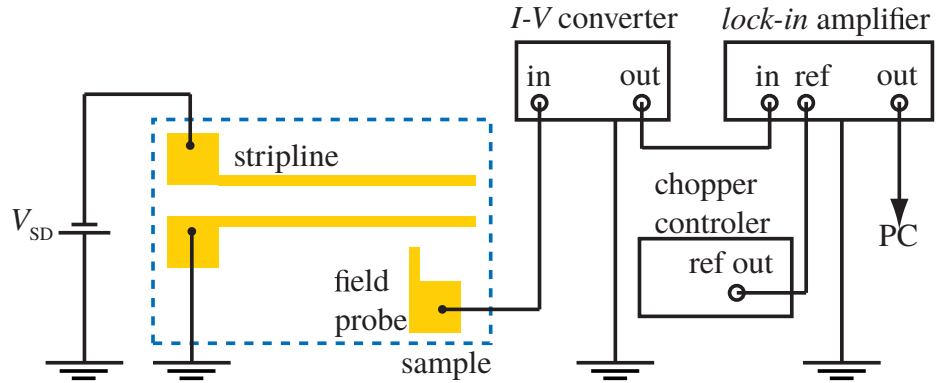


Figure 2.4 — Simplified sketch of the electronic measurement setup.

2.3 Sample preparation

The preparation of the samples used in chapters 3, 4, 5 and 6 will be described in this section. First, the employed wafer materials will be described, followed by a short outline of the optical lithography. Finally, processing steps particular to the incorporation of nanostructures in stripline circuits will be described.

2.3.1 Wafer materials for the sampling circuit

As has been described in section 2.1, a fast response function of the field probe is desirable for achieving a high temporal resolution of the deduced device response. This can be achieved by using a carrier lifetime limited Auston switch at the field probe (see section 1.1). Recombination lifetimes as short as 100 fs can be achieved in GaAs grown at low temperatures [War90, Yam90, Har93, Lok99, Yan03, Gre03]. Alternatively, also amorphous or ion implanted silicon have similar short recombination lifetimes [Aus80a, Smi81, Doa87]. The low temperature grown gallium arsenide (LT-GaAs) wafer material used for the experiments presented in chapter 3, 4 and 5 were grown by molecular beam epitaxy (MBE) by Dieter Schuh and Werner Wegscheider at the University of Regensburg. Growth parameters are given in table 2.1. Ion-implanted silicon (Si) on a sapphire (Al_2O_3) substrate was used for the experiments presented in chapter 6. Non-implanted silicon-on-sapphire wafers manufactured by Kyocera were purchased at Crystec GmbH, Berlin. Implantation with oxygen-ions was conducted by Helmut Karl at the University of Augsburg. Implantation and wafer parameters can be found in table 2.2.

	layer	material	thickness	parameter
1	wafer	GaAs	350 μm	Freiberger B6172
2	buffer layer	GaAs	100 nm	$T_{\text{Pyr}} = 637^\circ\text{C}$; $T_c = 898^\circ\text{C}$
3	sacrificial layer	$\text{Al}_{0.3}\text{Ga}_{0.7}\text{As}$	400 nm	$T_{\text{Pyr}} = 638^\circ\text{C}$; $T_c = 899^\circ\text{C}$
4	photoconductor	LT-GaAs	2 μm	$T_{\text{Pyr}} = 225^\circ\text{C}$; $T_c = 387^\circ\text{C}$
5	annealing	O_2 environment		$T = 600^\circ\text{C}$

Table 2.1 — Growth parameter of low-temperature grown Gallium-Arsenide (LT-GaAs) wafer (wafer number D080402C) used for the experiments presented in chapter 3, 4 and 5.

		material	parameter
1	wafer	Al_2O_3	thickness 0.43 mm, diameter 3 inch R-orientation (1-102), one-side polished
2	photoconductor	Si	thickness 300 nm, insulating resistivity $> 100 \Omega\text{cm}$
3	ion-implantation	O^+	dose and energy: $2 \times 10^{15} \text{ cm}^{-2}$ @ 60 keV $2 \times 10^{15} \text{ cm}^{-2}$ @ 90 keV

Table 2.2 — Wafer and ion-implantation parameters of the Silicon-on-Sapphire wafer used for the experiments presented in chapter 6.

2.3.2 Optical lithography

The definition of metal stripline circuits was performed by standard optical lithography and metal evaporation. Parameters for each lithography step using an image reversal photoresist (Microchemical, AZ 5214E) can be found in table 2.3. Prior to the spinning of the photoresist we clean the sample in an acetone bath, followed by an immediate isopropanol rinse to avoid surface contamination by acetone residues. Persistent dirt on the surface can be removed by wiping the sample with lens cleaning tissue in the acetone bath. Furthermore, oxygen plasma ($\sim 300\text{s}$) can be used to further remove organic surface contamination. It should be noted that the photoresist needs to be rehydrated after heating steps for satisfactory lithography results. In dry cleanroom conditions an additional re-hydration step can be employed after the prebake (step 2). For example, the sample can be put in a petri-dish floating in a hot water bath ($\sim 95^\circ\text{C}$) for $\sim 15\text{ min}$. A closed container is used as a housing to contain the water vapor. In step 11, 50 nm of nickel (Ni) is evaporated

	step	time	parameter
0	substrate cleaning	300 s	acetone bath isopropanol rinse oxygen plasma
1	spinning of AZ5214E	40 s	5000 rpm
2	prebake	50 s	(105 ± 5) °C
*3	re-hydration	15 min	
4	illumination	3 s	
5	cool down	10 min	
6	image reversal bake	2 min	(119.5 ± 0.5) °C
7	cool down	5 min	
8	development	30 s 18 sec	in AZ Developer 1:1 with H_2O or in AZ 351B 1:4 with H_2O
9	water bath	2 min	
*10	oxygen plasma	30 s	$P \approx 200\text{W}$, $P_{O_2} \approx 1.4\text{mbar}$
11	metal evaporation		5 nm Ti 200 nm Au *etch mask: 50 nm Ni
12	lift-off	10 min	90 °C AZ 100 Remover or acetone

Table 2.3 — Steps performed for the definition of metal stripline circuits by optical lithography. Optional steps are indicated by a star.

following the evaporation of gold (Au) and titanium (Ti) if the sample is further processed to obtain an etched trench in between the stripline (see section 2.3.4).

2.3.3 Mask design

Figure 2.5 shows a sketch of the mask design used for the optical lithography in the sample processing. Figure 2.5a shows a stripline circuit used for the experiments described in chapters 3, 4 and 5. Figure 2.5b shows a detailed view of the excitation region and the field probe. The coplanar stripline is formed by two metal strips with 5 µm width and 15 µm separation. The stripline is curled to increase the total stripline length on the sample. In that way, reflections at the end of the

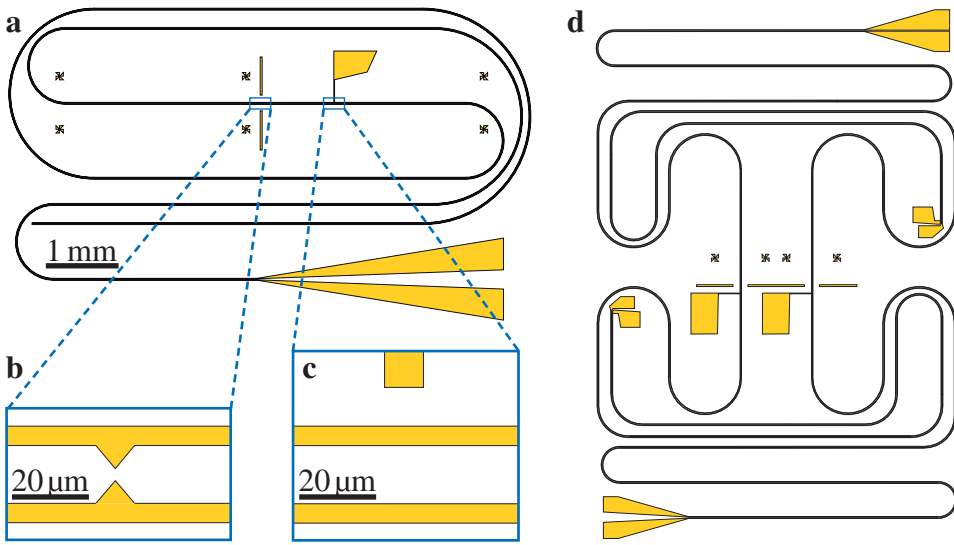


Figure 2.5 — Sketch of masks for optical lithography. (a) Stripline circuit used for the measurements described in chapters 3, 4 and 5. **(b)** Detailed view of the excitation region. For the experiments in chapters 3 and 5, the triangular shaped tapering is omitted. **(c)** Detailed view of the field probe. **(d)** Second generation mask design with two stripline circuits. Individual metal strips can not be resolved in (a) and (c).

stripline can be reduced (see section 1.8). Figure 2.5c shows an improved design, in which two stripline circuits are curled on one chip. This design can also be employed in two-chip correlation measurements, in which the upper half of the mask is transferred on one wafer material, and the lower half on another wafer material. This mask design was used for the experiments described in chapter 6.

2.3.4 Definition of a trench in the stripline

In order to perform cross-correlation measurements of carbon nanotubes and graphene as presented in chapters 4 and 5 the GaAs substrate material in between the stripline circuit had to be removed. For that purpose optical lithography was used to define a 50 nm Ni etch mask covering the whole sample but the GaAs surface between the stripline. Then inductive coupled plasma reactive ion etching (ICP-RIE) was used to etch the GaAs substrate material to a depth of $\approx 12 \mu\text{m}$. A positioning precision of the etch mask relative to the already processed stripline on the sample surface of $\sim 2 \mu\text{m}$ can be achieved. To account for $2 \mu\text{m}$ of misalignment, the etch mask is designed to extend up to the middle of the two metal strips. For

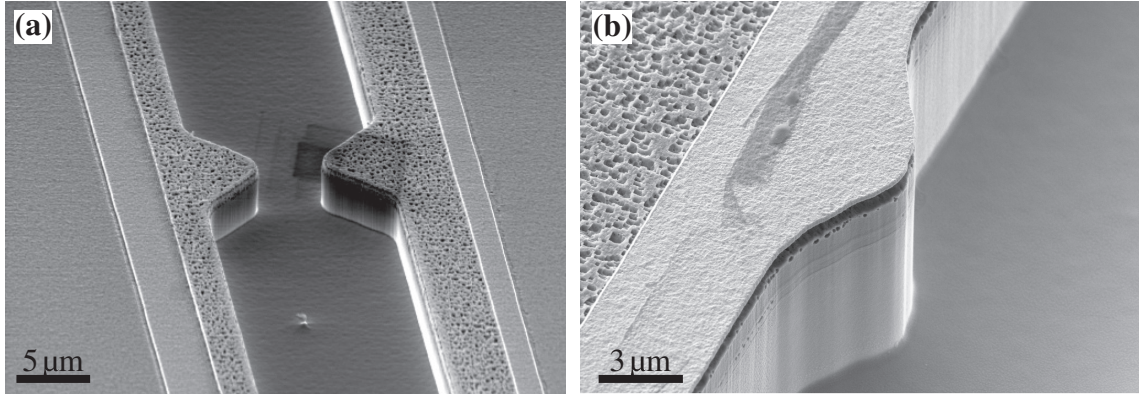


Figure 2.6 — SEM images of stripline circuits on a LT-GaAs substrate with an etched trench. (a) Stripline circuit after ICP-RIE etching, where the additional Ni layer for protecting the gold was omitted. (b) Stripline circuit with additional Ni layer for protecting the gold after removal of the Ni. The remaining LT-GaAs outside the stripline shows non-critical surface damage due to the aqueous solution used for removing the Ni. In this image the LT-GaAs layer, the sacrificial AlGaAs layer and the GaAs substrate can be distinguished at the trench wall.

example, if metal strips with a width of $5\text{ }\mu\text{m}$ and a separation of $15\text{ }\mu\text{m}$ are used for the stripline circuit, then the window of the etch mask should have a width of $2.5\text{ }\mu\text{m} + 15\text{ }\mu\text{m} + 2.5\text{ }\mu\text{m} = 20\text{ }\mu\text{m}$. Furthermore, 50 nm of Ni is additionally evaporated directly following the Ti and Au evaporation in the process of defining the metal stripline (section 2.3.2). In that way the underlying gold layer is always protected from suffering damage in the ICP-RIE step. Figure 2.6a shows an SEM image of a stripline circuit after ICP-RIE etching, where the Ni layer for protecting the gold was omitted. There, the Ni layer covers the region outside of the stripline and approximately half the gold strips. The LT-GaAs region inside the metal strips is etched to a depth of a few μm and the uncovered gold suffered severe surface damage in the etching step. Following the ICP-RIE etching, the nickel etch mask is removed using a aqueous solution of FeCl_3 and HCl . An SEM image of a typical stripline circuit with trench after Ni removal is shown in Figure 2.6. There, the remaining LT-GaAs outside the stripline shows non-critical surface damage due to the aqueous solution used for removing the Ni. The surface of the gold strip is intact due to the protecting Ni-layer. Furthermore, the LT-GaAs layer, the sacrificial AlGaAs layer and the GaAs substrate can be distinguished at the trench wall. Parameters for the definition of the trench can be found in table 2.4.

	step	value	parameter
1	Definition of etch mask		standard optical lithography evaporation of 50 nm Ni
2	ICP-RIE etch	5 sscm 75 W 1 W 38 V 150 W 10 °C 0.7 torr 10 min	SiCl_4 P_{forward} $P_{\text{reflected}}$ DC-bias P_{ICP} sample temperature chamber pressure duration
3	removal of Ni mask	20 sec	in solution of: $2 \text{ g } \text{FeCl}_3 + 8 \text{ ml } \text{HCl (32\%)} + 100 \text{ ml } \text{H}_2\text{O}$
4	water bath	2 min	

Table 2.4 — Steps performed for the definition of a trench in between the metal stripline.

2.3.5 Growth of carbon nanotubes

The growth of the carbon nanotubes (CNTs) employed for the experiments presented in chapter 4 was performed using a standard chemical vapor deposition (CVD) technique [Son08, Kan09]. Differing from standard CNT growth procedures, a small region of the stripline circuit at a distance of 0.3 mm from the field probe is defined by optical lithography as the *CNT region*. The whole sample but the *CNT region* is then covered by a standard optical photoresist. An exhaust pipe attached to the CVD furnace is continuously pumped during growth to extract material from the furnace. The sample is then positioned in the pipe at a distance of $\approx 15 \text{ cm}$ outside of the furnace housing for a deposition time of 4 min. The temperature at this position in the pipe was measured with a contactless, infrared thermometer to be $\approx 150^\circ\text{C}$. In this procedure, the temperature that the sample has to withstand is considerably lower than the furnace temperature of $T_{\text{furnace}} = 1100^\circ\text{C}$. Thereby, the pre-processed GaAs wafer with metal stripline circuits, as well as the photoresist do not suffer damage due to high temperature. After CVD growth the photoresist was removed in acetone. This method was utilized for the sample used in the measurements of chapter 4. No SEM image of this sample was collected to avoid damage or

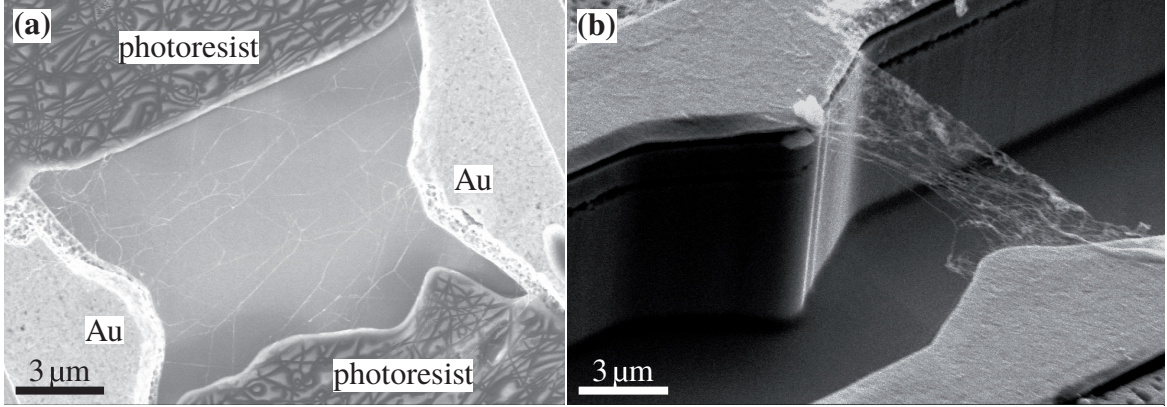


Figure 2.7 — SEM images of CNT networks suspended in a stripline circuit. (a) Thin CNT network suspended in a CNT-region defined by optical photoresist. (b) Suspended CNT network cleaned in a focused-ion-beam process utilizing water as precursor gas.

alteration of the CNT network. Figure 2.7a shows an SEM image of a sample used for testing the growth parameters. There, a suspended thin CNT network spans between the Au strips on the left and on the right. The photoresist covers the remaining sample and can be seen in the upper and lower part of the image.

Alternatively, the photoresist can be omitted if the sample is *cleaned* after CVD growth to leave only a small region with CNTs on the stripline. This can be achieved in a focused-ion-beam process utilizing water as precursor gas. This method was used for the sample shown in the SEM image in Figure 2.7b. More detail about the CNT-network can be found in chapter 4.

2.3.6 Growth and transfer of graphene

The growth of the graphene employed for the experiments in chapter 5 was performed using a CVD technique. In this procedure, the graphene samples were directly synthesized on copper (Cu) foil using liquid precursor hexane in the CVD system [Ci10, Sri10]. After growth, a thin poly-pethyl-peth-pcrylate (PMMA) film was deposited on the graphene/Cu substrate as supporting layer for the graphene transfer. The underlying Cu substrate was then dissolved in dilute HNO₃ and washed by DI water for several times. The floating graphene/PMMA film was controllably transferred onto the pre-processed LT-GaAs substrate, such that the graphene spans the two electrodes of the stripline circuit. The sample was immersed

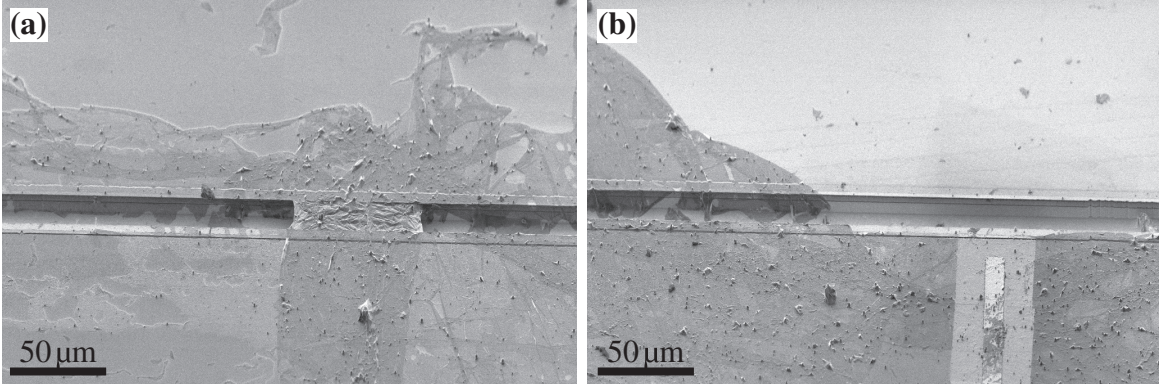


Figure 2.8 — (a) SEM image of a suspended graphene sheet in a stripline circuit. **(b)** SEM image of the field probe on the same sample. The region around the field probe is cleaned in a focused-ion-beam process utilizing water as precursor gas to avoid a short circuit of the stripline circuit with the field probe.

into acetone in order to remove the PMMA, and then dried in a critical point dryer to avoid the damage of the freely suspended graphene by liquid surface tension. In this procedure, one to three graphene layers are obtained. Figure 2.8a shows an SEM image of a such processed suspended graphene sheet in a stripline circuit. The region around the field probe (see Figure 2.8b) is cleaned in a focused-ion-beam process utilizing water as precursor gas to avoid a short circuit of the stripline circuit with the field probe by unintentionally deposited graphene. Precursor assisted scanning-electron-beam deposition of platinum onto the graphene covering the stripline is used to lower the contact resistance. The two-terminal resistance of the graphene device is measured to be $1.7\text{ k}\Omega$ at 300 K and $0.9\text{ k}\Omega$ at 77 K . In our sample geometry we are not able to change the charge carrier density in the graphene because we cannot apply a back-gate voltage. This limits the comparability of our two-terminal resistance with literature [Fel09]. Yet, the increase of the resistance with temperature and the absolute value of $\sim 1\text{ k}\Omega$ are in good agreement with typical values for suspended graphene [Fel09]. More details about the graphene can be found in chapter 5.

2.3.7 Growth of GaAs nanowires

A very suitable and versatile technique for nanowire growth is the direct synthesis on a substrate [Bry06, Lau02, Dic04, Bak04]. The GaAs nanowires used in

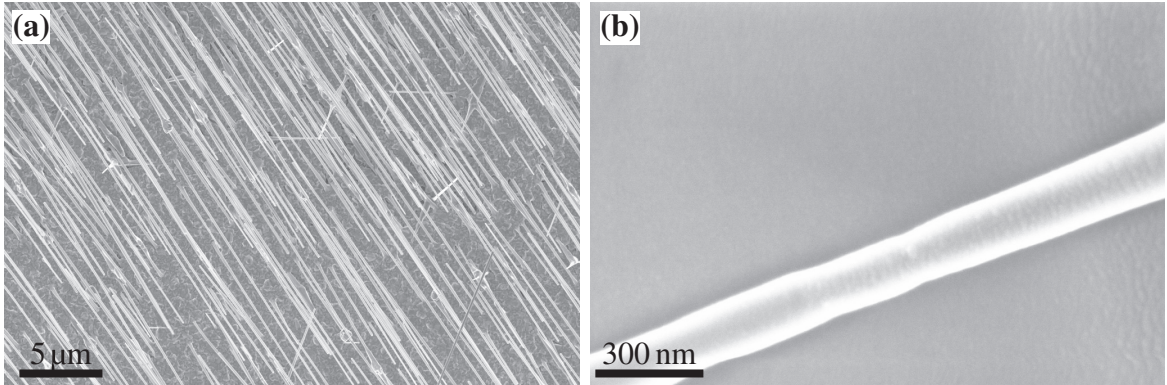


Figure 2.9 — (a) SEM image of GaAs nanowires grown by MBE on a GaAs substrate. **(b)** SEM image of a single GaAs nanowire.

chapter 6 were grown by A. Fontcuberta i Morral in the group of Prof. G. Abstreiter at the Walter-Schottky Institute. They are grown by molecular beam epitaxy (MBE) with the so-called vapor-liquid-solid method using Ga droplets as self-catalysts [Col08, Fon08, Col09]. The nanowires are grown on a SiO_2 covered (111)-oriented GaAs substrate as presented previously (growth rate of $\sim 0.25 \text{ \AA s}^{-1}$, As_4 partial pressure of $\sim 2 \times 10^{-6} \text{ mbar}$, growth temperature of 630°C , and 7 rpm rotation) [Col09]. The nanowires with {110}-facets have a length (diameter) of $\sim 10 \mu\text{m}$ ($\sim 140 \text{ nm}$), and they are doped type *p* with a carrier concentration of $\sim 10^{18} \text{ cm}^{-3}$ by adding a silicon flux during the growth [Col09]. Figure 2.9a shows an SEM image of such grown nanowires. Figure 2.9b shows a detailed view of a single nanowire.

2.3.8 Transfer and contacting of nanowires utilizing FIB

Starting point is a SiO_2 substrate onto which gold pads are evaporated utilizing a shadow mask. The SiO_2 substrate in between the pads is milled away to a depth of a few hundred nanometers by the help of a FIB microscope. Following the technique described in [Pen08], the selected nanowire is positioned to bridge two gold pads by using mechanical manipulators within the FIB recipient, as shown in Figure 2.10a. The nanowire is attached to the source-drain electrodes by a FIB induced deposition of carbon utilizing phenanthren ($\text{C}_{14}\text{H}_{10}$) or platinum as a precursor gas (see Figure 2.10b). A detailed description of the fabrication process is given in [Thu09a].

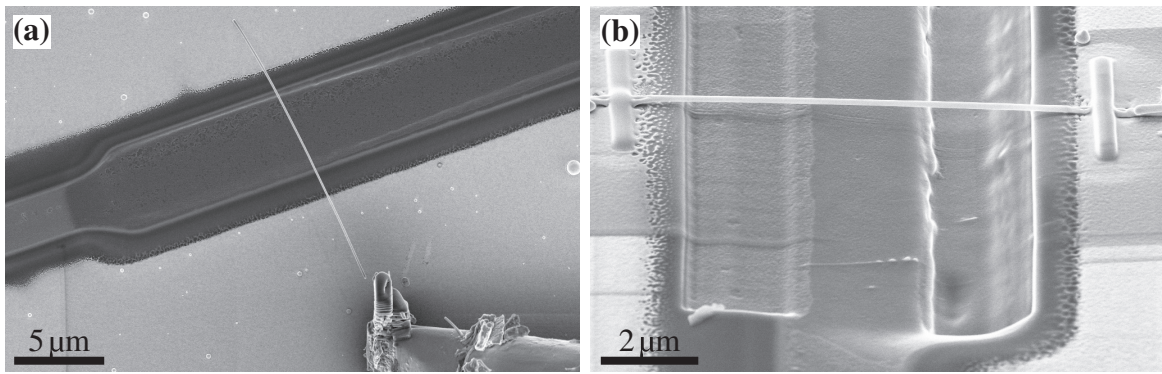


Figure 2.10 — (a) SEM image of a GaAs nanowire positioned on two gold pads using a mechanical manipulator (bottom right) within the FIB recipient. (b) SEM image of a suspended GaAs nanowire bridging two gold pads and contacted by a FIB induced deposition.

2.3.9 Transfer and contacting of nanowires by optical lithography

Starting point is an ion-implanted silicon-on-sapphire wafer (see section 2.3.1). The silicon is selectively etched to remain only at the later position of the field probe. Then nanowires are randomly transferred onto the bare sapphire by mechanical means (i.e. dropcasting or transfer with a tissue). Finally optical lithography is used to contact a nanowire in a gold stripline circuit (see Figure 2.11a). At the same time, the field probe is processed such that it lies directly on the remaining ion-implanted silicon (see Figure 2.11b). For details on the sample processing see [Pad11].

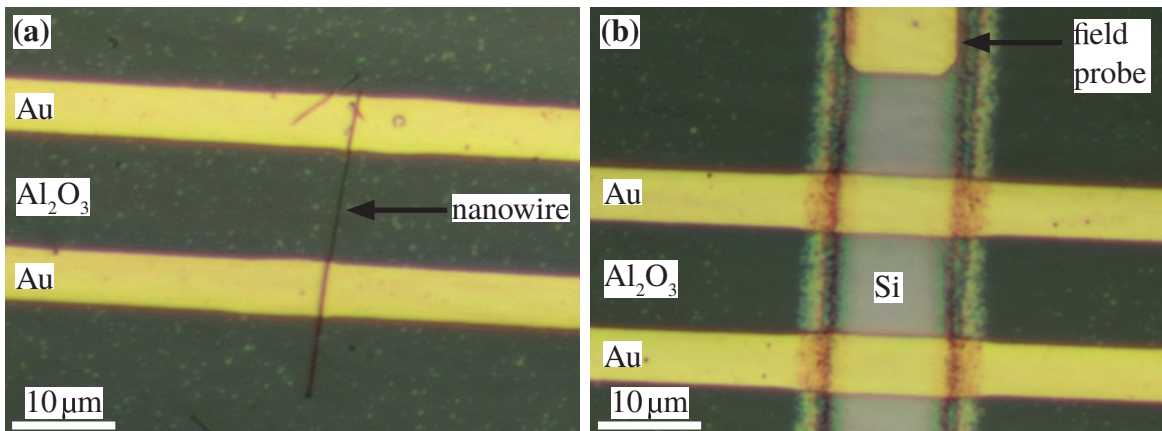


Figure 2.11 — (a) Optical image of a single nanowire contacted by optical lithography in a gold stripline circuit. (b) Optical image of the field probe positioned on the remaining silicon.

Chapter 3

Spatially resolved ultrafast transport current in GaAs photoswitches

The pump-probe measurement technique described in chapter 2 is applied to a gold stripline circuit on a LT-GaAs substrate to investigate the photocurrent response of GaAs photoswitches in time and space. The on-chip optoelectronic scheme allows us to resolve the photocurrent response of the photoswitch after a non-uniform illumination with micrometer and picosecond resolution (section 3.1). We find two photocurrent pulses in the time-resolved response of the photo switch. In section 3.2 we show that the first pulse is consistent with a displacement current pulse, as discussed in section 1.2. In section 3.3 we interpret the second pulse to result from a transport current process, as discussed in section 1.3. In section 3.4 we perform experiments at zero propagation length, in order to rule out THz reflections or dispersion effects in the coplanar stripline to account for the second pulse. By a time-of-flight analysis in section 3.5 we further determine the velocity of the photo-generated charge carriers of the transport current pulse to be $v_{\text{propagation}} = (1.3 \pm 0.2) \times 10^8 \text{ cm/s}$. This value exceeds drift, thermal and quantum velocities of single charge carriers. Hereby, we interpret the transport current pulse to stem from an electron-hole plasma excitation. We finally conclude with some remarks on the emission of optical phonons in our experiment in section 3.6. The results presented in this chapter are published in [Pre10].

3.1 Sample preparation and experimental procedure

A coplanar stripline made out of Au with 200nm height, 5 μm width, and a separation of 15 μm is fabricated by optical lithography (see section 2.3.2) on a LT-GaAs substrate (see section 2.3.1). A detailed description of the time-resolved measurement technique is given in chapter 2. Most importantly, the position of the focused pump-beam x_0 in between the stripline is set by a scanning-mirror with a resulting spatial resolution of $\sim 100\text{ nm}$, while the position of the probe-spot is kept constant throughout the experiments. At a distance d , the field-probe of the sampling circuit is short-circuited by the probe-pulse for the duration of the lifetime of the photo-generated charge-carriers in the LT-GaAs at this position. The transient electric field of the coplanar stripline located at the field-probe during this time-period drives the current I_{Sampling} in the sampling circuit (see Figure 2.1 in chapter 2). Varying the time-delay Δt between the optical pump-pulse and the probe-pulse gives access to the time evolution of $I_{\text{Sampling}} = I_{\text{Sampling}}(\Delta t)$. All experiments presented in this chapter are performed at a vacuum of $\sim 10^{-5}\text{ mbar}$ and room temperature.

3.2 Time-resolved displacement currents

Figure 3.1 depicts I_{Sampling} as a function of Δt for $d \approx 15\mu\text{m}$ and varying x_0 . The laser energy is $E_{\text{Laser}} = 1.59\text{ eV}$ in 3.1a and $E_{\text{Laser}} = 1.51\text{ eV}$ in 3.1b. We observe two peaks¹ of I_{Sampling} (the second peak is marked with a red triangle in Figure 3.1). For all x_0 , we observe that the first peak occurs at the same time delay $\Delta t \approx 3\text{ ps}$. Hereby, we interpret the first peak to result from a displacement current in the photo switch, which is consistent with the non-uniform illumination of a photoswitch in stripline circuits as discussed in section 1.2 [Kro89, San89, Ale94, Zho96]. The current-voltage characteristics of the stripline circuit without illumination demonstrate an ohmic transport between the Au and the LT-GaAs. Therefore, we can assume a linear bandstructure of the LT-GaAs in between the Au contacts [Yam90]. Figure 3.2a shows the resulting schematic of the bandstructure along x_0 . An applied source-drain voltage V_{SD} drops homogeneously across the gap between the stripline. The optical pump-pulse excites charge carriers in a region at x_0 with a diameter of $\sim 1.5\mu\text{m}$ (dashed lines in Figure 3.2a). Before illumination, the electric

¹We note that we detected the transport current peak, as discussed in this chapter, also for a photoswitch on a heterostructure without AlGaAs. See Appendix B.1.

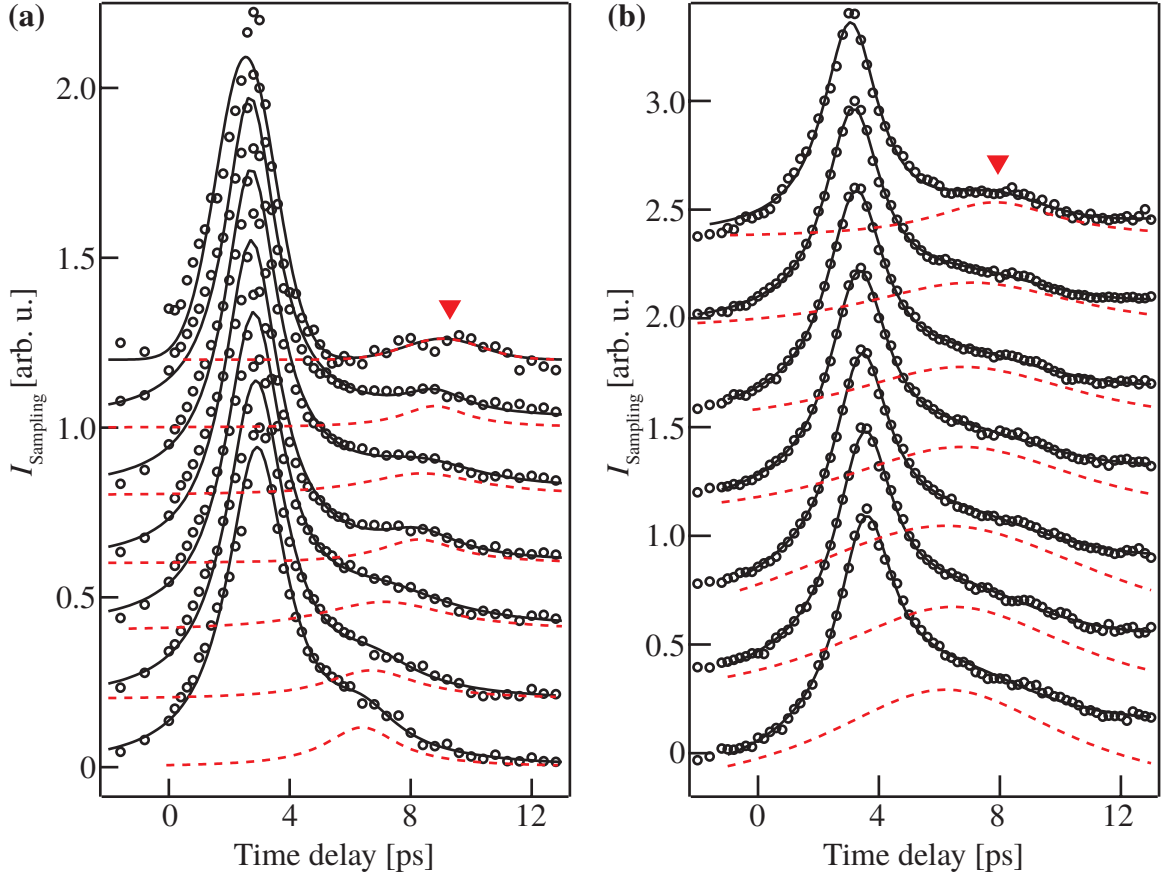


Figure 3.1 — (a) Time-resolved I_{Sampling} for $5.6 \mu\text{m} \leq x_0 \leq 9.4 \mu\text{m}$ in steps of 625 nm from bottom to top ($E_{\text{Laser}} = 1.59 \text{ eV}$, $P_{\text{Laser}} = 0.5 \text{ mW}$, $d \approx 15 \mu\text{m}$, $V_{\text{SD}} = 3 \text{ V}$), with a first peak at $\sim 3 \text{ ps}$ and second peak marked with a red triangle. Graphs are off-set. Solid/dashed lines are fits. (b) Data for $E_{\text{Laser}} = 1.51 \text{ eV}$ ($P_{\text{Laser}} = 880 \mu\text{W}$). [Pre10]

field

$$F = |\vec{F}| = V_{\text{SD}}/d \quad (3.1)$$

is constant in between the two contacts (solid line in Figure 3.2b). The excitation laser generates a high local electrical conductivity in the vicinity of x_0 [Zho96]. Therefore, the electric field can be assumed to drop to zero² at the position x_0 directly after laser excitation (dashed line in Figure 3.2b), while it increases in the

²The electric field will only drop to zero for sufficient excitation densities. Furthermore, the electric field depends on the light absorption, which can be described with the Lambert-Beer law. Therefore, the electric field drop will decrease with distance below the surface. Yet, the generation mechanism for a displacement current also holds for small electric field drops.

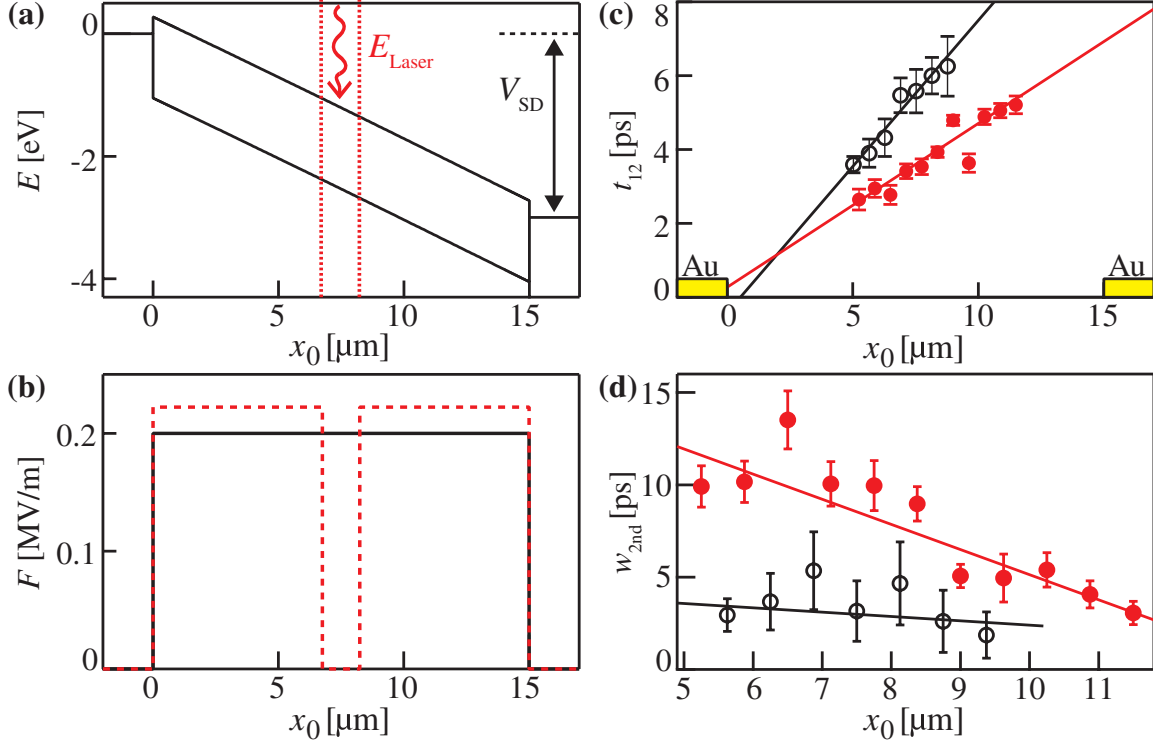


Figure 3.2 — (a) Schematic band structure of GaAs along x_0 at $V_{SD} = 3$ V. (b) Electric field before and directly after laser excitation (solid/dashed line). See also section 1.2. (c) t_{12} as a function of x_0 for $E_{Laser} = 1.59$ eV ($P_{Laser} = 0.5$ mW, open black circles) and $E_{Laser} = 1.51$ eV ($P_{Laser} = 880$ μW, full red circles) [Pre10]. (d) Full-width-half-maximum w_{2nd} of the second peak as a function of x_0 for $E_{Laser} = 1.59$ eV ($P_{Laser} = 0.5$ mW, open black circles) and $E_{Laser} = 1.51$ eV ($P_{Laser} = 880$ μW, full red circles).

remaining area to sustain the applied bias V_{SD} [Ale94, Zho96]. The resulting displacement current density (see also section 1.2)

$$\mathbf{j}_D = \epsilon_{\text{GaAs}} \epsilon_0 \frac{\partial \mathbf{F}}{\partial t} \quad (3.2)$$

is coupled into the stripline and sampled at the field-probe (ϵ_{GaAs} and ϵ_0 are the relative and vacuum permittivities). Hereby, we explain the occurrence of the first peak in I_{Sampling} at a constant Δt independent of the excitation position x_0 .

3.3 Time-resolved transport currents

The second peak in Figure 3.1 (marked with a filled red triangle) is found to shift in Δt as a function of x_0 . The solid lines in Figure 3.1 are least-squares fits with the sum of two Lorentzian curves at center positions t_1 and t_2 . For clarity, only the Lorentzian curves fitting the second peaks are individually drawn as dashed red lines. The difference

$$t_{12} = t_2 - t_1 \quad (3.3)$$

versus excitation position x_0 is plotted in Figure 3.2c for excitation energies of $E_{\text{Laser}} = 1.51 \text{ eV}$ (filled circles) and 1.59 eV (open circles). t_{12} ranges between 2.5 ps and 7 ps . We find that for both E_{Laser} , the linear fits of the data intersect at the position of the grounded metal stripline ($x_0 \approx 0 \mu\text{m}$) for $t_{12} \approx 0 \text{ ps}$ with an absolute spatial error of $2 \mu\text{m}$. The relative spatial error of the data in Figure 3.2c is given by the scanning mirror and is $\sim 100 \text{ nm}$. The absolute value of x_0 is measured by optical reflection.

The time-of-flight diagrams of Figure 3.2c already allow us to rule out THz reflections within the samples to explain the second peak. A THz pulse, which is re-absorbed at the position of the field probe, would be expected at a time-delay of

$$\Delta t' = 2 \cdot w \cdot \sqrt{\epsilon_{\text{GaAs}}} / c \approx 8.4 \text{ ps}, \quad (3.4)$$

with $w = 350 \mu\text{m}$ the height of the substrate. A reflected THz pulse, generated by the displacement current, would therefore be expected at $\Delta t' \geq 8 \text{ ps}$ after the displacement pulse. At the same time, a THz reflection at the interface between the LT-GaAs and the AlGaAs layer of the heterostructure would be expected at $\Delta t' \approx 0.1 \text{ ps}$. Therefore, THz reflections cannot account for the second peak of I_{Sampling} for $2.5 \text{ ps} \leq t_{12} \leq 7 \text{ ps}$. Finally, we point out that reflections of the propagating electromagnetic pulse at the end of the stripline cannot explain the second photocurrent peak, since they are expected at $\Delta t > 350 \text{ ps}$ due to a total stripline length of $\sim 45 \text{ mm}$. Therefore, we can rule out any kind of signal reflections as the origin of the second peak.

In Figure 3.2d we show the Lorentzian full-width-half-maximum $w_{2\text{nd}}$ of the second peak as a function of the excitation position x_0 for laser energies E_{Laser} of 1.51 eV and 1.59 eV . We observe a decreasing trend in $w_{2\text{nd}}$ with larger values of x_0 . This trend is possibly an artifact of the fitting procedure. If the second peak overlaps with the displacement peak, then a slight asymmetry of the displacement

peak can be accounted for by the second Lorentzian. The shift of $w_{2\text{nd}}$ to lower values for $E_{\text{Laser}} = 1.59 \text{ eV}$ compared to 1.51 eV might be due to better laser focussing conditions.

3.4 Measurements at zero-propagation length

In order to rule out dispersion effects in the coplanar stripline [Coo85, Has86, Gri87, Gri00], we move the pump-spot close to the field-probe. Figure 3.3a shows I_{Sampling} as a function of Δt for zero propagation length ($d \approx 0 \mu\text{m}$), at a fixed excitation position ($x_0 \approx 8 \mu\text{m}$), and for $1 \text{ V} \leq V_{\text{SD}} \leq 5 \text{ V}$. Again, we detect a second peak (marked with a filled triangle) at about $t_{12} = 6 \text{ ps}$ after the first peak, which is consistent with the observations at $d \approx 15 \mu\text{m}$ (Figure 3.1). The amplitude of both the first and the second peak in Figure 3.3a depend linearly on the applied bias V_{SD} (Figure 3.3b), as expected for displacement and transport currents. We note that a variation of the excitation position x_0 is not feasible at zero propagation length $d \approx 0 \mu\text{m}$, because then, the generation of a *shoulder* (see section 1.7 and [Ale94]) superimposes the second peak at small x_0 . Figure 3.3c shows the full-width-half-maximum $w_{2\text{nd}}$ of the second peak as a function of V_{SD} . We do not observe a clear dependence of $w_{2\text{nd}}$ on V_{SD} . The dashed line indicates the weighted average of $\langle w_{2\text{nd}} \rangle = (10 \pm 1) \text{ ps}$. This average value corresponds well to full-width-half-maximum values obtained in the measurements at non-zero propagation distance (see Figure 3.2d). We note, that the peak form at zero propagation length $d \approx 0 \mu\text{m}$ differs slightly from the observed peak form at $d \approx 15 \mu\text{m}$. As is explained in section 1.7, the local electric field distribution is probed in experiments with zero propagation distance, while only currents coupled into the stripline are probed in experiments with non-zero propagation distance. We therefore explain the different observed peak form at zero propagation distance by a measured electric field distribution.

3.5 Carrier velocities and plasma oscillations

We now turn again to the linear time-of-flight diagrams in Figure 3.2c. We would like to point out the following. The intersection of the linear fits at $x_0 \approx 0 \mu\text{m}$ and $t_{12} = 0 \text{ ps}$ cannot be explained by the reflection of THz radiation within the samples nor by dispersive effects. However, a charge transport process perpendicular to the stripline, as already described in section 1.3, can explain the time-of-flight

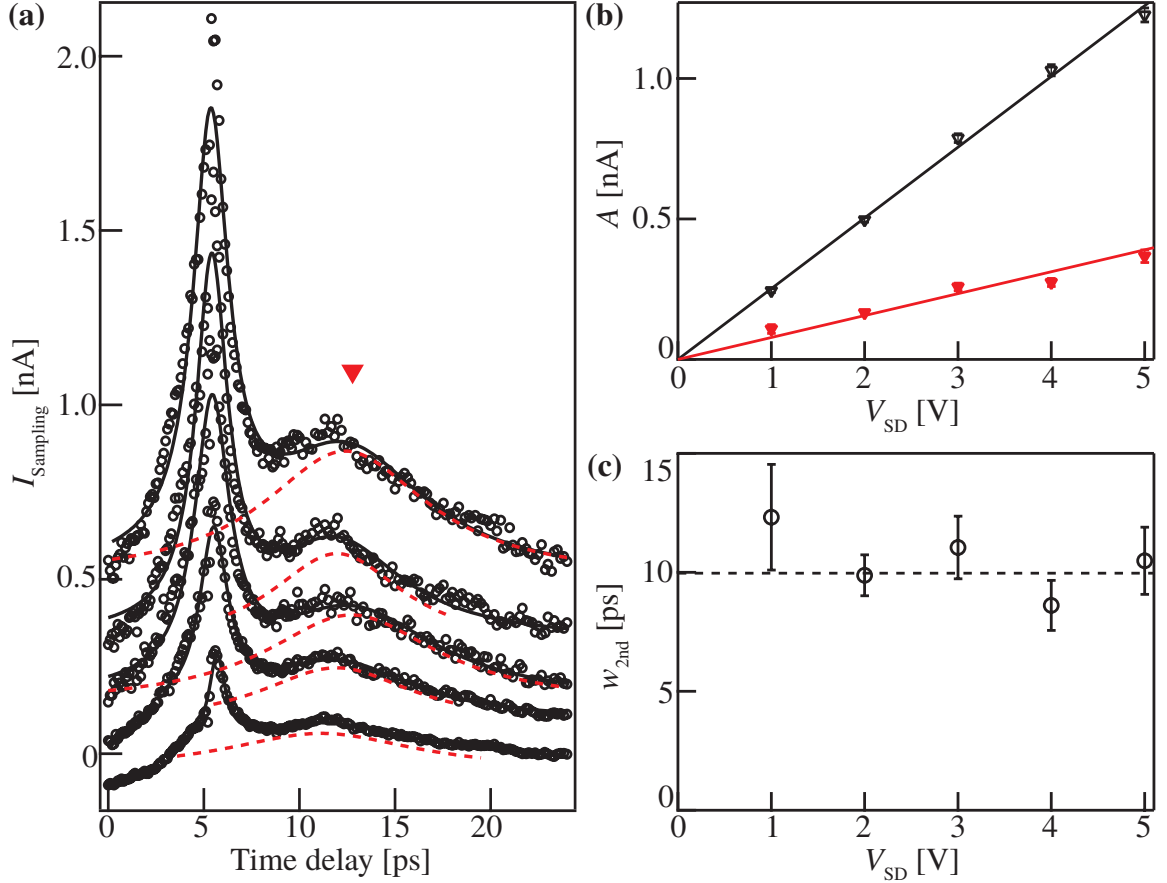


Figure 3.3 — (a) Time-resolved I_{Sampling} for $d \approx 0 \mu\text{m}$ ($V_{\text{SD}} = 1, 2, 3, 4, 5 \text{ V}$). Graphs are off-set ($E_{\text{Photon}} = 1.68 \text{ eV}$, $P_{\text{Laser}} = 1 \text{ mW}$, $x_0 \approx 8 \mu\text{m}$). (b) Amplitude of the first/second peak (open/filled triangles) as a function of V_{SD} . Lines are fits [Pre10]. (c) Full-width-half-maximum $w_{2\text{nd}}$ of the second peak as a function of V_{SD} . The dashed line indicates the weighted average of $w_{2\text{nd}}$.

graphs. We would like to emphasize here, that this interpretation is consistent with numerical predictions made by other groups [Pet87, Dun94, Dun96, Wil97]. Yet experimentally the time-of-flight of the transport peak has not been observed so far. The linear fits in Figure 3.2c give propagation velocities of

$$v_{\text{propagation}} = \partial x_0 / \partial t_{12} = (1.3 \pm 0.2) \times 10^8 \text{ cm/s} \quad (3.5)$$

for $E_{\text{Laser}} = 1.59 \text{ eV}$ and

$$v_{\text{propagation}} = (2.3 \pm 0.2) \times 10^8 \text{ cm/s} \quad (3.6)$$

for $E_{\text{Laser}} = 1.51 \text{ eV}$. All values of $v_{\text{propagation}}$ exceed typical thermal, drift and quantum velocities of single-particle charge excitations in GaAs at the utilized E_{Laser} . In the following, we calculate these velocities. The quantum (or group velocity) is defined as [Ash76]:

$$v_{\text{quantum}} = \frac{\partial E_e}{\hbar \partial k}. \quad (3.7)$$

Here, E_e is the energy of the electron in the conduction band. This energy can be easily calculated considering a parabolic dispersion relation of GaAs:

$$\begin{aligned} E_e &= \frac{\hbar^2 k_e^2}{2m_e^*} + E_{\text{gap}} \\ E_h &= \frac{\hbar^2 k_h^2}{2m_h^*}, \end{aligned} \quad (3.8)$$

with E_h the hole energy in the valence band, the wavenumber k , the effective electron mass $m_e^* = 0.067m_e$, the effective light-hole (heavy-hole) mass $m_h^* = m_{LH}^* = -0.082m_e$ ($m_h^* = m_{HH}^* = -0.56m_e$), the electron mass $m_e = 9.1 \times 10^{-31} \text{ kg}$, and the band-gap energy E_{gap} . For a laser excitation with energy E_{Laser} energy and momentum conservation needs to be fulfilled:

$$\begin{aligned} E_e &= E_{\text{Laser}} + E_h \\ k_e &= k_h \end{aligned} \quad (3.9)$$

The electron energy in the conduction band after laser excitation follows from equations 3.8 and 3.9:

$$E_e = \frac{E_{\text{Laser}} - E_{\text{gap}}}{1 + \frac{m_e^*}{m_h^*}}. \quad (3.10)$$

For a parabolic dispersion relation the quantum velocity is:

$$v_{\text{quantum}} = \sqrt{\frac{2E_e}{m_e^*}} = \sqrt{\frac{2(E_{\text{Laser}} - E_{\text{gap}})}{m_e^* \cdot (1 + \frac{m_e^*}{m_h^*})}}. \quad (3.11)$$

Yet, the parabolic dispersion breaks down for higher energies. Figure 3.4a shows a numerically calculated bandstructure of GaAs, utilizing the program *nextnano3* and a one-dimensional tight-binding model including spin-orbit coupling [Vog83, Kli00, Bir07, Bir11]. Also the quantum velocity as defined in equation 3.7 is shown in the same figure. The figure covers the range between the L- and the Γ -point

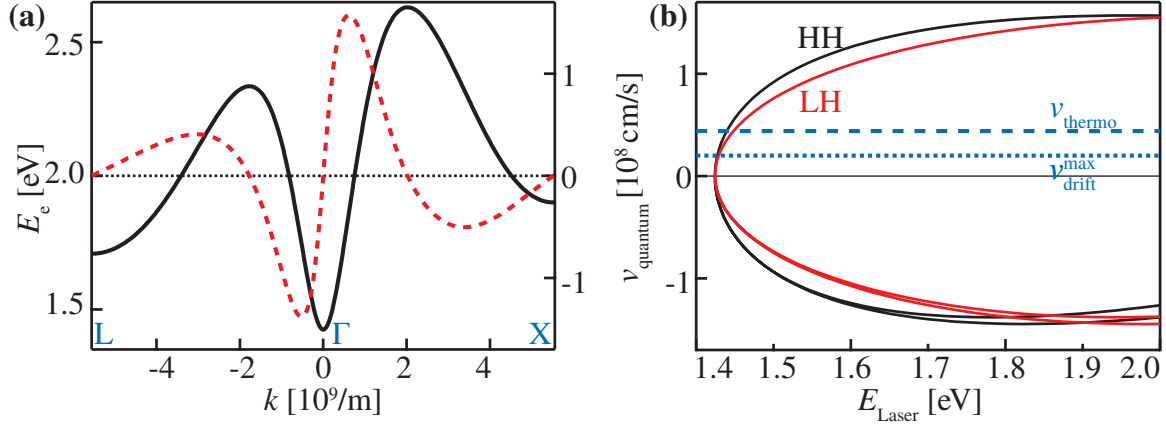


Figure 3.4— (a) First conduction band of GaAs (solid black line) and deduced quantum velocity v_{quantum} (dashed red line) as a function of the wavenumber k . (b) Calculated quantum velocity v_{quantum} as a function of the laser excitation energy E_{Laser} for excitation from the heavy-hole (HH, black line) and light-hole (LH, red line) valence band. The splitting in v_{quantum} observed for $E_{\text{Laser}} > 1.65 \text{ eV}$ is due to the bandstructure between the Γ and the U- or K-point. The calculated thermal velocity v_{thermal} is depicted as a horizontal dashed line. The maximum electron drift velocity v_{drift}^{\max} is depicted as a horizontal dotted line.

(negative values of k) and between the Γ - and the X-point (positive values of k). Figure 3.4b shows the calculated quantum velocity v_{quantum} as a function of the laser excitation energy E_{Laser} . The resulting v_{quantum} depends on the valence band, i.e. whether the electron is excited from the heavy-hole (HH, black line) or the light-hole (LH, red line) band. Both bands were numerically calculated in the same procedure as the conduction band. The splitting in v_{quantum} observed for $E_{\text{Laser}} > 1.65 \text{ eV}$ is due to the bandstructure between the Γ and the U- or K-point. For the employed laser energies in Figure 3.1 we calculate quantum velocities of $v_{\text{quantum}}(1.51 \text{ eV}) = 1 \times 10^8 \text{ cm/s}$ and $v_{\text{quantum}}(1.59 \text{ eV}) = 1.2 \times 10^8 \text{ cm/s}$.

The thermal speed of electrons can be calculated using Maxwell-Boltzmann statistics [Bla82]:

$$\frac{1}{2} m_e^* v_{\text{thermal}}^2 = \frac{3}{2} k_b T, \quad (3.12)$$

and consequently

$$v_{\text{thermal}} = \sqrt{3k_b T/m_e^*}. \quad (3.13)$$

At $T = 300 \text{ K}$ we calculate $v_{\text{thermal}} = 0.44 \times 10^8 \text{ cm s}^{-1}$. Figure 3.4b shows the calculated thermal velocity, which is independent of the laser energy, as a horizontal

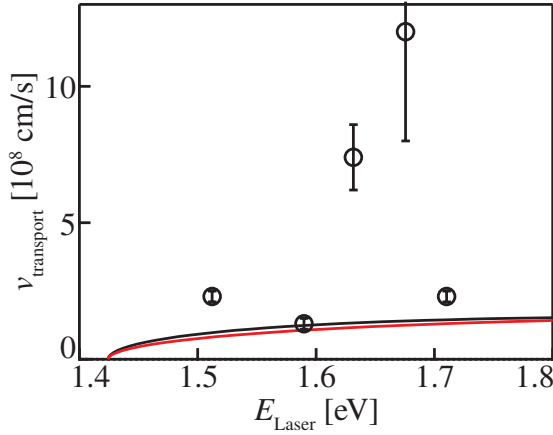


Figure 3.5 — Propagation velocity $v_{\text{propagation}}$ as a function of the laser energy E_{Laser} as determined from linear fits of t_{12} versus excitation position x_0 .

dotted line.

At high electric fields F electrons in GaAs are scattered to low-mobility conduction band minima (e.g. from the Γ valley to the L and X valley). This velocity overshoot is called the Gunn-effect [Gun63]. Therefore, the electron drift velocity $v_{\text{drift}} = \mu_e \cdot F$ has a maximum value (here, μ_e is the electron mobility). Experimentally, a maximum drift velocity of $v_{\text{drift}}^{\max} = 0.2 \times 10^8 \text{ cm/s}$ is achieved at a electric field of $F \sim 4 \text{ kV/cm}$ [Bla82]. v_{drift}^{\max} is depicted in Figure 3.4b as a horizontal dotted line.

In Figure 3.5 we show the experimentally determined propagation velocity $v_{\text{propagation}}$ as a function of the laser energy E_{Laser} . For comparison we also show the quantum velocity as a solid line. We do not observe a clear dependence of $v_{\text{propagation}}$ on E_{Laser} . Furthermore, $v_{\text{propagation}}$ exceeds the maximum drift velocity, the calculated thermal velocity, and the calculated quantum-velocity of single-particle charge excitations at the utilized E_{Laser} . However, the determined values of $v_{\text{propagation}}$ are consistent with values for collective electron-hole plasma excitations within a GaAs photo switch. There, charge plasma waves with $\sim 1 \times 10^8 \text{ cm/s}$ have been reported [Gli08], which oscillate perpendicular to the surface of the utilized heterostructures within the top LT-GaAs layer. Therefore, we tentatively ascribe the second peaks in Figure 3.1 and 3.3a to arise from the first initial transient oscillation of a plasma wave propagating parallel to the LT-GaAs surface. We find values for $v_{\text{propagation}}$ to be $\geq 1.3 \times 10^8 \text{ cm/s}$ for $1.51 \text{ eV} \leq E_{\text{Laser}} \leq 1.72 \text{ eV}$ with a non-systematic variation (see Figure 3.5). In this energy range, charge carriers are not excited into

the L - and X -side-valleys in GaAs [Bla82, Lei00], we therefore do not expect velocity overshoot or other effects related to intervalley scattering [Gun63].

3.6 Conclusions

In summary, we present ultrafast photocurrent measurements of LT-GaAs. We show that a first pulse in the time-resolved measurements is consistent with a displacement current pulse. We interpret a second pulse to result from a transport current process. We further determine the velocity of the photo-generated charge carriers of the transport current pulse in a time-of-flight experiment. This velocity exceeds drift, thermal and quantum velocities of single charge carriers. Hereby, we interpret the transport current pulse to stem from an electron-hole plasma excitation.

In principle, the influence of the excitation power density must be considered in the transport velocity analysis, since a phonon bottleneck can alter the decay dynamics of charge carriers in GaAs [Mur97]. Although the observed variations in $v_{\text{propagation}}$ with wavelength are significant, we could not find a systematic trend. The variations are tentatively attributed to the emission of optical phonons. It would be desirable to excite at an E_{Laser} less than 35 meV above the band-gap of GaAs to avoid the excitation of optical phonons [Gli08]. However, we find that our one-color on-chip detection scheme is not sensitive enough to detect I_{Sampling} at $E_{\text{Laser}} \approx E_{\text{GaAs}}$, since the light absorption in the LT-GaAs vanishes at the bandgap. Therefore, reducing the laser energy from $E_{\text{Laser}} \approx 1.51 \text{ eV}$ to $E_{\text{Laser}} = E_{\text{GaAs}}(T_{\text{bath}} = 300 \text{ K}) = 1.42 \text{ eV}$ effectively reduces the sensitivity of the field probe. These insights gave rise to the development of a two-color pump-probe scheme, where the probe beam can be frequency-doubled, thereby preserving the field probe sensitivity. At the same time the energy of the pump beam can be tuned close to (or even below) the bandgap of GaAs. Alternatively, a different semiconducting material with lower bandgap energy can be used for the field probe (see section 6).

Chapter 4

Time-resolved picosecond photocurrents in contacted carbon nanotubes

In this chapter the measurement technique introduced in chapter 2 is employed to investigate the ultrafast photocurrent dynamics in freely suspended carbon nanotubes (CNTs) in the time-domain. We demonstrate that CNTs, contacted by metal electrodes, exhibit a picosecond photocurrent response. We find that a combination of an optically induced ultrafast displacement current, a transport of photo-generated charge-carriers at the Fermi velocity to the electrodes, and interband charge-carrier recombination processes dominate the ultrafast photocurrent of the CNTs. A detailed understanding of such ultrafast charge carrier dynamics will become essential to design and build high-frequency devices based upon CNTs [Avo07, Rut09]. Our results show that CNTs can act as ultrafast photoswitches in electronic THz-circuits with a picosecond switching time. Section 4.1 introduces optoelectronic properties of CNTs. In section 4.2, we show the device geometry and investigate the temperature dependent conductance of the CNTs. Section 4.3 explains time-integrated photocurrent measurements by a crossover from *n* to *p*-type in between the CNT network. In section 4.4, we interpret time-resolved measurements in terms of a combination of displacement and transport currents. In section 4.5, we show that the time-resolved photocurrent is finally terminated by the recombination lifetime of the charge carriers. We show the temperature dependence of the time-resolved photocurrent in section 4.6 and conclude in section 4.7. The results presented in this chapter are published in [Pre11b].

4.1 Optoelectronic properties of carbon nanotubes

Single-walled carbon nanotubes (CNTs) are promising building blocks for future optoelectronic devices because of their compelling electronic and optical properties. A comprehensive review on the growth of CNTs and their structural and electronic properties can be found in [End97]. Their (radiofrequency) electrical [Avo07, Rut09] and optoelectronic [Avo08] properties have also been subject to extensive research. Due to the 1D-nature of CNTs, the electron-hole attraction energy becomes large [And97]. Therefore, excitonic effects play a major role in the optical properties of CNTs [Dre07]. Generally, photo-created excitons in CNTs can be dissociated by electric fields. Both external electric fields, generated by a bias voltage [Avo08, Fre03, Per07] and intrinsic fields (e.g. at defect sites [Bal05] or in the vicinity of Schottky barriers [Bal05, Kan09]) can be large enough to overcome the large excitonic binding energy of up to ~ 1 eV [Dre07]. So far, time-integrated optoelectronic experiments have revealed that hereby a photocurrent [Bal05, Kan09] and a photovoltage [Bal05] can originate. At large bias, energetic carriers in CNTs can also excite optical phonons [Yao00] and cause a non-equilibrium phonon distribution [Avo08]. The latter can give rise to a phonon-assisted dissociation of excitons [Per08] and to bolometric photoconductance phenomena [Itk06, Tse09, Zeb09]. So far, only optical methods have been used to characterize the ultrafast dynamics of photo-generated charge carriers in CNTs in the time domain. Typical fluorescence decay times of individual CNTs have been measured to be in the range of ten to hundreds of picoseconds [Ost04, Ma04, Hua04, Wan04, Hag05, Per05].

A THz time-domain measurement technique was recently developed by P.L. McEuen et al. to determine the ultrafast electrical response of CNTs [Zho08]. While this technique focuses on electrical excitations of the CNTs, the technique presented in this thesis utilizes an optical laser excitation of the CNTs and focuses on the time-resolved dynamics of photo-generated electrons.

4.2 Carbon nanotubes in a stripline circuit

Figure 4.1a shows an SEM image of a CNT network incorporated into a stripline circuit. At the location of the CNTs, the electrodes of the stripline have a distance of $9\ \mu\text{m}$. A sketch of the sample geometry is given in Figure 4.1b. For device fabrication see section 2.3. By Raman measurements (see Appendix B.5), the diameter of the CNTs is estimated to be $d_{\text{CNT}} = (1.0 \pm 0.1)\ \text{nm}$.

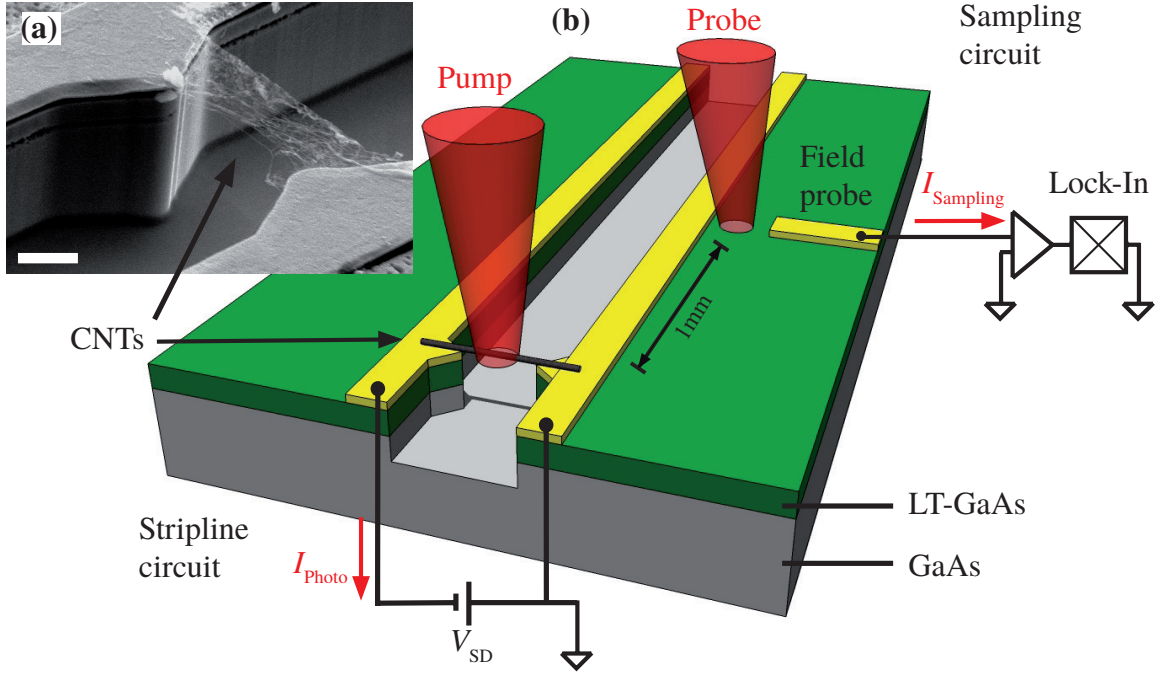


Figure 4.1 — Device geometry and optoelectronic pump-probe circuit. (a) Scanning electron microscope (SEM) image of freely suspended single-walled carbon nanotubes (CNTs) spanning two gold electrodes. Scale bar, $3\text{ }\mu\text{m}$. (b) Schematic on-chip detection geometry. The pump laser pulse is focused on the CNTs contacted by the stripline circuit. The probe-pulse triggers the sampling circuit. Gold electrodes are depicted in yellow. [Pre11b]

The freely suspended CNTs and the two electrodes form a two-terminal stripline circuit driven by a bias voltage V_{SD} (Figure 4.1b). Such CNT networks have recently been exploited to build biosensors [Sno05], transparent electrodes [Wu04], and bolometric photodetectors [Itk06]. Figure 4.2a shows the normalized conductance $\sigma(T)/\sigma_{RT}$ of the studied CNT network without illumination as a function of temperature T (σ_{RT} is the conductance value at room temperature). A good least-squares fit to the data is achieved by a model (green line), which considers fluctuation-induced tunneling between metallic regions within the CNT network that are separated by tunneling barriers [Bek05]:

$$\frac{\sigma(T)}{\sigma_{RT}} = B \cdot e^{-T_b/(T_s + T)} \quad (4.1)$$

with B a geometrical factor and $k_b T_b$ the magnitude of typical barrier energies. The

Fluctuation induced tunneling	Variable range hopping
$B = (1379 \pm 1) \text{ K}$	$\sigma_0 = (358 \pm 1) \text{ S}$
$T_b = (3891 \pm 1) \text{ K}$	$d = 0.7 \pm 0.3$
$T_s = (249 \pm 1) \text{ K}$	$T_0 = 55\,371 \text{ K}$

Table 4.1 — Fitting parameters obtained for the fluctuation-induced-tunneling and the variable-range-hopping model.

ratio T_s/T_b represents the quantum-induced tunneling in the absence of fluctuations and accounts for the suppression of the conductance at low temperature [Bek05, Kai98]. Fitting the model to our data, we obtain $k_b T_b = 335 \text{ meV}$ (see also table 4.1). A second model considers variable-range-hopping (VRH) by the following expression [Ska06]:

$$\sigma(T) = \sigma_0 \cdot \exp\left[-\left(\frac{T_0}{T}\right)^{\frac{1}{1+d}}\right] \quad (4.2)$$

with σ_0 and T_0 constants and d the dimensionality of the conducting paths. This model is not in good agreement within a least-squares fit with the conductance data at a temperature below 200K (red line). The fitting parameters obtained with the two different models are reported in Table 4.1. We therefore conclude that charge-carrier transport across the studied CNT network is dominated by fluctuation-induced tunneling [Kai98] between metallic regions that are separated by barriers of 335 meV.

Figure 4.2b shows the dark current I as a function of the applied source-drain bias V_{SD} for temperatures of $T_{\text{bath}} = 77 \text{ K}$ and $T_{\text{bath}} = 300 \text{ K}$. The magnitude of the dark-current is about two orders of magnitude higher for $T_{\text{bath}} = 300 \text{ K}$, as is expected from the temperature-dependent conductance measurements shown in Figure 4.2a. Figure 4.2c shows the differential conductance dI/dV_{SD} as a function of the applied source-drain bias V_{SD} for $T_{\text{bath}} = 300 \text{ K}$. dI/dV_{SD} decreases for $|V_{SD}| \leq 1.5 \text{ V}$. We interpret this decrease as an indication of a non-equilibrium phonon distribution generated by the applied electric field, as recently reported [Pur07, Jav04]. We note here, that a negative differential conductance is usually only observed for metallic CNT. We therefore interpret the positive differential conductance to arise from the semiconducting CNTs in our network, whereas the decrease of the differential conductance at small V_{SD} is due to the metallic CNTs in our network. As is shown in Figure 4.2d, dI/dV_{SD} increases linearly with $|V_{SD}|$ for $T_{\text{bath}} = 77 \text{ K}$. The

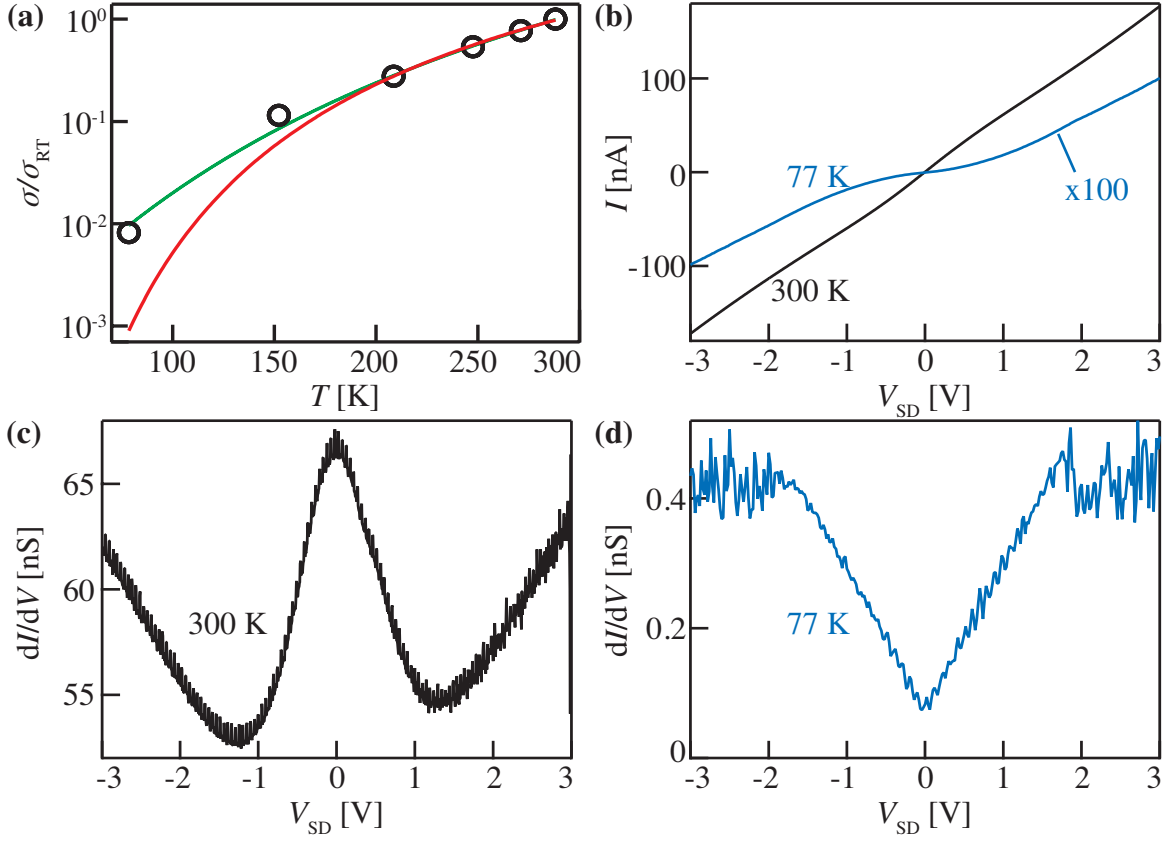


Figure 4.2 — (a) Normalized conductance $\sigma(T)/\sigma_{RT}$ of the studied CNT network without illumination as a function of temperature T . The green solid line is a least-squares fit with a fluctuation-induced-tunneling model. The red solid line is a least-squares fit with a variable-range-hopping model. [Pre11b] (b) Dark current I as a function of the source-drain bias V_{SD} for temperatures of 77 K (blue line, data values multiplied by 100) and 300 K (black line). (c) Differential conductance dI/dV_{SD} as a function of V_{SD} for $T_{bath} = 300$ K. (d) Differential conductance dI/dV_{SD} as a function of V_{SD} for $T_{bath} = 77$ K.

behavior of the differential conductance at 300 K has been observed in single-wall CNTs with low resistance contacts, while the behavior at 77 K has been observed in CNTs with high resistance contacts [Yao00] and in scanning tunneling experiments on single CNTs with highly conductive contacts dragged out of a CNT network [Col97]. Monte Carlo simulations, including disorder, of tunnel junction arrays predict a scaling law for the $I - V$ characteristics [Zab08, Mid93]:

$$I \propto (V - V_T)^\zeta. \quad (4.3)$$

Here, V_T is a Coulomb blockade voltage threshold below which current is zero and ζ is a scaling exponent that depends on the array dimensionality. For a finite array the simulations predict $\zeta \approx 2$ [Mid93]. In this interpretation, we can explain the measured linear differential conductance at 77K by charge carrier tunneling in a two-dimensional tunnel array above the Coulomb blockade voltage threshold.

To summarize, both the temperature dependent conductance measurements and the differential conductance measurements show, that the charge carrier transport at low temperatures is dominated by tunneling processes.

4.3 Electric fields in a carbon nanotube network

In Figure 4.3 we show the time-integrated, spatially resolved photocurrent I_{Photo} of the freely suspended CNTs in the stripline circuit. The suspended CNTs in the stripline circuit are optically excited by a pump-pulse at the second inter-subband transition E_{22} of the semiconducting CNTs in the network (see Appendix B.5 and [Kat99, Dre05, Avo08]) with $\sim 160\text{fs}$ pulse length generated by a Titanium:Sapphire laser¹. At zero V_{SD} , we find two spatial extrema of I_{Photo} , each of which in the vicinity of an electrode² (Figure 4.3b). The extrema are consistent with intrinsic potential differences between semiconducting CNTs and the metal electrodes [Bal05, Kan09] in combination with tube-tube junctions between semiconducting and metallic CNTs. In electrostatically undoped CNTs (we apply no back-gate voltage), the Fermi energy can be assumed to lie in the bandgap of the CNTs [Bus09]. Therefore, the Fermi energy varies strongly with a voltage bias applied across the CNT network. In turn, at large V_{SD} , the doping-type crosses from n - to p -type in between the two electrodes, and a larger fraction of the voltage drop occurs within the CNT network instead of at the contacts [Bus09]. The lower insets in Figure 4.3 show simplified sketches of such a bandstructure of a CNT network under applied bias V_{SD} [Bus09, Bal05, Kan09].

This explains that at $V_{\text{SD}} = -1\text{V}$ (1V) only one minimum (maximum) of I_{Photo}

¹The photocurrent in single semiconducting CNTs shows resonances with the energy of corresponding exciton states [Fre03]. We therefore excite resonantly with E_{22} to maximize I_{Photo} . In Appendix B.5 we find a broad diameter and therefore E_{22} distribution in our network. The energy width of the laser pulses is $\sim 20\text{meV}$. We consequently excite a CNT diameter distribution resonantly.

²We note that the spatial extrema are not spherically shaped but vertically elongated. This is not only due to the width of the CNT network, but also due to aberration effects of the microscope objective, which the laser beam enters under a large angle with respect to the optical axes (i.e. coma).

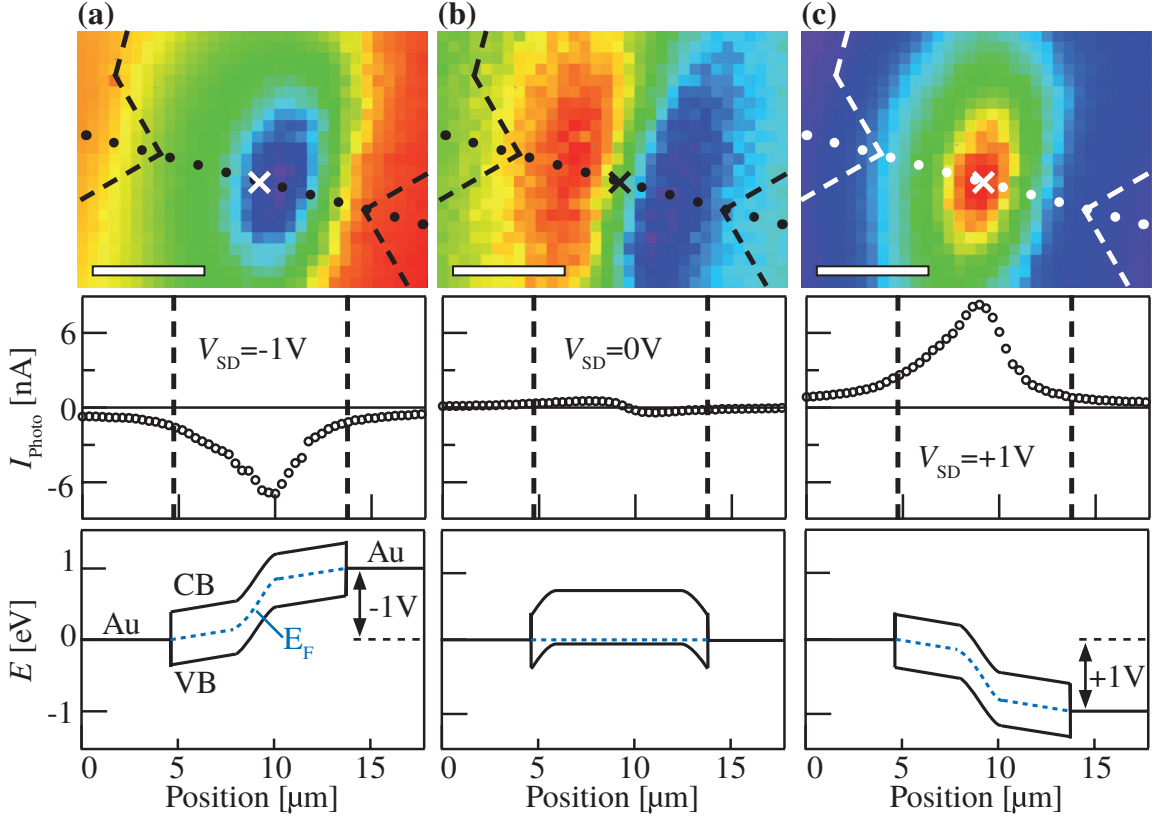


Figure 4.3 — Time-integrated photocurrent maps of the CNTs measured in the stripline circuit. (a) Spatially resolved, time-integrated photocurrent I_{Photo} of the CNTs at a bias voltage $V_{SD} = -1V$ and laser power $P_{Laser} = 100\mu W$. Dashed lines indicate the position of the electrodes. Dotted lines depict the shortest distance $d = 9\mu m$ between the electrodes. (b) and (c) Equivalent data for $V_{SD} = 0V$ and $1V$. Scale bars, $5\mu m$. The middle insets show sketches of the conduction band (CB), the valence band (VB) and the Fermi energy E_F of the CNT network between the two electrodes (Au) [Bus09, Bal05, Kan09].

is observed (Figure 4.3a and c). Then, excitons are dissociated by the large electric fields in the middle of the CNT network and in turn, they contribute to the time-integrated photocurrent I_{Photo} [Avo08, Fre03].

4.4 Time-resolved displacement and transport currents

The time-resolved measurement technique employed for this experiment is described in detail in section 2.1. Figure 4.4a shows the time-resolved $I_{Sampling}$ as a

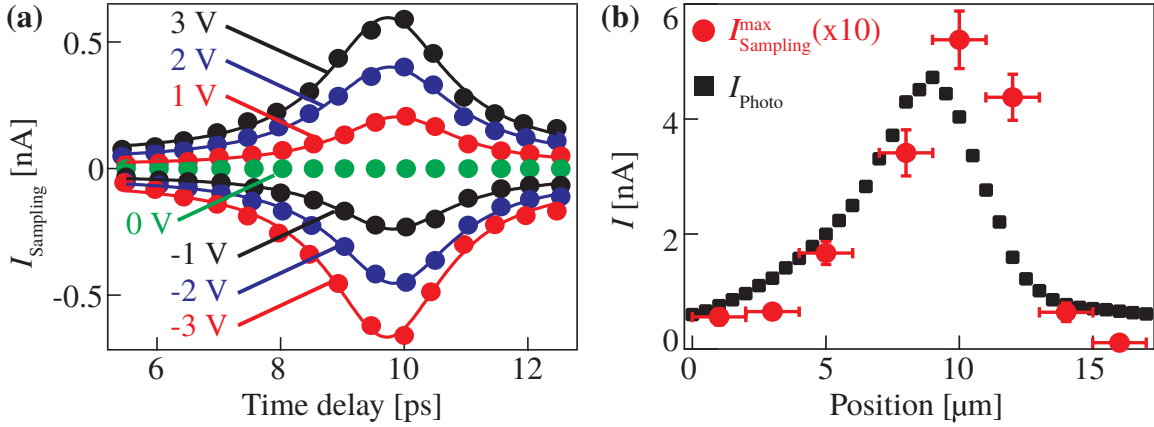


Figure 4.4 — Comparison of the time-resolved with the time-integrated photocurrent of the CNTs. (a) Photocurrent signal I_{Sampling} at the sampling circuit for a time delay $t_{\text{Delay}} \leq 13 \text{ ps}$. The pump laser beam is focused at the position marked with a cross in Figures 4.3a-c ($|V_{\text{SD}}| \leq 3 \text{ V}$, $P_{\text{Laser}} = 200 \mu\text{W}$). (b) Maximum value of I_{Sampling} and I_{Photo} as a function of the distance along the direction indicated by the dotted lines in Figure 4.3 ($V_{\text{SD}} = 3 \text{ V}$, $P_{\text{Laser}} = 200 \mu\text{W}$). [Pre11b]

function of t_{Delay} for $|V_{\text{SD}}| \leq 3 \text{ V}$. To reduce noise intrinsic to the electronic measurement setup we typically average five to seven data-sets of I_{Sampling} with a lock-in integration time of one to five seconds. For $t_{\text{Delay}} \leq 7 \text{ ps}$, I_{Sampling} equals nearly zero, because during this time-delay, the electro-magnetic pulse generated at the CNTs has not reached the field probe. At $t_{\text{Delay}} \approx 10 \text{ ps}$, I_{Sampling} exhibits a first peak with a full width at half maximum of $w_{1\text{stPeak}} \approx (2.1 \pm 0.1) \text{ ps}$. The sign of the time-resolved I_{Sampling} can be tuned by V_{SD} , and it directly corresponds to the one of the time-integrated I_{Photo} . Furthermore both signals vary in the same manner as a function of the position of the pump-laser, when it is scanned between the two electrodes (Figure 4.4b). Additionally, both I_{Photo} and I_{Sampling} depend linearly on the pump-laser power P_{Laser} , as is shown in Figure 4.5. Therefore I_{Sampling} is proportional to the electric potential landscape within the CNTs.

Generally, directly after optical excitation, the photo-generated charge-carriers redistribute in order to decrease the local potential differences in the CNT network [Moh06, Pre10]. This displacement of the charge carriers decreases the electric field \mathbf{F} in the irradiated region. In turn, the current density in the CNTs can be described by a transient displacement current density \mathbf{j}_d , as described in section 1.2:

$$\mathbf{j}_d = \epsilon_r \epsilon_0 \frac{\partial \mathbf{F}}{\partial t} \quad (4.4)$$

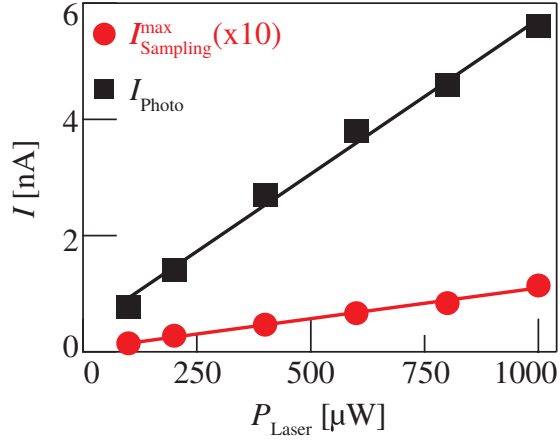


Figure 4.5 — Time-integrated photocurrent I_{Photo} (black squares) and maximal amplitude of the time-resolved current $I_{\text{Sampling}}^{\text{max}}$ (red circles) as a function of the pump-laser power P_{Laser} . Solid lines are linear fits.

with ϵ_r and ϵ_0 the relative and vacuum permittivity. For a femtosecond excitation, the displacement current can have a subpicosecond duration, although the carrier lifetime exceeds hundreds of picoseconds [Kro89]. Therefore, we interpret the peak of I_{Sampling} in Figure 4.4a to result from an optically induced displacement current [Pre10, Kro89] in accordance with equation 4.4 and section 1.2.³

As depicted in Figure 4.6a, we find that I_{Sampling} also exhibits a second peak, marked with a triangle. It is delayed by $t_{\text{2ndPeak}} = (4.8 \pm 0.2)\text{ps}$ with respect to the first peak at $\approx 10\text{ps}$. Such a second peak results from the transport of photo-generated charge-carriers to the electrodes, as has been demonstrated for LT-GaAs in chapter 3. There, the time delay of the second peak with respect to the first peak varies linearly with the excitation position between the contacts. In the case of LT-GaAs, a time-integrated and time-resolved photocurrent is homogeneously generated in the complete region between the contacts, because in LT-GaAs, a bias voltage generates a constant electric field between the contacts. In the case of CNT-networks, the amplitude of I_{Sampling} and I_{Photo} strongly varies with the excitation position (see Figure 4.4), since at large V_{SD} , the Fermi energy crosses from *n*- to *p*-type in between the two electrodes, and a larger fraction of the voltage drop occurs within the CNT network. For excitation in the middle between the contacts, the

³We note, that the peak form of I_{Sampling} in Figure 4.4a is slightly asymmetric. This is likely due to dispersion of propagating pulses on a stripline (see section 1.6.1).

present sensitivity of the circuit allows resolving the second peak, as shown in Figure 4.6a. We note that two experimental problems arise, when the laser excitation is moved closer to the contacts. First, the amplitude of I_{Sampling} strongly decreases (Figure 4.4b). Second, the time-delay between the first and the second peak is obscured by the full width at half maximum of the first peak of $w_{1\text{stPeak}} \approx (2.1 \pm 0.1) \text{ ps}$.

In the following, we rule out optical and THz reflections within the samples to explain the second peak. A reflection of the optical pump pulse at the bottom of the $10 \mu\text{m}$ deep trench, which is then re-absorbed in the CNTs, would be expected at a time delay of

$$\Delta t' = 2 \cdot 10 \mu\text{m} \cdot /c_0 \approx 0.1 \text{ ps} \quad (4.5)$$

after the displacement pulse. A THz pulse, generated by the displacement current in the CNTs, reflected at the back contact, and reabsorbed in the CNTs is expected at a time delay of

$$\Delta t' = 2 \cdot w \cdot \sqrt{\epsilon_{\text{GaAs}}} / c \approx 8.4 \text{ ps} \quad (4.6)$$

after the displacement pulse, with $w = 350 \mu\text{m}$ the height of the substrate. A THz pulse, generated by the displacement current, reflected at the back contact, and reabsorbed at the field probe would be expected at

$$\Delta t' \geq 13 \text{ ps} - 15 \text{ ps} \quad (4.7)$$

after the displacement pulse. Here, $\Delta t'$ depends on the location of the reflection in between the CNTs and the fieldprobe. At the same time, a THz reflection at the interface between the LT-GaAs and the AlGaAs layer of the heterostructure would be expected at $\Delta t' \approx 0.1 \text{ ps}$. Therefore, THz reflections cannot account for the second peak of I_{Sampling} at $t_{2\text{ndPeak}} = (4.8 \pm 0.2) \text{ ps}$. Finally, we point out that reflections of the propagating electromagnetic pulse at the end of the stripline cannot explain the second I_{Sampling} peak, since they are expected at $\Delta t > 350 \text{ ps}$ due to a total stripline length of $\sim 45 \text{ mm}$. Therefore, we can rule out any kind of signal reflections as the origin of the second peak and conclude that it results from the transport of photo-generated charge-carriers to the electrodes.

The occurrence of a second peak in I_{Sampling} , when exciting the CNTs at the center between the two contacts, already allows determining the group velocity of the photo-generated charge carriers in the CNT-network. In that case, the photo-generated charge-carriers in the CNTs need to propagate $\frac{d}{2} \approx (4.5 \pm 0.5) \mu\text{m}$, before they reach the metal contacts. Assuming an average group velocity of the

photo-generated charge-carriers in the CNT network, we can estimate its value to be $v_{\text{Group}} = d/(2 \cdot t_{\text{2ndPeak}}) \approx (0.9 \pm 0.1) \times 10^6 \text{ m s}^{-1}$. Within the experimental error, the value does not vary with V_{SD} in our experiment (see Figure 4.6a). Generally, the deduced value of v_{Group} is consistent with the Fermi velocity [Zho08] in CNTs of $v_{\text{Fermi}} \approx 0.8 \times 10^6 \text{ m s}^{-1}$. Furthermore, the value is significantly less than the propagation velocity of plasmon modes in CNTs of $v_{\text{Plasmon}} = 2.7 \times 10^6 \text{ m s}^{-1}$ [Zho08]. Hereby, the measurements suggest that single electron excitations and not plasmon modes dominate the ultrafast optoelectronic response of freely suspended CNTs.

4.5 Carrier recombination lifetime

As can be seen in Figure 4.6b and c, I_{Sampling} also exhibits a slow decay component. We utilize the sum of two Lorentzian functions and an exponentially convoluted Gaussian to account for all features in I_{Sampling} . The individual fit functions are exemplarily plotted in Figure 4.6c. A fitting parameter τ_{Slow} describes the exponential decay of the convoluted Gaussian, and it can be associated with the slow decay. We find a value of $\tau_{\text{Slow}} = (248 \pm 2) \text{ ps}$, independent of V_{SD} . We note that such a large value of τ_{Slow} is not present when a LT-GaAs substrate substitutes the CNTs in the stripline circuit, as is shown in chapter 3. We can neglect bolometric photoconductance phenomena in freely suspended CNT networks to describe the ultrafast photocurrent dynamics, because the typical timescale of bolometric effects in such networks are in the range of milliseconds [Itk06, Zeb09]. Following the work by D.H. Auston [Aus80b, Aus83], we interpret τ_{Slow} to be the lifetime of photo-generated charge carriers in the CNT network [Per05]. We stress that it is outstanding to measure carrier lifetimes in freely suspended CVD grown CNTs, because such CNTs have a typical interband transition energy E_{11} below 1 eV [Jor08, Avo08]. This energy range lacks a sufficiently fast photo-detector.

4.6 Temperature dependence of I_{Sampling}

The amplitude A_{1stPeak} of the displacement peak only weakly depends on T_{Bath} , as is shown in Figure 4.7a. This finding is consistent with rather large barriers in the CNT network with a height of $k_{\text{B}}T_{\text{b}} = k_{\text{B}}(3891 \pm 1)\text{K} \approx 346 \text{ meV}$ (see section 4.2), since a displacement current is generated at the presence of an electric field. The generation mechanism of the time-dependent photocurrent as proposed

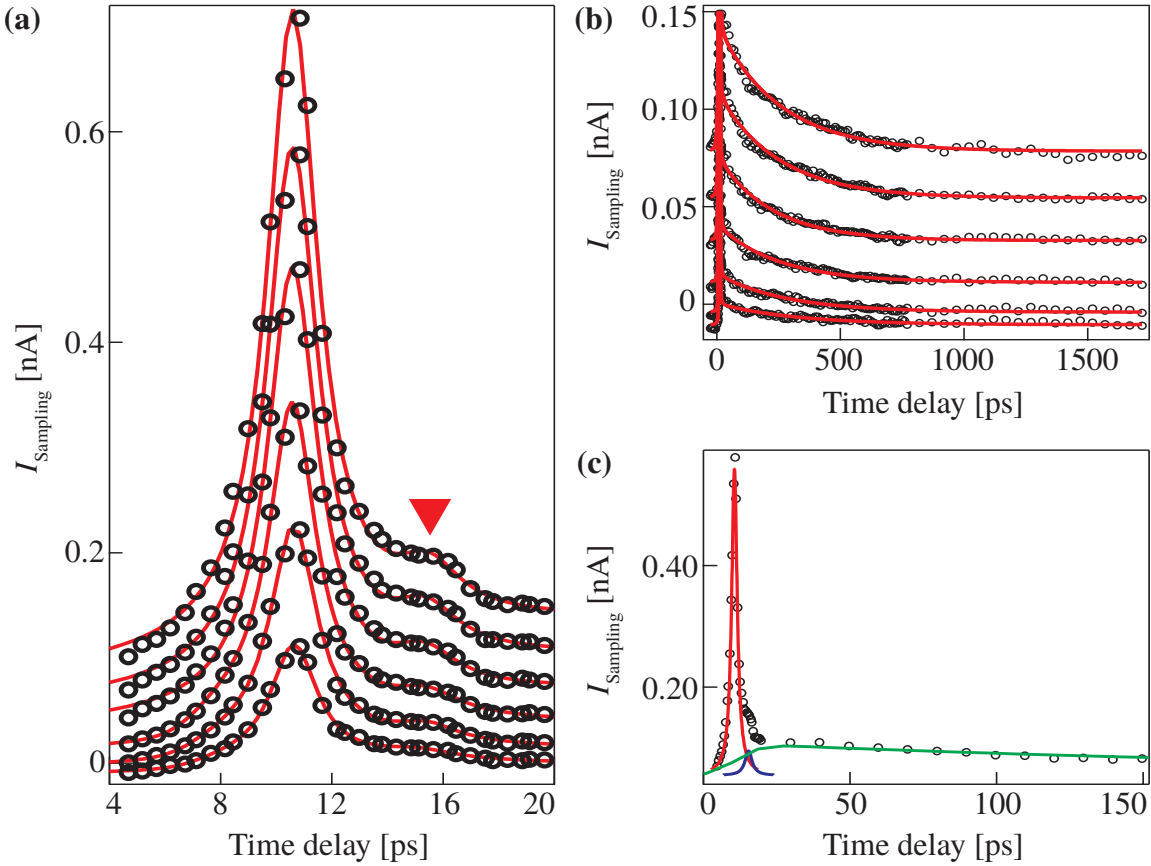


Figure 4.6 — Time-resolved photocurrent dynamics of the CNTs. (a) I_{Sampling} for t_{Delay} up to 20 ps ($P_{\text{Laser}} = 200 \mu\text{W}$). It exhibits a first and a second peak (marked with a triangle), both of which are fitted by Lorentzian functions (red solid lines) ($V_{SD} = 0.5 \text{ V}$ to 3 V in steps of 0.5 V , from bottom to top). (b) I_{Sampling} for t_{Delay} extended to 1.8 ns with fit functions (lines). (c) I_{Sampling} for $V_{SD} = 2.5 \text{ V}$ and the individual components of the fit function (lines). The first and the second peak are fitted by Lorentzians depicted in red and blue. The slow decay is fitted by an exponentially convoluted Gaussian function with fitting parameter τ_{Slow} , depicted in green. [Pre11b]

by D.H. Auston [Aus83], however, depends critically on the contact resistance of the photoconductor. In the regime of ohmic contacts and uniform illumination of the photoconductor, the decay of the generated current pulse will be governed by the recombination dynamics of the photogenerated charge carriers [Aus83]. At room temperature, we obtain a rather linear I - V curve (see Figure 4.2b and c), and therefore can assume ohmic contacts. Consequently, we identify the exponential decay at room temperature to be the recombination lifetime of the photogenerated

4.6. Temperature dependence of $I_{Sampling}$

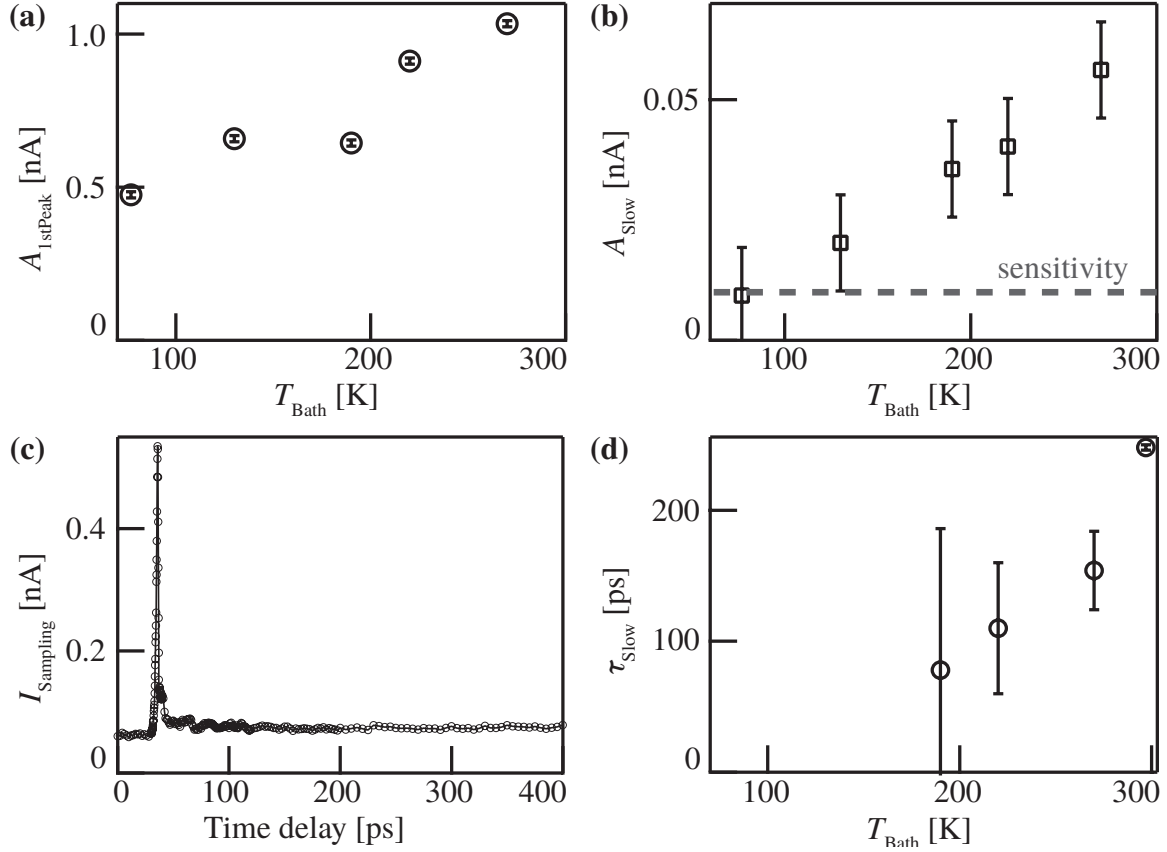


Figure 4.7 — Temperature dependence of the time-resolved photocurrent of the CNTs. (a) Amplitude $A_{1stPeak}$ of the first peak as a function of the bath temperature T_{Bath} . (b) Amplitude A_{Slow} as a function of T_{Bath} . (c) $I_{Sampling}$ as a function of the time delay at $T_{Bath} = 77$ K. (d) Decay time τ_{Slow} as a function of T_{Bath} ($V_{SD} = 3$ V, $P_{Laser} = 200 \mu\text{W}$).

charge carriers in the CNTs. Contrarily, at $T_{Bath} = 77$ K the I - V curve is strongly non-linear (see Figure 4.2b and d) and the resistance of the CNTs increases by two orders of magnitude compared to room temperature (see Figure 4.2a). Therefore, when T_{Bath} is decreased, one expects a decrease of the time-dependent photocurrent, and furthermore, the slow decay is not strictly governed by the recombination dynamics as proposed by D.H. Auston. Figure 4.7b shows the amplitude A_{Slow} of the slow-decaying photocurrent of the CNTs as a function of the bath temperature T_{Bath} . A_{Slow} decreases with lower T_{Bath} and cannot be resolved at $T_{Bath} = 77$ K within the experimental noise (indicated by a dashed line in Figure 4.7b). For instance, Figure 4.7c shows a time-resolved $I_{Sampling}$ -curve of the CNT network at

$T_{\text{Bath}} = 77\text{ K}$. Figure 4.7d shows the decay time τ_{Slow} as a function of the bath temperature T_{Bath} . For decreasing T_{Bath} from room temperature down to 190K, the decay time decreases from $\tau_{\text{Slow}} = (248 \pm 2)\text{ ps}$ down to $\tau_{\text{Slow}} = (78 \pm 110)\text{ ps}$. We could not deduce τ_{Slow} at bath temperatures lower than 190K due to the low amplitude A_{Slow} of the slow-decaying photocurrent. The general increasing trend of τ_{Slow} with T_{Bath} in this temperature range is in agreement with the temperature dependence of the expected exciton radiative lifetime τ_{rad} in semiconducting CNTs within a tight-binding approach [Per05]. We would like to note here, that also increasing lifetimes with decreasing temperatures have been measured by time-resolved photoluminescence for individual, uncontacted (6, 4) CNTs on a glass substrate [Hag05]. Time-resolved photoluminescence measurements on the same sample used for the measurements of I_{Sampling} and similarly processed samples were carried out in collaboration with the groups of Prof. J. Finley (TU München) and Prof. A. Hartschuh (Ludwig-Maximilian-Universität München). The first intersubband transition energy in our CNT network is $E_{11} \approx 0.8\text{ eV}$ (see Appendix B.5). Due to the lack of a sufficiently fast photodetector in the energy range $< 1\text{ eV}$ we were not able to measure the time-resolved photoluminescence of the suspended CNT network.

To the best of our knowledge, we present in this section the first recombination lifetime measurements of contacted, suspended, CVD grown CNT networks. Due to the non-ohmic behavior, we are not able to determine the radiative lifetime at temperatures below 190K. In the temperature range above, we find an increase of τ_{Slow} with T , which is in agreement with theoretical predictions [Per05].

4.7 Conclusions

In summary, we demonstrate that the ultrafast photocurrent response of CNTs comprises a displacement current and a transport current. Therefore, CNT networks can be exploited as ultrafast photodetectors with a switching time in the picosecond time-scale. The data further suggests that the photocurrent is finally terminated by the recombination lifetime of the charge carriers. Measurements of the recombination lifetime at low temperatures were impeded by the non-ohmic behavior. We consequently suggest single CNTs with ohmic contacts to further investigate the recombination and transit dynamics of photo generated charge carriers in contacted CNTs. For that purpose, first samples of single CNTs grown by CVD on a sapphire chip, contacted in a stripline circuit with ion-implanted Si at the field

4.7. Conclusions

probe have been processed in collaboration with the group of Prof. H. Maki (Keio University, Tokyo, Japan). The time-resolved photocurrent experiments on these samples will be carried out in the group of Prof. A. Holleitner.

Chapter 5

Ultrafast photocurrents and terahertz generation in graphene

We apply the pump-probe photocurrent spectroscopy scheme introduced in chapter 2 to graphene-based devices in order to resolve their photo-electric response up to 1 THz. Our ultrafast experiments clarify the optoelectronic mechanisms contributing to the photocurrent generation at graphene-metal interfaces. So far, this photocurrent has been extensively investigated by spatially resolved, but time-integrated photocurrent imaging techniques [Xia09a, Mue09, Xu10]. We demonstrate that both built-in electric fields, similar to those in semiconductor-metal interfaces, and a photo-thermoelectric effect give rise to the photocurrent at graphene-metal interfaces at different time scales. Built-in electric fields give rise to a photocurrent with a full-width-half-maximum of ~ 4 ps and the photo-thermoelectric effect generates a current with a decay time of (130 ± 10) ps. Our results open the possibility to design and fabricate ultrafast photodetectors and phototransistors, THz-sources, photovoltaic cells, and even lasers made out of graphene. The results presented in this chapter are summarized in [Pre11c].

Section 5.1 introduces optoelectronic properties of graphene. In section 5.2, we recapitulate the measurement scheme. The observation of a displacement and a photo-thermoelectric current at the graphene-metal interface is described in section 5.3. In section 5.4, we explain photocurrent oscillations that occur for optical excitation of the freely suspended graphene by the generation of terahertz radiation. We finally conclude in section 5.5.

5.1 Optoelectronic properties of graphene

Generally, graphene is a promising building block for a wide range of optoelectronic devices due to its extraordinary electrical and optical properties [Nov05, Zha05, Sta06, Gei07, Wan08b, Cas09, Kim09]. A review of the electronic properties of graphene, including basic theoretical concepts is given in [Cas09]. A comprehensive review of the optoelectronic properties of graphene, including some applications, can be found in [Bon10]. Major properties of graphene include:

- Graphene is a two-dimensional layer of carbon atoms arranged in a honeycomb lattice [Slo58, Wal47]. It is the building material for buckyballs and carbon nanotubes.
- The bandstructure of graphene is in a first approximation linear. As a consequence, electrons and holes have the same mobility and behave as massless, quasi-relativistic Dirac-fermions [Nov05].
- In an ambipolar electric field effect the charge carriers can be tuned continuously between electrons and holes up to densities as high as 10^{13} cm^{-2} and their mobilities can exceed $15\,000\text{ cm}^2/\text{Vs}$ [Nov04].
- Graphene absorbs $\sim 2\%$ of incident light over a broad wavelength range [Nai08].

The relatively high electron and hole mobility in graphene has spurred a tremendous interest in graphene-based high-speed electronic devices such as field-effect transistors and *pn*-junctions [Gei07, Cas09]. The frequency of plasma waves [Ran08], the gap of graphene nanoribbons [Son06, Han07, Sta09], and the tunable bandgap in bilayer graphene [Wan08a] are in the THz-range. Therefore, various graphene-based THz-sources and detectors have been proposed, for example optically pumped graphene incorporated in a slotline structure as active medium in a THz-laser [Ryz10, Kar11]. Graphene has also been employed as a photodetector [Xia09b, Mue10]. It has been shown, that the response-time does not degrade for frequencies up to 40GHz. While the RC-limited bandwidth of graphene-based photodetectors can be estimated to be as large as 640GHz [Xia09b], conventional electronic measurement techniques lack for analyzing photocurrents at such frequencies.

5.2 Experimental procedure

The time-resolved measurement technique for the experiments presented in this chapter is described in detail in section 2.1. The device fabrication is reported in section 2.3. Figure 5.1a shows an SEM image of the suspended graphene incorporated into a stripline circuit. The suspended graphene is optically excited by a pump-pulse with $\sim 160\text{fs}$ pulse length generated by a titanium:sapphire laser with a photon energy of $E_{\text{Laser}} = 1.59\text{ eV}$. After excitation, an electromagnetic pulse starts to travel along the stripline [Pre10, Pre11b]. A field probe senses the transient electric field of the traveling pulse (Figure 5.1d). Here, we utilize an Auston-switch based on the LT-GaAs substrate. This Auston-switch at the field probe is short-circuit by the probe laser-pulse for the duration of the lifetime $\leq 1\text{ ps}$ of the photo-generated charge-carriers in the LT-GaAs. The transient electric field located at the field probe during this time-period drives the current I_{Sampling} into the field probe. The time-delay t_{Delay} between the pump- and the probe-pulse is controlled by a delay stage. Measuring the current I_{Sampling} at the field probe as a function of t_{Delay} yields information on the optoelectronic response of the graphene with a picosecond time-resolution. The position of the pump-spot x perpendicular to the stripline is set by a scanning-mirror with a resulting spatial resolution of $\sim 100\text{ nm}$, while the position of the probe-spot is kept constant throughout the experiments. All room-temperature measurements of I_{Sampling} were carried out utilizing an optical chopper system, a current-voltage-converter connected to the field-probe, and a lock-in amplifier. The measurements at 77K were carried out with a retroreflector oscillating at 20Hz (*ScanDelay50*, APE Berlin) and an oscilloscope, which averaged 128 times for each excitation position. The spot size of the pump-laser is $(2.0 \pm 0.2)\mu\text{m}$. The laser power of the pump (probe) pulse is chosen to be in the range of $100\mu\text{W} - 800\mu\text{W}$ ($50\text{mW} - 120\text{mW}$). In this range the laser power of the probe-pulse only influences the sensitivity of the measurement.

5.3 Photocurrent generation at a graphene-metal interface

In Figure 5.1b we show the time-integrated, spatially resolved photocurrent I_{Photo} of the freely suspended graphene in the stripline circuit. At zero bias voltage V_{SD} , we find two spatial extrema of I_{Photo} , each of which in the vicinity of a

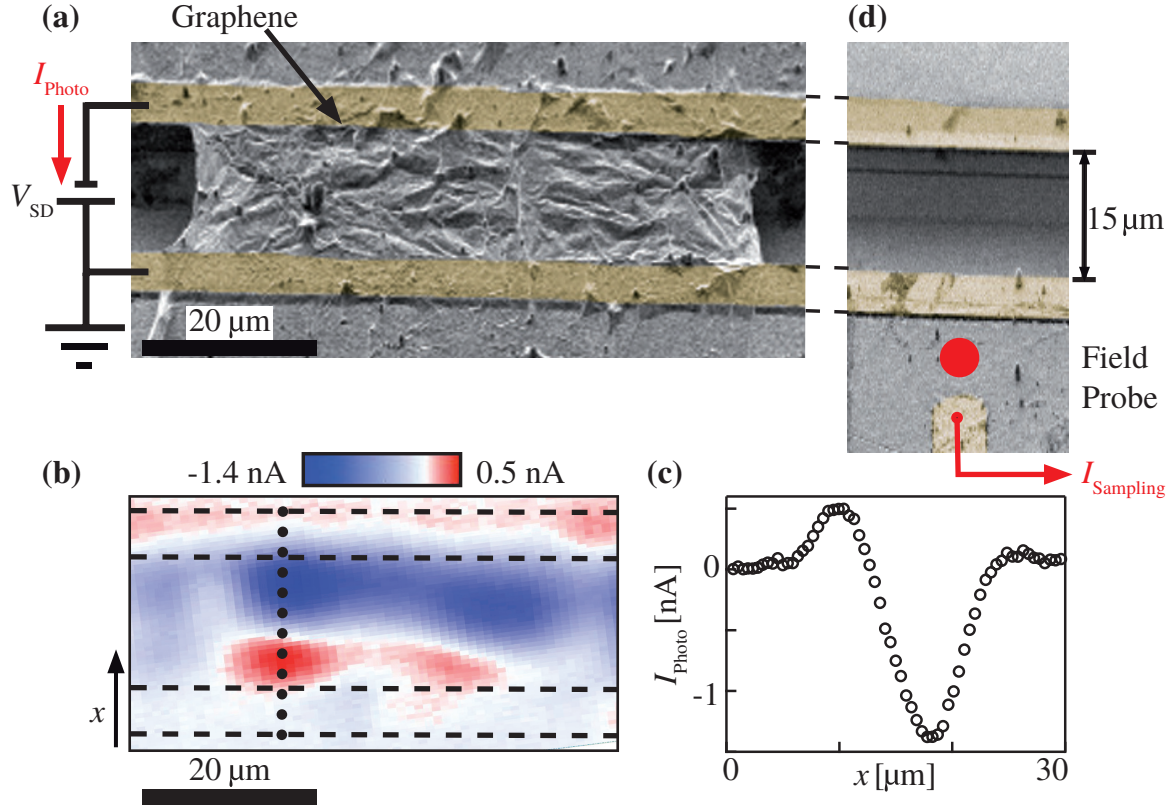


Figure 5.1 — Ultrafast photocurrent circuitry for graphene. (a) Freely suspended graphene is incorporated into a coplanar stripline circuit. A pump laser pulse focused onto the graphene-sheet generates the time-integrated photocurrent I_{Photo} . (b) Spatially resolved scan of I_{Photo} . The position of the striplines is indicated with dashed lines ($E_{\text{Laser}} = 1.6 \text{ eV}$, $P_{\text{Laser}} = 200 \mu\text{W}$, $V_{\text{SD}} = 0 \text{ V}$, $T_{\text{Bath}} = 300 \text{ K}$). (c) Single line-sweep of I_{Photo} along the dashed line in Figure 5.1b. (d) The time-resolved photocurrent response I_{Sampling} is measured at the field probe, located $\sim 0.3 \text{ mm}$ away from the graphene. The probe laser pulse (indicated with a red circle) triggers the read-out of I_{Sampling} . Adapted from [Pre11c].

metal electrode (Figure 5.1b and 5.1c). The extrema are consistent with recent scanning photocurrent results [Lee08, Xia09a, Xu10]. They can be explained in terms of built-in electric fields and/or a photo-thermoelectric current at graphene-metal interfaces, as will be discussed below in detail.

To investigate the temporal optoelectronic dynamics in graphene, we measure I_{Sampling} at the field-probe as a function of the time delay t_{Delay} between the pump- and probe-pulse (see Figure 5.1d). Figure 5.2a shows I_{Sampling} as a function of t_{Delay} for excitation positions starting at the graphene-metal interface in steps of $2 \mu\text{m}$

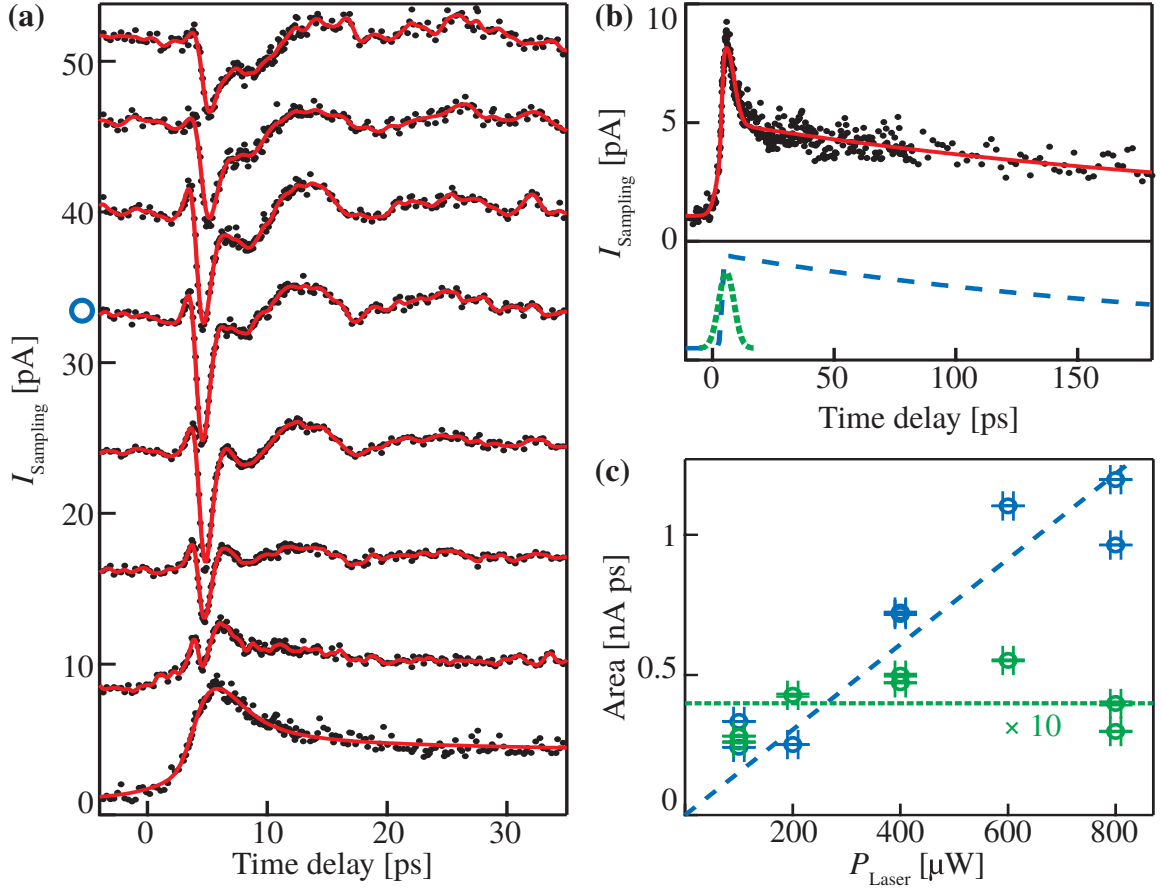


Figure 5.2 — Time-resolved photocurrents in graphene. **(a)** I_{Sampling} for excitation positions starting at the graphene-metal interface in steps of $2\mu\text{m}$ (from bottom to top) along the dotted line in Figure 5.1b. Solid lines are guide to the eye. Data are offset for clarity ($E_{\text{Laser}} = 1.59\text{ eV}$, $P_{\text{Laser}} = 800\mu\text{W}$, $V_{\text{SD}} = 0\text{ V}$, $T_{\text{Bath}} = 300\text{ K}$). **(b)** Lowest trace in Figure 5.2a and its fitting function (red solid line) for t_{Delay} up to 180 ps . The individual components of the fitting function are offset for clarity and depicted as blue dashed (exponentially convoluted Gaussian) and green dotted lines (Gaussian). **(c)** Area of the individual components of the fitting function for $0.1\text{ mW} \leq P_{\text{Laser}} \leq 0.8\text{ mW}$. The Gaussian contribution is depicted in green, the exponentially convoluted Gaussian in blue. Lines are linear fits. Adapted from [Pre11c].

(from bottom to top along the dotted line in Figure 5.1b). The amplitude of the main peak of I_{Sampling} centered around 5 ps reverses sign from the lowest to the topmost trace. This finding is consistent with the spatial dependence of I_{Photo} (Figure 5.1b and 5.1c), which indicates the direct correlation between the time-integrated I_{Photo} and the time-resolved I_{Sampling} [Pre10, Pre11b].

5.3.1 Displacement current

Generally, directly after an optical excitation of graphene the photogenerated charge-carriers redistribute in order to decrease local potential differences. This displacement of the charge-carriers decreases the electric field \mathbf{F} in the irradiated region, as described in section 1.2. In turn, the optoelectronic response can be described by the transient displacement current density given in equation 1.3 [Kro89, Zho96]. This mechanism also holds for built-in electric fields and can produce displacement currents even with sub-picosecond duration [Kro89, Zho96, Pre10]. The amplitude of the displacement current saturates if the electric field \mathbf{F} is set to zero by the displacement of the optically excited charge-carriers. Figure 5.2b shows the trace of I_{Sampling} at the graphene-metal interface extended to $t_{\text{Delay}} = 180 \text{ ps}$ (dots). The solid line is a fit with the sum of a Gaussian and an exponentially convoluted Gaussian, which are shown individually as dotted and dashed lines, respectively. The full-width-half-maximum of $(4.4 \pm 0.2) \text{ ps}$ of the dotted Gaussian contribution is comparable to values of displacement currents found in low temperature grown gallium arsenide ($\sim 1.5 \text{ ps}$) discussed in chapter 3 and in carbon nanotubes ($\sim 2.1 \text{ ps}$) reported in chapter 4. In Figure 5.3a we show the time-resolved I_{Sampling} for $100 \mu\text{W} \leq P_{\text{Laser}} \leq 800 \mu\text{W}$. The corresponding areas of the Gaussian and exponentially convoluted Gaussian fitting functions are shown in Figure 5.2c. The area of the dotted Gaussian contribution is approximately constant for the shown pump laser power (dotted green line in Figure 5.2c), identifying this photocurrent to be a displacement current in saturation. Generally, we expect the saturation of the displacement current in two-dimensional materials at lower laser powers than in bulk materials. Numerical three-dimensional simulations of the electric field redistribution after pulsed laser excitation show, that the electric field at the surface of a bulk material is set to zero for low photon fluxes, but the displacement current does not saturate at such fluxes [Zho96]. Also the field redistribution beneath the surface contributes to the displacement current. Due to the exponential light absorption in the substrate material the electric field is not set to zero in regions beneath the surface. Contrarily, in two-dimensional materials only the electric field at the surface contributes to the displacement current. Therefore, we expect the saturation of the displacement current in graphene at fairly low photon fluxes.

A second graphene structure¹ (structure #2) on the same chip shows the same

¹The second graphene structure is similar to the first structure, besides that the contacts to the stripline were not improved by electron beam induced deposition of platinum.

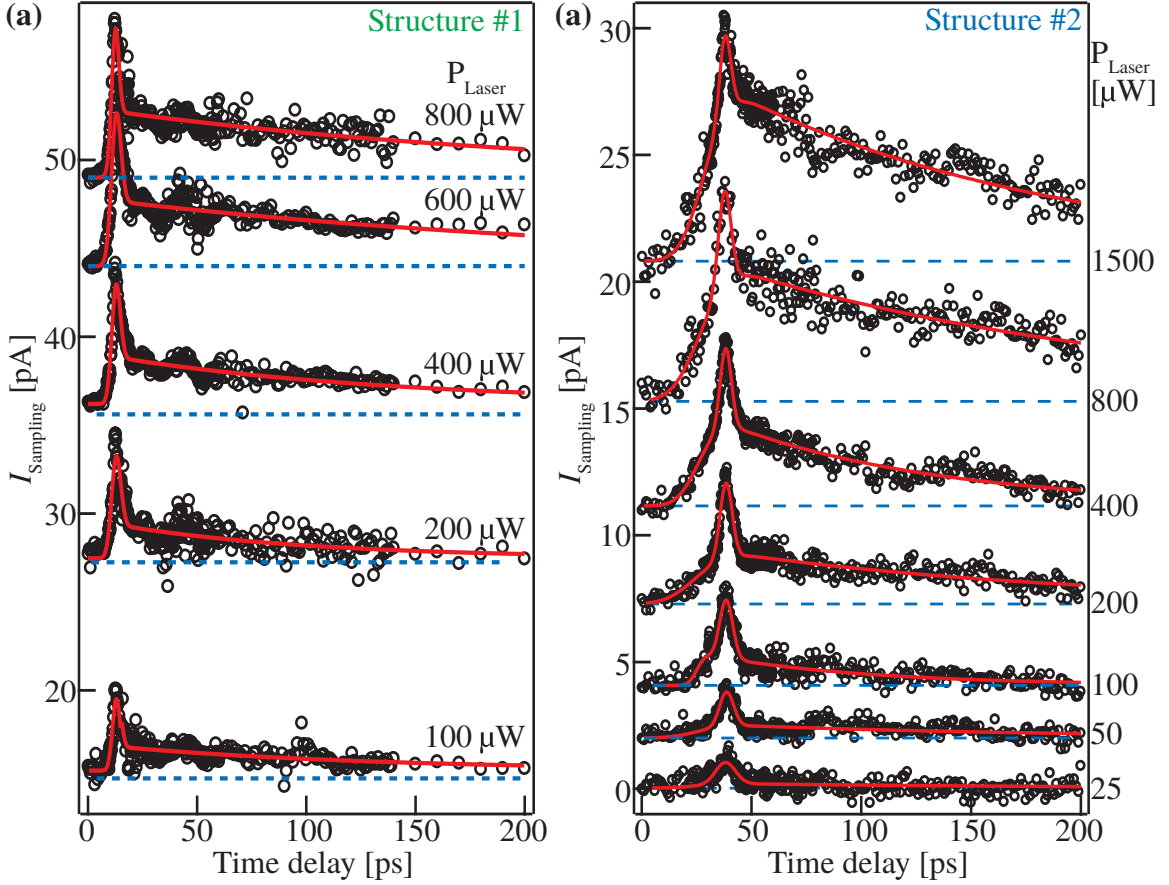


Figure 5.3 — Time-resolved photocurrents in graphene as a function of the pump laser power P_{Laser} . **(a)** I_{Sampling} for $100 \mu\text{W} \leq P_{\text{Laser}} \leq 800 \mu\text{W}$ for excitation close to the graphene-metal interface in structure #1. **(b)** I_{Sampling} for $25 \mu\text{W} \leq P_{\text{Laser}} \leq 1500 \mu\text{W}$ for excitation close to the graphene-metal interface in structure #2. In (b), traces are offset for clarity. Adapted from [Pre11c].

qualitative behavior. In Figure 5.3b we show the time-resolved I_{Sampling} of structure #2 for the pump laser power in the range $25 \mu\text{W} \leq P_{\text{Laser}} \leq 1500 \mu\text{W}$. The corresponding areas of the fit function components are shown in Figure 5.4a. The area of the exponentially convoluted Gaussian depends linearly on the laser power P_{Laser} for both structures, while the area of the Gaussian component is approximately constant for $P_{\text{Laser}} \geq 100 \mu\text{W}$. For $P_{\text{Laser}} < 100 \mu\text{W}$ the area of the Gaussian component increases with P_{Laser} . The absolute area values obtained for structure #1 and #2 cannot be compared, since the sensitivity of I_{Sampling} depends sensitively on the position of the probe laser spot at the field probe and on the probe laser power. Therefore

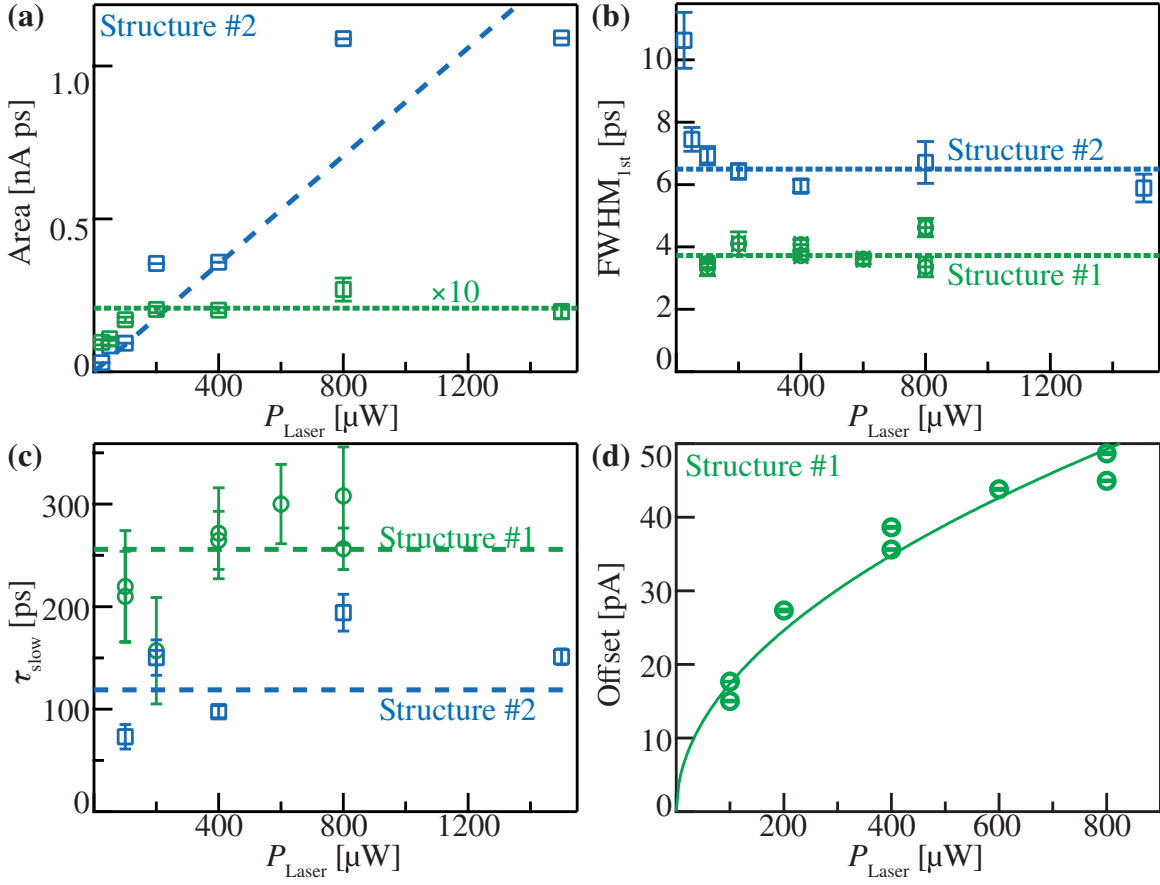


Figure 5.4 — Fitparameters of the first and the second graphene structure as function of the laser power P_{Laser} . **(a)** Area of the individual components of the fitting function of structure #2 for $25 \mu\text{W} \leq P_{\text{Laser}} \leq 1.5 \text{ mW}$. The Gaussian contribution is depicted in green, the exponentially convoluted Gaussian in blue. Lines are linear fits. **(b)** Full-width-half-maximum (FWHM) of the Gaussian component. Lines are weighted averages. **(c)** Fitparameter τ_{slow} of the exponentially convoluted Gaussian. Lines are weighted averages. **(d)** Offset of the I_{Sampling} traces (structure #1). The solid line is a fit with a square-root function.

the sensitivity can change from experiment to experiment. Nevertheless, the ratio $R_{\text{areas}}(P_{\text{Laser}})$ of the areas of the exponentially convoluted Gaussian and the Gaussian contribution can be compared for structure #1 and #2. We therefore divide the slope (exponentially convoluted Gaussian) by the weighted average (Gaussian contribution). For structure #1 we obtain $R_{\text{areas}} = (0.038 \pm 0.005) \mu\text{W}^{-1}$ and for structure #2 $R_{\text{areas}} = (0.042 \pm 0.006) \mu\text{W}^{-1}$. Within the error we obtain the same ratio R_{areas} for both structures. We therefore conclude, that both structures show the same relative

power dependence for excitation close to the graphene-metal interface.

In Figure 5.4b we show the full-width-half-maximum (FWHM) of the Gaussian component for structure #1 and #2. We obtain weighted averages of (3.7 ± 0.1) ps (structure #1) and (6.5 ± 0.2) ps (structure #2). Both values are comparable to values of displacement currents found in LT-GaAs (~ 1.5 ps, see chapter 3) and in carbon nanotubes (~ 2.1 ps, see chapter 4). We note, that short voltage pulses propagating across a material can experience dispersion (see section 1.6.1). Since we excite the graphene at least $10\text{ }\mu\text{m}$ away from its boundary (in the direction parallel to metal striplines) it is therefore possible that an initially shorter displacement current peak is broadened during the propagation across the graphene. We further note, that also a thermoelectric effect could in principle explain the generation of such short current pulses, but not the observed saturation of I_{Sampling} with P_{Laser} .

Based on the area saturation and the full-width-half-maximum of the Gaussian peak in I_{Sampling} we conclude that a displacement current due to built-in electric fields at the graphene-metal interface is generating this ultrafast photoresponse.

5.3.2 Photo-thermoelectric current

The slow decay of I_{Sampling} in Figure 5.2b can be described by an exponential decay of the convoluted Gaussian with fitting parameter τ_{Slow} . In Figure 5.4c we show τ_{Slow} as a function of the laser power P_{Laser} . We find that τ_{Slow} is approximately constant over the investigated range of $100\text{ }\mu\text{W} \leq P_{\text{Laser}} \leq 800\text{ }\mu\text{W}$ and we deduce a weighted average of $\tau_{\text{Slow}} = (260 \pm 20)$ ps (dashed green line). For structure #2 we obtain slightly lower values for τ_{Slow} independent of the laser power in the range $100\text{ }\mu\text{W} \leq P_{\text{Laser}} \leq 1500\text{ }\mu\text{W}$. We deduce a weighted average of $\tau_{\text{Slow}} = (120 \pm 10)$ ps (dashed blue line). For $P_{\text{Laser}} < 100\text{ }\mu\text{W}$ we cannot deduce τ_{Slow} due to the small amplitude of the exponentially convoluted Gaussian at such P_{Laser} . For both structures, we find a weighted average of (130 ± 10) ps.

We further note that the offset of I_{Sampling} (see Figure 5.4d and the blue dashed lines in Figure 5.3a) increases with the square-root of P_{Laser} . This is an indication, that slow processes with characteristic time-constants larger than the laser repetition rate of 13 ns ($\hat{=} 76$ MHz) generate a photocurrent in the graphene. In our measurement scheme, processes slower than the laser repetition rate cannot be resolved but they can only contribute to a constant background signal.

The area of the exponentially convoluted Gaussian increases linearly with P_{Laser} (dashed blue line in Figure 5.2c for structure #1 and Figure 5.4a for structure #2).

This suggests that the exponentially convoluted Gaussian is associated with a thermoelectric effect as described in section 1.4 because the thermovoltage V_{Thermo} can be described as

$$V_{\text{Thermo}} = (S_{\text{Graphene}} - S_{\text{Stripline}}) \cdot \Delta T, \quad (5.1)$$

with ΔT the optically induced temperature difference and S_{Graphene} and $S_{\text{Stripline}}$ the Seebeck coefficients or thermopower of graphene and the metal stripline [Xu10]. The thermopower of graphene depends on the charge carrier density and changes sign when the Fermi energy crosses the charge neutrality point [Gei07, Ada07]. S_{Graphene} depends linearly on the temperature T_{bath} and has a maximum measured value of $80 \mu\text{VK}^{-1}$ at $T_{\text{bath}} = 300\text{K}$ [Wei09, Hwa09, Zue09]. The magnitude of S_{Graphene} ranges under the highest measured so far. Theoretically, S_{Graphene} can be further enhanced by periodic electrode patterning to reach values up to 30mVK^{-1} [Dra07]. The thermopower of gold instead depends only weakly on T_{bath} in the temperature range $70\text{K} - 300\text{K}$ and has values of only $1 \mu\text{VK}^{-1} - 2 \mu\text{VK}^{-1}$. Therefore, the influence of $S_{\text{Stripline}}$ can be neglected in the following discussion of the power dependence of V_{Thermo} . The thermopower of graphene can be derived from the Mott-relation [Cut69, Zue09, Wei09, Xu10]:

$$S_{\text{Graphene}} = -\frac{\pi^2 k_b^2 T}{3e} \frac{1}{G} \left. \frac{dG}{dE} \right|_{E=E_{\text{Fermi}}} \quad (5.2)$$

with k_b the Boltzmann constant, e the electron charge, G the conductance and E_{Fermi} the Fermi energy. The conductance G is proportional to $n\mu$, with n the charge carrier density and μ the electron mobility. If the Fermi energy is far away from the Dirac point, μ is approximately constant. Then $\frac{dG}{dE}$ is proportional to the density of states $D(E)$ of graphene. Furthermore, the Fermi energy is $E_{\text{Fermi}} = \hbar v_{\text{Fermi}} \sqrt{\pi n}$ with v_{Fermi} the Fermi velocity of $1 \times 10^8 \text{ cm/s}$ [Cas09]. Inserting equation 5.2 in equations 5.1 it follows that

$$V_{\text{Thermo}} \propto T \cdot \Delta T \quad (5.3)$$

In our measurements we are exciting the graphene close to the metal contact. First, we estimate the maximum ΔT for excitation of the graphene considering the heat flow as a radial wave [Xu10] and neglecting the effects of pulsed excitation:

$$P \cdot \alpha = \kappa 2\pi h \Delta T \quad (5.4)$$

with P the incident laser power, $\alpha = 2.3\%$ the absorption coefficient of a single layer

graphene, $\kappa = 5 \times 10^3 \text{ W m}^{-1} \text{ K}^{-1}$ the thermal conductivity of graphene at room temperature, and $h = 3 \text{ \AA}$ the thickness of graphene [Nov04]. This yields a temperature increase of

$$\Delta T = \frac{P \cdot \alpha}{\kappa 2\pi h} = \frac{800 \mu\text{W} \cdot 0.023}{5 \times 10^3 \text{ W m}^{-1} \text{ K}^{-1} \cdot 2\pi \cdot 3 \times 10^{-10} \text{ m}} \approx 2 \text{ K}. \quad (5.5)$$

Since $T \gg \Delta T$, we can neglect the non-linear temperature dependence of κ , which effects a sub-linear power dependence of I_{Thermo} at low temperatures and high laser powers [Xu10]. We conclude that $\Delta T \propto P$ and consequently

$$V_{\text{Thermo}} \propto T \cdot P. \quad (5.6)$$

Indeed, the area of the exponentially convoluted Gaussian depends linearly on the laser power, as is shown in Figure 5.2c and Figure 5.4a. We infer, therefore, that the exponentially convoluted Gaussian can be associated with a photo-thermoelectric current.

For excitation close to the graphene-metal interface part of incident light will hit the metal structure. In the following, we discuss the effects of heating of the gold contact by the incident light. The estimation of the temperature increase for excitation of the gold is not as straightforward as in the case of graphene, since most of the absorbed energy is initially absorbed by the electrons and subsequently transferred to the lattice. Since the thermalization of the electrons and the energy transfer from the electrons to the lattice occurs on a fast timescale of $< 1 \text{ ps}$ [Fan92], pulsed excitation may not be neglected. The initial electron temperature T_e can be estimated by [Cor88]:

$$T_e = \left(\frac{4}{\pi \chi \tau_p} \right)^{1/4} \left(\frac{F}{C'_e} \right)^{1/2} \propto F^{1/2} / \tau_p^{1/4} \propto \sqrt{P} \quad (5.7)$$

with χ the thermal diffusivity, κ the heat conductivity, τ_p the laser pulse length, $F = \frac{P}{f_{\text{rep}} \cdot 2\pi r^2}$ the absorbed laser fluence (i.e. the laser energy per pulse per area) with the pulse repetition rate f_{rep} and the laser spot radius r , and C'_e the electron heat capacity [Kan98]. We estimate $T_e = 3 \times 10^2 \text{ }^\circ\text{C}$ by scaling the results obtained in [Kan98] to the parameters of our experiment ($\tau_p = 160 \text{ fs}$, $F \approx 0.3 \text{ mJ/cm}^2$, absorption $\sim 2\%$). One can expect that the maximum lattice temperature is about a factor of three smaller than the maximum electron temperature [Ees86]. Even though $1 \times 10^2 \text{ }^\circ\text{C}$ is a considerable temperature increase, the square-root power de-

pendence of T_e in equation 5.7 is not reproduced in our time-resolved measurements of I_{Sampling} . We therefore rule out the direct heating of the gold contacts to be responsible for the slow decay observed in I_{Sampling} .

In section 1.4 we showed that the decay of the gold lattice temperature T_l is dominated by heat diffusion rates along the metal stripline [Ees86]. The decay occurs on a timescale of several hundred ps, which is on the same order of magnitude of τ_{slow} . Based on these findings and the observed linear power dependence (Figure 5.2c), we conclude that the incident light is absorbed in the graphene and that the time-constant τ_{slow} is governed by heat diffusion in the metal. This interpretation is further corroborated by the fact that τ_{Slow} is constant for the examined range of P_{Laser} .

The estimation of absolute values of I_{Thermo} is complicated by the pulsed laser excitation. For that purpose, the time-resolved heat transport into the graphene and into the gold need to be numerically analyzed to obtain absolute values for $\Delta T(t)$. This task is not in the scope of this thesis and it is therefore only referred to literature [Row05, Kan08, Gro11]. Furthermore, we are not able to change or measure the charge carrier density n in our measurement scheme. We therefore cannot deduce absolute values of S_{Graphene} .

5.4 Terahertz generation in freely suspended graphene

At positions away from metal contacts photoexcited charge-carriers in graphene relax efficiently by the emission of optical phonons with a subsequent interband recombination process. The relaxation has been measured to be on a sub-picosecond time-scale, while the recombination depends on the carrier density, and it happens on a picosecond timescale [Daw08, Geo08, Hua10, Kar11]. Furthermore, the photoexcited electrons and holes can interact via instantaneous Coulomb potential in the graphene [Sto10]. For the pulsed laser excitation in our experiments ($\lambda = 780 \text{ nm}$, $P_{\text{Laser}} = 800 \mu\text{W}$, laser pulse energy $\sim 10 \text{ pJ}$, laser spot diameter $\sim 2 \mu\text{m}$, 2.3% absorption) we estimate an electron and hole density in the graphene of $\sim 0.3 \text{ nm}^{-2}$. At such high densities collisions of the previously monoenergetic electron-hole pairs lead to broadening of the energy distribution [Sto10]. In similar experimental conditions (electron-hole pair density 14 nm^{-2}) the fluorescence of an electron-hole plasma was observed [Sto10]. For both scenarios the emission of coherent terahertz emission has been theoretically predicted [Ran08, Ryz10].

In the first scenario (interband recombination after optical phonon relaxation), a population inversion of the photogenerated charge-carriers can be achieved [Ryz10]. First experimental observations of amplified stimulated terahertz emission in optically pumped graphene has been claimed [Kar11]. The minimum energy E_{THz} of the final interband recombination process can be estimated to be [Ryz07, Bon10]:

$$E_{\text{THz}} = E_{\text{Laser}} - 2 \cdot N \cdot E_{\text{Phonon}}, \quad (5.8)$$

with E_{Phonon} the optical phonon energy of 196 meV and N the maximum number of optical phonon excitations. In our experiment, E_{THz} can be estimated to be 22 meV with $E_{\text{Laser}} = 1.59 \text{ eV}$ (with a full-width-half-maximum of 13 meV). Hereby, one can expect photon emission up to a frequency of $f_{\text{THz}} = E_{\text{THz}}/h = 5.3 \text{ THz}$ with h the Planck's constant. In the second scenario (electron-hole plasma generation) the process of stimulated emission is not required for the emission of coherent radiation, since plasmons are a many-particle excitations and they are therefore naturally coherent. It has been theoretically shown, that the frequency of surface plasmons in graphene lies in the terahertz range and is carrier density dependent [Ran08, Ran10, Dub11]. We note, that surface plasmons can also be generated after relaxation via optical phonons.

In both scenarios, the coplanar striplines can pick up the generated electromagnetic radiation at frequencies up to $\sim 1 \text{ THz}$ (see section 1.5 and Appendix B.2). Indeed, for an optical excitation in the middle of the freely suspended graphene, we detect strong oscillations of I_{Sampling} that start at $t_{\text{Delay}} \approx 5 \text{ ps}$ (Figure 5.2a). The oscillatory amplitude increases towards the center of the graphene. We further investigate the oscillations by performing a Fast-Fourier-Transformation (FFT) (Figure 5.5a) of the I_{Sampling} trace indicated with an open circle in Figure 5.2a. Most prominently, we find amplitudes at frequencies up to 0.8 THz. We interpret this THz-radiation to arise either from a population inversion at E_{THz} resulting from the ultrafast relaxation via optical phonons and a comparatively slow interband recombination [Ryz10], or alternatively from electron-hole surface plasmon oscillations. The interpretation of THz-generation in the graphene is corroborated by the fact that the oscillatory behavior of I_{Sampling} does not have a counterpart in the time-integrated I_{Photo} , which decreases from the contacts towards the middle of the graphene (Figure 5.1c). At the graphene-metal interfaces (e.g. lowest trace in Figure 5.2a), the photo-thermoelectric effect and built-in electric fields dominate the optoelectronic response. Therefore, the fast oscillations of I_{Sampling} are generic

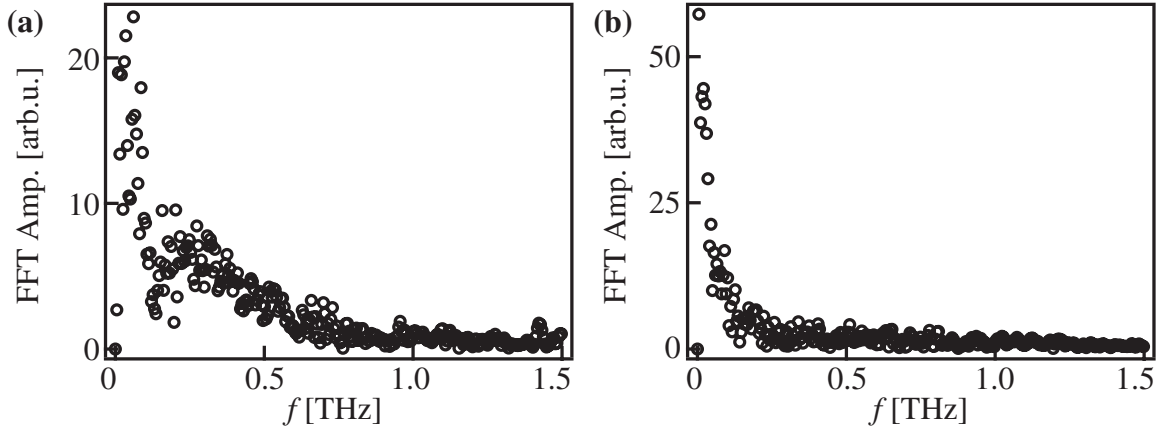


Figure 5.5 — Frequency analysis of ultrafast photocurrents in graphene. **(a)** Fast-Fourier-Transformation of I_{Sampling} for excitation in the center of the freely suspended graphene (trace indicated by open circle in Figure 5.2a). **(b)** Fast-Fourier-Transformation of I_{Sampling} for the excitation position close to the metal contact (lowest trace in Figure 5.2a). [Pre11c]

to the freely suspended graphene sections. For comparison, Figure 5.5b shows a Fast-Fourier-Transformation of I_{Sampling} measured at the graphene-metal interface (lowest trace in Figure 5.2a).

Figure 5.6a shows I_{Sampling} for excitation in the middle of the suspended graphene for laser powers $50 \mu\text{W} \leq P_{\text{Laser}} \leq 800 \mu\text{W}$. The amplitude of the oscillation centered around 5 ps to 10 ps increases with P_{Laser} . In Figure 5.6b we show the Fast-Fourier-Transformation of the I_{Sampling} traces shown in Figure 5.6a. Generally, the plasmon frequency depends on the charge carrier density, e.g. for electrons with quadratic energy dispersion in a 3D or 2D-system $f_{\text{plasmon}} \propto \sqrt{n_e}$ [Kit95, Ash76, Hwa07]. For graphene with linear energy dispersion, the plasmon frequency dependence is $f_{\text{plasmon}}^{\text{graphene}} \propto n^{1/4}$ [Hwa07]. Therefore, a shift of the observed oscillation spectrum to higher frequencies would indicate plasmons to be responsible for the oscillations. Contrarily, the oscillation spectrum for stimulated interband recombination would depend on the energy of the laser. The data shown in Figure 5.6a and b shows a slight shift to higher frequencies with P_{Laser} , supporting the interpretation of an electron-hole plasma. Yet, we cannot clearly rule out the stimulated interband recombination.

To further substantiate our interpretation, we show I_{Sampling} measured at a bath temperature $T_{\text{Bath}} = 77 \text{ K}$ in Figure 5.7a for excitation positions along the dotted line in Figure 5.1b. In a first approximation, S_{Graphene} linearly depends on temper-

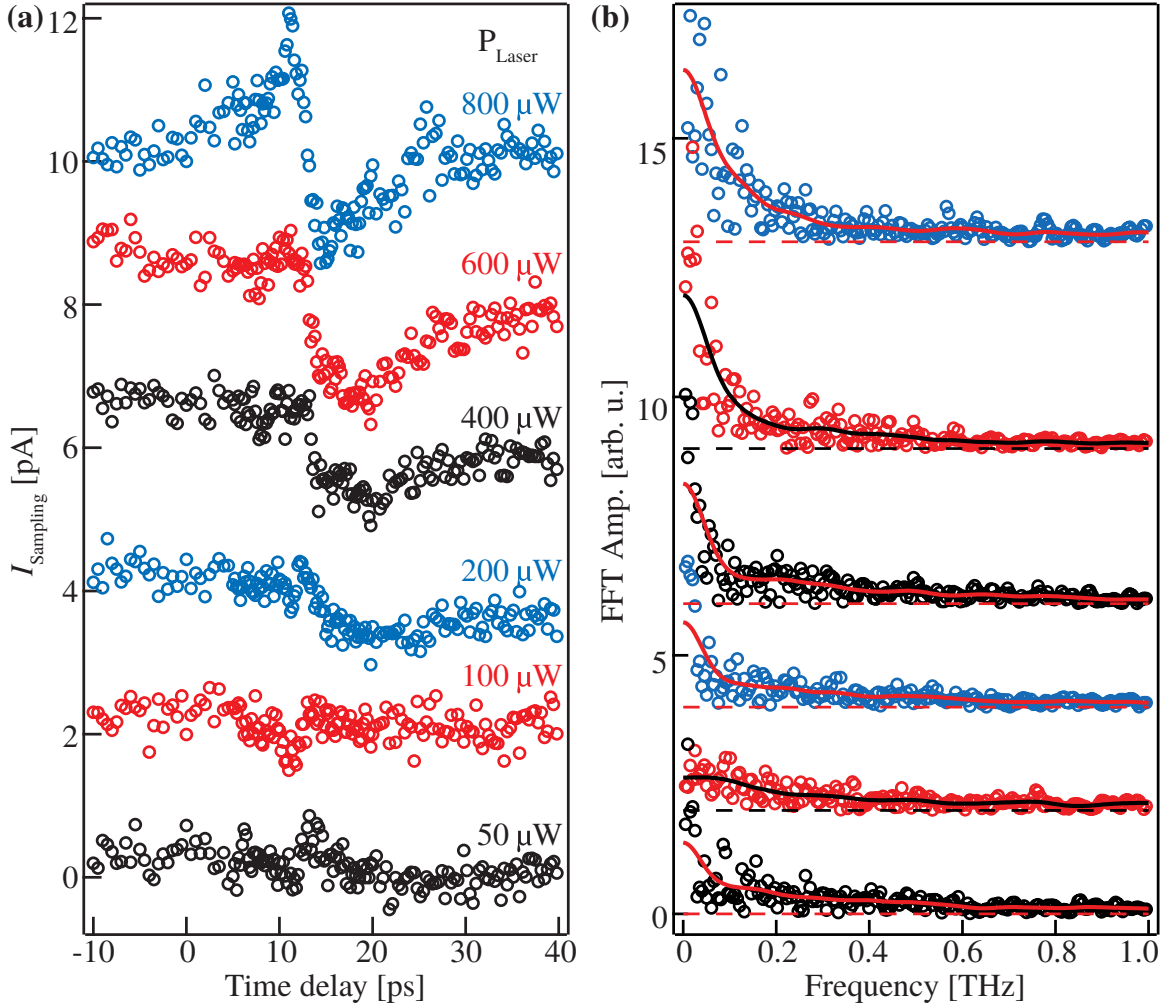


Figure 5.6 — Power dependence of the photocurrent generation for excitation in the center of the suspended graphene. **(a)** I_{Sampling} for $50 \mu\text{W} \leq P_{\text{Laser}} \leq 800 \mu\text{W}$. **(b)** Fast-Fourier-Transformation of the I_{Sampling} traces in a. Solid lines are smoothed data points. Dashed lines indicate the offset level. [Pre11c]

ature [Wei09, Hwa09]. Therefore, we expect a decrease of the thermoelectrically induced photocurrent to about 1/4 of its room-temperature value when lowering T_{Bath} down to 77 K. Indeed, at the graphene-metal interface, the slow-decaying signal of I_{Sampling} is suppressed (Figure 5.7a). In the middle of the freely suspended graphene, however, fast oscillations of I_{Sampling} again occur for $t_{\text{Delay}} \geq 5 \text{ ps}$. The Fast-Fourier-Transformation yields amplitudes for frequencies up to 1 THz (Figure 5.7b). Generally, the spectral response of our measurements is limited to below 1 THz by

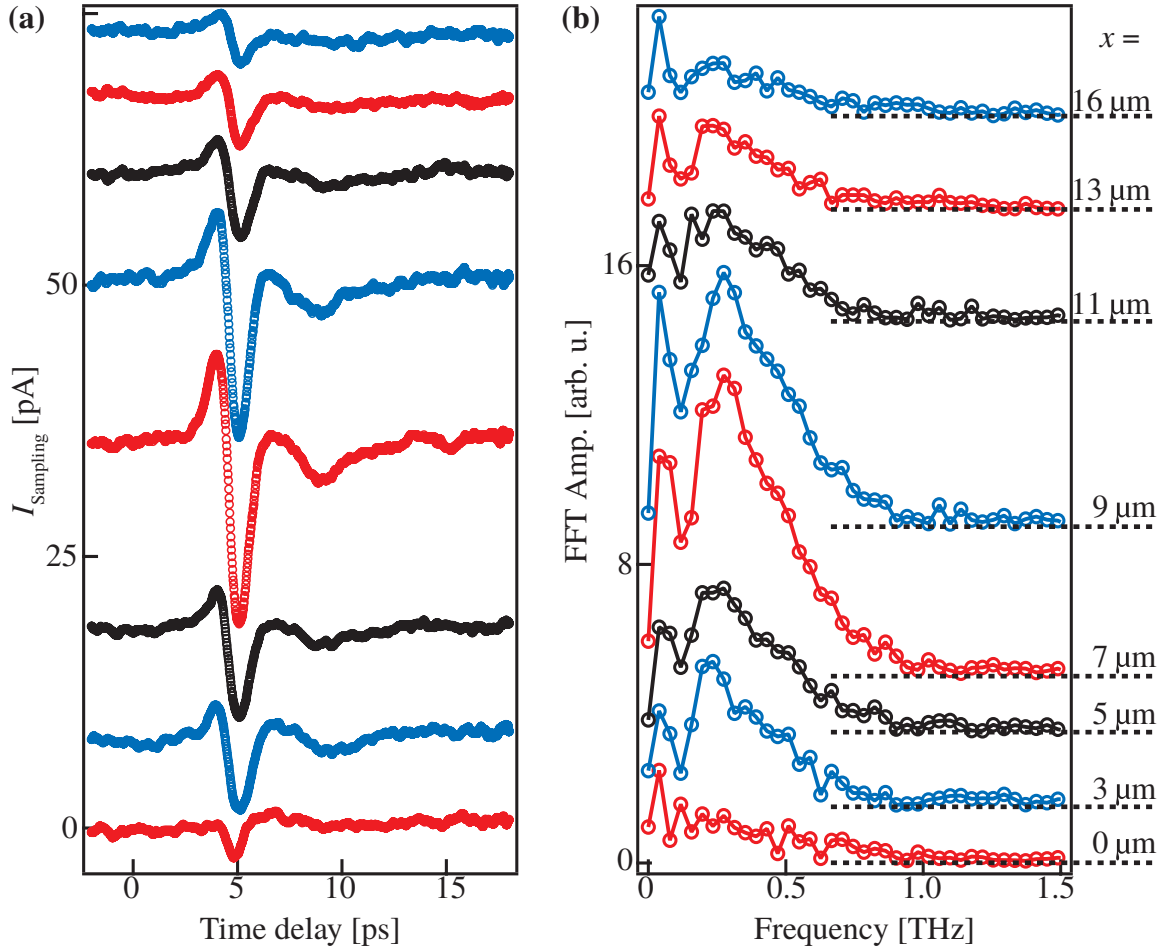


Figure 5.7 — THz response of graphene. **(a)** Time-resolved I_{Sampling} at $T_{\text{Bath}} = 77 \text{ K}$ for excitation positions starting at the graphene-metal interface along the dotted line in Figure 5.1c. Data are offset for clarity ($E_{\text{Laser}} = 1.59 \text{ eV}$, $P_{\text{Laser}} = 800 \mu\text{W}$, $V_{\text{SD}} = 0 \text{ V}$). **(b)** Corresponding Fast-Fourier-Transformation of interpolated I_{Sampling} as displayed in Figure 5.7a and excitation position x along the dotted line in Figure 5.1c. The data offset level is indicated with dashed lines. [Pre11c]

the bandwidth of our detection scheme [Par99]. However, we point out that our stripline detection scheme is a factor of $10^4 - 10^5$ more sensitive than a far-field detection of electromagnetic radiation in the tested frequency range (see section 1.5). We note that the THz-signal in Figure 5.7 decreases towards the metal contacts. In our interpretation, the photo-thermoelectric and displacement currents still contribute to I_{Sampling} at the graphene-metal interface. However, experimentally we cannot resolve the two optoelectronic processes at 77 K due to a dominating THz

response. At room temperature, however, all processes can be resolved at specific excitation positions e.g. at the second trace in Figure 5.2a from the bottom.

5.5 Conclusions

To conclude, we spatially resolve picosecond photocurrents in freely suspended graphene contacted by metal striplines. We identify both built-in electric fields and the photo-thermoelectric effect to contribute to the photocurrent generation at graphene-metal interfaces. In addition, optical pumping of the freely suspended graphene gives rise to strong photocurrent oscillations in the time-domain. We interpret these oscillations with Fast-Fourier-Transformation-amplitudes up to 1 THz to originate from THz-radiation emitted from the optically pumped graphene.

Chapter 6

Photocurrent dynamics in GaAs nanowires

In this chapter, we investigate the photocurrent dynamics of contacted GaAs nanowires by time-integrated and time-resolved photocurrent spectroscopy.

In the time-integrated measurements, we investigate photocurrent and photoconductance processes in freely suspended *p*-doped single GaAs nanowires, which are electrically contacted by a focused ion beam deposition technique. The observed photocurrent is generated at the Schottky contacts between the nanowire and metal source-drain electrodes, while the observed photoconductance signal can be explained by a photogating effect induced by optically generated charge carriers located at the surface of the nanowire. Both optoelectronic effects are sensitive to the polarization of the exciting laser field, enabling polarization dependent photodetectors. Finally, first time-resolved photocurrent experiments are shown. A response time of $\sim 3\text{ ps}$ suggests such processed freely suspended nanowires to be used as ultrafast photodetectors. The results of these time-integrated measurements are published in [Thu09b].

Furthermore, we investigate the photocurrent dynamics of a *p*-doped GaAs nanowire lying on a sapphire substrate and contacted by optical lithography. Contacting by optical lithography avoids damage of the nanowires by high energy electrons or ions [Che10], which is introduced in the contacting procedure by focused ion beam. In the experiments, we are able to resolve displacement currents, transport currents of holes, as well as a carrier lifetime limited currents. These results are very well reproduced by numerical simulations of bulk GaAs photoswitches [Dun94, Dun96]. The data further suggests, that a photo-thermoelectric current is

generated in the nanowires for excitation close to the contacts. The results of these time-resolved measurements are summarized in [Pre11a].

In section 6.1, we introduce basic properties and possible applications of nanowires. In section 6.2 we investigate the time-integrated photocurrent and photoconductance processes in freely suspended *p*-doped single GaAs nanowires. The photocurrent dynamics of *p*-doped GaAs nanowire lying on a sapphire substrate and contacted by optical lithography are investigated in the section 6.3. We finally conclude in 6.4.

6.1 Introduction to GaAs nanowires

Nanowires are filamentary crystals with diameters in the range of few to several tens of nanometers. Their length can extend up to tens of micrometers. Due to their diameter reduction in size, their physical and chemical properties are expected to change with respect to their bulk counterpart. For example, nanowires can exhibit novel electronic and optical properties due to the confinement of carriers in zero, one or two dimensions with possible quantization of energy and modification of the density of states [Bjo02, de 03, Sam04]. Semiconductor nanowires have attracted considerable attention in the past few years, both for fundamental research [Cui01, de 03] and possible applications. It has been shown, that nanowires can act as sensitive photodetectors [Wan01, Hay06, Gu05, Kin02, Pet06, Gal11]. Nanowires can also be used in light emitting devices [Wan01, Min07]. Furthermore, nanowires have been incorporated into field effect transistors, boosting the miniaturization of future computer chip generations [Bjo07, Bry06]. Thermoelectric materials have been investigated for decades, but their efficiency is still too low to use them cost-effectively to convert waste-heat into electrical energy. Nanowires are promising candidates for efficient thermoelectrics [Bou08, Hoc08, Soi10]. Furthermore, nanowires have been successfully introduced into solar cells [Tia09, Col09] and lithium batteries [Cha08].

6.2 Optoelectronic properties of nanowires contacted by focused ion beam

In this section we investigate the optoelectronic properties of photodetectors based on single *p*-doped GaAs nanowires, which were grown by A. Fontcuberta i

Morral in the group of Prof. G. Abstreiter at the Walter-Schottky Institute. They are electrically contacted by metal electrodes using a focused ion beam (FIB) deposition technique [Pen08]. For this purpose we utilize a FIB machine NVISION40 of ZEISS in combination with Kleindieck manipulators.

6.2.1 Photocurrent and photoconductance

The scanning electron micrograph (SEM) image in Figure 6.1a shows the photodetector circuit with a *p*-type GaAs nanowire bridging two gold pads acting as *source* and *drain* electrodes. The circuit in Figure 6.1a features three positions: I, II, and III. At positions I and III, Schottky contacts between the nanowire and the gold electrodes can be assumed. At position III, however, the nanowire is covered by an opaque carbon layer with a thickness of $\sim 350\text{nm}$. At position II, the nanowire is freely suspended. Hereby, the circuit allows locally addressing the optoelectronic processes in the middle of the nanowires (position II) independently from the ones occurring at the metal-semiconductor contact (position I).

We present optoelectronic measurements of two independent samples *A* and *B*, which are typical for the measured *p*-doped nanowires. Figure 6.1b depicts the typical $I - V$ characteristics of the devices. Since the $I - V$ characteristics are non-linear and symmetric with respect to the bias voltage, we infer that FIB-fabricated samples act as metal-semiconductor-metal devices with equivalent Schottky barriers at each end of the nanowires [Zha06]. Most importantly, the reported optoelectronic findings only rely on the presence of back-to-back Schottky barriers with a *p*-doped GaAs nanowire in between. Optical excitation occurs by focusing the light of a mode-locked titanium:sapphire laser with a repetition rate of 76MHz through the objective of a microscope onto the nanowire circuits. The laser is tuned in the energy range of $1.24\text{eV} \leq E_{\text{Photon}} \leq 1.77\text{eV}$. With a spot diameter of $\sim 2\mu\text{m}$ the light intensity I_{Laser} is of the order of 100W/cm^2 for all E_{Photon} . Generally, we modulate the laser with an optical chopper system at a frequency f_{chop} . For the optoelectronic measurements discussed below, the current I_{Photo} is detected by a lock-in amplifier utilizing the reference signal f_{chop} provided by the chopper system.

We acquire photocurrent images of the nanowire circuits by recording the change of I_{Photo} at a finite source-drain bias V_{SD} , when the laser spot is laterally scanned across the samples. $I_{\text{Photo}} = I_{\text{Photo}}(x, y)$ is plotted using a linear false color scale as a function of the coordinates x and y . For all V_{SD} , we observe a dominating contribution of $|I_{\text{Photo}}|$ at position I compared to $|I_{\text{Photo}}|$ at position II of sample *A*.

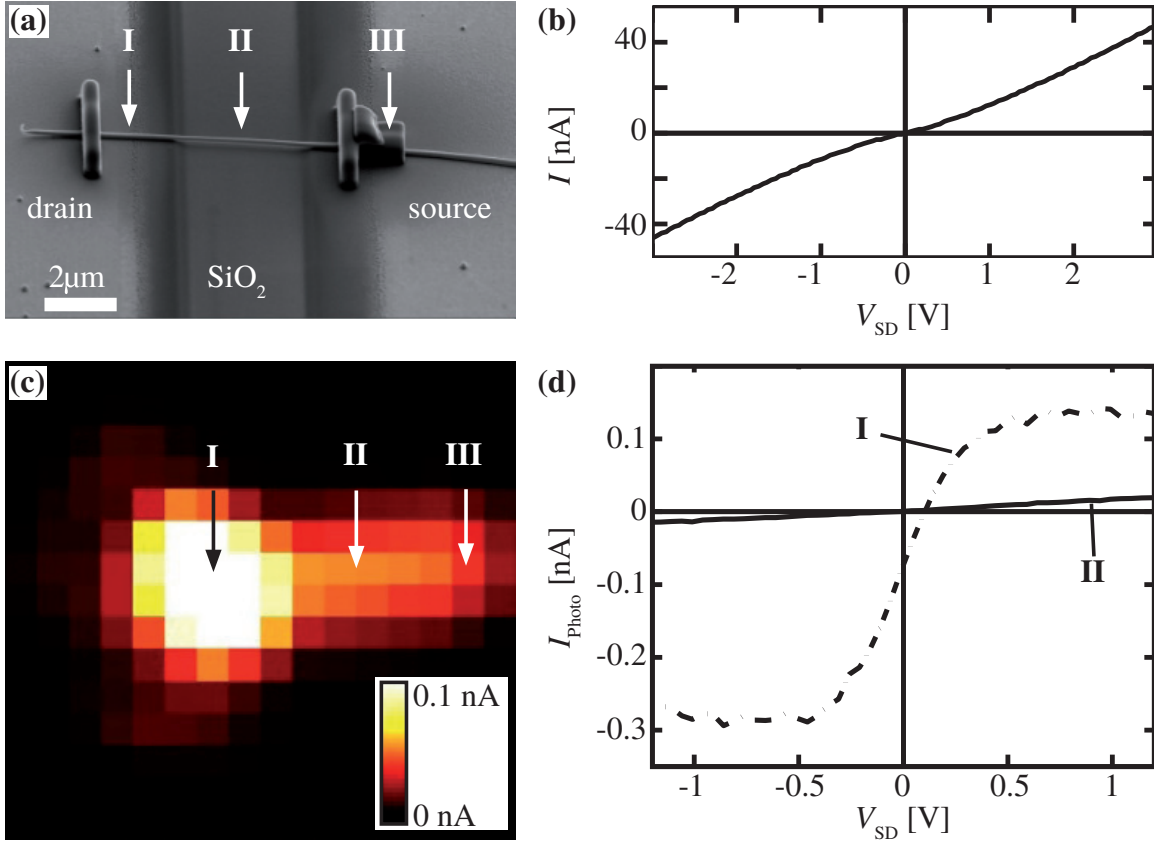


Figure 6.1 — (a) SEM image of a freely suspended *p*-doped GaAs nanowire bridging two gold electrodes (sample A). (b) I – V characteristics of sample A without laser excitation. (c) Photocurrent contour plot of $|I_{Photo}|$ as a function of the spatial coordinates of sample A ($T_{bath} \approx 296\text{ K}$, $I_{Laser} \approx 60\text{ W/cm}^2$, $f_{chop} = 1028\text{ Hz}$, $\lambda = 780\text{ nm}$, and $V_{SD} = 1\text{ V}$). (d) I_{Photo} as function of V_{SD} for positions I and II of sample A ($T_{bath} \approx 296\text{ K}$, $I_{Laser} \approx 30\text{ W/cm}^2$, $f_{chop} = 930\text{ Hz}$, and $\lambda = 730\text{ nm}$).

(Figure 6.1c). We also detect I_{Photo} as a function of V_{SD} at positions I and II (Figure 6.1d). At position I, we observe a finite photocurrent I_0 at $V_{SD} = 0\text{ V}$ and a finite photovoltage V_0 at $I_{Photo} = 0\text{ A}$. Hereby, we confirm recent reports that a Schottky contact between a semiconductor nanowire and a metal pad can give rise to both a photocurrent and a photovoltage [Gu05]. In this process, the electron-hole pairs, which are locally created by photoexcitation in the *p*-doped GaAs nanowires, are separated due to the local built-in electric field at the Schottky contacts, and a maximum (minimum) photocurrent signal can be detected when the illuminated Schottky contact is reverse-biased (forward-biased). We note that at position I, I_{Photo} satu-

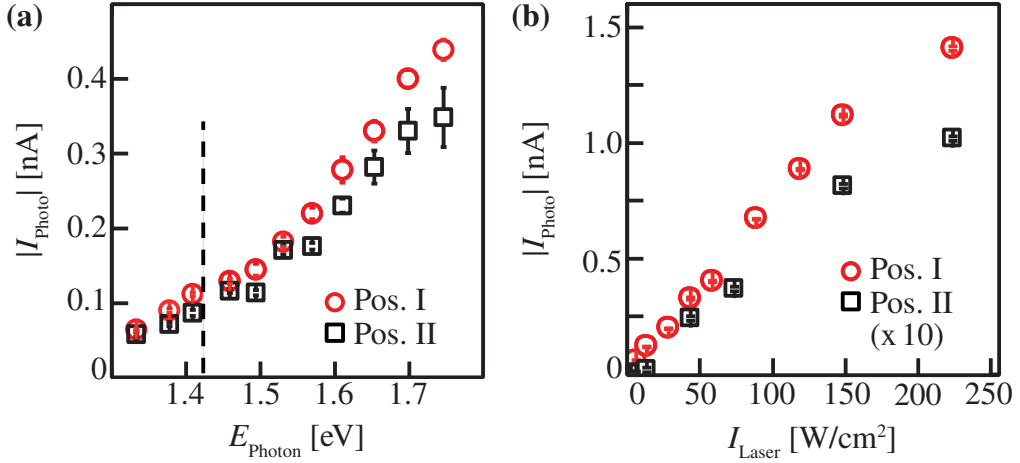


Figure 6.2 — (a) $|I_{\text{Photo}}|$ as a function of E_{Photon} for sample B for positions I (circles) and II (squares) as defined in Figure 6.1a ($V_{\text{SD}} = -1 \text{ V}$, $T_{\text{bath}} \approx 296 \text{ K}$, $I_{\text{Laser}} \approx 100 \text{ W}/\text{cm}^2$, and $f_{\text{chop}} = 930 \text{ Hz}$). **(b)** $|I_{\text{Photo}}|$ as a function of the exciting laser intensity for sample A for positions I (circles) and II (squares) ($V_{\text{SD}} = -1 \text{ V}$, $T_{\text{bath}} \approx 296 \text{ K}$, $f_{\text{chop}} = 930 \text{ Hz}$, and $\lambda = 780 \text{ nm}$).

rates at a source-drain voltage of $|V_{\text{sat}}| \approx 0.5 \text{ V}$, and that both V_{sat} and $I_{\text{Photo}}(V_{\text{sat}})$ depend on the laser intensity, as expected for a photocurrent process (data not shown) [Thu09a, Beh01]. At position II we observe only a negligible photocurrent and photovoltage signal at zero V_{SD} (Figure 6.1d). We find that I_{Photo} linearly depends on V_{SD} up to $\pm 1.5 \text{ V}$ (data not shown).

Figure 6.2a depicts $|I_{\text{Photo}}|$ of sample B as a function of E_{Photon} for a laser excitation at positions I and II, which are equally defined as in Figure 6.1a. The dashed line in Figure 6.2a indicates the band gap energy of $E_{\text{GaAs}} \approx 1.43 \text{ eV}$ of GaAs at room temperature¹. The noise level in the setup without laser excitation is below $\sim 2 \text{ pA}$. Since we detect a finite $|I_{\text{Photo}}|$ for $E_{\text{Photon}} \leq E_{\text{GaAs}}$ for all positions on the nanowires, we conclude that there are parts of the nanowires, where an electric field gives rise to a Franz-Keldysh effect of the absorption energy [Sch94, Bau97, Cav07] or, alternatively, where surface states are optically excited. In the case of the Franz-Keldysh effect, we assume that the electric field can be attributed to the Fermi-level pinning of the oxidized {110}-facets of the *p*-doped GaAs with respect to the electrostatic potential of the holes in the center of the nanowires [Spi79]. We note that all data of

¹We performed photoluminescence measurements on an ensemble of the *p*-doped nanowires located on top of a SiO_2 -chip at room temperature. The maximum of the photoluminescence at $E_{\text{PL}} \approx 1.43 \text{ eV}$ agrees reasonably well with the band gap energy E_{GaAs} at room temperature.

the samples are taken in the linear response regime (Figure 6.2b). In this regime, the expected field strength can be estimated by the energy difference of 0.4 eV - 0.5 eV between the surface states and the Fermi-level within the nanowires [Spi79] and the lateral depletion length of typically $l_{\text{dep}} \approx 20 \text{ nm} - 30 \text{ nm}$ [Rie97]. The resulting field strength $F \approx (0.4 \text{ eV} - 0.5 \text{ eV})/(e \cdot l_{\text{dep}}) \approx 10^5 \text{ V cm}^{-1}$ is sufficient to ionize optically created excitons at the surface region of the nanowires [Cav07, Gae07]. Separated charge carriers can contribute two-fold to the photoconductance of the nanowires. On the one hand, the electrons can drift to the surface of the *p*-doped nanowires, acting as a local negative gating voltage (photogating effect or normal surface photovoltage). Hereby, the conductive part of the nanowire is widened. On the other hand, the holes increase the hole density within the nanowires (photodoping effect). Both effects can result in an optically increased conductance of the nanowire circuits [Ros08, Hof08]. In addition, we note that the optical excitation of surface states for $E_{\text{Photon}} \leq E_{\text{GaAs}}$ can cause similar photogating and photodoping effects since the effective band bending favors a charge configuration with photon-generated electrons being localized on the surface of the nanowires, while the holes drift to the center of the nanowires.

6.2.2 Dielectric confinement

The observed photoconductance and photocurrent signals depend on the polarization of the exciting laser field for both positions I and II (as depicted for sample A in Figure 6.3a). The corresponding signals follow a $\cos\Phi$ -like dependence, where Φ is the angle between the wire and the light polarization. This observation is in agreement with recent reports that the nanowire geometry strongly affects the polarization of emitted or absorbed photons [Cao09, Wan01] due to a dielectric confinement effect. We observe that the polarization ratio

$$\rho = \frac{I_{\text{Photo}}^{\parallel} - I_{\text{Photo}}^{\perp}}{I_{\text{Photo}}^{\parallel} + I_{\text{Photo}}^{\perp}} \quad (6.1)$$

of I_{Photo} with parallel ($I_{\text{Photo}}^{\parallel}$) and perpendicular (I_{Photo}^{\perp}) polarization orientations is larger at position II ($\sim 35\%$) than close to the Schottky contact of position I ($\sim 15\%$).

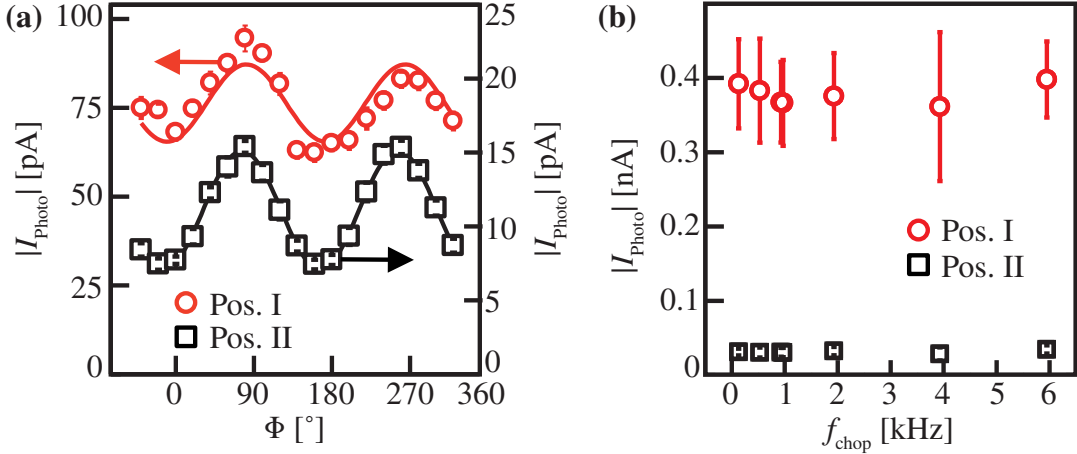


Figure 6.3 — (a) $|I_{\text{Photo}}|$ as a function of the angle Φ between the linearly polarized laser field and the orientation of the nanowire for sample A for positions I (circles) and II (squares) ($V_{SD} = 0.5$ V, $T_{\text{bath}} \approx 296$ K, $I_{\text{Laser}} \approx 60$ W/cm 2 , $f_{\text{chop}} = 930$ Hz, and $\lambda = 800$ nm). (b) $|I_{\text{Photo}}|$ as a function of f_{chop} for sample A for positions I (circles) and II (squares) ($V_{SD} = -1$ V, $T_{\text{bath}} \approx 296$ K, $I_{\text{Laser}} \approx 60$ W/cm 2 , and $\lambda = 780$ nm).

6.2.3 Defect enhanced charge carrier recombination

In order to test the response time of the metal-nanowire-metal photodetector, we measure I_{Photo} of the devices as a function of f_{chop} (Figure 6.3b). For both positions I and II, we do not detect any dependence of I_{Photo} on f_{chop} for frequencies between 0.1 and 6 kHz. This already reveals that the effects causing the photocurrent (position I) and the photoconductance (position II) occur on a time scale shorter than $\sim (6\text{ kHz})^{-1} = 167\text{ }\mu\text{s}$.

We further investigate the photocurrent dynamics by positioning an as-grown *p*-doped GaAs nanowire on a stripline circuit (see Figure 6.4a) employing the FIB contacting procedure described above. A time-resolved pump-probe measurement of I_{Sampling} (see chapter 2 for details on the measurement scheme) is shown in Figure 6.4b. The nanowire is excited at the position of maximal photocurrent I_{Photo} close to a metal contact. The signal-to-noise ratio is fairly low. Yet the response can be fitted with an exponentially convoluted Gaussian (solid red line) with a decay constant of $\tau_{\text{FIB}} \approx (2.7 \pm 0.5)$ ps. This response time is several orders of magnitude shorter than typical recombination lifetimes found in GaAs nanowires. For defect-free Ga-assisted nanowires, a recombination lifetime of (2.5 ± 0.1) ns has been reported [Bre11]. Using gold as a catalyst incorporates defects, which results in

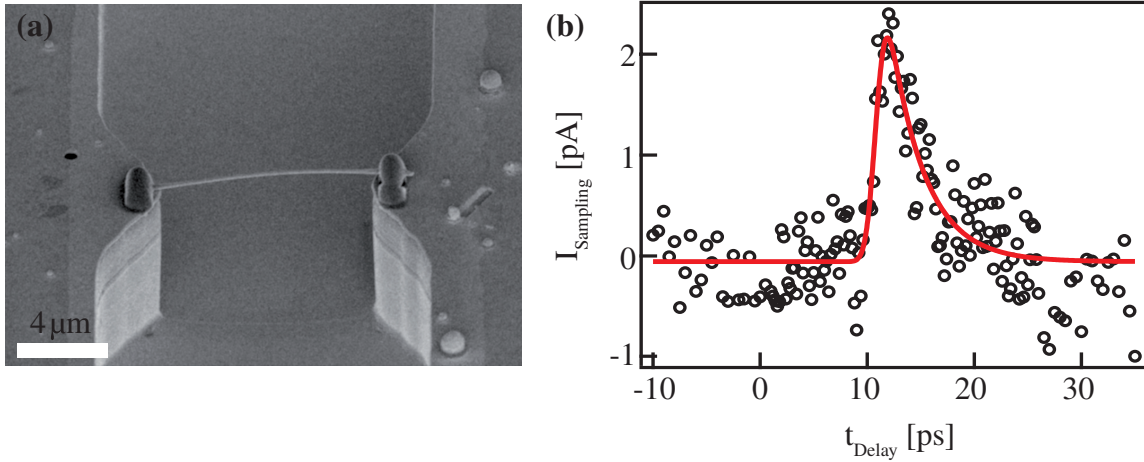


Figure 6.4 — (a) SEM image of a freely suspended *p*-doped GaAs nanowire bridging two gold electrodes. (b) Time-resolved photocurrent I_{Sampling} averaged over two successive scans. The response can be fitted with an exponentially convoluted Gaussian (solid red line) with a decay constant of $\tau \approx (2.7 \pm 0.5)$ ps. ($V_{SD} = -3$ V, $P_{\text{Pump}} = 100 \mu\text{W}$, $\lambda = 785$ nm, $T_{\text{bath}} \approx 296$ K, pump excitation on nanowire close to metal contact).

a faster recombination lifetime of (9 ± 1) ps [Bre11]. The generation of defects by high energy electrons and ions has been investigated [Che10]. It has been found, that ion beam induced deposition significantly modifies the transport properties of nanowires, likely by the generation of defects. We therefore explain our ultrafast response time τ_{FIB} by defects introduced in the contacting procedure.

6.3 Photocurrent dynamics in nanowires contacted by optical lithography

The photocurrent dynamics of *p*-doped GaAs nanowire lying on a sapphire substrate and contacted by optical lithography are investigated in this section. Contacting by optical lithography avoids damage of the nanowires by high energy electrons or ions [Che10], which is introduced during the contacting procedure by the focused ion beam (section 6.2). In a recent study of the response time of Au-assisted grown nanowire-based photodetectors, a 35 ps response time for bare GaAs nanowires and a 10 ps response time for GaAs/AlGaAs core/shell nanowire has been found [Gal11]. There, the time-resolution was limited to 10 ps and the nanowires were uniformly excited with a defocused laser beam. By performing spatially and

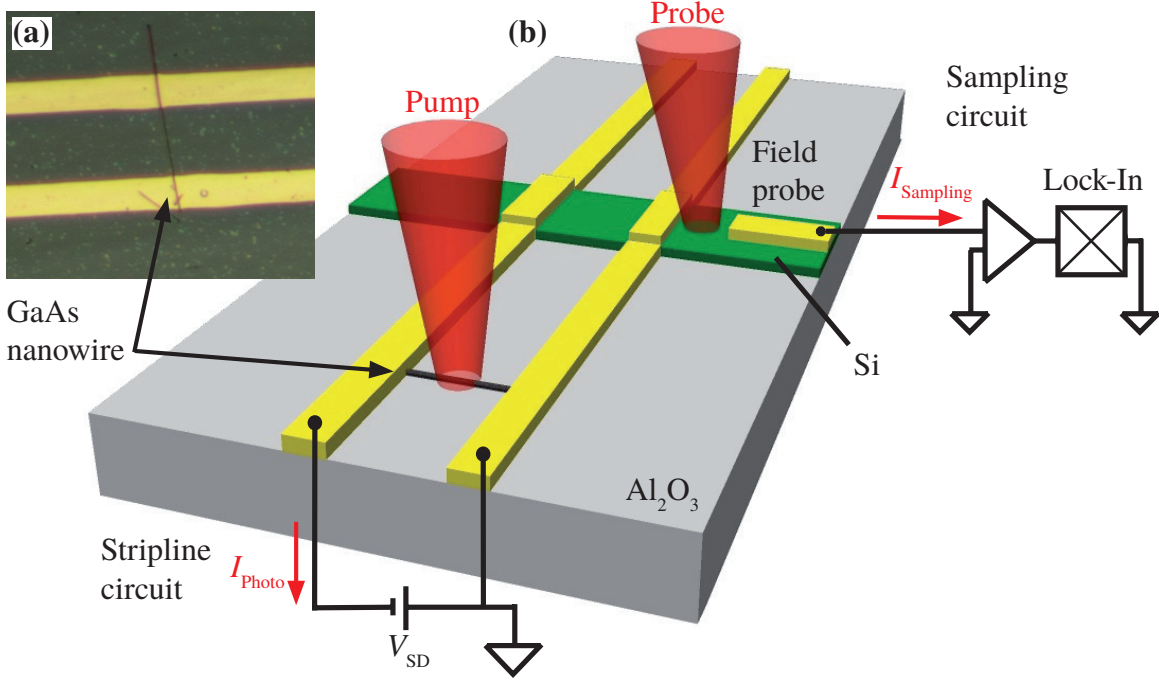


Figure 6.5 — Device geometry and optoelectronic pump-probe circuit. **(a)** Optical microscopy image of a GaAs nanowire incorporated into the stripline circuit. **(b)** Schematic on-chip detection geometry. The pump laser pulse is focused on the GaAs nanowire contacted by the stripline circuit. The probe-pulse triggers the sampling circuit. Gold electrodes are depicted in yellow, ion-implanted silicon (Si) in green.

time-resolved photocurrent measurements, we are able to resolve a displacement current, transport current of photogenerated electrons and holes, as well as a carrier lifetime limited current. The data further suggest, that a photo-thermoelectric current is generated in the vicinity of the contacts.

Figure 6.5a shows an optical microscopy image of a *p*-doped GaAs nanowire lying on a sapphire substrate and incorporated into a gold stripline circuit. For details on the sample processing see section 2.3.9. Figure 6.5b shows a sketch of the on-chip detection geometry employed in the time-resolved measurements of $I_{Sampling}$. For details on the measurement scheme see chapter 2.

6.3.1 Time-integrated photocurrent measurements

First we perform spatially resolved and time-integrated photocurrent measurements of I_{Photo} . Figure 6.6a shows a spatially resolved reflectivity map of the

sample, which was acquired simultaneously with the photocurrent I_{Photo} shown in Figures 6.6b-d for bias-voltages of $V_{\text{SD}} = 5 \text{ V}$, -5 V and 0 V . All scans were deconvoluted with a Gaussian shaped instrument-response function with diameter $4 \mu\text{m}$, and the individual color-scales are normalized. From the reflectivity map we deduce the exact position of the metal stripline circuit, which are depicted as dashed blue lines in Figures 6.6a-d. Figure 6.6e shows a scan along the dotted line in the deconvoluted photocurrent maps. At a bias-voltage of 5 V (-5 V) a positive (negative) current I_{Photo} is generated for excitation of the nanowire approximately $3 \mu\text{m}$ from the left contact². At a bias-voltage of 0 V a positive (negative) current I_{Photo} is generated for excitation close to the right (left) contact, in agreement with charge carrier separation at Schottky-barriers and previous photocurrent measurements (see section 6.2.1 and [Thu09b]). The asymmetry in I_{Photo} with respect to the left and right contact is likely due to a varying doping profile along the nanowire [Duf10], which results in different Fermi levels in the nanowire at the position close to the left and right contact. Therefore the Schottky barriers in the two contacts can be different, which results in an asymmetric photocurrent map. Furthermore, negative photocurrent is generated for excitation of the left (right) contact at $V_{\text{SD}} = 5 \text{ V}$ (-5 V). We can exclude radial Schottky barriers to be responsible for this photocurrent signal, since the gold contacts are $\sim 300 \text{ nm}$ thick and therefore opaque to light.

6.3.2 Spatially resolved measurements of I_{Sampling}

The GaAs nanowire in the stripline circuit is optically excited by a pump-pulse at $\lambda = 780 \text{ nm}$ with $\sim 160 \text{ fs}$ pulse length generated by a Titanium:Sapphire laser. After the excitation, an electro-magnetic pulse starts to travel along the stripline. A sampling circuit senses the transient electric field of the travelling pulse at the position of a field probe (Figure 6.5a). Here, we utilize an Auston switch [Aus83] based on the ion-implanted silicon on the sapphire substrate. The time delay t_{Delay} between the pump- and the probe-pulse is controlled by a delay stage (see chapter 2). Measuring the current I_{Sampling} in the sampling circuit as a function of t_{Delay} yields information on the optoelectronic response of the nanowire in the stripline circuit with a picosecond time-resolution. For details on the measurement scheme see chapter 2.

Figure 6.7a and b show a time-resolved measurement of I_{Sampling} for excitation

²The absolute amplitudes are lost in the process of deconvolution with the freely available program *ImageJ*. We therefore rescale the images after deconvolution to the measured amplitudes.

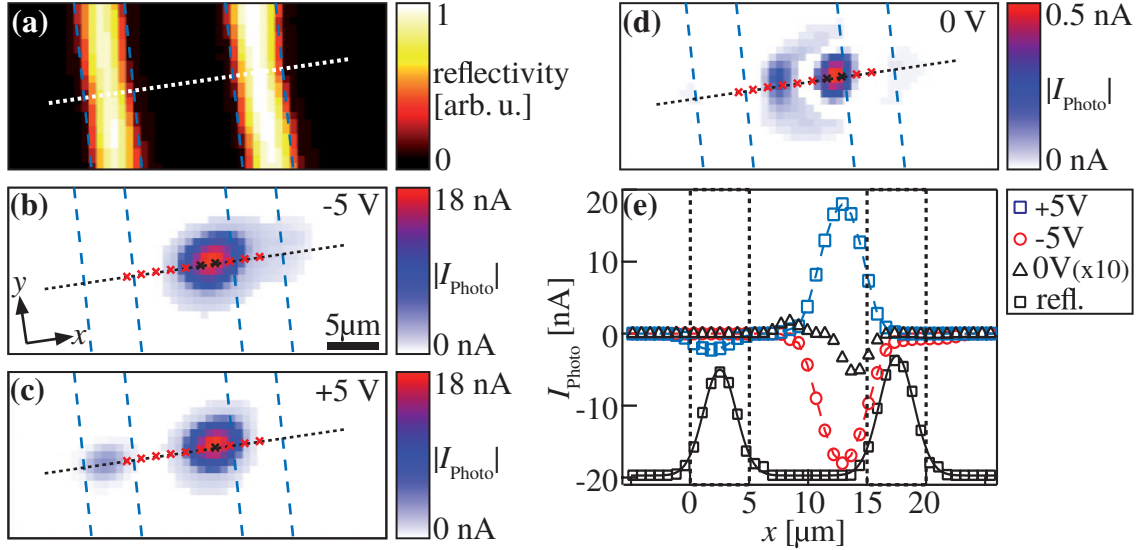


Figure 6.6 — (a) Deconvoluted reflection scan. (b) Deconvoluted I_{photo} maps for $V_{\text{SD}} = -5 \text{ V}$, (c) $V_{\text{SD}} = 5 \text{ V}$ and (d) $V_{\text{SD}} = 0 \text{ V}$. Each red cross corresponds to the position of one time-resolved scan in the following measurements (e.g. Figure 6.7). (e) Cut along the dotted lines in a-d. Amplitudes are rescaled after deconvolution to the measured maximal values. The vertical dashed lines indicate the position of the gold contacts. $\lambda = 780 \text{ nm}$, $P_{\text{Pump}} = 26 \mu\text{W}$, $T_{\text{bath}} \approx 296 \text{ K}$.

positions starting at the left metal contact (lowest trace) in steps of $\sim 1.5 \mu\text{m}$ along the dotted line in Figure 6.6 at $V_{\text{SD}} = 5 \text{ V}$, and for $V_{\text{SD}} = -5 \text{ V}$, respectively. A positive short peak centered around $\sim 22 \text{ ps}$ can be observed for positive bias voltage in Figure 6.7a. The peak amplitude increases starting from the left contact (lowest trace) towards the middle of the nanowire and then decreases again towards the right contact (highest trace). Reversing the bias-voltage to -5 V reverses the peak amplitudes for excitation in the middle of the nanowire. Yet the lowest four traces keep the positive amplitude despite the opposite bias-voltage. After the peak at 22 ps a slow increase and an offset of I_{Sampling} is observed for excitation in the middle of the nanowire, both for positive (Figure 6.8a) and negative (Figure 6.8b) voltage polaritiy. Finally the signal decays on a slow timescale back to the initial value of I_{Sampling} , as can be observed in Figure 6.9 for time delay up to 2 ns .

6.3.3 Fitting the data

We fit the dataset depending on the excitation position. For central excitation positions we employ the sum of a Gaussian shaped peak centered around $\sim 22 \text{ ps}$,

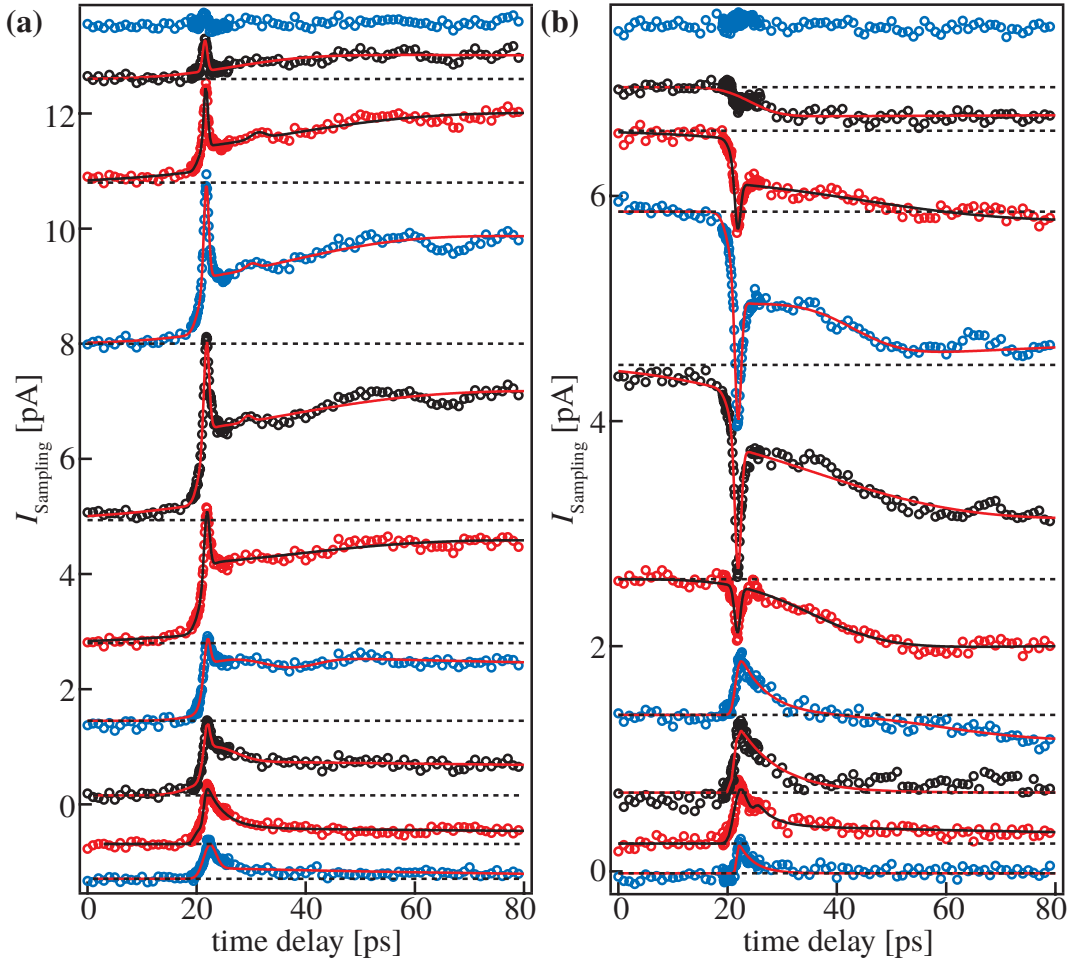


Figure 6.7 — Time-resolved measurement of I_{Sampling} for excitation positions marked with a red cross in Figures 6.6b and c. Here, the lowest trace corresponds to the leftmost red cross, stepsize is $\sim 1.5 \mu\text{m}$. Solid lines are fits to the data. The data offset level is indicated by dashed lines. **(a)** $V_{\text{SD}} = 5 \text{ V}$. **(b)** $V_{\text{SD}} = -5 \text{ V}$.

a first exponentially convoluted Gaussian with fitting parameter τ_{rec} and a second exponentially convoluted Gaussian with fitting parameter τ_{trans} . The resulting fitting functions are plotted along with the data as solid lines in Figures 6.7, 6.8 and 6.9. Exemplarily, the individual components of the fitting function are plotted separately for $V_{\text{SD}} = 5 \text{ V}$ and central excitation position (5th trace from the bottom in Figure 6.7a) in Figures 6.10a and b. There, the Gaussian contribution is plotted as a solid green line, the first exponentially convoluted Gaussian with fitting parameter τ_{rec} is plotted as a dashed black line, and the second exponentially convoluted

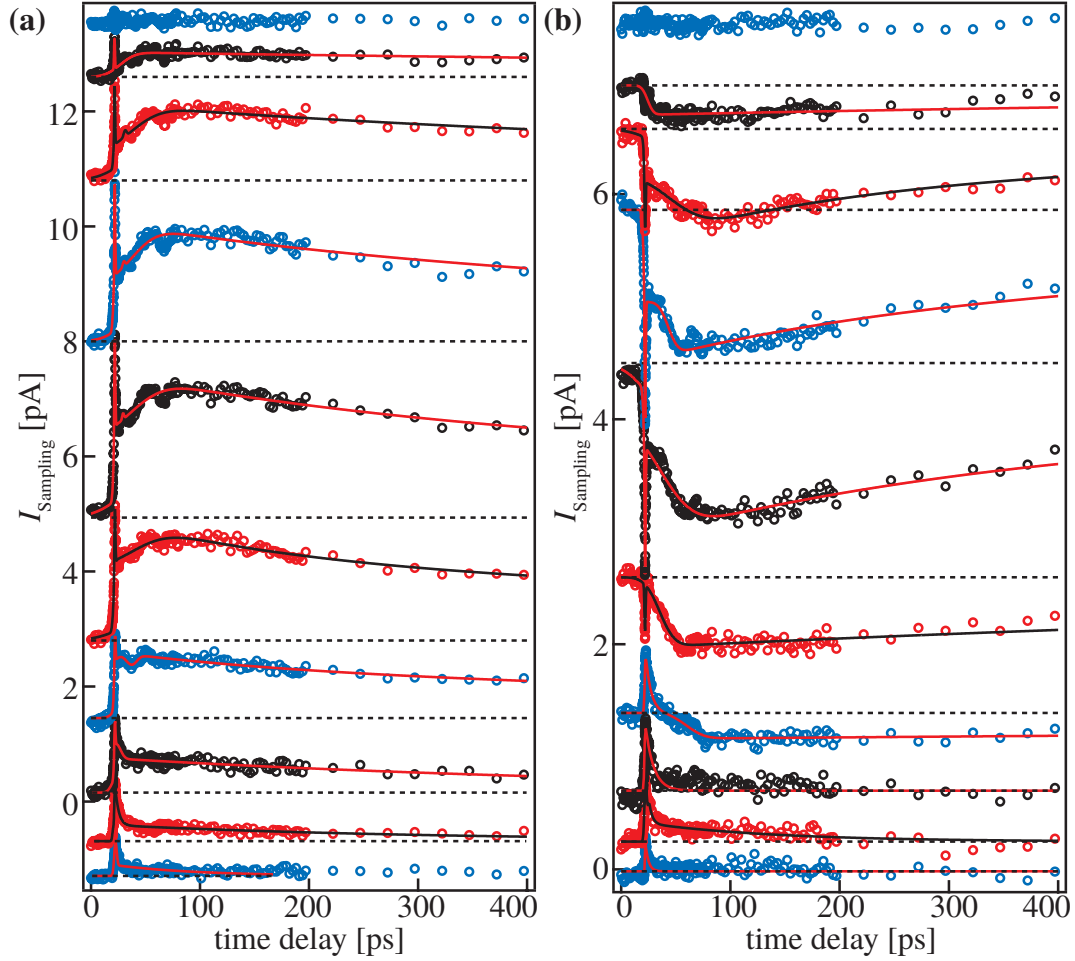


Figure 6.8 — Time-resolved measurement of I_{Sampling} for excitation positions starting at the left metal contact in steps of $\sim 1.5 \mu\text{m}$ along the dotted line in Figure 6.6a-d. Solid lines are fits to the data. Data offset level indicated by dashed lines. (a) $V_{SD} = 5 \text{ V}$. (b) $V_{SD} = -5 \text{ V}$.

Gaussian with fitting parameter τ_{trans} is plotted as a dotted blue line.

Here, the Gaussian component is set to fit the sharp peak centered around $\sim 22 \text{ ps}$. The first exponentially convoluted Gaussian is set in such a way, that it accounts for the offset after the Gaussian peak at $\sim 22 \text{ ps}$ (for that purpose, the Gaussian width is 1 ps to 2 ps and the Gaussian position is $\sim 22 \text{ ps}$). The second exponentially convoluted Gaussian is set in such a way, that it accounts for the signal increase after the Gaussian peak at $\sim 22 \text{ ps}$. As will be discussed below, we tentatively associate the Gaussian shaped peak with a displacement current. We furthermore tentatively associate the first exponentially convoluted Gaussian with

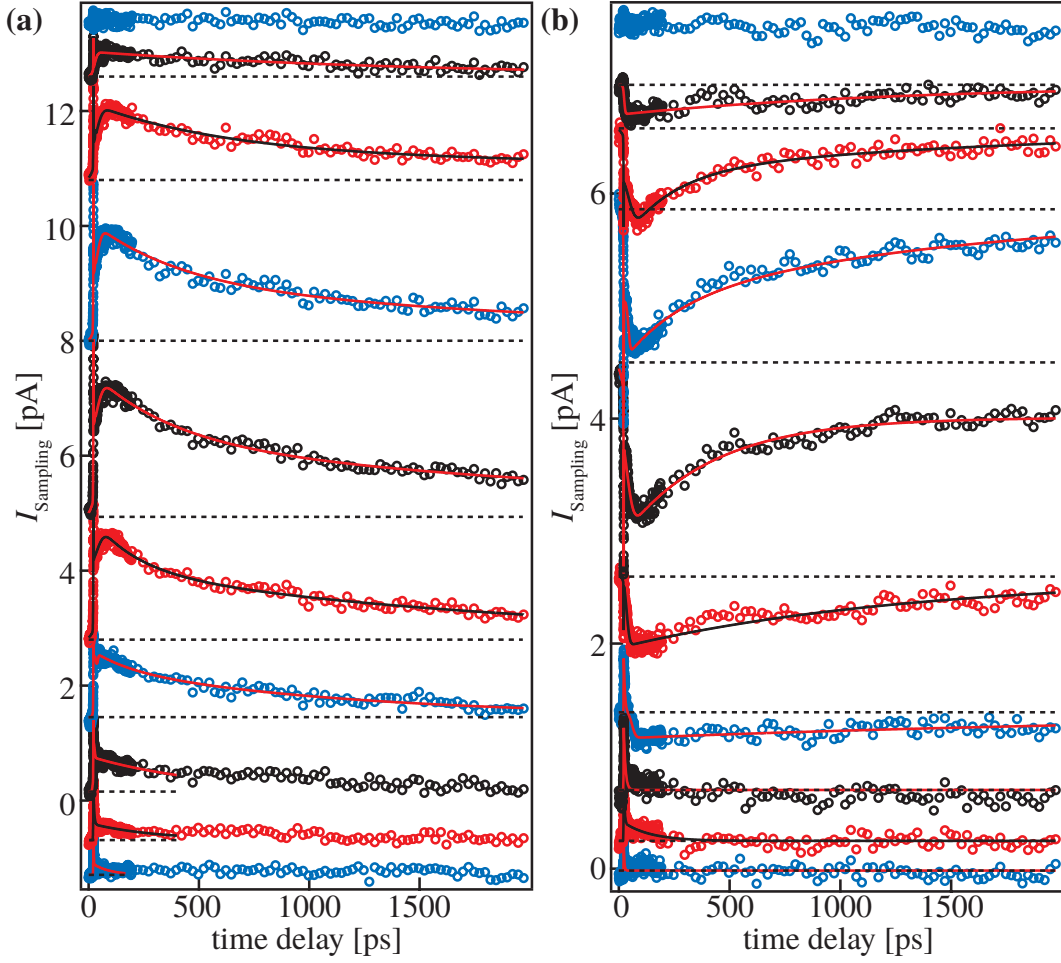


Figure 6.9 — Time-resolved measurement of I_{Sampling} for excitation positions starting at the left metal contact in steps of $\sim 1.5 \mu\text{m}$ along the dotted line in Figure 6.6a-d. Solid lines are fits. Data offset level indicated by dashed lines. **(a)** $V_{SD} = 5 \text{ V}$. **(b)** $V_{SD} = -5 \text{ V}$.

fitting parameter τ_{rec} with the recombination of charge carriers, and the second exponentially convoluted Gaussian with fitting parameter τ_{trans} with the transport of photogenerated holes to the contacts. For the lowest three traces in Figures 6.7, 6.8 and 6.9, we fit the first peak at $\sim 22 \text{ ps}$ with an exponentially convoluted Gaussian instead of a Gaussian to account for the slightly less steep falling signal compared to the rising signal. The data and the fit functions for the second lowest trace are plotted for $V_{SD} = 5 \text{ V}$, 0 V and -5 V in Figures 6.11a-c.

Figure 6.12 shows fitting parameters as a function of the excitation position for $V_{SD} = -5 \text{ V}$ (red circles), 5 V (blue squares) and 0 V (black triangles). The area

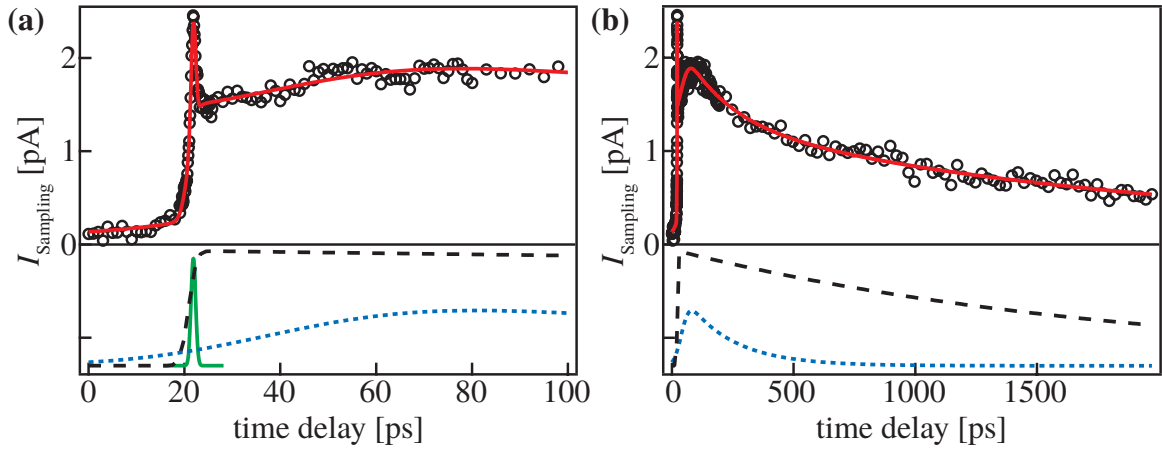


Figure 6.10 — The individual components of the fitting function for $V_{\text{SD}} = 5 \text{ V}$ and central excitation position (5th trace from the bottom in Figure 6.7a, red data points). The Gaussian contribution is plotted as a solid green line, the first exponentially convoluted Gaussian with fitting parameter τ_{rec} is plotted as a dashed black line, and the second exponentially convoluted Gaussian with fitting parameter τ_{trans} is plotted as a dotted blue line. (a) Time delay up to 100 ps. (b) Time delay up to 2 ns. The first (green) Gaussian fit component has been omitted in (b).

$A_{1\text{st}}$ of the first peak at $\sim 22 \text{ ps}$ as a function of excitation position x is shown in Figure 6.12a. Figure 6.12b shows the area A_{rec} of the first exponentially convoluted Gaussian, which we associate with the charge carrier recombination. Figure 6.12c shows the fitting parameter τ_{rec} and Figure 6.12d the fitting parameter τ_{trans} .

6.3.4 Current amplitude considerations

By comparing Figure 6.12a with Figure 6.12b, we can estimate that the area A_{rec} of the exponentially convoluted Gaussian is a factor 10^3 bigger than the areas $A_{1\text{st}}$ of the first peak at $\sim 22 \text{ ps}$. Furthermore, for $V_{\text{SD}} = \pm 5 \text{ V}$ the area $A_{\text{rec}}(x)$ has the same spatial dependence on x as the time-integrated photocurrent amplitudes $I_{\text{Photo}}(x)$ in Figure 6.6e. We therefore conclude, that the time-integrated photocurrent measurements at $V_{\text{SD}} = \pm 5 \text{ V}$ are dominated by the contributions fitted with the exponentially convoluted Gaussian with fitting parameter τ_{rec} , and that the displacement currents do not play a major role due to their comparatively small area.

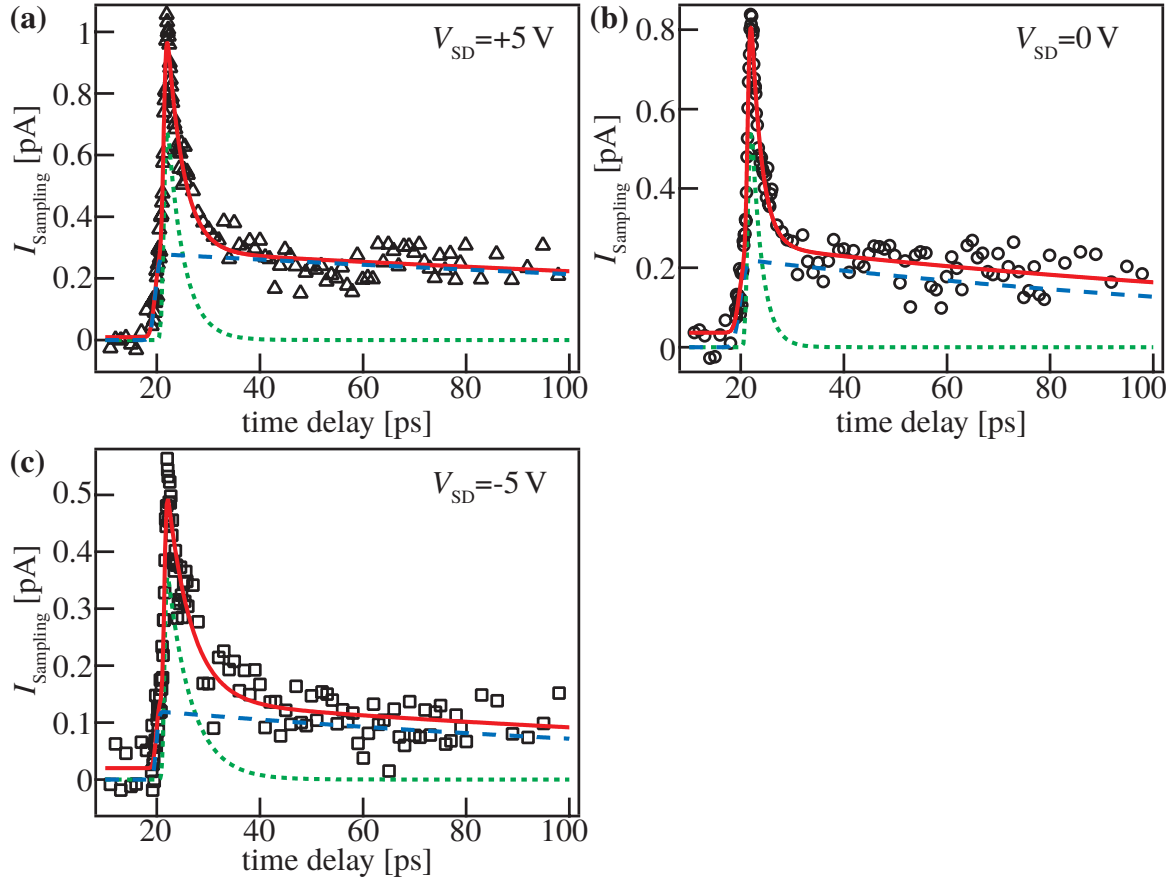


Figure 6.11 — I_{Sampling} for excitation of the nanowire close to the left contact (second lowest trace in Figures 6.7 second red cross from the left in Figure 6.6) and corresponding fit functions (solid red lines) for (a) $V_{\text{SD}} = 5 \text{ V}$, (b) $V_{\text{SD}} = 0 \text{ V}$ and (c) $V_{\text{SD}} = -5 \text{ V}$. The exponentially convoluted Gaussian fitting the first peak is drawn separately as dotted green line. A second exponentially convoluted Gaussian is drawn separately as dashed blue lines.

6.3.5 Displacement and thermoelectric current

At excitation positions $x = 5 \mu\text{m}$ to $10 \mu\text{m}$ no time-integrated photocurrent is generated for all three voltages V_{SD} , as is shown in Fig. 6.6e. Yet, in the time-resolved measurements we detect a sharp first peak with an area of up to $\sim 5 \text{ ps pA}$. Most importantly, this peak is always positive for all V_{SD} , as is shown in Figure 6.11 for excitation on the nanowire close to the left contact (second lowest trace in Figure 6.7 and second red cross from the left in Figure 6.6). We attribute the first sharp peak for excitation close to the left contact (see Fig. 6.11) either to a displacement current due

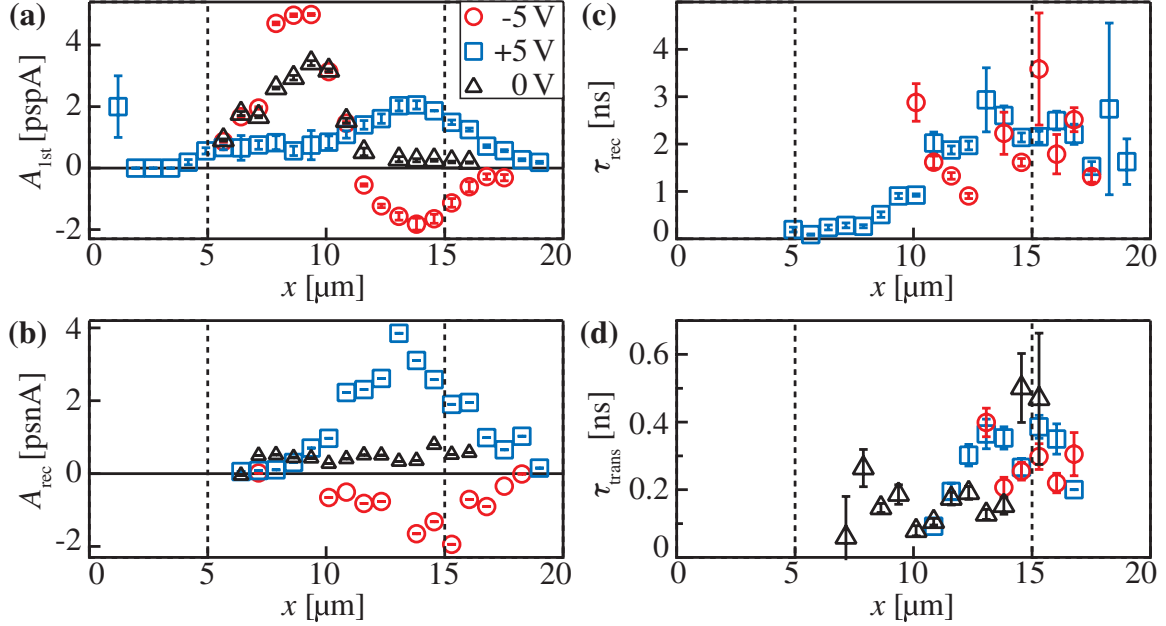


Figure 6.12 — Fitting parameters as a function of the excitation position x for $V_{SD} = -5$ V (red circles), 5 V (blue squares) and 0 V (black triangles). The vertical dashed lines indicate the position of the gold contacts. **(a)** Area A_{1st} of the first peak at ~ 22 ps **(b)** Area A_{rec} of the first exponentially convoluted Gaussian, which we associate with the charge carrier recombination. **(c)** Fitting parameter τ_{rec} . **(d)** Fitting parameter τ_{trans} .

to intrinsic fields of a Schottky barrier, or alternatively to a photo-thermoelectric current. The interpretation of a displacement current is based on two observations. First, the temporal duration of ~ 5 ps is in good agreement with displacement currents found in LT-GaAs (chapter 3) and carbon nanotubes (chapter 4). Secondly, in a biased nanowire with varying doping profile along the growth axis one would expect the electric field to be strongest close to the contact with high carrier concentration. At the same time, the electric fields close to the other contact with lower carrier concentration would be comparatively small. There, one can expect that the intrinsic fields (due to the Schottky contact) are not influenced by the applied bias, since the electric field drops at the other contact with high carrier concentration. Consequently, one expects that a displacement current is generated in the lowly doped Schottky region that does not change amplitude or sign under applied bias voltage V_{SD} .

Alternatively, a thermoelectric current could explain the observation that the sign of the first peak at ~ 22 ps in Figure 6.11 does not change sign under applied

bias voltage. A thermoelectric current can be described with (see section 1.4):

$$I_{\text{thermo}} = \frac{S_{\text{nanowire}} - S_{\text{stripline}}}{R} \Delta T. \quad (6.2)$$

The direction of I_{thermo} depends only on the sign of ΔT if the Seebeck coefficients are bias voltage independent. The excitation positions under discussion are clearly located on the nanowire and not on the metal contact. Therefore a temperature increase in the nanowire needs to be considered. The temperature increase of an as-grown *p*-doped GaAs nanowire has been recently investigated by micro-Raman spectroscopy combined with laser heating [Soi10]. A local temperature increase of up to $T_{\text{ref}} = 200\text{K}$ has been observed at comparable laser powers ($220\mu\text{W}$) and smaller laser spot size ($d_{\text{ref}} = 720\text{nm}$). We can estimate the local temperature increase T_{max} in our measurements (neglecting the different wavelengths³ and assuming a linear power dependence) by accounting for the different power densities⁴:

$$T_{\text{max}} \approx T_{\text{ref}} \cdot \left(\frac{d_{\text{ref}}}{d_{\text{Pump}}} \right)^2 = 200\text{K} \cdot \left(\frac{720\text{nm}}{3\mu\text{m}} \right)^2 = 12\text{K}. \quad (6.3)$$

The temperature profile after pulsed laser heating usually follows an exponential decay (see section 1.4). A strong indication for a thermoelectric current is therefore the observed exponential decay of the first peak in I_{Sampling} in Figure 6.11 with $\tau_{\text{first}} = (3.2 \pm 0.2)\text{ps}$ for $V_{\text{SD}} = 5\text{V}$, $(2.0 \pm 0.2)\text{ps}$ for 0V and $(4.7 \pm 0.6)\text{ps}$ for -5V . Contrarily, a displacement current has the shape of a Gaussian if dispersion can be neglected (see section 1.6.1). Laser power and wavelength dependent measurements could clarify the generation mechanisms. We furthermore plan to investigate the heating mechanism by spatially resolved Raman measurements.

6.3.6 Recombination lifetime τ_{rec}

Figure 6.12c shows the fitting parameter τ_{rec} as a function of excitation position x . We identify τ_{rec} as the recombination lifetime in accordance with the model for charge carrier lifetime limited currents in section 1.1 [Aus83]. Yet, we believe

³In [Soi10] a wavelength of 514.5nm was employed. Generally, the absorption increases with laser energy close to the bandgap. Additionally, hot electrons created at higher laser energy further contribute to the heating of the lattice by relaxation processes involving the generation of phonons. The estimation of T_{max} is therefore considered an upper limit to the local temperature increase.

⁴The laser spot size d_{Pump} in our experiments is estimated by optical reflection measurements to be $\sim 3\mu\text{m}$.

that in the region close to the left contact ($x = 5\text{ }\mu\text{m} - 10\text{ }\mu\text{m}$) and directly on the right contact ($x = 15\text{ }\mu\text{m} - 20\text{ }\mu\text{m}$) other processes (e.g. thermoelectric currents) govern the dynamics of the exponentially convoluted gaussian. We therefore only average τ_{rec} in the region $x = 10\text{ }\mu\text{m} - 15\text{ }\mu\text{m}$ to obtain the average charge carrier lifetime $\tau_{\text{avg}} = (1510 \pm 30)\text{ ps}$. This value is in decent agreement with recent time-resolved photoluminescence measurements on gold-catalyst-free grown GaAs nanowires of $(2.5 \pm 0.1)\text{ ns}$ [Bre11]. The influence of the crystal structure on the time-resolved luminescence was investigated [Spi09]. A lifetime of indirect excitons at wurtzite / zinc blende intersections was measured to be $(8 \pm 1)\text{ ns}$, while the lifetime of free excitons was found to be $< 300\text{ ps}$. In a detailed study of recombination energy dependent lifetimes in wurtzite / zinc blende GaAs nanowires it was found that the lifetime decreases from 8.4 ns at 1.443 eV to 175 ps at 1.56 eV [Pem09]. Our determined value of $\tau_{\text{avg}} = (1510 \pm 30)\text{ ps}$ lies in this range. Nevertheless, time-resolved photoluminescence measurements should be performed on the same nanowire to correlate the lifetime measured by luminescence with the lifetime deduced in photocurrent measurements.

6.3.7 Transport current of holes

We associate the increase of I_{Sampling} after the displacement current peak (see e.g. trace 7 in Figures 6.7 and 6.8) with the transport of holes to the contacts, as described in section 1.3. This interpretation is based on numerical simulations performed by Dunn et al. [Dun94, Dun96]. Experimentally, we do not observe a consistent shift of the hole transport peak position with excitation position. The hole drift velocity v_h depends on the electric field F via the hole mobility μ_h :

$$v_h = \mu_h \cdot F. \quad (6.4)$$

We investigate the hole drift velocity and the hole mobility by fixing the excitation position to the middle of the nanowire⁵ and measuring I_{Sampling} as a function of the applied bias voltage. In Figure 6.13 we show I_{Sampling} for bias voltages between -5 V and 5 V in steps of 1 V (traces from bottom to top). We fit the data as described in section 6.3.3. We observe a linear dependence of the area of the first peak on the applied bias voltage (data not shown). For positive bias voltages we observe a

⁵The excitation position is $\sim 4\text{ }\mu\text{m}$ to the right and $\sim 6\text{ }\mu\text{m}$ to the left contact. This corresponds to excitation between the 6th and the 7th trace (counted from the bottom) in Figure 6.7.

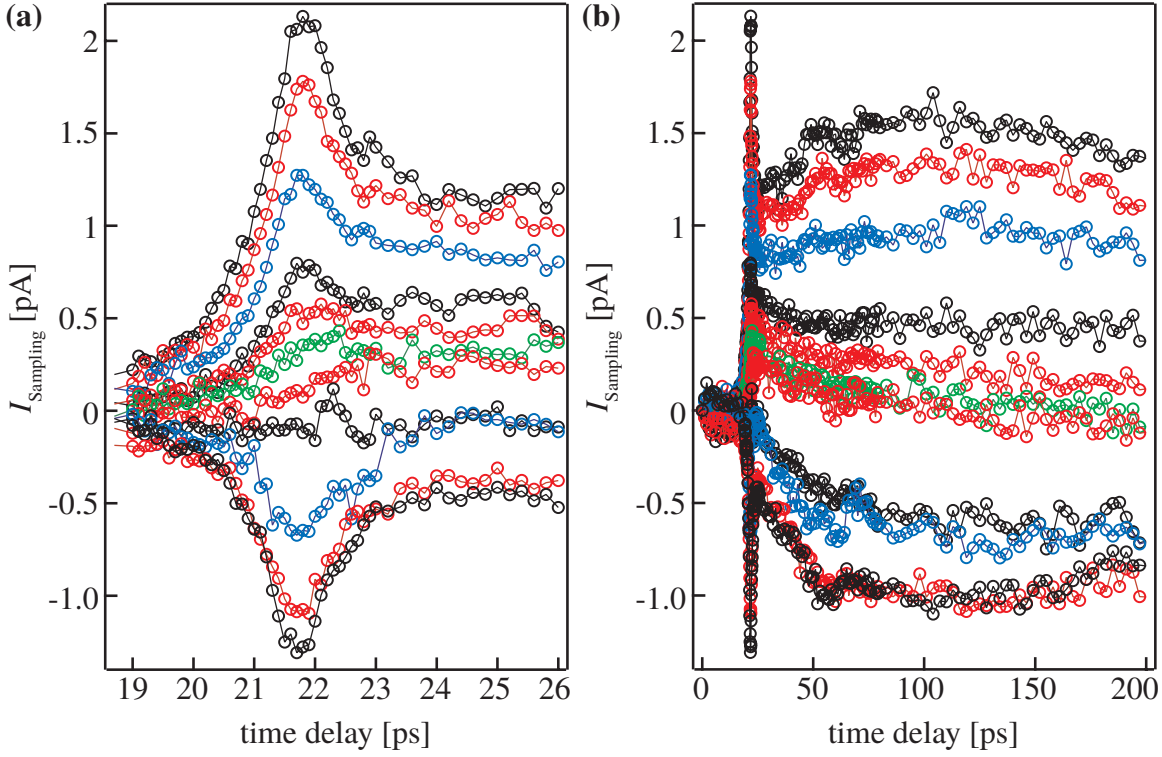


Figure 6.13 — Time-resolved I_{Sampling} for bias voltages $V_{\text{SD}} = -5 \text{ V}$ to 5 V in steps of 1 V from bottom to top. **(a)** I_{Sampling} for a time delay up to 26 ps . **(b)** I_{Sampling} extended to a time delay of 200 ps .

shift of the temporal position of the exponentially convoluted Gaussian associated with the transport of holes. We show the arrival time⁶ of the hole transport peak relative to the displacement current peak in Figure 6.14a. At negative bias voltages the global fit function, comprising a Gaussian and two exponentially convoluted Gaussians, does not give a consistent trend for t_{trans} . We therefore fit only the local region after the displacement peak with a single exponentially convoluted Gaussian and obtain again a shift of the transport current peak with V_{SD} .

We calculate the transport velocity:

$$v_h = \frac{d_{\text{contact}}}{t_{\text{trans}} - t_{1\text{st}}}. \quad (6.5)$$

⁶The arrival time t_{trans} of the holes is not a fit parameter in the fitting procedure but a numerically deduced value. Therefore no fitting errors are obtained.

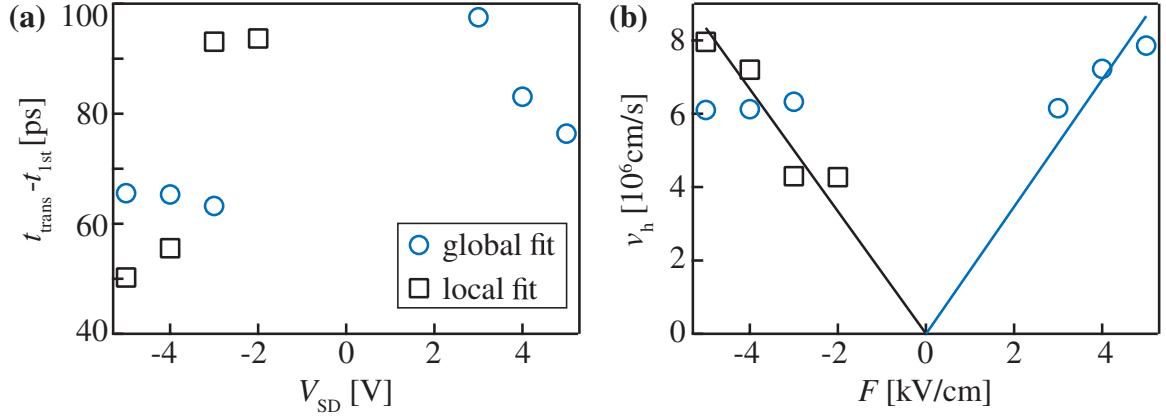


Figure 6.14 — Fitting parameters obtained in the measurements of I_{Sampling} as a function of V_{SD} in the range between -5 V and 5 V in steps of 1 V , and fixed excitation position. Blue circles correspond to a global fit of the data, while black squares correspond to a local fit of the region after the displacement current peak at $\sim 22 \text{ ps}$. (a) Arrival time of the hole current peak with respect to the displacement current peak. (b) Deducing hole velocity v_h as a function of the applied electric field F . We calculate the hole mobility μ_h by the inclination of the linear fit (solid lines).

Here, d_{contact} is the distance to the contact in the direction of the drifting holes. This value is different for positive and negative voltages, since we do not excite exactly in the middle of the stripline. Figure 6.14b shows the calculated values v_h as a function of the applied electric field F . Linear fits (solid lines) with offset set to zero yield mobilities of $\mu_h = (1730 \pm 130) \text{ cm}^2/\text{Vs}$ for positive voltages and $\mu_h = (1670 \pm 110) \text{ cm}^2/\text{Vs}$ for negative voltages.

Generally, the mobility of holes in bulk GaAs depends on the temperature and the hole density [Wil75] and is usually considered to be $\leq 400 \text{ cm}^2/\text{Vs}$. We would like to note here, that the values obtained here are for optically excited holes, and therefore they are expected to be different to values in bulk. Furthermore, we expect the mobility to depend on the laser wavelength λ , as was discussed in section 3.5 for photo excited electrons. Wavelength dependent I_{Sampling} measurements are currently being performed by Dipl. Phys. N. Erhard.

6.3.8 I_{Sampling} for $V_{\text{SD}} = 0 \text{ V}$

Figure 6.15a and b show a time-resolved measurement of I_{Sampling} for excitation positions starting at the left metal contact (lowest trace) in steps of $\sim 1.5 \mu\text{m}$ along the dotted line in Figure 6.6 at $V_{\text{SD}} = 0 \text{ V}$. A positive short peak centered

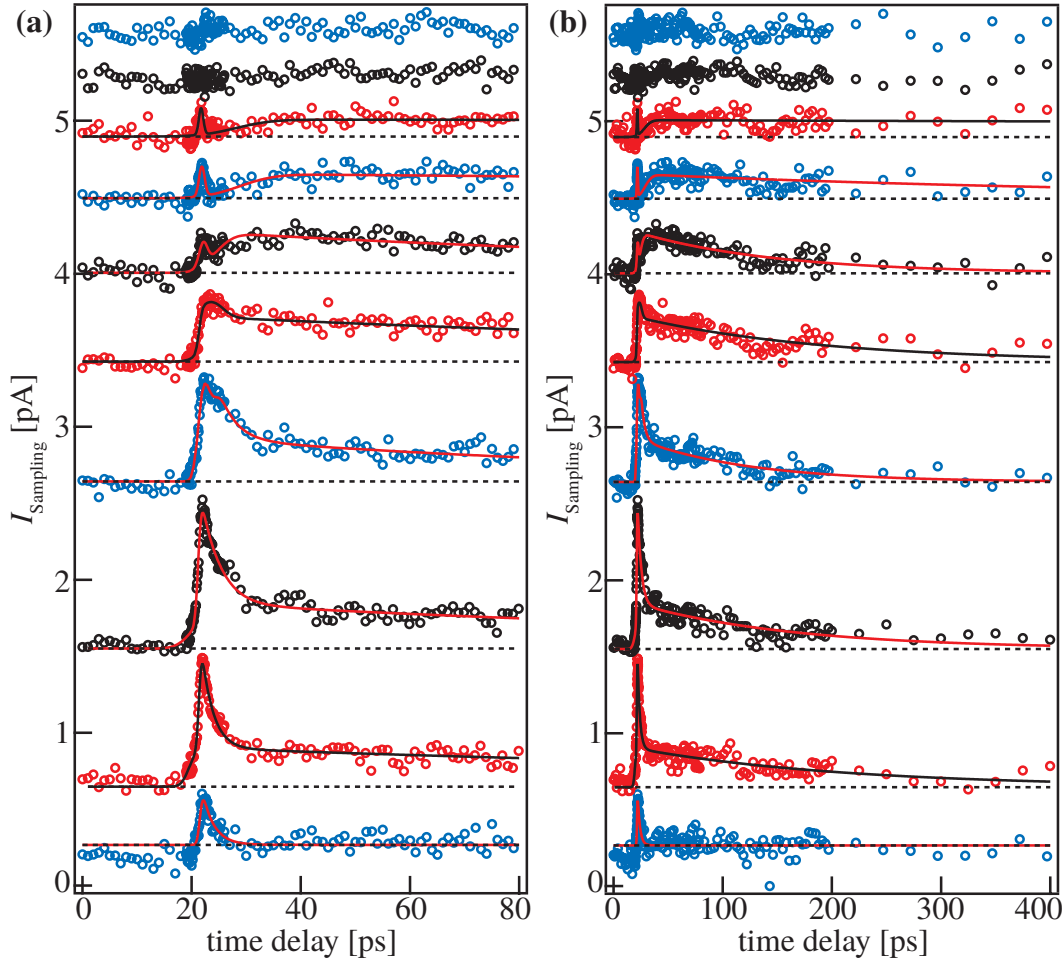


Figure 6.15 — Time-resolved measurement of I_{Sampling} for $V_{\text{SD}} = 0\text{ V}$ for excitation positions starting at the left metal contact in steps of $\sim 1.5\text{ }\mu\text{m}$ along the dotted line in Figure 6.6a-d. Solid lines are fits to the data. Data offset level indicated by dashed lines. **(a)** I_{Sampling} for time delay up to 80 ps. **(b)** I_{Sampling} extended to a time-delay of 400 ps.

around $\sim 22\text{ ps}$ can be observed. The peak amplitude increases starting from the left contact (lowest trace) towards the middle of the nanowire and then decreases again towards the right contact (highest trace). After the peak at 22 ps an offset of I_{Sampling} is observed in traces number two to six counted from bottom to top. In traces six to eight a slow increase is observed after the peak at 22 ps. Finally the signal decays on a slow timescale back to the initial value of I_{Sampling} , as can be observed in Figure 6.15b.

At 0 V we expect mainly displacement currents and photo-thermoelectric cur-

rents to contribute to the time-resolved I_{Sampling} . Consequently, we tentatively assign these two effects to the fast peak at 22 ps and the following offset and slow decay. The origin for the slowly increasing signal after the peak at 22 ps (traces 6 to 8 in Figure 6.15 counted from bottom to top) is unclear. Potentially, drift and diffusion of photo excited charge carriers to one contact could be responsible for this feature. We note, that the varying doping profile along the nanowire can generate intrinsic fields [Duf10]. Consequently, optically excited charge carriers would experience an electric field along the nanowire. Furthermore, the doping profile could also result in a displacement current far away from the electric fields of the Schottky contacts. The spatially resolved time-integrated measurements resolve positive and negative photocurrents at $V_{\text{SD}} = 0 \text{ V}$, as is shown in Figure 6.6d. Contrarily, the time-resolved measurements of I_{Sampling} in Figure 6.15a do not show a change of sign, but the signal is always positive. This behavior can be explained, if the e.g. positive current mechanism happens on a fast time-scale, while the negative current mechanism happens on a time-scale slower than the laser repetition rate. In our measurement scheme processes slower than the laser repetition rate cannot be resolved, therefore only the positive current mechanism would be observable. Physically, such a slow current mechanism could possibly be the transport of heavy and therefore slow holes. Further experiments are needed to clarify the origin of I_{Sampling} at $V_{\text{SD}} = 0 \text{ V}$.

6.4 Conclusions

In summary, we present time-integrated spatially and spectrally resolved optoelectronic measurements on freely suspended *p*-doped GaAs nanowires contacted by a focused ion beam deposition technique. We interpret the results in terms of the combination of a photogating and a photodoping effect, i.e. the consequence of the spatial separation of holes and electrons, in combination with a photocurrent effect, which is generated at the Schottky barriers between the GaAs nanowires and the metal electrodes. We demonstrate that both effects allow building a polarization dependent photodetector with a response time faster than 200 μs . First time-resolved photocurrent measurements yield a response time as fast as 3 ps, which suggests such processed nanowires as ultrafast photodetectors. We explain the ultrafast response time by defects, which are introduced by high energy electrons and ions in the contacting procedure.

We furthermore present time-resolved measurements of the photocurrent dynamics of a *p*-doped GaAs nanowire lying on a sapphire substrate and contacted by optical lithography. In the experiments we are able to resolve displacement currents, transport currents of holes, as well as a carrier lifetime limited currents. These results are very well reproduced by numerical simulations of bulk GaAs photoswitches performed by Dunn et al. [Dun94, Dun96]. We are able to spatially relate the time-integrated measurements to the time-resolved measurements of I_{Sampling} . We deduce, that the time-integrated measurements are dominated by the contributions fitted with an exponentially convoluted Gaussian with fitting parameter $\tau_{\text{rec}} = (1510 \pm 30) \text{ ps}$. We associate τ_{rec} with the recombination lifetime of photo electrons and holes in the GaAs nanowire. The data further suggests, that a photo-thermoelectric current is generated in the nanowires for excitation close to the contacts. There, we find a photocurrent with an exponential decay with $\tau_{\text{first}} = (2.9 \pm 0.3) \text{ ps}$.

Chapter 7

Conclusions and outlook

In this thesis we developed a measurement technique that is based on a common pump-probe scheme and coplanar stripline circuits. The technique enables time-resolved photocurrent measurements with a micrometer spatial and a picosecond time resolution. We investigated the ultrafast photocurrent response of low-temperature grown GaAs, CNTs, graphene, and GaAs nanowires.

In chapter 3 we investigated the ultrafast photocurrent response of low-temperature grown GaAs. We found two photocurrent pulses in the time-resolved response. We showed that the first pulse is consistent with a displacement current pulse. We interpreted the second pulse to result from a transport current process. In a time-of-flight analysis we further determine the velocity of the photo-generated charge carriers of the transport current pulse. The found value exceeds drift, thermal and quantum velocities of single charge carriers. Hereby, we interpreted the transport current pulse to stem from an electron-hole plasma excitation. Although the observed variations in $v_{\text{propagation}}$ with laser wavelength were significant, we could not find a systematic trend. The variations were tentatively attributed to the emission of optical phonons. Therefore, it would be desirable to excite at an E_{Laser} less than 35 meV above the band-gap of GaAs to avoid the excitation of optical phonons.

In chapter 4 we demonstrated that the ultrafast photocurrent response of CNTs comprises a displacement current and a transport current. Therefore, CNT networks can be exploited as ultrafast photodetectors with a switching time in the picosecond time-scale. The data further suggested that the photocurrent is finally terminated by the recombination lifetime (~ 250 ps at room temperature) of the charge carriers. To the best of our knowledge, we presented in this section the first recombination lifetime measurements of contacted, suspended, CVD grown CNT

networks. Due to the non-ohmic behavior, we were not able to determine the radiative lifetime at temperatures below 190K. In the temperature range above, we found an increase of τ_{Slow} with T , which is in agreement with theoretical predictions [Per05]. I consequently suggest single CNTs with ohmic contacts to further investigate the recombination and transit dynamics of photo generated charge carriers in contacted CNTs. For that purpose, first samples of single CNTs grown by CVD on a sapphire chip, contacted in a stripline circuit with ion-implanted Si at the field probe have been processed in collaboration with the group of Prof. H. Maki (Keio University, Tokyo, Japan).

In chapter 5 we investigated the ultrafast photocurrent dynamics of freely suspended graphene contacted by metal electrodes. At the graphene-metal interface, we demonstrated that built-in electric fields give rise to a photocurrent with a full-width-half-maximum of $\sim 4\text{ps}$ and that a photo-thermoelectric effect generates a current with a decay time of $\sim 130\text{ps}$. Furthermore, we showed that in optically pumped graphene electromagnetic radiation up to 1 THz is generated. We explain the THz generation either by an electron-hole plasma or by stimulated interband recombination after relaxation via optical phonons. I suggest to investigate graphene lying on a sapphire substrate and contacted in a stripline geometry as presented in chapter 6. In that fashion, the influence of the substrate on the photocurrent dynamics and the generation of electromagnetic radiation can be investigated. Furthermore, the graphene can be processed into nanoribbons after being contacted in the stripline circuit. The expected opening of a bandgap in the THz-regime might be observable in the time resolved measurements.

In chapter 6 we investigated the time-integrated photocurrent and photoconductance processes of suspended *p*-doped gallium arsenide nanowires contacted by a focused ion beam deposition technique. The observed photocurrent is generated at the Schottky contacts between the nanowire and metal source-drain electrodes, while the observed photoconductance signal can be explained by a photogating effect induced by optically generated charge carriers located at the surface of the nanowire. Both optoelectronic effects were sensitive to the polarization of the exciting laser field, enabling polarization dependent photodetectors. We furthermore studied the time-resolved photocurrent dynamics of *p*-doped gallium arsenide nanowires lying on a sapphire substrate and contacted by optical lithography. In the experiments we were able to resolve displacement currents, transport currents of holes, as well as a carrier lifetime limited currents. These results were very well reproduced by numerical simulations of bulk GaAs photoswitches performed by

Dunn et al. [Dun94, Dun96]. We were able to spatially relate the time-integrated measurements to the time-resolved measurements of I_{Sampling} . We deduced, that the time-integrated measurements were dominated by the contributions fitted with an exponentially convoluted Gaussian with fitting parameter $\tau_{\text{rec}} = (1510 \pm 30) \text{ ps}$. We associated τ_{rec} with the recombination lifetime of photo electrons and holes in the GaAs nanowire. The data further suggests, that a photo-thermoelectric current is generated in the nanowires for excitation close to the contacts. There, we found a photocurrent with an exponential decay with $\tau_{\text{first}} = (2.9 \pm 0.3) \text{ ps}$.

I suggest to investigate the time-resolved photoresponse of $p - i - n$ modulation-doped nanowires, which are voltage biased to work in the avalanche regime. In this manner the dynamics of avalanche processes after single-photon absorption can be investigated. Silicon $p - i - n$ nanowires grown by Heike Riel at IBM Zürich are currently being investigated in the group of Prof. A.W. Holleitner.

I furthermore suggest superconducting nanowires or films to be investigated with the experimental scheme of chapter 6. If the superconducting nanowires are driven exactly below the critical current density, an absorbed photon will locally generate heat and consequently cease the superconducting state of the nanowire. The abrupt change in current will generate an easily observable signal. The dynamics of the superconducting breakdown and the following return to the superconducting state can then be investigated in the proposed measurement.

Finally, I suggest to modify the experimental setup, so that a higher spatial resolution can be obtained. This can be achieved by focusing the probe beam from the back side of the sample through the transparent sapphire substrate onto the field probe. In that way, both the pump and the probe laser beam are focussed through a separate objective and can be positioned independently with two piezo scanners. Microscope objectives with higher magnification, numerical aperture, and resolution can then be used. Optical aberrations are avoided, since the laser beams can then be guided along the optical axes through each objective. Furthermore spurious excitation of the nanostructure with the probe laser or excitation of the field probe by the pump laser can be reduced. This experimental setup can also be designed as a cryogenic confocal microscope with two optical fibers for pump and probe.

Chapter 7. Conclusions and outlook

Appendix A

Properties of stripline circuits

The odd-mode effective index of diffraction n_{eff} as a function of frequency for a 5/15/5 μm stripline circuit fabricated on a GaAs substrate is discussed in section 1.6.1. There, it was found that a dispersion sets in at about 1 THz. For the trench geometry, we estimate the effective index to be $n_{\text{eff}} = 2.2 \pm 0.1$ for frequencies below 1 THz. The resulting wave-impedance Z can be estimated to be $\approx 178.9\Omega$ using a finite element method [COM07]. The time an electromagnetic pulse travels from the CNTs to the field probe can be estimated via

$$t_{\text{Travel}} = d \cdot n_{\text{eff}} / c_0 = 1 \text{ mm} \cdot (2.2 \pm 0.1) / c_0 \approx (7.3 \pm 0.3) \text{ ps}, \quad (\text{A.1})$$

with d the propagation distance and c_0 the vacuum speed of light. For the graphene sample, $d \approx 0.3 \text{ mm}$ and consequently $t_{\text{Travel}} \approx (2.2 \pm 0.3) \text{ ps}$. The striplines have a total length exceeding 48 mm. Thus, reflections at the end of the stripline are expected for $t_{\text{Delay}} \geq 350 \text{ ps}$. The amplitude of the reflections is strongly reduced due to damping and radiation losses (see section 1.6.2). Therefore, no reflections overlap with the electro-magnetic signal coming directly from the CNTs or the graphene in our data.

The RC -time of the entire CNT-sample geometry including the wiring was measured with an oscilloscope to be $(21 \pm 2) \text{ ms}$. The capacity per unit length of the coplanar stripline circuit can be estimated to be $\bar{C}_{\text{stripline}} = (41 \pm 1) \text{ pF m}^{-1}$ using a finite element method [COM07]. The resulting total capacitance of the stripline with a length of 48 mm can be calculated to be 2 pF, which is much smaller than the capacitance of the attached cables of $\approx 100 \text{ pF}$. Therefore, the RC -time is dominated by the cable capacitance of the experimental circuit.

For stripline circuits without an etched trench also analytical formulas can be used to calculate the effective index of diffraction n_{eff} , the wave impedance Z and the capacity per unit length $\bar{C}_{\text{stripline}}$ [Gup96].

Appendix B

Additional data

B.1 Time-resolved photocurrent measurements on LT-GaAs without AlGaAs

Figure B.1 shows time-resolved photocurrent measurements on gold stripline circuits (10/15/10 μm) on a 2 μm LT-GaAs substrate without an AlGaAs layer. In both samples #LT7 and #LT9 a first peak at ~ 8 ps and a delayed second peak can be observed. In these measurements taken from [Pre07] the pump beam could not be positioned independently of the probe beam with high precision. Yet the existence of the second peak (fitted with blue lines in Figure B.1) in these samples lets us conclude that the AlGaAs layer employed in the experiments presented in chapter 3, 4 and 5 is not responsible for the second peak.

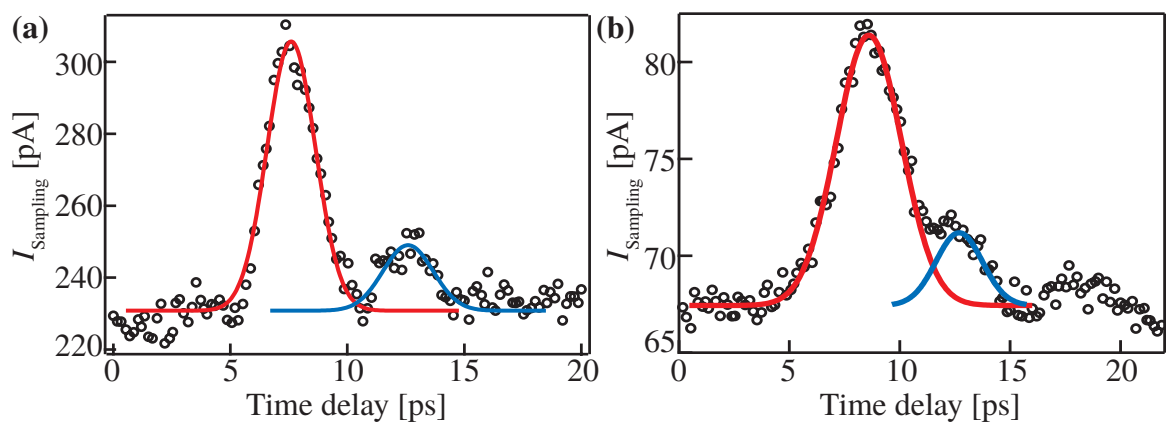


Figure B.1 — Time-resolved photocurrent measurements of a 10/15/10 μm Au stripline circuit on a 2 μm LT-GaAs substrate without a AlGaAs layer. Data taken from [Pre07]. **(a)** Sample #LT7, $\lambda = 830\text{ nm}$, $P = 60\text{ mW}$, $V_{SD} = -0.5\text{ V}$. **(b)** Sample #LT9, $\lambda = 850\text{ nm}$, $P = 2.5\text{ mW}$, $V_{SD} = -0.5\text{ V}$. Solid lines are fits with Lorentzian functions.

B.2 Time-resolved photocurrent measurements on LT-GaAs at room temperature and at 77 K

Figure B.2 below shows the time-resolved I_{Sampling} for a similar stripline circuit fabricated on LT-GaAs without an etched trench. Figure B.2a shows I_{Sampling} at room temperature. The bandwidth can be estimated from the FFT spectrum in Figure B.2b to extend up to ~ 1 THz. At 77 K we obtain similar data for I_{Sampling} (Figure B.2c) and for the FFT spectrum (Figure B.2d).

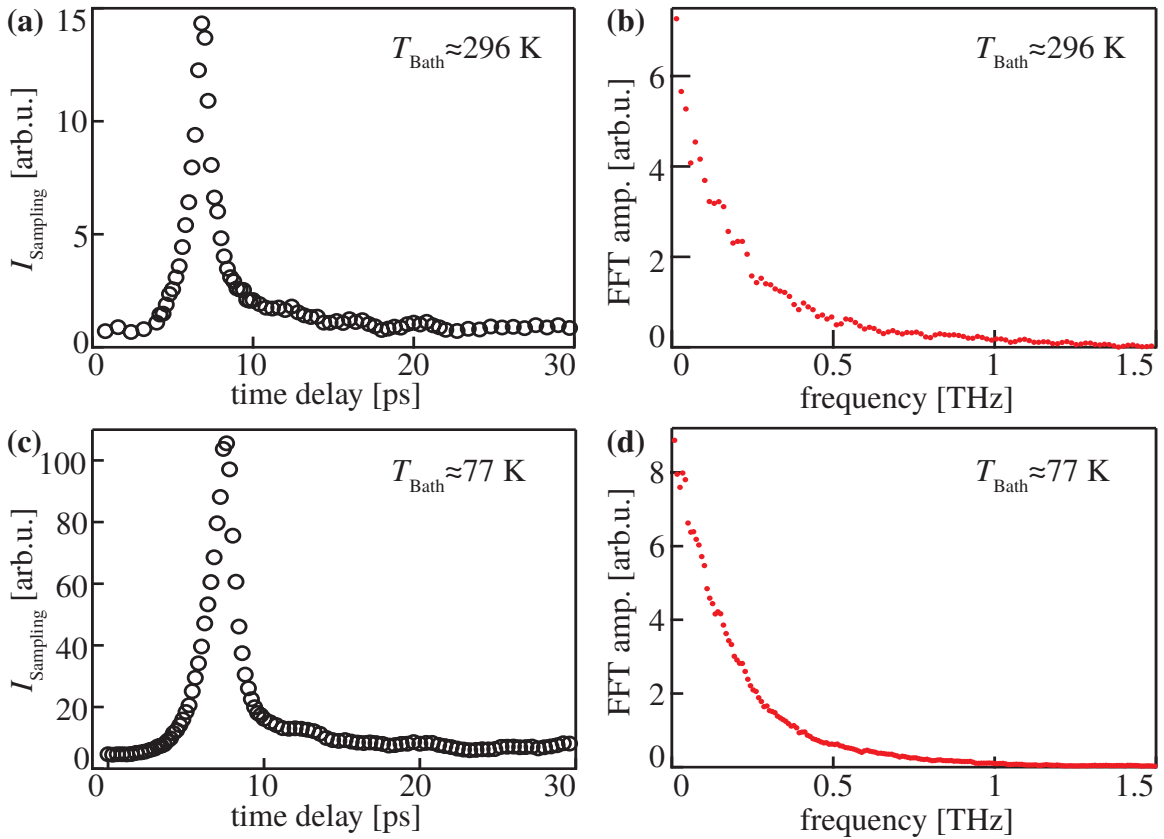


Figure B.2 — Control experiment on a stripline circuit without a GaAs trench. (a) Time resolved I_{Sampling} at $T_{\text{Bath}} = 296$ K ($V_{SD} = 3$ V, $P_{\text{Laser}} = 300 \mu\text{W}$, $\lambda = 780$ nm). (b) Fast-Fourier-Transformation of I_{Sampling} shown in a. (c) Time resolved I_{Sampling} at $T_{\text{Bath}} = 77$ K ($V_{SD} = 2$ V, $P_{\text{Laser}} \approx 50$ mW, $\lambda = 740$ nm). (d) Fast-Fourier-Transformation of I_{Sampling} shown in c.

B.3 Measurements of a bare trench

In this section we experimentally address a *non-uniform excitation* scenario, namely that photogenerated charge-carriers are excited both in the suspended nano-structure (e.g. CNTs and graphene) and in the GaAs at the bottom of the trench (with different relaxation and charge carrier expansion dynamics). In the Figure B.3, we present a corresponding control experiment of I_{Sampling} for a sample with an etched trench but without graphene. Again, the trench has a depth of $\sim 12 \mu\text{m}$. In such a stripline circuit, the photoexcitation can give rise to charge-carriers in the GaAs with a lifetime definitely longer than the one in LT-GaAs. Hence, one does not expect a fast time-integrated signal for experimental conditions as reported in the manuscript. Figure B.3a shows the spatially resolved reflectivity of the stripline circuit with an etched trench. We perform this measurement by scanning a stepper motor, which is mounted to a scanning mirror directly in front of the microscope objective. We determine the relative image scale of the scanning mirror with respect to the displacement of the laser spot on the sample by the distance of the centre positions of the two Gaussian functions and the known distance of the two metal strips. In Figure B.3b we show the time-resolved I_{Sampling} for scanning mirror position $0 \mu\text{m}$ to $90 \mu\text{m}$ in steps of $10 \mu\text{m}$ (traces from bottom to top, $P_{\text{Laser}} = 800 \mu\text{W}$, $T_{\text{Bath}} = 296 \text{ K}$). For all excitation positions, we do not detect a signal in I_{Sampling} at such laser power and focusing conditions in agreement with our expectations. Figure B.3c shows I_{Sampling} for excitation in the middle of the stripline (scanning mirror position $60 \mu\text{m}$) for laser power up to 13 mW . Again, we do not detect a time-resolved signal. Most importantly, to prove that the field probe is sensitive to time-resolved signals, we then perform a laser annealing step by increasing the laser power to $\sim 160 \text{ mW}$ for several minutes ($p = 10^{-6} \text{ mbar}$, $T_{\text{Bath}} = 296 \text{ K}$). In a simplified picture, the annealing gives rise to defect states in the GaAs which change the relaxation dynamics of the photogenerated charge carriers. Figure B.3d shows I_{Sampling} before and directly after this annealing step without performing any changes to the measurement setup in between (i.e. the same position of the probe laser spot at the field probe). After the annealing step we observe a slowly varying signal in I_{Sampling} (for laser powers which are slightly larger than the ones used during the experiments on graphene). Specifically, we do not detect an oscillatory signal. In the course of the experiments on the graphene, we have never applied a laser power as high as is necessary for an annealing of the GaAs. We thereby prove that the time-resolved I_{Sampling} discussed in the main part of the manuscript

solely originates from the suspended CNTs or graphene and not from the trench or a combination of both.

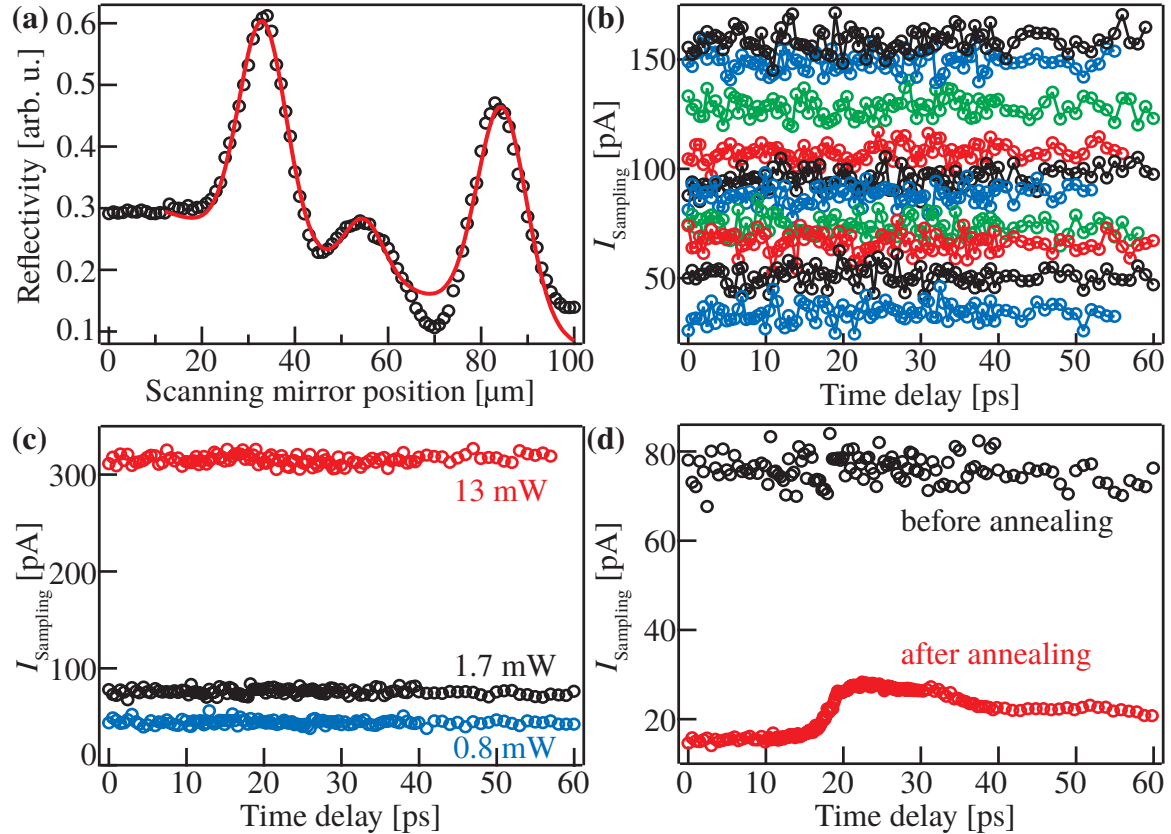


Figure B.3 — (a) Spatially resolved reflectivity of a stripline circuit with an etched trench performed with a scanning mirror. The reproduction scale of the scanning mirror with respect to the displacement of the laser spot on the sample is deduced by the distance of the center positions of the two Gaussian functions. (b) Time-resolved photocurrent for scanning mirror positions 0 μm to 90 μm in steps of 10 μm . Traces are offset for clarity. ($P_{\text{pump}} = 800 \mu\text{W}$, $\lambda = 780 \text{ nm}$, $V_{SD} = 0 \text{ mV}$, $T_{\text{bath}} = 296 \text{ K}$). (c) I_{Sampling} for excitation in the middle of the trench at $T_{\text{bath}} = 77 \text{ K}$ with laser powers of $P_{\text{pump}} = 0.8 \text{ mW}$, 1.7 mW and 13 mW ($\lambda = 780 \text{ nm}$, $V_{SD} = 0 \text{ mV}$, $T_{\text{bath}} = 77 \text{ K}$). (d) I_{Sampling} measured before and after annealing of the trench with $P_{\text{annealing}} = 160 \text{ mW}$ ($P_{\text{pump}} \approx 1.5 \text{ mW}$, $\lambda = 780 \text{ nm}$, $V_{SD} = 0 \text{ mV}$, $T_{\text{bath}} = 77 \text{ K}$).

B.4 Spatially resolved photocurrent scans of graphene at 77 K

In Figure B.4 we show the spatially resolved, time-integrated photocurrent signal of the graphene structure #1 at 77 K. The spatial scan is characterized by a one-directional current generated homogeneously in between the metal strips, even for excitation of the suspended graphene. We attribute this signal to the excitation of surface states and long-living charge carriers in the etched GaAs trench. This signal occurs on a slow timescale and is therefore absent in the time-resolved measurements (see Appendix B.3). We note that we observe a high-background signal when using the optical chopper system and the lock-in amplifier to measure I_{Sampling} . The observation of a background is in agreement with photocurrent processes occurring on a timescale slower than the laser repetition rate. We therefore utilize the oscillating retroreflector in combination with the oscilloscope to measure I_{Sampling} . In that manner, we constantly excite the etched trench and the background level in I_{Sampling} is strongly reduced.

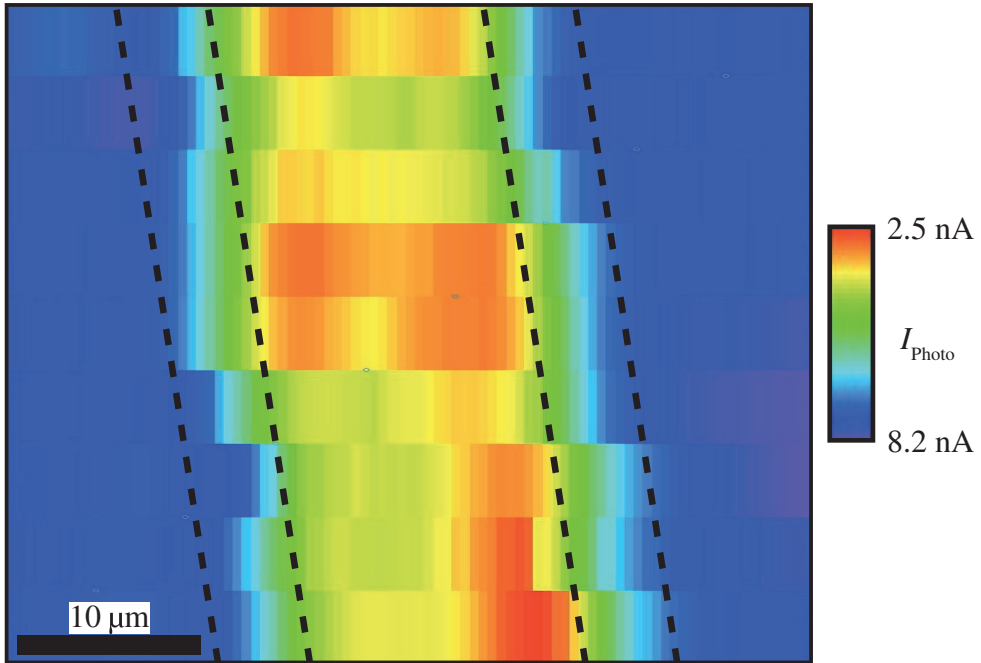


Figure B.4 — Spatially resolved photocurrent I_{Photo} of the graphene at 77 K ($P_{\text{Pump}} = 400 \mu\text{W}$, $\lambda = 780 \text{ nm}$, $V_{SD} = 0 \text{ mV}$, $T_{\text{bath}} = 77 \text{ K}$).

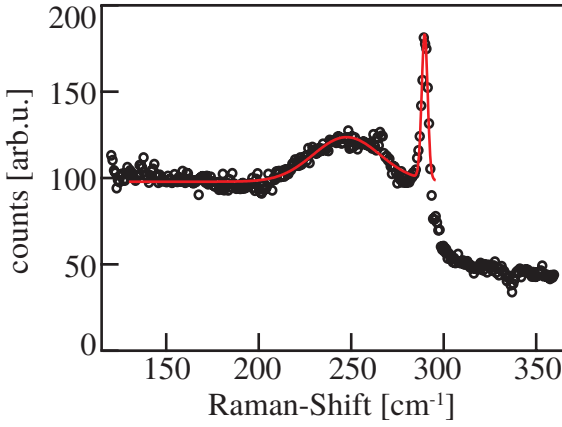


Figure B.5 — Raman measurements of a freestanding CNT network. We fit the radial breathing mode with a Gaussian with center frequency $(248 \pm 1)\text{cm}^{-1}$ and full-width-half-maximum of $(43 \pm 2)\text{cm}^{-1}$. The sharp peak at $(290 \pm 1)\text{cm}^{-1}$ corresponds to the LO-phonon of the GaAs substrate [Moo66, Yu05].

B.5 Raman measurements of carbon nanotubes

Figure B.5 shows a Raman measurement of a suspended CNT network, which is grown in a similar way as the network investigated in chapter 4. The diameter d_{CNT} of the CNT in the network can be deduced from the radial breathing mode ω_{rbm} by the empirical formula [Jor01, Dre05]

$$d_{\text{CNT}} = \frac{248 \text{ nm cm}^{-1}}{\omega_{\text{rbm}}}. \quad (\text{B.1})$$

The relatively broad peak with a full-width-half maximum of $(43 \pm 2)\text{cm}^{-1}$ indicates a large diameter distribution. From the center position and the width of the Gaussian fit-function we calculate using equation B.1 a diameter distribution of $(1.0 \pm 0.1)\text{nm}$ using equation B.1. The CNT diameter can be related to the bandgap energy using the so-called Kataura plot [Kat99, Dre05]. For $d_{\text{CNT}} \approx 1\text{ nm}$ we deduce a resulting first intersubband transition energy of $E_{11} \approx 0.8\text{ eV}$ and a second intersubband transition energy of $E_{22} \approx 1.6\text{ eV} - 1.7\text{ eV}$ [Kat99, Dre05].

In Figure B.6 we show Raman measurements of a suspended CNT network under applied bias V_{SD} . Figure B.6a shows the Anti-Stokes (AS) G+ and the G-mode for $V_{\text{SD}} = 0\text{ V}$ (black), 1 V (blue), 2 V (red) and 3 V (green). Solid lines are least-square fits of a sum of two Breit-Wigner-Fano functions, to account for the G+ and

G- mode [Dre05]. The amplitude of the AS G+ mode increases with V_{SD} , while the amplitude of the Stokes G+ mode does not change (data not shown). Therefore the temperature T of the phonons in the G+ mode increases with applied bias voltage. We calculate T using the formula [Oro08]

$$\frac{I_{\text{AS}}}{I_{\text{S}}} \propto \exp\left(\frac{-E_{\text{phonon}}}{k_{\text{B}} T}\right), \quad (\text{B.2})$$

with I_{AS} (I_{S}) the Anti-Stokes (Stokes) amplitude, E_{phonon} the phonon energy, and k_{B} the Boltzmann constant. In Figure B.6b we show the calculated relative temperature T/T_0 versus the applied bias voltage V_{SD} . A temperature increase of about 10% is observed at $V_{\text{SD}} = 3\text{ V}$. We interpret the high AS-amplitude at $V_{\text{SD}} = 0\text{ V}$ to arise from laser-induced heating of our CNT network. Alternatively, the temperature of the CNT network can be determined by the downshift of the G mode frequency. Figure B.6c shows the frequency of the G+ mode as a function of V_{SD} . Using a Stokes G band downshift calibration curve [Des09] and assuming symmetric Stokes and Anti-Stokes frequencies, we estimate a G+ phonon temperature increase from 730K at $V_{\text{SD}} = 0\text{ V}$ to 870K at $V_{\text{SD}} = 3\text{ V}$. Again, the Raman-shift of -1587 cm^{-1} at $V_{\text{SD}} = 0\text{ V}$ is a clear indication of a high phonon temperature, possibly by laser induced heating.

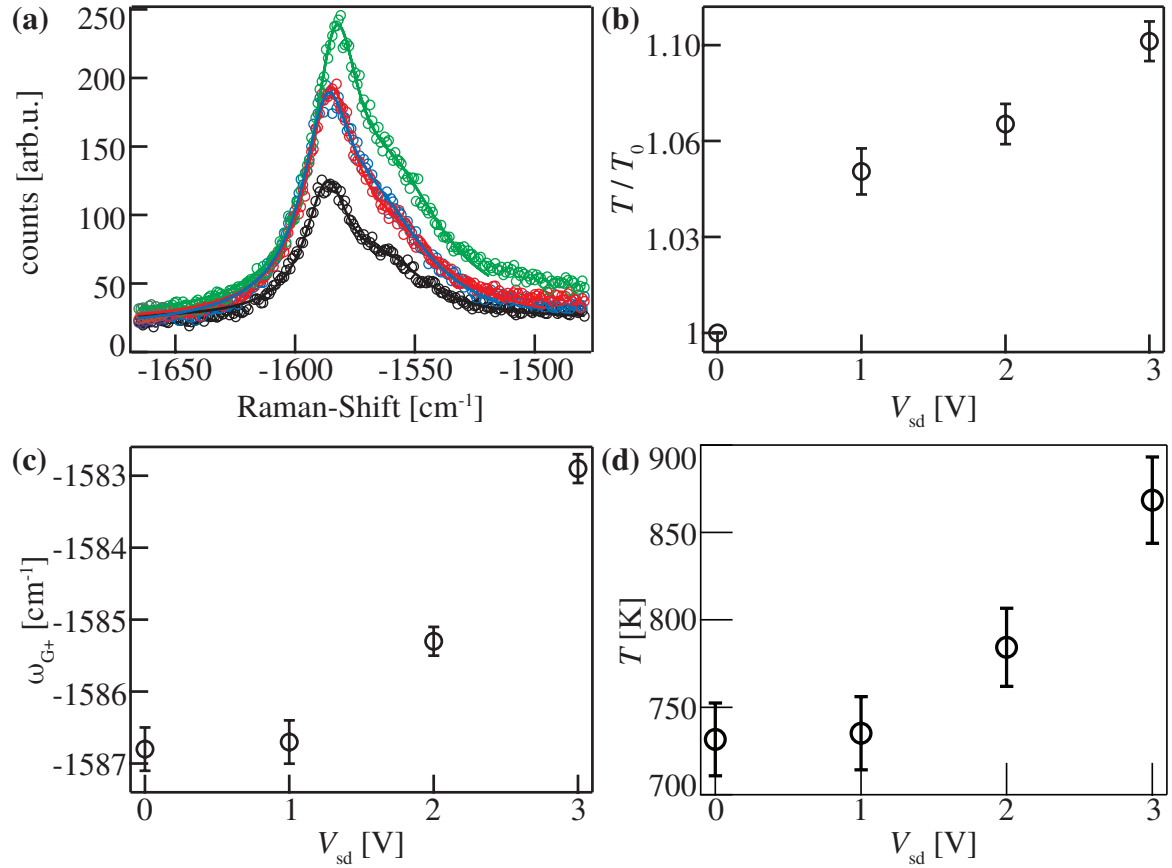


Figure B.6 — (a) G-mode Anti-Stokes Raman spectrum of a similar suspended CNT network for $V_{SD} = 0\text{ V}$ (black), 1 V (blue), 2 V (red) and 3 V (green). Solid lines are least-square fits of a sum of two Breit-Wigner-Fano functions. ($P_{\text{Laser}} = 4\text{ mW}$, $\lambda_{\text{Laser}} = 530\text{ nm}$, grating = 1500 mm^{-1} , $T_c = 180\text{ second}$, averaging over three spectra) (b) Calculated relative G-band phonon temperature using the Anti-Stoke/Stokes-amplitude ratio. (c) Raman shift of the AS G+ mode with V_{SD} . (d) Estimated G+ phonon temperature using a Stokes G band downshift calibration curve [Des09].

B.6 Raman measurements of graphene

In this section we show Raman measurements of the suspended graphene sample investigated in chapter 5. The number of graphene layers can be determined from Raman spectra by analyzing the shape of the 2D-peak ($\sim 2700\text{cm}^{-1}$), which is Lorentzian shaped only for a single layer of graphene [Fer06, Dre10, Rou10]. Furthermore, the center frequency of the 2D-peak is upshifted for a multilayer. Alternatively, the number of graphene layer can be determined by the amplitude ratio A_G/A_{2D} of the G-peak ($\sim 1580\text{cm}^{-1}$) and the 2D-peak. A ratio smaller than one indicates a monolayer of graphene [Fer06, Cal07, Dre10]. In the employed growth procedure (see section 2.3.6) we typically obtain 1-3 layers of graphene, as is determined from Raman measurements of non-suspended graphene. Figure B.7a shows typical Raman measurements of such obtained mono-, bi-, and tri-layers of graphene. In Fig. B.7b we show the 2D-peak (sometimes called G'-peak) of the suspended graphene sample #1 investigated in chapter 5. The center frequency of the 2D-peak at $(2693.4 \pm 0.3)\text{cm}^{-1}$ indicates a single layer of graphene. Fig. B.7c shows the D-peak at $\sim 1350\text{cm}^{-1}$ and the G-peak at $\sim 1580\text{cm}^{-1}$ of the suspended graphene sample #1 investigated in chapter 5. We note, that we cannot use these measurements to obtain the number of graphene layers by the amplitude ratio A_G/A_{2D} . In this measurement we utilize a high-resolution grating (1500mm^{-1}) which needs to be rotated to obtain the G and 2D peaks in a consecutive measurement. The sensitivity of the spectrometer is subject to change in this process, and therefore the absolute intensities of the G and 2D peaks cannot be compared. Furthermore, a possible shift of the laser spot on the sample over the measurement time ($\sim 80\text{min}$) can alter the absolute amplitudes. The nature of the background level in this measurement is unclear. We suspect stray light from the bottom of the trench to be responsible for this signal.

We conclude that the suspended graphene sample consists of 1 to 3 layers.

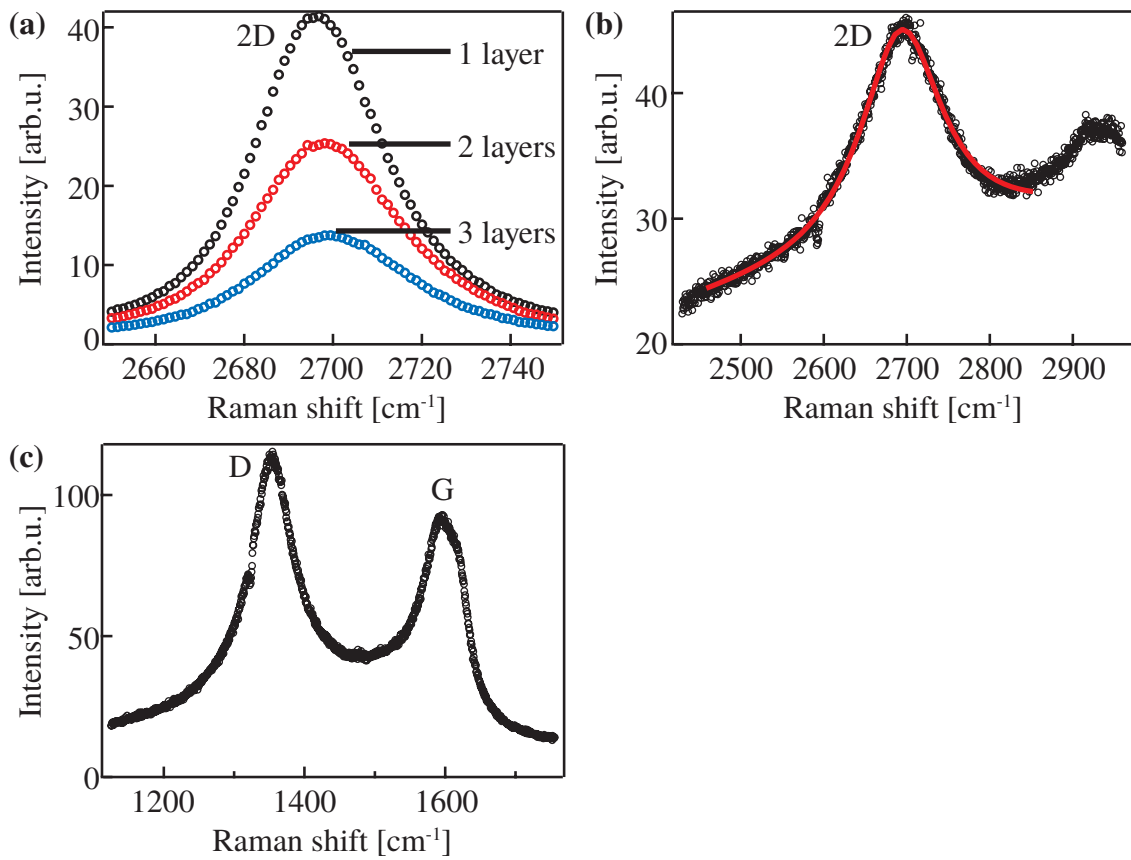


Figure B.7 — Raman measurements of the suspended graphene investigated in chapter 5. **(a)** Typical Raman measurements of non-suspended graphene mono layer (black), bi-layer (red) and tri-layer (blue) obtained in the employed growth process. **(b)** Measurement of the 2D-peak ($\lambda = 514\text{nm}$, $P = 300\mu\text{W}$, $T_c = 300\text{s}$, average of 10 consecutive spectra). The solid line is a fit with a Lorentzian yielding a central position of $(2693.4 \pm 0.3)\text{cm}^{-1}$. **(c)** Measurement of the D-peak at $\sim 1350\text{cm}^{-1}$ and the G-peak at $\sim 1580\text{cm}^{-1}$ ($\lambda = 514\text{nm}$, $P = 300\mu\text{W}$, $T_c = 300\text{s}$, average of 5 consecutive spectra).

Appendix C

Numerical Simulations

C.1 Finite-element-simulation parameters

C.1.1 Transient thermal transport of gold on sapphire

The following parameters were used for the simulation of heat transport discussed in chapter 1.4.

Material	Material parameters	
	Gold	Sapphire
density [kg m^{-3}]	19300	3965
heat capacity [$\text{J kg}^{-1} \text{K}^{-1}$]	129	730
thermal conductivity [$\text{W mol}^{-1} \text{K}^{-1}$]	317	35

Table C.1 — Material parameters used for the simulation of heat transport. All parameters are taken from the material library integrated with the software package [COM07].

C.1.2 Effective index of diffraction simulation parameters

The following section describes the simulation of the effective index of diffraction in chapter 1.6.1. In this simulation hybrid eigenmodes of a coplanar metal stripline (width $5\text{ }\mu\text{m}$, distance $15\text{ }\mu\text{m}$) were calculated as a function of frequency f . The upper simulation half (and in one case the trench) consists of air ($n = 1$), the lower half of a sapphire or gallium-arsenide substrate. The dielectric function of GaAs is [Bla82, Ada89]:

$$\epsilon_r(f) = \epsilon_\infty + \frac{f_{TO}^2(\epsilon_s - \epsilon_\infty)}{f_{TO}^2 - f^2 + i\gamma_p f} \quad (\text{C.1})$$

with the static dielectric constant $\epsilon_s = 13.1$, the high-frequency dielectric constant $\epsilon_\infty = 10.9$, the transversal-optical phonon frequency $f_{TO} = 8.032 \text{ THz}$ and a attenuation constant $\gamma_p = 60.48 \text{ GHz}$ [Bla82, Ada89]. The employed index of diffraction n_{sapphire} and absorption coefficient α of sapphire [Gri90] as a function of frequency are shown in Figure C.1. The metal stripes were modeled as ideal conductors. Perfectly-matched layers were used as boundary conditions.

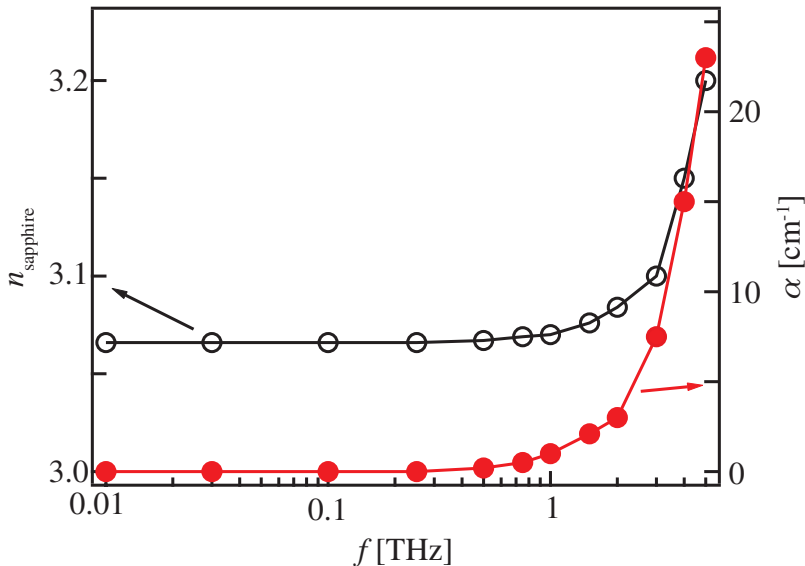


Figure C.1 — Index of diffraction n_{sapphire} and absorption coefficient α of sapphire as a function of frequency. From [Gri90].

C.2 Finite-Differences-Time-Domain simulation parameters

The freely available software package *Meep* was used for Finite-Differences-Time-Domain simulations [Osk10]. An input-script is used for defining all simulation parameters. All calculations in *Meep* are carried out in unitless dimensions. That means, that defining the geometry in units of $1 \mu\text{m}$ results in a frequency-unit

of $\frac{c}{1\mu\text{m}} = 300 \text{ THz}$. In the input-script *set! geometry* defines the material properties of the simulation geometry (e.g. the dielectric index for semiconductors or *metal* for an ideal conductor). Furthermore *Perfectly-Matched-Layers* (PML) are used for the absorption of all fields at the simulation boundaries. A source producing electric fields polarized in the y -axes with central frequency 0.001 and frequency-width 0.00066 (corresponding to $f = 0.3 \text{ THz}$ and $\Delta f = 0.2 \text{ THz}$) is defined. Thereafter, flux-regions are defined in which the flux of y -polarized electric field is gathered. Finally, the electric fields are output into files and the field-fluxes are printed. The following script has been used for the numerical investigations presented in section 1.4:

```
(set! geometry-lattice (make lattice (size 200 100 300)))
(set! geometry (list
    (make block (center 0 0 -135) (size infinity infinity 1)
        (material metal))
    (make block (center 0 0 -75) (size infinity infinity 150)
        (material (make dielectric (epsilon 12) )))
    (make block (center 0 0 75) (size infinity infinity 150)
        (material vacuum))
    (make block (center 0 0 -2.5) (size infinity 10 5)
        (material vacuum))
    (make block (center 0 7.5 1) (size infinity 5 1)
        (material metal))
    (make block (center 0 -7.5 1) (size infinity 5 1)
        (material metal))))
(set! pml-layers (list (make pml (thickness 10))))
(set! resolution 2)
(define-param fcen 0.001) ; pulse center frequency
(define-param df 0.00066) ; pulse width (in frequency)
(set! sources (list
    (make source
        (src (make gaussian-src (frequency fcen) (fwidth df)))
        (component Ey)
        (center -65 0 0)
        (size 0 10 0))))
(define-param nfreq 200)
(define fluxwg
    (add-flux fcen df nfreq
        (make flux-region
            (center 65 0 0) (size 0 20 20)
        )
    )
)
(define fluxair ; flux in air
```

```
(add-flux fcen df nfreq
  (make flux-region
    (center -65 0 130) (size 20 20 0)
  )
)
(use-output-directory)
(run-sources+ 500 (at-beginning output-epsilon)
  (to-appended "extdataset" (at-every 400 output-efield-x))
  (to-appended "eytdataset" (at-every 400 output-efield-y))
  (to-appended "eztdataset" (at-every 400 output-efield-z))
)
(display-fluxes fluxair fluxwg)
```

Publications

PUBLISHED PAPERS

- *Photocurrent and photoconductance properties of a GaAs nanowire*
S. Thunich, L. Prechtel, D. Spirkoska, G. Abstreiter, A. Fontcuberta I Morral, and A. W. Holleitner
Applied Physics Letters vol. 95, 8, 083111, (2009).
- *Spatially resolved ultrafast transport current in GaAs photoswitches*
L. Prechtel, S. Manus, D. Schuh, W. Wegscheider, and A. W. Holleitner
Applied Physics Letters vol. 96, 26, 261110, (2010).
- *Time-Resolved Picosecond Photocurrents in Contacted Carbon Nanotubes*
L. Prechtel, L. Song, S. Manus, D. Schuh, W. Wegscheider, and A. W. Holleitner
Nano Letters vol. 11, 269-272, (2011).

SUBMITTED PAPERS

- *Time-resolved ultrafast photocurrents and terahertz generation in freely suspended graphene*
L. Prechtel, L. Song, D. Schuh, P. Ajayan, W. Wegscheider, and A. W. Holleitner

PAPERS IN PREPARATION

- *Spatially resolved ultrafast photo-thermoelectric and transport currents in GaAs nanowires*
L. Prechtel, M. Padilla, N. Erhard, H. Karl, A. Fontcuberta I Morral, G. Abstreiter, and A. W. Holleitner

AWARDS

- *Best Poster Prize at the 457. WE-Heraeus-Seminar on Graphene Electronics - Material, Physics and Devices* in Bad Honnef (15. - 18.8.2010) for the contribution *Ultrafast photocurrent response of freely suspended Graphene*.

Publications

Bibliography

- [Ada89] S. Adachi, *Optical dispersion relations for GaP, GaAs, GaSb, InP, InAs, InSb, $Al_xGa_{1-x}As$, and $In_{1-x}Ga_xAs_yP_{1-y}$* , Journal of Applied Physics, **66**, 6030–6040 (1989).
- [Ada07] S. Adam, E. H. Hwang, V. M. Galitski, and S. Das Sarma, *A self-consistent theory for graphene transport*, Proceedings of the National Academy of Science, **104**, 18392–18397 (2007).
- [Ale94] S. Alexandrou, C.-C. Wang, R. Sobolewski, and T. Y. Hsiang, *Generation of subpicosecond electrical pulses by nonuniform illumination of GaAs transmission-line gaps*, IEEE Journal of Quantum Electronics, **30**, 1332–1338 (1994).
- [And97] T. Ando, *Excitons in Carbon Nanotubes*, Journal of the Physical Society of Japan, **66**(4), 1066–1073 (1997).
- [Ash76] Neil W. Ashcroft and David N. Mermin, *Solid State Physics*. Thomson Learning, Toronto, 1 edition, (1976).
- [Aus75] D. H. Auston, *Picosecond optoelectronic switching and gating in silicon*, Applied Physics Letters, **26**, 101–103 (1975).
- [Aus80a] D. H. Auston, P. Lavallard, N. Sol, and D. Kaplan, *An amorphous silicon photodetector for picosecond pulses*, Applied Physics Letters, **36**, 66 (1980).
- [Aus80b] D. H. Auston, P. R. Smith, J. C. Bean, and A. M. Johnson, *Picosecond optoelectronic detection, sampling, and correlation measurements in amorphous semiconductors*, Applied Physics Letters, **37**, 371–373 (1980).
- [Aus82] D. H. Auston and P. R. Smith, *Picosecond optical electronic sampling - Characterization of high-speed photodetectors*, Applied Physics Letters, **41**, 599–601 (1982).
- [Aus83] D. H. Auston, *Impulse response of photoconductors in transmission lines*, IEEE Journal of Quantum Electronics, **19**, 639–648 (1983).

Bibliography

- [Avo07] P. Avouris, Z. Chen, and V. Perebeinos, *Carbon-based electronics*, Nature Nanotechnology, **2**, 605–615 (2007).
- [Avo08] P. Avouris, M. Freitag, and V. Perebeinos, *Carbon-nanotube photonics and optoelectronics*, Nature Photonics, **2**, 341–350 (2008).
- [Bae10] S. Bae, H. Kim, Y. Lee, X. Xu, J.-S. Park, Y. Zheng, J. Balakrishnan, T. Lei, H. Ri Kim, Y. I. Song, Y.-J. Kim, K. S. Kim, B. Özyilmaz, J.-H. Ahn, B. H. Hong, and S. Iijima, *Roll-to-roll production of 30-inch graphene films for transparent electrodes*, Nature Nanotechnology, **5**, 574–578 (2010).
- [Bak04] E. P. A. M. Bakkers, J. A. van Dam, S. de Franceschi, L. P. Kouwenhoven, M. Kaiser, M. Verheijen, H. Wondergem, and P. van der Sluis, *Epitaxial growth of InP nanowires on germanium*, Nature Materials, **3**, 769–773 (2004).
- [Bal05] K. Balasubramanian, M. Burghard, K. Kern, M. Scolari, and A. Mews, *Photocurrent Imaging of Charge Transport Barriers in Carbon Nanotube Devices*, Nano Letters, **5**, 507–510 (2005).
- [Bau97] P. Baumgartner, C. Engel, G. Boehm, and G. Abstreiter, *Franz-Keldysh effect in lateral GaAs/AlGaAs based npn structures*, Applied Physics Letters, **70**, 2876–2878 (1997).
- [Beh01] E. Beham, A. Zrenner, F. Findeis, M. Bichler, and G. Abstreiter, *Nonlinear ground-state absorption observed in a single quantum dot*, Applied Physics Letters, **79**, 2808 (2001).
- [Bek05] E. Bekyarova, M. E. Itkis, N. Cabrera, B. Zhao, A. Yu, J. Gao, and R. C. Haddon, *Electronic Properties of Single-Walled Carbon Nanotube Networks*, Journal of the American Chemical Society, **127**(16), 5990–5995 (2005).
- [Bir07] S. Birner, T. Zibold, T. Andlauer, T. Kubis, M. Sabathil, A. Trellakis, and P. Vogl, *nextnano: General Purpose 3-D Simulations*, IEEE Transactions on Electron Devices, **54**, 2137–2142 (2007).
- [Bir11] S. Birner, http://www.nextnano.de/nextnano3/tutorial/1Dtutorial_TightBinding_bulk_GaAs_GaP.htm (2011).
- [Bjo02] M. T. Bjoerk, B. J. Ohlsson, T. Sass, A. I. Persson, C. Thelander, M. H. Magnusson, K. Deppert, L. R. Wallenberg, and L. Samuelson, *One-dimensional heterostructures in semiconductor nanowhiskers*, Applied Physics Letters, **80**, 1058 (2002).

- [Bjo07] M. T. Bjoerk, O. Hayden, H. Schmid, H. Riel, and W. Riess, *Vertical surround-gated silicon nanowire impact ionization field-effect transistors*, Applied Physics Letters, **90**(14), 142110 (2007).
- [Bla82] J. S. Blakemore, *Semiconducting and other major properties of gallium arsenide*, Journal of Applied Physics, **53**, 123 (1982).
- [Boe93] E. H. Boettcher, F. Hieronymi, D. Kuhl, E. Dröge, and D. Bimberg, *Transient response of lateral photodetectors*, Applied Physics Letters, **62**, 2227–2229 (1993).
- [Bon10] F. Bonaccorso, Z. Sun, T. Hasan, and A. C. Ferrari, *Graphene photonics and optoelectronics*, Nature Photonics, **4**(9), 611–622 (2010).
- [Bou08] A. I. Boukai, Y. Bunimovich, J. Tahir-Kheli, J.-K. Yu, W. A. Goddard, III, and J. R. Heath, *Silicon nanowires as efficient thermoelectric materials*, Nature, **451**, 168–171 (2008).
- [Bre11] S. Breuer, C. Pfueller, T. Flissikowski, O. Brandt, H. T. Grahn, L. Geelhaar, and H. Riechert, *Suitability of Au- and Self-Assisted GaAs Nanowires for Optoelectronic Applications*, Nano Letters, **11**, 1276–1279 (2011).
- [Bro87] S. D. Brorson, J. G. Fujimoto, and E. P. Ippen, *Femtosecond electronic heat-transport dynamics in thin gold films*, Physical Review Letters, **59**, 1962–1965 (1987).
- [Bry06] T. Bryllert, L.-E. Wernersson, T. Loewgren, and L. Samuelson, *Vertical wrap-gated nanowire transistors*, Nanotechnology, **17**, 227 (2006).
- [Bus09] A. W. Bushmaker, V. V. Deshpande, S. Hsieh, M. W. Bockrath, and S. B. Cronin, *Gate Voltage Controllable Non-Equilibrium and Non-Ohmic Behavior in Suspended Carbon Nanotubes*, Nano Letters, **9**, 2862–2866 (2009).
- [Cal07] I. Calizo, W. Bao, F. Miao, C. N. Lau, and A. A. Balandin, *The effect of substrates on the Raman spectrum of graphene: Graphene-on-sapphire and graphene-on-glass*, Applied Physics Letters, **91**(20), 201904 (2007).
- [Cao09] L. Cao, J. S. White, J.-S. Park, J. A. Schuller, B. M. Clemens, and M. L. Brongersma, *Engineering light absorption in semiconductor nanowire devices*, Nature Materials, **8**, 643–647 (2009).
- [Cas09] A. H. Castro Neto, F. Guinea, N. M. R. Peres, K. S. Novoselov, and A. K. Geim, *The electronic properties of graphene*, Rev. Mod. Phys., **81**(1), 109–162 (2009).

Bibliography

- [Cav07] A. Cavallini, L. Polenta, M. Rossi, T. Stoica, R. Calarco, R. J. Meijers, T. Richter, and H. Lüth, *Franz-Keldysh Effect in GaN Nanowires*, Nano Letters, **7**, 2166–2170 (2007).
- [Cha08] C. K. Chan, H. Peng, G. Liu, K. McIlwrath, X. F. Zhang, R. A. Huggins, and Y. Cui, *High-performance lithium battery anodes using silicon nanowires*, Nature Nanotechnology, **3**(1), 31–35 (2008).
- [Che10] G. Chen, E. M. Gallo, J. Burger, B. Nabet, A. Cola, P. Prete, N. Lovergne, and J. E. Spanier, *On direct-writing methods for electrically contacting GaAs and Ge nanowire devices*, Applied Physics Letters, **96**(22), 223107 (2010).
- [Ci10] L. Ci, L. Song, C. Jin, D. Jariwala, D. Wu, Y. Li, A. Srivastava, Z. F. Wang, K. Storr, L. Balicas, F. Liu, and P. M. Ajayan, *Atomic layers of hybridized boron nitride and graphene domains*, Nature Materials, **9**, 430–435 (2010).
- [Col97] P. G. Collins, A. Zettl, H. Bando, A. Thess, and R. E. Smalley, *Nanotube Nanodevice*, Science, **278**(5335), 100–102 (1997).
- [Col08] C. Colombo, D. Spirkoska, M. Frimmer, G. Abstreiter, and A. Fontcuberta I Morral, *Ga-assisted catalyst-free growth mechanism of GaAs nanowires by molecular beam epitaxy*, Phys. Rev. B, **77**(15), 155326 (2008).
- [Col09] C. Colombo, M. Heiß, M. Grätzel, and A. Fontcuberta I Morral, *Gallium arsenide p-i-n radial structures for photovoltaic applications*, Applied Physics Letters, **94**(17), 173108 (2009).
- [COM07] COMSOL Multiphysics GmbH, Göttingen, Germany, *COMSOL Multiphysics*, version 3.4 (2007).
- [Coo85] D. E. Cooper, *Picosecond optoelectronic measurement of microstrip dispersion*, Applied Physics Letters, **47**, 33–35 (1985).
- [Cor88] P. B. Corkum, F. Brunel, N. K. Sherman, and T. Srinivasan-Rao, *Thermal Response of Metals to Ultrashort-Pulse Laser Excitation*, Phys. Rev. Lett., **61**(25), 2886–2889 (1988).
- [Cui01] Y. Cui and C. M. Lieber, *Functional Nanoscale Electronic Devices Assembled Using Silicon Nanowire Building Blocks*, Science, **291**, 851–854 (2001).
- [Cut69] M. Cutler and N. F. Mott, *Observation of Anderson Localization in an Electron Gas*, Physical Review, **181**, 1336–1340 (1969).
- [Daw08] J. M. Dawlaty, S. Shivaraman, M. Chandrashekhar, F. Rana, and M. G. Spencer, *Measurement of ultrafast carrier dynamics in epitaxial graphene*, Applied Physics Letters, **92**(4), 042116 (2008).

- [de 03] S. de Franceschi, J. A. van Dam, E. P. A. M. Bakkers, L. F. Feiner, L. Gurevich, and L. P. Kouwenhoven, *Single-electron tunneling in InP nanowires*, Applied Physics Letters, **83**, 344 (2003).
- [Des09] V. V. Deshpande, S. Hsieh, A. W. Bushmaker, M. Bockrath, and S. B. Cronin, *Spatially Resolved Temperature Measurements of Electrically Heated Carbon Nanotubes*, Physical Review Letters, **102**(10), 105501 (2009).
- [Dic04] K. A. Dick, K. Deppert, M. W. Larsson, T. Mårtensson, W. Seifert, L. R. Wallenberg, and L. Samuelson, *Synthesis of branched 'nanotrees' by controlled seeding of multiple branching events*, Nature Materials, **3**, 380–384 (2004).
- [Doa87] F. E. Doany, D. Grischkowsky, and C.-C. Chi, *Carrier lifetime versus ion-implantation dose in silicon on sapphire*, Applied Physics Letters, **50**, 460–462 (1987).
- [Dra07] D. Dragoman and M. Dragoman, *Giant thermoelectric effect in graphene*, Applied Physics Letters, **91**(20), 203116 (2007).
- [Dre05] M. S. Dresselhaus, G. Dresselhaus, R. Saito, and A. Jorio, *Raman spectroscopy of carbon nanotubes*, Physics Reports, **409**, 47–99 (2005).
- [Dre07] M. S. Dresselhaus, G. Dresselhaus, R. Saito, and A. Jorio, *Exciton photo-physics of carbon nanotubes*, ANNUAL REVIEW OF PHYSICAL CHEMISTRY, **58**, 719–747 (2007).
- [Dre10] M. S. Dresselhaus, A. Jorio, M. Hofmann, G. Dresselhaus, and R. Saito, *Perspectives on Carbon Nanotubes and Graphene Raman Spectroscopy*, Nano Letters, **10**, 751–758 (2010).
- [Dub11] A. A. Dubinov, V. Y. Aleshkin, V. Mitin, T. Otsuji, and V. Ryzhii, *Terahertz surface plasmons in optically pumped graphene structures*, Journal of Physics: Condensed Matter, **23**(14), 145302 (2011).
- [Duf10] J. Dufouleur, C. Colombo, T. Garma, B. Ketterer, E. Uccelli, M. Nicotra, and A. Fontcuberta I Morral, *P-Doping Mechanisms in Catalyst-Free Gallium Arsenide Nanowires*, Nano Letters, **10**, 1734–1740 (2010).
- [Dun94] G. M. Dunn, A. B. Walker, J. H. Jefferson, and D. C. Herbert, *Monte Carlo simulation of GaAs optically activated switches*, Semiconductor Science Technology, **9**, 2116–2122 (1994).

Bibliography

- [Dun96] G. M. Dunn, A. B. Walker, A. J. Vickers, and V. R. Wicks, *Transient response of photodetectors*, Journal of Applied Physics, **79**, 7329–7338 (1996).
- [Ees86] G. L. Eesley, *Generation of nonequilibrium electron and lattice temperatures in copper by picosecond laser pulses*, Phys. Rev. B, **33**, 2144–2151 (1986).
- [End97] M. Endo, S. Iijima, and M.S. Dresselhaus, *Carbon Nanotubes (Carbon , Vol 33)*. Pergamon, (1997).
- [Fan92] W. S. Fann, R. Storz, H. W. K. Tom, and J. Bokor, *Electron thermalization in gold*, Phys. Rev. B, **46**, 13592–13595 (1992).
- [Fel09] B. E. Feldman, J. Martin, and A. Yacoby, *Broken-symmetry states and divergent resistance in suspended bilayer graphene*, Nature Physics, **5**, 889–893 (2009).
- [Fer06] A. C. Ferrari, J. C. Meyer, V. Scardaci, C. Casiraghi, M. Lazzeri, F. Mauri, S. Piscanec, D. Jiang, K. S. Novoselov, S. Roth, and A. K. Geim, *Raman Spectrum of Graphene and Graphene Layers*, Physical Review Letters, **97**(18), 187401 (2006).
- [Fon08] A. Fontcuberta I Morral, C. Colombo, G. Abstreiter, J. Arbiol, and J. R. Morante, *Nucleation mechanism of gallium-assisted molecular beam epitaxy growth of gallium arsenide nanowires*, Applied Physics Letters, **92**(6), 063112 (2008).
- [Fra91] M. Y. Frankel, S. Gupta, J. A. Valdmanis, and G. A. Mourou, *Terahertz attenuation and dispersion characteristics of coplanar transmission lines*, IEEE Transactions on Microwave Theory Techniques, **39**, 910–916 (1991).
- [Fre03] M. Freitag, Y. Martin, J. A. Misewich, R. Martel, and P. Avouris, *Photoconductivity of Single Carbon Nanotubes*, Nano Letters, **3**, 1067–1071 (2003).
- [Gae07] A. Gaertner, L. Prechtel, D. Schuh, A. W. Holleitner, and J. P. Kotthaus, *Micropatterned electrostatic traps for indirect excitons in coupled GaAs quantum wells*, Phys. Rev. B, **76**(8), 085304 (2007).
- [Gal11] E. M. Gallo, G. Chen, M. Currie, T. McGuckin, P. Prete, N. Lovergne, B. Nabet, and J. E. Spanier, *Picosecond response times in GaAs/AlGaAs core/shell nanowire-based photodetectors*, Applied Physics Letters, **98**(24), 241113 (2011).
- [Gei07] A. K. Geim and K. S. Novoselov, *The rise of graphene*, Nature Materials, **6**, 183–191 (2007).

- [Geo08] P. A. George, J. Strait, J. Dawlaty, S. Shivaraman, M. Chandrashekhar, F. Rana, and M. G. Spencer, *Ultrafast Optical-Pump Terahertz-Probe Spectroscopy of the Carrier Relaxation and Recombination Dynamics in Epitaxial Graphene*, Nano Letters, **8**, 4248–4251 (2008).
- [Gli08] Y. D. Glinka, D. Maryenko, and J. H. Smet, *Thickness-tunable terahertz plasma oscillations in a semiconductor slab excited by femtosecond optical pulses*, Phys. Rev. B, **78**(3), 035328 (2008).
- [Gre03] I. S. Gregory, C. Baker, W. R. Tribe, M. J. Evans, H. E. Beere, E. H. Linfield, A. G. Davies, and M. Missous, *High resistivity annealed low-temperature GaAs with 100 fs lifetimes*, Applied Physics Letters, **83**, 4199 (2003).
- [Gri87] D. Grischkowsky, I. N. Duling, III, J. C. Chen, and C.-C. Chi, *Electromagnetic shock waves from transmission lines*, Physical Review Letters, **59**, 1663–1666 (1987).
- [Gri90] D. R. Grischkowsky, S. R. Keiding, M. P. van Exter, and C. Fattinger, *Far-infrared time-domain spectroscopy with terahertz beams of dielectrics and semiconductors*, Journal of the Optical Society of America B Optical Physics, **7**, 2006–2015 (1990).
- [Gri00] D.R. Grischkowsky, *Optoelectronic characterization of transmission lines and waveguides by terahertz time-domain spectroscopy*, Selected Topics in Quantum Electronics, IEEE Journal of, **6**(6), 1122 –1135 (2000).
- [Gro11] K. L. Grosse, M.-H. Bae, F. Lian, E. Pop, and W. P. King, *Nanoscale Joule heating, Peltier cooling and current crowding at graphene-metal contacts*, Nature Nanotechnology, **6**(5), 287–290 (2011).
- [Gu05] Y. Gu, E.-S. Kwak, J. L. Lensch, J. E. Allen, T. W. Odom, and L. J. Lauhon, *Near-field scanning photocurrent microscopy of a nanowire photodetector*, Applied Physics Letters, **87**(4), 043111 (2005).
- [Gun63] J. Gunn, *Microwave oscillations of current in III V semiconductors*, Solid State Communications, **1**, 88–91 (1963).
- [Gup96] K. C. Gupta, R. Garg, and I. J. Bahl, *Microstrip Lines and Slotlines*, volume 2nd edition. Artech House Publishers, (1996).
- [Hag05] A. Hagen, M. Steiner, M. B. Raschke, C. Lienau, T. Hertel, H. Qian, A. J. Meixner, and A. Hartschuh, *Exponential Decay Lifetimes of Excitons in Individual Single-Walled Carbon Nanotubes*, Physical Review Letters, **95**(19), 197401 (2005).

Bibliography

- [Han07] M. Y. Han, B. Özyilmaz, Y. Zhang, and P. Kim, *Energy Band-Gap Engineering of Graphene Nanoribbons*, Physical Review Letters, **98**(20), 206805 (2007).
- [Har93] E. S. Harmon, M. R. Melloch, J. M. Woodall, D. D. Nolte, N. Otsuka, and C. L. Chang, *Carrier lifetime versus anneal in low temperature growth GaAs*, Applied Physics Letters, **63**, 2248–2250 (1993).
- [Has86] G. Hasnain, J. R. Whinnery, and A. Dienes, *Dispersion of picosecond pulses in coplanar transmission lines*, IEEE Transactions on Microwave Theory Techniques, **34**, 738–741 (1986).
- [Has90] G. Hasnain, K. W. Goossen, and W. H. Knox, *Effect of optical phonons on femtosecond pulse propagation in coplanar striplines*, Applied Physics Letters, **56**, 515–517 (1990).
- [Hay06] O. Hayden, R. Agarwal, and C. M. Lieber, *Nanoscale avalanche photodiodes for highly sensitive and spatially resolved photon detection*, Nature Materials, **5**, 352–356 (2006).
- [Hoc08] A. I. Hochbaum, R. Chen, R. D. Delgado, W. Liang, E. C. Garnett, M. Najar, A. Majumdar, and P. Yang, *Enhanced thermoelectric performance of rough silicon nanowires*, Nature, **451**, 163–167 (2008).
- [Hof08] K.-D. Hof, C. Rossler, S. Manus, J. P. Kotthaus, A. W. Holleitner, D. Schuh, and W. Wegscheider, *Dynamic photoconductive gain effect in shallow-etched AlGaAs/GaAs quantum wires*, Phys. Rev. B, **78**(11), 115325 (2008).
- [Hu94] B. B. Hu, A. S. Weling, D. H. Auston, A. V. Kuznetsov, and C. J. Stanton, *dc-electric-field dependence of THz radiation induced by femtosecond optical excitation of bulk GaAs*, Phys. Rev. B, **49**, 2234–2237 (1994).
- [Hua04] L. Huang, H. N. Pedrosa, and T. D. Krauss, *Ultrafast Ground-State Recovery of Single-Walled Carbon Nanotubes*, Physical Review Letters, **93**(1), 017403 (2004).
- [Hua10] L. Huang, G. V. Hartland, L.-Q. Chu, Luxmi, R. M. Feenstra, C. Lian, K. Tahy, and H. Xing, *Ultrafast Transient Absorption Microscopy Studies of Carrier Dynamics in Epitaxial Graphene*, Nano Letters, **10**, 1308–1313 (2010).
- [Hwa07] E. H. Hwang and S. Das Sarma, *Dielectric function, screening, and plasmons in two-dimensional graphene*, Physical Review B, **75**(20), 205418 (2007).

- [Hwa09] E. H. Hwang, E. Rossi, and S. Das Sarma, *Theory of thermopower in two-dimensional graphene*, Phys. Rev. B, **80**(23), 235415 (2009).
- [Itk06] M. E. Itkis, F. Borondics, A. Yu, and R. C. Haddon, *Bolometric Infrared Photoresponse of Suspended Single-Walled Carbon Nanotube Films*, Science, **312**, 413–416 (2006).
- [Jav04] A. Javey, J. Guo, M. Paulsson, Q. Wang, D. Mann, M. Lundstrom, and H. Dai, *High-Field Quasiballistic Transport in Short Carbon Nanotubes*, Physical Review Letters, **92**(10), 106804 (2004).
- [Jor01] A. Jorio, R. Saito, J. H. Hafner, C. M. Lieber, M. Hunter, T. McClure, G. Dresselhaus, and M. S. Dresselhaus, *Structural (n, m) Determination of Isolated Single-Wall Carbon Nanotubes by Resonant Raman Scattering*, Physical Review Letters, **86**, 1118–1121 (2001).
- [Jor08] A. Jorio, G. Dresselhaus, and Eds. Dresselhaus, M. S., *Carbon Nanotubes*. Springer: Berlin, Heidelberg, (2008).
- [Kai98] A. B. Kaiser, G. Düsberg, and S. Roth, *Heterogeneous model for conduction in carbon nanotubes*, Phys. Rev. B, **57**, 1418–1421 (1998).
- [Kan98] A. P. Kanavin, I. V. Smetanin, V. A. Isakov, Y. V. Afanasiev, B. N. Chichkov, B. Wellegehausen, S. Nolte, C. Momma, and A. Tünnermann, *Heat transport in metals irradiated by ultrashort laser pulses*, Phys. Rev. B, **57**, 14698–14703 (1998).
- [Kan08] A. P. Kanavin and S. A. Uryupin, *Nonlocal heat transfer in nanostructures*, PHYSICS LETTERS A, **372**(12), 2069–2072 (2008).
- [Kan09] S. M. Kaniber, L. Song, J. P. Kotthaus, and A. W. Holleitner, *Photocurrent properties of freely suspended carbon nanotubes under uniaxial strain*, Applied Physics Letters, **94**(26), 261106 (2009).
- [Kar11] H. Karasawa, T. Komori, T. Watanabe, A. Satou, H. Fukidome, M. Suemitsu, V. Ryzhii, and T. Otsuji, *Observation of Amplified Stimulated Terahertz Emission from Optically Pumped Heteroepitaxial Graphene-on-Silicon Materials*, Journal of Infrared, Millimeter and Terahertz Waves, **32**, 655–665 (2011), 10.1007/s10762-010-9677-1.
- [Kat99] H. Kataura, Y. Kumazawa, Y. Maniwa, I. Umezu, S. Suzuki, Y. Ohtsuka, and Y. Achiba, *Optical properties of single-wall carbon nanotubes*, Synthetic Metals, **103**(1-3), 2555–2558 (1999).

Bibliography

- [Kei92] U. D. Keil and D. R. Dykaar, *Electro-optic sampling and carrier dynamics at zero propagation distance*, Applied Physics Letters, **61**, 1504–1506 (1992).
- [Ker97] R. Kersting, K. Unterrainer, G. Strasser, H. F. Kauffmann, and E. Gornik, *Few-Cycle THz Emission from Cold Plasma Oscillations*, Physical Review Letters, **79**, 3038–3041 (1997).
- [Ket86] M. B. Ketchen, D. Grischkowsky, T. C. Chen, C.-C. Chi, and I. N. Duling, *Generation of subpicosecond electrical pulses on coplanar transmission lines*, Applied Physics Letters, **48**, 751–753 (1986).
- [Kim09] K. S. Kim, Y. Zhao, H. Jang, S. Y. Lee, J. M. Kim, K. S. Kim, J.-H. Ahn, P. Kim, J.-Y. Choi, and B. H. Hong, *Large-scale pattern growth of graphene films for stretchable transparent electrodes*, Nature, **457**(7230), 706–710 (2009).
- [Kin02] H. Kind, H. Yan, B. Messer, M. Law, and P. Yang, *Nanowire Ultraviolet Photodetectors and Optical Switches*, Advanced Materials, **14**(2), 158–160 (2002).
- [Kit95] C. Kittel, *Introduction to Solid State Physics*. Wiley, 5th edition, (1995).
- [Kli00] G. Klimeck, R. C. Bowen, T. B. Boykin, and T. A. Cwik, *sp₃s^{*} Tight-binding parameters for transport simulations in compound semiconductors*, Superlattices and Microstructures, **27**(5-6), 519 – 524 (2000).
- [Koi99] Y. Koide, T. Maeda, T. Kawakami, S. Fujita, T. Uemura, N. Shibata, and M. Murakami, *Effects of annealing in an oxygen ambient on electrical properties of ohmic contacts to p-type GaN*, Journal of Electronic Materials, **28**, 341–346 (1999).
- [Kro89] D. Kroekel, D. Grischkowsky, and M. B. Ketchen, *Subpicosecond electrical pulse generation using photoconductive switches with long carrier lifetimes*, Applied Physics Letters, **54**, 1046–1047 (1989).
- [Lau02] L. J. Lauhon, M. S. Gudiksen, D. Wang, and C. M. Lieber, *Epitaxial core-shell and core-multishell nanowire heterostructures*, Nature, **420**, 57–61 (2002).
- [Lee08] E. J. H. Lee, K. Balasubramanian, R. T. Weitz, M. Burghard, and K. Kern, *Contact and edge effects in graphene devices*, Nature Nanotechnology, **3**, 486–490 (2008).

- [Lei00] A. Leitenstorfer, S. Hunsche, J. Shah, M. C. Nuss, and W. H. Knox, *Femtosecond high-field transport in compound semiconductors*, Phys. Rev. B, **61**, 16642–16652 (2000).
- [Lok99] H. S. Loka, *Influence of material growth and annealing conditions on recombination processes in low-temperature-grown GaAs*, Optics Communications, **161**, 232–235 (1999).
- [Ma04] Y.-Z. Ma, J. Stenger, J. Zimmermann, S. M. Bachilo, R. E. Smalley, R. B. Weisman, and G. R. Fleming, *Ultrafast carrier dynamics in single-walled carbon nanotubes probed by femtosecond spectroscopy*, J. Chem. Phys., **120**, 3368–3373 (2004).
- [Mar93] J. Marciak-Kozlowska, *Wave characteristic of femtosecond heat conduction in thin films*, International Journal of Thermophysics, **14**, 593–598 (1993).
- [McG99] R. W. McGowan and D. Grischkowsky, *Experimental time-domain study of THz signals from impulse excitation of a horizontal surface dipole*, Applied Physics Letters, **74**, 1764 (1999).
- [Mey88] K. Meyer, M. Pessot, G. Mourou, R. Grondin, and S. Chamoun, *Subpicosecond photoconductivity overshoot in gallium arsenide observed by electro-optic sampling*, Applied Physics Letters, **53**, 2254–2256 (1988).
- [Mid93] A. A. Middleton and N. S. Wingreen, *Collective transport in arrays of small metallic dots*, Physical Review Letters, **71**, 3198–3201 (1993).
- [Min07] E. D. Minot, F. Kelkensberg, M. van Kouwen, J. A. van Dam, L. P. Kouwenhoven, V. Zwiller, M. T. Borgstroem, O. Wunnicke, M. A. Verheijen, and E. P. A. M. Bakkers, *Single Quantum Dot Nanowire LEDs*, Nano Letters, **7**, 367–371 (2007).
- [Moh06] A. Mohite, J.-T. Lin, G. Sumanasekera, and B. W. Alphenaar, *Field-Enhanced Photocurrent Spectroscopy of Excitonic States in Single-Wall Carbon Nanotubes*, Nano Letters, **6**, 1369–1373 (2006).
- [Moo66] A. Mooradian and G. B. Wright, *First order Raman effect in III-V compounds*, Solid State Communications, **4**, 431–434 (1966).
- [Mue09] T. Mueller, F. Xia, M. Freitag, J. Tsang, and P. Avouris, *Role of contacts in graphene transistors: A scanning photocurrent study*, Physical Review B, **79**(24), 245430 (2009).
- [Mue10] T. Mueller, F. Xia, and P. Avouris, *Graphene photodetectors for high-speed optical communications*, Nature Photonics, **4**(5), 297–301 (2010).

Bibliography

- [Mur97] B. N. Murdin, W. Heiss, C. J. G. M. Langerak, S.-C. Lee, I. Galbraith, G. Strasser, E. Gornik, M. Helm, and C. R. Pidgeon, *Direct observation of the LO phonon bottleneck in wide GaAs/Al_xAs quantum wells*, Physical Review B, **55**, 5171–5176 (1997).
- [Nai08] R. R. Nair, P. Blake, A. N. Grigorenko, K. S. Novoselov, T. J. Booth, T. Stauber, N. M. R. Peres, and A. K. Geim, *Fine Structure Constant Defines Visual Transparency of Graphene*, Science, **320**, 1308– (2008).
- [Nob11] Nobelprize.org, http://nobelprize.org/nobel_prizes/physics/laureates/, "The Nobel Prize in Physics 2010". (2011).
- [Nov04] K. S. Novoselov, A. K. Geim, S. V. Morozov, D. Jiang, Y. Zhang, S. V. Dubonos, I. V. Grigorieva, and A. A. Firsov, *Electric Field Effect in Atomically Thin Carbon Films*, Science, **306**, 666–669 (2004).
- [Nov05] K. S. Novoselov, A. K. Geim, S. V. Morozov, D. Jiang, M. I. Katsnelson, I. V. Grigorieva, S. V. Dubonos, and A. A. Firsov, *Two-dimensional gas of massless Dirac fermions in graphene*, Nature, **438**, 197–200 (2005).
- [Oro08] M. Oron-Carl and R. Krupke, *Raman Spectroscopic Evidence for Hot-Phonon Generation in Electrically Biased Carbon Nanotubes*, Physical Review Letters, **100**(12), 127401 (2008).
- [Osk10] A. F. Oskooi, D. Roundy, M. Ibanescu, P. Bermel, J. D. Joannopoulos, and S. G. Johnson, *MEEP: A flexible free-software package for electromagnetic simulations by the FDTD method*, Computer Physics Communications, **181**, 687–702 (2010).
- [Ost04] G. N. Ostojic, S. Zaric, J. Kono, M. S. Strano, V. C. Moore, R. H. Hauge, and R. E. Smalley, *Interband Recombination Dynamics in Resonantly Excited Single-Walled Carbon Nanotubes*, Physical Review Letters, **92**(11), 117402 (2004).
- [Pad86] C. A. Paddock and G. L. Eesley, *Transient thermoreflectance from thin metal films*, Journal of Applied Physics, **60**, 285–290 (1986).
- [Pad11] M. Padilla, Photocurrent dynamics of semiconducting nanowires, Diploma thesis, Walter Schottky Institut, TU München, (2011).
- [Par99] S.-G. Park, M. R. Melloch, and A. M. Weiner, *Analysis of terahertz waveforms measured by photoconductive and electrooptic sampling*, IEEE Journal of Quantum Electronics, **35**, 810–819 (1999).

- [Pem09] K. Pemasiri, M. Montazeri, R. Gass, L. M. Smith, H. E. Jackson, J. Yarrison-Rice, S. Paiman, Q. Gao, H. H. Tan, C. Jagadish, X. Zhang, and J. Zou, *Carrier Dynamics and Quantum Confinement in type II ZB-WZ InP Nanowire Homostructures*, Nano Letters, **9**, 648–654 (2009).
- [Pen08] Y. Peng, I. Luxmoore, M. D. Forster, A. G. Cullis, and B. J. Inkson, *Nanomanipulation and electrical behaviour of a single gold nanowire using in-situ SEM-FIB-nanomanipulators*, Journal of Physics Conference Series, **126**(1), 012031 (2008).
- [Per05] V. Perebeinos, J. Tersoff, and P. Avouris, *Radiative Lifetime of Excitons in Carbon Nanotubes*, Nano Letters, **5**, 2495–2499 (2005).
- [Per07] V. Perebeinos and P. Avouris, *Exciton Ionization, Franz-Keldysh, and Stark Effects in Carbon Nanotubes*, Nano Letters, **7**, 609–613 (2007).
- [Per08] V. Perebeinos and P. Avouris, *Phonon and Electronic Nonradiative Decay Mechanisms of Excitons in Carbon Nanotubes*, Physical Review Letters, **101**(5), 057401 (2008).
- [Pet87] R. L. Peterson, *Numerical study of currents and fields in a photoconductive detector*, IEEE Journal of Quantum Electronics, **23**, 1185–1192 (1987).
- [Pet06] H. Pettersson, J. Trägårdh, A. I. Persson, L. Landin, D. Hessman, and L. Samuelson, *Infrared Photodetectors in Heterostructure Nanowires*, Nano Letters, **6**, 229–232 (2006).
- [Pha90] D. S. Phatak and A. P. Defonzo, *Dispersion characteristics of optically excited coplanar striplines - Pulse propagation*, IEEE Transactions on Microwave Theory Techniques, **38**, 654–661 (1990).
- [Pre07] L. Prechtel, Zeitaufgelöste Photostrommessungen an Wellenleiter-schaltkreisen, Diplomarbeit, Ludwig-Maximilians-Universität München, Lehrstuhl für experimentelle Halbleiterphysik, J. P. Kotthaus, (2007).
- [Pre10] L. Prechtel, S. Manus, D. Schuh, W. Wegscheider, and A. W. Holleitner, *Spatially resolved ultrafast transport current in GaAs photoswitches*, Applied Physics Letters, **96**(26), 261110 (2010).
- [Pre11a] L. Prechtel, M. Padilla, N. Erhard, G. Abstreiter, A. Fontcuberta I Morral, and A. W. Holleitner, *Spatially resolved ultrafast photo-thermoelectric and transport currents in GaAs nanowires*, in preparation (2011).

Bibliography

- [Pre11b] L. Prechtel, L. Song, S. Manus, D. Schuh, W. Wegscheider, and A. W. Holleitner, *Time-Resolved Picosecond Photocurrents in Contacted Carbon Nanotubes*, Nano Letters, **11**, 269–272 (2011).
- [Pre11c] L. Prechtel, L. Song, D. Schuh, A. Pulickel, W. Wegscheider, and A. W. Holleitner, *Time-resolved ultrafast photocurrents and terahertz generation in freely suspended graphene*, to be published (2011).
- [Pur07] M. S. Purewal, B. H. Hong, A. Ravi, B. Chandra, J. Hone, and P. Kim, *Scaling of Resistance and Electron Mean Free Path of Single-Walled Carbon Nanotubes*, Physical Review Letters, **98**(18), 186808 (2007).
- [Ran08] F. Rana, *Graphene Terahertz Plasmon Oscillators*, IEEE Transactions on Nanotechnology, **7**, 91–99 (2008).
- [Ran10] F. Rana, J. H. Strait, H. Wang, and C. Manolatou, *Ultrafast Carrier Recombination and Generation Rates for Plasmon Emission and Absorption in Graphene*, ArXiv e-prints (2010).
- [Rie97] S. P. Riege, T. Kurth, F. Runkel, D. Heitmann, and K. Eberl, *Confinement potential and surface state density in deep-mesa etched quantum wires*, Applied Physics Letters, **70**, 111–113 (1997).
- [Ros08] C. Rossler, K.-D. Hof, S. Manus, S. Ludwig, J. P. Kotthaus, J. Simon, A. W. Holleitner, D. Schuh, and W. Wegscheider, *Optically induced transport properties of freely suspended semiconductor submicron channels*, Applied Physics Letters, **93**(7), 071107 (2008).
- [Rou10] F. P. Rouxinol, R. V. Gelamo, R. G. Amici, A. R. Vaz, and S. A. Moshkalev, *Low contact resistivity and strain in suspended multilayer graphene*, Applied Physics Letters, **97**(25), 253104 (2010).
- [Row05] D.M. Rowe, editor, *Thermoelectrics Handbook: Macro to Nano*. CRC Press, (2005).
- [Rut83] D. B. Rutledge, D. P. Neikirk, D. P. Kasilingham, and K. J. Button (Ed.), *Infrared and Millimeter Waves*, volume Vol. 10, PT. II. Academic, New York, (1983).
- [Rut09] C. Rutherford, D. Jain, and P. Burke, *Nanotube electronics for radiofrequency applications*, Nature Nanotechnology, **4**, 811–819 (2009).
- [Ryz07] V. Ryzhii, M. Ryzhii, and T. Otsuji, *Negative dynamic conductivity of graphene with optical pumping*, Journal of Applied Physics, **101**(8), 083114 (2007).

- [Ryz10] V. Ryzhii, A. A. Dubinov, T. Otsuji, V. Mitin, and M. S. Shur, *Terahertz lasers based on optically pumped multiple graphene structures with slot-line and dielectric waveguides*, Journal of Applied Physics, **107**(5), 054505 (2010).
- [Sam04] L. Samuelson, C. Thelander, M. T. Björk, M. Borgstroem, K. Deppert, K. A. Dick, A. E. Hansen, T. Mårtensson, N. Panev, A. I. Persson, W. Seifert, N. Sköld, M. W. Larsson, and L. R. Wallenberg, *Semiconductor nanowires for 0D and 1D physics and applications*, Physica E Low-Dimensional Systems and Nanostructures, **25**, 313–318 (2004).
- [San89] E. Sano and T. Shibata, *Mechanism of subpicosecond electrical pulse generation by asymmetric excitation*, Applied Physics Letters, **55**, 2748–2750 (1989).
- [Sch94] A. Schmeller, W. Hansen, J. P. Kotthaus, G. Tränkle, and G. Weimann, *Franz-Keldysh effect in a two-dimensional system*, Applied Physics Letters, **64**, 330–332 (1994).
- [Sha99] J. Shah, *Ultrafast Spectroscopy of Semiconductors and Semiconductor Nanostructures (Springer Series in Solid-State Sciences)*. Springer, (1999).
- [Ska06] V. Skakalova, A. B. Kaiser, Y.-S. Woo, and S. Roth, *Electronic transport in carbon nanotubes: From individual nanotubes to thin and thick networks*, Phys. Rev. B, **74**(8), 085403 (2006).
- [Slo58] J. C. Slonczewski and P. R. Weiss, *Band Structure of Graphite*, Physical Review, **109**, 272–279 (1958).
- [Smi81] P. R. Smith, D. H. Auston, W. M. Augustyniak, and A. M. Johnson, *Picosecond photoconductivity in radiation-damaged silicon-on-sapphire films*, Applied Physics Letters, **38**, 47–50 (1981).
- [Sno05] E. S. Snow, F. K. Perkins, E. J. Houser, S. C. Badescu, and T. L. Reinecke, *Chemical Detection with a Single-Walled Carbon Nanotube Capacitor*, Science, **307**, 1942–1945 (2005).
- [Sny08] G. J. Snyder and E. S. Toberer, *Complex thermoelectric materials*, Nature Materials, **7**, 105–114 (2008).
- [Soi10] M. Soini, I. Zardo, E. Uccelli, S. Funk, G. Koblmüller, A. Fontcuberta I Morral, and G. Abstreiter, *Thermal conductivity of GaAs nanowires studied by micro-Raman spectroscopy combined with laser heating*, Applied Physics Letters, **97**(26), 263107 (2010).

Bibliography

- [Son93] J. Son, W. Sha, J. Kim, T. B. Norris, J. F. Whitaker, and G. A. Mourou, *Transient velocity overshoot dynamics in GaAs for electric fields about 200 kV/cm*, Applied Physics Letters, **63**, 923–925 (1993).
- [Son06] Y.-W. Son, M. L. Cohen, and S. G. Louie, *Half-metallic graphene nanoribbons*, Nature, **444**, 347–349 (2006).
- [Son08] Li Song, Alexander W. Holleitner, Huihong Qian, Achim Hartschuh, Markus Döblinger, Eva M. Weig, and Jörg P. Kotthaus, *A Carbon Nanofilament-Bead Necklace*, The Journal of Physical Chemistry C, **112**(26), 9644–9649 (2008).
- [Spi79] W.E. Spicer, P.W. Chye, C.M. Garner, I. Lindau, and P. Pianetta, *The surface electronic structure of 3-5 compounds and the mechanism of Fermi level pinning by oxygen (passivation) and metals (Schottky barriers)*, Surface Science, **86**, 763 – 788 (1979), Proceedings of the International Conference on Solid Films and Surfaces Tokyo, Japan, 5-8 July 1978.
- [Spi09] D. Spirkoska, J. Arbiol, A. Gustafsson, S. Conesa-Boj, F. Glas, I. Zardo, M. Heigoldt, M. H. Gass, A. L. Bleloch, S. Estrade, M. Kaniber, J. Rossler, F. Peiro, J. R. Morante, G. Abstreiter, L. Samuelson, and A. Fontcuberta I Morral, *Structural and optical properties of high quality zinc-blende/wurtzite GaAs nanowire heterostructures*, Phys. Rev. B, **80**(24), 245325 (2009).
- [Sri10] Anchal Srivastava, Charudatta Galande, Lijie Ci, Li Song, Chaitra Rai, Deep Jariwala, Kevin F. Kelly, and Pulickel M. Ajayan, *Novel Liquid Precursor-Based Facile Synthesis of Large-Area Continuous, Single, and Few-Layer Graphene Films*, Chemistry of Materials, **22**(11), 3457–3461 (2010).
- [Sta06] S. Stankovich, D. A. Dikin, G. H. B. Dommett, K. M. Kohlhaas, E. J. Zimney, E. A. Stach, R. D. Piner, S. T. Nguyen, and R. S. Ruoff, *Graphene-based composite materials*, Nature, **442**, 282–286 (2006).
- [Sta09] C. Stampfer, J. Güttinger, S. Hellmüller, F. Molitor, K. Ensslin, and T. Ihn, *Energy Gaps in Etched Graphene Nanoribbons*, Physical Review Letters, **102**(5), 056403 (2009).
- [Sto10] R. J. Stoehr, R. Kolesov, J. Pflaum, and J. Wrachtrup, *Fluorescence of laser-created electron-hole plasma in graphene*, Physical Review B, **82**(12), 121408 (2010).
- [Sun93] C.-K. Sun, F. Vallée, L. Acioli, E. P. Ippen, and J. G. Fujimoto, *Femtosecond investigation of electron thermalization in gold*, Phys. Rev. B, **48**, 12365–12368 (1993).

- [Thu09a] S. Thunich, Optoelektronische Eigenschaften von GaAs-Nanodrähten, Diplomarbeit, Walter Schottky Institut, TU München, (2009).
- [Thu09b] S. Thunich, L. Prechtel, D. Spirkoska, G. Abstreiter, A. Fontcuberta I Moral, and A. W. Holleitner, *Photocurrent and photoconductance properties of a GaAs nanowire*, Applied Physics Letters, **95**(8), 083111 (2009).
- [Tia09] Tian, Bozhi, Kempa, J. Thomas, and C. M. Lieber, *Single nanowire photovoltaics*, Chem. Soc. Rev., **38**, 16–24 (2009).
- [Tse09] A. W. Tsen, L. A. K. Donev, H. Kurt, L. H. Herman, and J. Park, *Imaging the electrical conductance of individual carbon nanotubes with photothermal current microscopy*, Nature Nanotechnology, **4**, 108–113 (2009).
- [van88] M. van Exter and A. Lagendijk, *Ultrashort surface-plasmon and phonon dynamics*, Physical Review Letters, **60**, 49–52 (1988).
- [Veg86] R. L. Veghte and C. A. Balanis, *Dispersion of transient signals in microstrip transmission lines*, IEEE Transactions on Microwave Theory Techniques, **34**, 1427–1436 (1986).
- [Vog83] P. Vogl, H. P. Hjalmarson, and J. D. Dow, *A Semi-empirical tight-binding theory of the electronic structure of semiconductors*, Journal of Physics and Chemistry of Solids, **44**(5), 365 – 378 (1983).
- [Wal47] P. R. Wallace, *The Band Theory of Graphite*, Physical Review, **71**, 622–634 (1947).
- [Wan01] J. Wang, M. S. Gudiksen, X. Duan, Y. Cui, and C. M. Lieber, *Highly Polarized Photoluminescence and Photodetection from Single Indium Phosphide Nanowires*, Science, **293**, 1455–1457 (2001).
- [Wan04] F. Wang, G. Dukovic, L. E. Brus, and T. F. Heinz, *Time-Resolved Fluorescence of Carbon Nanotubes and Its Implication for Radiative Lifetimes*, Physical Review Letters, **92**(17), 177401 (2004).
- [Wan08a] F. Wang, Y. Zhang, C. Tian, C. Girit, A. Zettl, M. Crommie, and Y. R. Shen, *Gate-Variable Optical Transitions in Graphene*, Science, **320**, 206 (2008).
- [Wan08b] X. Wang, Y. Ouyang, X. Li, H. Wang, J. Guo, and H. Dai, *Room-Temperature All-Semiconducting Sub-10-nm Graphene Nanoribbon Field-Effect Transistors*, Physical Review Letters, **100**(20), 206803 (2008).

Bibliography

- [War90] A. C. Warren, J. M. Woodall, J. L. Freeouf, D. Grischkowsky, D. T. McInturff, M. R. Melloch, and N. Otsuka, *Arsenic precipitates and the semi-insulating properties of GaAs buffer layers grown by low-temperature molecular beam epitaxy*, Applied Physics Letters, **57**, 1331–1333 (1990).
- [Wei09] P. Wei, W. Bao, Y. Pu, C. N. Lau, and J. Shi, *Anomalous Thermoelectric Transport of Dirac Particles in Graphene*, Physical Review Letters, **102**(16), 166808 (2009).
- [Wil75] J. D. Wiley, R. K. (Ed.) Willardson, and A. C. (Ed.) Beer, *Semiconductors and Semimetals*, volume 10, page 91. Academic Press, N. Y., (1975).
- [Wil97] S. P. Wilson and A. B. Walker, *One- and two-dimensional models of the transient response of metal - semiconductor - metal photodetectors including diffraction*, Semiconductor Science Technology, **12**, 1265–1272 (1997).
- [Wu04] Z. Wu, Z. Chen, X. Du, J. M. Logan, J. Sippel, M. Nikolou, K. Kamaras, J. R. Reynolds, D. B. Tanner, A. F. Hebard, and A. G. Rinzler, *Transparent, Conductive Carbon Nanotube Films*, Science, **305**, 1273–1277 (2004).
- [Xia09a] F. Xia, T. Mueller, R. Golizadeh-Mojarad, M. Freitag, Y.-M. Lin, J. Tsang, V. Perebeinos, and P. Avouris, *Photocurrent Imaging and Efficient Photon Detection in a Graphene Transistor*, Nano Letters, **9**, 1039–1044 (2009).
- [Xia09b] F. Xia, T. Mueller, Y.-M. Lin, A. Valdes-Garcia, and P. Avouris, *Ultrafast graphene photodetector*, Nature Nanotechnology, **4**, 839–843 (2009).
- [Xu10] X. Xu, N. M. Gabor, J. S. Alden, A. M. van der Zande, and P. L. McEuen, *Photo-Thermoelectric Effect at a Graphene Interface Junction*, Nano Letters, **10**, 562–566 (2010).
- [Yam90] H. Yamamoto, Z.-Q. Fang, and D. C. Look, *Nonalloyed ohmic contacts on low-temperature molecular beam epitaxial GaAs: Influence of deep donor band*, Applied Physics Letters, **57**, 1537–1539 (1990).
- [Yan03] R. Yano, Y. Hirayama, S. Miyashita, N. Uesugi, and S. Uehara, *Arsenic pressure dependence of carrier lifetime and annealing dynamics for low-temperature grown GaAs studied by pump-probe spectroscopy*, Journal of Applied Physics, **94**, 3966–3971 (2003).
- [Yan08] S. Yanagi, M. Onuma, J. Kitagawa, and Y. Kadoya, *Propagation of Terahertz Pulses on Coplanar Strip-lines on Low Permittivity Substrates and a Spectroscopy Application*, Applied Physics Express, **1**(1), 012009 (2008).

- [Yao00] Z. Yao, C. L. Kane, and C. Dekker, *High-Field Electrical Transport in Single-Wall Carbon Nanotubes*, Physical Review Letters, **84**, 2941–2944 (2000).
- [Yu05] P. Y. Yu and M. Cardona, *Fundamentals of Semiconductors*. Springer, 3rd edition, (2005).
- [Zab08] A. Zabet-Khosousi and A.-A. Dhirani, *Charge Transport in Nanoparticle Assemblies*, Chemical Reviews, **108**(10), 4072–4124 (2008), PMID: 18811216.
- [Zeb09] B. Zebli, H. A. Vieyra, I. Carmeli, A. Hartschuh, J. P. Kotthaus, and A. W. Holleitner, *Optoelectronic sensitization of carbon nanotubes by CdTe nanocrystals*, Phys. Rev. B, **79**(20), 205402 (2009).
- [Zha92] X.-C. Zhang and D. H. Auston, *Optoelectronic measurement of semiconductor surfaces and interfaces with femtosecond optics*, Journal of Applied Physics, **71**, 326–338 (1992).
- [Zha05] Y. Zhang, Y.-W. Tan, H. L. Stormer, and P. Kim, *Experimental observation of the quantum Hall effect and Berry's phase in graphene*, Nature, **438**, 201–204 (2005).
- [Zha06] Z. Y. Zhang, C. H. Jin, X. L. Liang, Q. Chen, and L.-M. Peng, *Current-voltage characteristics and parameter retrieval of semiconducting nanowires*, Applied Physics Letters, **88**(7), 073102 (2006).
- [Zho95a] X. Zhou, *On the physics of femto-second electrical pulse generation in transmission-line gaps*, Optoelectronics - Devices and Technologies, **10**(4), 491–504 (1995).
- [Zho95b] X. Zhou, S. Alexandrou, and T. Y. Hsiang, *Monte Carlo investigation of the intrinsic mechanism of subpicosecond pulse generation by nonuniform illumination*, Journal of Applied Physics, **77**, 706–711 (1995).
- [Zho96] X. Zhou, *Numerical physics of subpicosecond electrical pulse generation by nonuniform gap illumination*, IEEE Journal of Quantum Electronics, **32**, 1672–1679 (1996).
- [Zho08] Z. Zhong, N. M. Gabor, J. E. Sharping, A. L. Gaeta, and P. L. McEuen, *Terahertz time-domain measurement of ballistic electron resonance in a single-walled carbon nanotube*, Nature Nanotechnology, **3**(4), 201–205 (2008).
- [Zue09] Y. M. Zuev, W. Chang, and P. Kim, *Thermoelectric and Magnetothermoelectric Transport Measurements of Graphene*, Physical Review Letters, **102**(9), 096807 (2009).

Bibliography

Acknowledgements

- First of all, I want to thank Alexander Holleitner for more than 5 years of great physics! Everything started with nextnano simulations of indirect excitons in double quantum wells. And now we are discussing thermoelectrics in nanowires. You taught me a lot, you pushed me when I needed to be pushed, and you encouraged me when I was desperate. I wish you and your family only the best for your future.
- Without Li Song this thesis would not have any C written anywhere. I hope the nano-carbon we breathed in at the CVD made its way out by now. Keep up that work! I am also thankful to Pulickel Ajayan for providing valuable help.
- I want to thank Gerhard Abstreiter and Jörg Kotthaus for providing excellent research facilities, for organizing excellent conferences, and for inspiring us students.
- I thank Dieter Schuh and Werner Wegscheider for providing us with numerous LT-GaAs wafers, even though the results needed some time.
- I thank Gregor Koblmüller and Max Bichler for growing the next generation of LT-GaAs wafers.
- Thanks to Stefan Manus and Jörg Kotthaus for great support in the beginning of the project. Stefan also helped me a lot in understanding stripline circuits.
- I thank Anna Fontcuberta i Morral for providing us with excellent nanowires.
- I thank Helmut Karl (Universität Augsburg) for the ion implantation of the silicon wafers and for his valuable help finding the right implantation parameters.
- I thank Heike Riel (IBM Zürich) for sending us $p - i - n$ silicon nanowires. Unfortunately, I didn't have enough time during my PhD to measure them.

Acknowledgments

- Many experiments in this thesis were performed in external labs. Especially Achim Hartschuh contributed a lot to my understanding of photoluminescence in carbon nanotubes. It was an honor to measure together with the *munich-god-of-carbon-nanotubes*.
- The Raman measurements were performed with Ilaria Zardo and Martin Soini in the labs of Gerhard Abstreiter. Thanks a lot!
- I also thank Jon Finley and the Jon-boys, especially Arne Laucht, Michael Kaniber and Daniel Rudolph for measuring with me in their labs.
- I thank Dirk Grundler, Georg Dürr and Sebastian Neusser for their help and support with high-frequency electrical measurements.
- I thank Peter Vogl both for keeping the Mac-community at the WSI alive, as well as for fascinating discussions about physics.
- I thank Peter Weiser for his important work at the ZNN. Without him, we would still use the upper technology. I also thank Hubert Riedl, Max Bichler and Sonja Matich for their helpfulness and support.
- Thanks to Claudia Paulus for producing an infinite amount of excellent optical masks, and for keeping the OT running!
- Thanks to Fritz Sedlmeir and Wolfgang Bendak for their excellent work in the machine shop.
- I thank Irmgard Neuner, Sonja Kraus and Liane Lindner. They are the heart of the WSI & ZNN!
- I thank Stefan Birner for his valuable nextnano support.
- I thank Gerhard Abstreiter and Ulrich Rant for access to their laboratory facilities.
- I thank Vito Dantona for valuable help in the frequency domain.
- I thank Maki Hideyuki and his family. I am still waiting for that letter from your son! Is it in german or english?
- I thank Markus Stallhofer and Max Seifert for a great atmosphere in our group. I enjoyed the discussions and the beer with you!
- Thanks to my (former) colleagues Andi Gärtner, Klaus-Dieter Hof, Xaver Vögele, Simone Kaniber, Jens Repp, Nadine Erhard, Andreas Brenneis, Christoph Kastl, Selcuk Zorlu, Marcel Brändlein and Martin Schwarz.

- I thank Frederik Hetsch and Rebecca Saive for valuable supervision experience.
- I thank Markus Mangold and Sebastian Thunich for being good colleagues and very good friends.
- I thank Milan Padilla for being an excellent diploma student. It was a pleasure working with you. I hope you will find a PhD project that you like as much as the one you didn't want.
- I thank Alex Schwemer and Markus Schuster for drinking coffee, for conversations about the important things in life (rocks and snow), and for being very good friends.
- I thank Sara and Luciano for one entire weekend of proof-reading. I also thank Sara for being more a friend than a roommate and colleague.
- Thanks to Christoph Hohmann at NIM for that extremely nice movie explaining the measurement principle. The movie also ended up on the cover of this thesis!
- Thanks to Ilaria who organized the party after my PhD defense. Thanks to my mother, Philipp, Sara, Beni, Sonja Kraus, Markus Schuster, Markus Mangold, Alex Schwemer and everybody else who helped.
- I thank my parents for supporting me during my university career, for providing a place where I feel at home, and for being wonderful (grand-) parents.
- Thanks to Katrin & Schüssel and Agnes & Ralf! You are not only my sisters and brothers-in-law, but also very good friends. Being with you and your families shows me that there are more important things in life than snow and work.
- Grazie a Rita, Francesco e Mauro per dare il benarrivato a me.
- Finally, I thank Ilaria. Every morning she opened the door for me and my bike, then she measured with me. She contributed to this thesis not only with measurements and discussions, but she also pushed, encouraged, and supported me. Without you, this thesis wouldn't be what it is. But more importantly, I wouldn't be who I am now. Grazie per una vita con il mio amore!

Acknowledgments

In der Schriftenreihe des Walter Schottky Instituts der Technischen Universität München sind bisher folgende Bände erschienen:

Vol. 1
Cornelia Engel
Si/SiGe basierende Phototransistoren
131 Seiten
ISBN 3-932749-01-4

Vol. 7
Markus Sexl
Verspannte und gitterrelaxierte In(GaAl)As Heterostrukturen
144 Seiten
ISBN 3-932749-07-3

Vol. 2
Peter Schittenhelm
Selbst-Organisation und Selbst-Ordnung in Si/SiGe-Heterostrukturen
151 Seiten
ISBN 3-932749-02-2

Vol. 8
Christian Obermüller
Photolumineszenzspektroskopie mit optischen Nahfeldmethoden an GaAs-Nanostrukturen
140 Seiten
ISBN 3-932749-08-1

Vol. 3
Andreas Nutsch
Selektive Epitaxie von (GaIn)(AsP) Schichtstrukturen
129 Seiten
ISBN 3-932749-03-0

Vol. 9
Edilson Silveira
Inelastische Lichtstreuung an niedrig-dimensionalen Halbleiterstrukturen
104 Seiten
ISBN 3-932749-09-X

Vol. 4
Peter Baumgartner
Optische und elektronische Eigenschaften lasergeschriebener GaAs-Nanostrukturen
180 Seiten
ISBN 3-932749-04-9

Vol. 10
Eberhard Christian Rohrer
Photoleitungs-Spektroskopie von Diamant
153 Seiten
ISBN 3-932749-10-03

Vol. 5
Walter Franz Rieger
Untersuchung der elektronischen und strukturellen Eigenschaften von GaNAlN und deren Legierungen
158 Seiten
ISBN 3-932749-05-7

Vol. 11
Thomas Wimbauer
Magnetische Resonanz-Untersuchungen an modernen Halbleitermaterialien
125 Seiten
ISBN 3-932749-11-1

Vol. 6
Markus Hauser
Oberflächenemittierende Laserdioden mit Mehrfachepitaxie
148 Seiten
ISBN 3-932749-06-5

Vol. 12
Herbert Verhoeven
Thermische Eigenschaften von CVD-Diamantschichten
154 Seiten
ISBN 3-932749-12-X

- Vol. 13
Hans-Christoph Ostendorf
Trennung von Volumen- und Oberflächenrekombination in Silizium
128 Seiten
ISBN 3-932749-13-8
- Vol. 14
Martin Städele
Dichtefunktionaltheorie mit exaktem Austausch für Halbleiter
202 Seiten
ISBN 3-932749-14-6
- Vol. 15
Helmut Angerer
Herstellung von Gruppe III-Nitriden mit Molekularstrahlepitaxie
144 Seiten
ISBN 3-932749-15-4
- Vol. 16
Wolfgang Heller
Spektroskopie einzelner Quantenpunkte in magnetischen und elektrischen Feldern
128 Seiten
ISBN 3-932749-16-2
- Vol. 17
Molela Moukara
Pseudopotentiale mit exaktem Austausch
117 Seiten
ISBN 3-932749-17-0
- Vol. 18
Ralph Oberhuber
Elektronische Struktur und Transport in verspannten Halbleiterschichtsystemen
110 Seiten
ISBN 3-932749-18-9
- Vol. 19
Reiner Pech
High-Energy Boron-Implantation into Different Silicon Substrates
158 Seiten
ISBN 3-932749-19-7
- Vol. 20
Christoph Martin Engelhardt
Zyklotronresonanz zweidimensionaler Ladungsträgersysteme in Halbleitern, Effekte der Elektron-Elektron-Wechselwirkung und Lokalisierung
317 Seiten
ISBN 3-932749-20-0
- Vol. 21
Eduard Neufeld
Erbium-dotierte Si/SiGe-Lichemitter und -Wellenleiter
136 Seiten
ISBN 3-932749-21-9
- Vol. 22
Gert Schedelbeck
Optische Eigenschaften von Halbleiter-nanostrukturen hergestellt durch Überwachsen von Spaltflächen
154 Seiten
ISBN 3-932749-22-7
- Vol. 23
Jürgen Zimmer
Optoelektronisches Verhalten von Dünnschichtbauelementen aus amorphem und mikrokristallinem Silizium
171 Seiten
ISBN 3-932749-23-5
- Vol. 24
Berthold Schmidt
Leistungsoptimierung abstimmbarer InGaAsP/InP Halbleiterlaser
85 Seiten
ISBN 3-932749-24-3
- Vol. 25
Jianhong Zhu
Ordering of self-assembled Ge and SiGe nanostructures on vicinal Si surfaces
120 Seiten
ISBN 3-932749-25-1

- Vol. 26
 Gerhard Groos
Herstellung und Charakterisierung von Silizium-Nanostrukturen
 168 Seiten
 ISBN 3-932749-26-X
- Vol. 27
 Uwe Hansen
Theorie der Reaktionskinetik an Festkörperoberflächen
 119 Seiten
 ISBN 3-932749-27-8
- Vol. 28
 Roman Dimitrov
Herstellung und Charakterisierung von AlGaN/GaN-Transistoren
 196 Seiten
 ISBN 3-932749-28-6
- Vol. 29
 Martin Eickhoff
Piezowiderstandsmechanismen in Halbleitern mit großer Bandlücke
 151 Seiten
 ISBN 3-932749-29-4
- Vol. 30
 Nikolai Wieser
Ramanspektroskopie an Gruppe III-Nitriden
 161 Seiten
 ISBN 3-932749-30-8
- Vol. 31
 Rainer Janssen
Strukturelle und elektronische Eigenschaften amorpher Silizium-Suboxide
 275 Seiten
 ISBN 3-932749-31-6
- Vol. 32
 Martin W. Bayerl
Magnetic resonance investigations of group III-nitrides
 155 Seiten
 ISBN 3-932749-32-4
- Vol. 33
 Martin Rother
Elektronische Eigenschaften von Halbleiternanostrukturen hergestellt durch Überwachsen von Spaltflächen
 196 Seiten
 ISBN 3-932749-33-2
- Vol. 34
 Frank Findeis
Optical spectroscopy on single self-assembled quantum dots
 156 Seiten
 ISBN 3-932749-34-0
- Vol. 35
 Markus Ortsiefer
Langwellige Vertikalresonator-Laserdioden im Materialsystem InGaAlAs/InP
 152 Seiten
 ISBN 3-932749-35-9
- Vol. 36
 Roland Zeisel
Optoelectronic properties of defects in diamond and AlGaN alloys
 140 Seiten
 ISBN 3-932749-36-7
- Vol. 37
 Liwen Chu
Inter- und Intraband Spektroskopie an selbstorganisierten In(Ga)As/GaAs Quantenpunkten
 124 Seiten
 ISBN 3-932749-37-5
- Vol. 38
 Christian Alexander Miesner
Intra-Valenzbandspektroskopie an SiGe-Nanostrukturen in Si
 100 Seiten
 ISBN 3-932749-38-3
- Vol. 39
 Szabolcs Kátai
Investigation of the nucleation process of chemical vapour deposited diamond films
 178 Seiten
 ISBN 3-932749-39-1

Vol. 40
Markus Arzberger
Wachstum, Eigenschaften und Anwendungen selbstorganisierter InAs-Quantenpunkte
236 Seiten
ISBN 3-932749-40-5

Vol. 41
Markus Oliver Markmann
Optische Eigenschaften von Erbium in Si/Si_{1-x}C_x, Si/Si_{1-x}Ge_x und Si/SiO_x Heterostrukturen
182 Seiten
ISBN 3-932749-41-3

Vol. 42
Rainer Alexander Deutschmann
Two dimensional electron systems in atomically precise periodic potential
210 Seiten
ISBN 3-932749-42-1

Vol. 43
Uwe Karrer
Schottky-Dioden auf Galliumnitrid: Eigenschaften und Anwendungen in der Sensorik
182 Seiten
ISBN 3-932749-43-X

Vol. 44
Günther Anton Johann Vogg
Epitaxial thin films of Si and Ge based Zintl phases and sheet polymers
169 Seiten
ISBN 3-932749-44-8

Vol. 45
Christian Strahberger
Vertikaler Transport und extreme Magnetfelder in Halbleitern
167 Seiten
ISBN 3-932749-45-6

Vol. 46
Jan Schalwig
Feldeffekt-Gassensoren und ihre Anwendung in Abgas-nachbehandlungssystemen
125 Seiten
ISBN 3-932749-46-4

Vol. 47
Christopher Eisele
Novel absorber structures for Si-based thin film solar cells
126 Seiten
ISBN 3-932749-47-2

Vol. 48
Stefan Hackenbuchner
Elektronische Struktur von Halbleiter-Nanobauelementen im thermodynamischen Nichtgleichgewicht
213 Seiten
ISBN 3-932749-48-0

Vol. 49
Andreas Sticht
Herstellung und Charakterisierung von dünnen Silizium/Siliziumoxid-Schichtsystemen
166 Seiten
ISBN 3-932749-49-9

Vol. 50
Giuseppe Scarpa
Design and fabrication of Quantum Cascade Lasers
193 Seiten
ISBN 3-932749-50-2

Vol. 51
Jörg Frankenberger
Optische Untersuchungen an zweidimensionalen Ladungsträgersystemen
158 Seiten
ISBN 3-932749-51-0

- Vol. 52
Doris Heinrich
Wavelength selective optically induced charge storage in self-assembled semiconductor quantum dots
144 Seiten
ISBN 3-932749-52-9
- Vol. 53
Nicolaus Ulbrich
Entwurf und Charakterisierung von Quanten-Kaskadenlasern und Quantenpunkt-kaskaden
133 Seiten
ISBN 3-932749-53-7
- Vol. 54
Lutz Carsten Görgens
Analyse stickstoffhaltiger III-V Halbleiter-Heterosysteme mit hochenergetischen schweren Ionen
116 Seiten
ISBN 3-932749-54-5
- Vol. 55
Andreas Janotta
Doping, light-induced modification and biocompatibility of amorphous silicon suboxides
180 Seiten
ISBN 3-932749-55-3
- Vol. 56
Sebastian Tobias Benedikt Gönnenwein
Two-dimensional electron gases and ferromagnetic semiconductors: materials for spintronics
198 Seiten
ISBN 3-932749-56-1
- Vol. 57
Evelin Beham
Photostromspektroskopie an einzelnen Quantenpunkten
186 Seiten
ISBN 3-932749-57-X
- Vol. 58
Po-Wen Chiu
Towards carbon nanotube-based molecular electronics
116 Seiten
ISBN 3-932749-58-8
- Vol. 59
Tobias Graf
Spin-spin interactions of localized electronic states in semiconductors
194 Seiten
ISBN 3-932749-59-6
- Vol. 60
Stefan Klein
Microcrystalline silicon prepared by hot wire CVD: preparation and characterisation of material and solar cells
157 Seiten
ISBN 3-932749-60-X
- Vol. 61
Markus Krach
Frequenzverdreifacher mit Anti-Serielllem Schottky-Varaktor für den Terahertz-bereich
156 Seiten
ISBN 3-932749-61-8
- Vol. 62
Ralph Thomas Neuberger
AlGaN/GaN-Heterostrukturen als chemische Sensoren in korrosiven Medien
153 Seiten
ISBN 3-932749-62-6
- Vol. 63
Sonia Perna
Wasserstoff-Passivierung von trikristallinem Silizium durch hydrogenisiertes Siliziumnitrid
136 Seiten
ISBN 3-932749-63-4

- Vol. 64
 Oliver Schumann
Einfluss von Stickstoff auf das Wachstum und die Eigenschaften von InAs-Quantenpunkten
 148 Seiten
 ISBN 3-932749-64-2
- Vol. 65
 Gerhard Rösel
Entwicklung und Charakterisierung von Typ-II-Heterostrukturen für die Abstimmregion in abstimmbaren Laserdioden
 101 Seiten
 ISBN 3-932749-65-0
- Vol. 66
 Angela Link
Zweidimensionale Elektronen- und Löcher-Gase in GaN/AlGaN Heterostrukturen
 156 Seiten
 ISBN 3-932749-66-9
- Vol. 67
 Matthias Sabathil
Opto-electronic and quantum transport properties of semiconductor nanostructures
 156 Seiten
 ISBN 3-932749-67-7
- Vol. 68
 Frank Fischer
Growth and electronic properties of two-dimensional systems on (110) oriented GaAs
 139 Seiten
 ISBN 3-932749-68-5
- Vol. 69
 Robert Shau
Langwellige oberflächenemittierende Laserdioden mit hoher Ausgangsleistung und Modulationsbandbreite
 198 Seiten
 ISBN 3-932749-69-3
- Vol. 70
 Andrea Baumer
Structural and electronic properties of hydrosilylated silicon surfaces
 163 Seiten
 ISBN 3-932749-70-7
- Vol. 71
 Andreas Florian Kreß
Manipulation of the Light-Matter-Interaction in Photonic Crystal Nanocavities
 185 Seiten
 ISBN 3-932749-71-5
- Vol. 72
 Markus Grau
Molekularstrahlepitaktische Herstellung von antimonidischen Laserdioden für die Gassensorik
 138 Seiten
 ISBN 3-932749-72-3
- Vol. 73
 Karin Buchholz
Microprocessing of silicon on insulator substrates and biofunctionalisation of silicon dioxide surfaces for sensing applications in fluids
 170 Seiten
 ISBN 3-932749-73-1
- Vol. 74
 Dominique Bougeard
Spektroskopische Charakterisierung von Germanium-Quantenpunkten in Silizium
 154 Seiten
 ISBN 3-932749-74-X
- Vol. 75
 Jochen Bauer
Untersuchungen zum kontrollierten Wachstum von InAs-Nanostrukturen auf Spaltflächen
 140 Seiten
 ISBN 3-932749-75-8
- Vol. 76
 Ingo Bormann
Intersubband Spektroskopie an Silizium-Germanium Quantenkaskadenstrukturen
 124 Seiten
 ISBN 3-932749-76-6

- Vol. 77
Hubert Johannes Krenner
Coherent quantum coupling of excitons in single quantum dots and quantum dot molecules
160 Seiten
ISBN 3-932749-77-4
- Vol. 78
Ulrich Rant
Electrical manipulation of DNA-layers on gold surfaces
249 Seiten
ISBN 3-932749-78-2
- Vol. 79
René Todt
Widely tunable laser diodes with distributed feedback
152 Seiten
ISBN 3-932749-79-0
- Vol. 80
Miroslav Kroutvar
Charge and spin storage in quantum dots
150 Seiten
ISBN 3-932749-80-4
- Vol. 81
Markus Maute
Mikromechanisch abstimmbare Laser-Dioden mit Vertikalresonator
170 Seiten
ISBN 3-932749-81-2
- Vol. 82
Frank Ertl
Anisotrope Quanten-Hall-Systeme, Vertikale Ultrakurzkanal- und Tunneltransistoren
170 Seiten
ISBN 3-932749-82-0
- Vol. 83
Sebastian M. Luber
III-V semiconductor structures for biosensor and molecular electronics applications
212 Seiten
ISBN 978-3-932749-83-4
- Vol. 84
Claudio Ronald Miskys
New substrates for epitaxy of group III nitride semiconductors: challenges and potential
207 Seiten
ISBN 978-3-932749-84-1
- Vol. 85
Sebastian Friedrich Roth
n- and p-type transport in (110) GaAs substrates, single- and double-cleave structures
138 Seiten
ISBN 978-3-932749-85-8
- Vol. 86
Mario Gjukic
Metal-induced crystallization of silicon-germanium alloys
309 Seiten
ISBN 978-3-932749-86-5
- Vol. 87
Tobias Zibold
Semiconductor based quantum information devices: Theory and simulations
151 Seiten
ISBN 978-3-932749-87-2
- Vol. 88
Thomas Jacke
Weit abstimmbare Laserdiode mit vertikal integriertem Mach-Zehnder-Interferometer
165 Seiten
ISBN 978-3-932749-88-9
- Vol. 89
Nenad Ocelić
Quantitative near-field phonon-polariton spectroscopy
174 Seiten
ISBN 978-3-932749-89-6

Vol. 90
Kenji Arinaga
Control and manipulation of DNA on gold and its application for biosensing
111 Seiten
ISBN 978-3-932749-90-2

Vol. 91
Hans-Gregor Hübl
Coherent manipulation and electrical detection of phosphorus donor spins in silicon
162 Seiten
ISBN 978-3-932749-91-9

Vol. 92
Andrea Friedrich
Quanten-Kaskaden-Laser ohne Injektorbereiche
140 Seiten
ISBN 978-3-932749-92-6

Vol. 93
Oliver Dier
Das Materialsystem (AlGaIn) (AsSb): Eigenschaften und Eignung für GaSb-basierte Vertikalresonator-Laserdioden
174 Seiten
ISBN 978-3-932749-93-3

Vol. 94
Georg Steinhoff
Group III-nitrides for bio- and electrochemical sensors
197 Seiten
ISBN 978-3-932749-94-0

Vol. 95
Stefan Harrer
Next-generation nanoimprint lithography: Innovative approaches towards improving flexibility and resolution of nanofabrication in the sub-15-nm region
161 Seiten
ISBN 978-3-932749-95-7

Vol. 96
Stefan Ahlers
Magnetic and electrical properties of epitaxial GeMn
184 Seiten
ISBN 978-3-932749-96-0

Vol. 97
Emanuele Uccelli
Guided self-assembly of InAs quantum dots arrays on (110) surfaces
172 Seiten
ISBN 978-3-932749-97-1

Vol. 98
Shavaji Dasgupta
Growth optimization and characterization of high mobility two-dimensional electron systems in AlAs quantum wells
152 Seiten
ISBN 978-3-932749-98-8

Vol. 99
Werner Hofmann
InP-based long-wavelength VCSELs and VCSEL arrays for high-speed optical communication
142 Seiten
ISBN 978-3-932749-99-5

Vol. 100
Robert Lechner
Silicon nanocrystal films for electronic applications
227 Seiten
ISBN 978-3-941650-00-8

Vol. 101
Nebile Işık
Investigation of Landau level spin reversal in (110) oriented p-type GaAs quantum wells
114 Seiten
ISBN 978-3-941650-01-5

- Vol. 102
Andreas Florian Härtl
Novel concepts for biosensors using diamond-based field effect transistors
255 Seiten
ISBN 978-3-941650-02-2
- Vol. 103
Felix Florian Georg Hofbauer
Realization of electrically tunable single quantum dot nanocavities
160 Seiten
ISBN 978-3-941650-03-9
- Vol. 104
Dominic F. Dorfner
Novel photonic biosensing based on silicon nanostructures
169 Seiten
ISBN 978-3-941650-04-6
- Vol. 105
Till Andlauer
Optoelectronic and spin-related properties of semiconductor nanostructures in magnetic fields
157 Seiten
ISBN 978-3-941650-05-3
- Vol. 106
Christoph Bihler
Magnetic semiconductors
190 Seiten
ISBN 978-3-941650-06-0
- Vol. 107
Michael Huber
Tunnel-Spektroskopie im Quanten-Hall-Regime
164 Seiten
ISBN 978-3-941650-07-7
- Vol. 108
Philipp Achatz
Metal-insulator transition and super-Conductivity in heavily boron-doped diamond and related materials
151 Seiten
ISBN 978-3-941650-08-4
- Vol. 109
Sebastian Strobel
Nanoscale contacts to organic molecules based on layered semiconductor substrates
140 Seiten
ISBN 978-3-941650-09-1
- Vol. 110
Ying Xiang
Semiconductor nanowires and templates for electronic applications
152 Seiten
ISBN 978-3-941650-10-7
- Vol. 111
Michael Kaniber
Non-classical light generation in photonic crystal nanostructures
177 Seiten
ISBN 978-3-941650-11-4
- Vol. 112
Martin Hermann
Epitaktische AlN-Schichten auf Saphir und Diamant
216 Seiten
ISBN 978-3-941650-12-1
- Vol. 113
Dominik Heiss
Spin storage in quantum dot ensembles and single quantum dots
196 Seiten
ISBN 978-3-941650-13-8
- Vol. 114
Tillmann Christoph Kubis
Quantum transport in semiconductor nanostructures
253 Seiten
ISBN 978-3-941650-14-5

- Vol. 115
Lucia Steinke
Magnetotransport of coupled quantum Hall edges in a bent quantum well
194 Seiten
ISBN 978-3-941650-15-2
- Vol. 116
Christian Lauer
Antimonid-basierte Vertikalresonator-Laserdioden für Wellenlängen oberhalb 2 µm
180 Seiten
ISBN 978-3-941650-16-9
- Vol. 117
Simone Maria Kaniber
Optoelektronische Phänomene in hybriden Schaltkreisen aus Kohlenstoffnanoröhren und dem Photosystem I
136 Seiten
ISBN 978-3-941650-17-6
- Vol. 118
Martin Heiß
Growth and properties of low-dimensional III-V semiconductor nanowire heterostructures
172 Seiten
ISBN 978-3-941650-18-3
- Vol. 119
Sandro Francesco Tedde
Design, fabrication and characterization of organic photodiodes for industrial and medical applications
277 Seiten
ISBN 978-3-941650-19-0
- Vol. 120
Danche Spirkoska Jovanov
Fundamental properties of self-catalyzed GaAs nanowires and related heterostructures
200 Seiten
ISBN 978-3-941650-20-6
- Vol. 121
Jürgen Sailer
Materials and devices for quantum Information processing in Si/SiGe
158 Seiten
ISBN 978-3-941650-21-3
- Vol. 122
Ilaria Zardo
Growth and raman spectroscopy studies of gold-free catalyzed semiconductor nanowires
184 Seiten
ISBN 978-3-941650-22-0
- Vol. 123
Andre Rainer Stegner
Shallow dopants in nanostructured and in isotopically engineered silicon
185 Seiten
ISBN 978-3-941650-23-7
- Vol. 124
Andreas J. Huber
Nanoscale surface-polariton spectroscopy by mid- and far-infrared near-field microscopy
144 Seiten
ISBN 978-3-941650-24-4
- Vol. 125
Marco Andreas Höb
Funktionalisierung von Gruppe IV-Halbleitern
186 Seiten
ISBN 978-3-941650-25-1
- Vol. 126
Daniel Claudio Pedone
Nanopore analytics – electro-optical studies on single molecules
114 Seiten
ISBN 978-3-941650-26-8
- Vol. 127
Casimir Richard Simeon Katz
Multi-alloy structures for injectorless Quantum Cascade Lasers
131 Seiten
ISBN 978-3-941650-27-5
- Vol. 128
Barbara Annemarie Kathrin Baur
Functionalization of group III-nitrides for biosensor applications
215 Seiten
ISBN 978-3-941650-28-2

Vol. 129
Arne Laucht
**Semiconductor quantum optics with
tailored photonic nanostructures**
232 Seiten
ISBN 978-3-941650-29-9

Vol. 130
Jia Chen
**Compact laser-spectroscopic gas sensors
using Vertical-Cavity Surface-Emitting
Lasers**
150 Seiten
ISBN 978-3-941650-30-5

Vol. 131
Leonhard Prechtel
**Ultrafast Photocurrents and Terahertz
Radiation in Gallium Arsenide and Carbon
Based Nanostructures**
160 Seiten
ISBN 978-3-941650-31-2